Structural Characterisation of MBE Grown Si and SiGe Material

Adrian R Powell

**Thesis submitted in partial fulfilment
of the requirements for the
degree of Doctor of Philosophy.
University of Warwick,
Department of Physics.**

December 1991

Summary

The application of advanced X-ray techniques, using both laboratory and synchrotron radiation sources, to the structural characterisation of semiconductor multilayer systems is described with reference to their use in understanding the growth by Molecular Beam Epitaxy of SiGe layers. These layers, prepared using VG V80 and VG V90 growth systems have been characterised for x-y uniformity and compositional reproducibility. The superlattice period dispersion, due to short term flux instabilities in the growth fluxes, has been measured by consideration of the relative heights of Pendellosung fringes present between the superlattice fringes in the X-ray diffraction rocking curve. This has allowed the period dispersion to be found to an accuracy of ± 0.3 nm. Interface roughness has been measured with X-ray reflectivity. This has shown significant (1.0±3 nm) long range (~70 nm) roughness at the $Si_{1-x}Ge_x$ to Si interface for $x = 0.4$ and $x = 0.6$ superlattices.

SiGe layers have been grown to well beyond the metastable critical thickness, and the residual strain remaining in the structures found from use of two reflections in double crystal X-ray diffraction. This work has demonstrated an empirical relationship between thickness/critical thickness and the degree of residual strain remaining in the layer. This relationship is found to be independent of the Ge content of the epitaxial layer. SiGe layers have also been grown beyond the equilibrium critical thickness but less than the metastable critical thickness. Standard anneals have been carried out on these layers allowing determination of how the layers relax with varying composition and thickness. The misfit dislocations created are found to be longer for layers with lower degrees of strain. By growing layers with longer misfit dislocations relaxed buffer layers have been produced with threading dislocation densities of ~10^6 cm^{-2} and a surface roughness of ±3 nm.

To avoid growing highly dislocated SiGe layers SiGe has been grown on a Si substrate which has been etched to provide "mesa" structures of size varying from 1500 μm to 1 μm in width. Mesa islands smaller than 15 microns across show no misfit dislocations and rectangular islands 15 microns wide and 100 microns long have misfit dislocations running in one direction only indicating that relaxation in the other direction has taken place by elastic rather than plastic processes.

Characterisation of delta layers in Si using SIMS. is limited by cascade mixing to a depth resolution of 3 nm. Double axis X-ray diffraction using the interference effects between the Si below the delta layer and the Si above the delta layer has allowed the width of B delta layers to be determined to ±0.5 nm. This technique has also been used to measure the strain due to the B delta thus allowing determination of the degree of activation of the dopant. Thermal annealling of B delta layers has shown that anneals at 700°C for 1 hour causes measurable broadening of the delta layers. Sb delta layers have also been examined and their widths found to be less than 2 nm.

Contents

Figure Captions

Acknowledgements

This research was carried out in the Physics and Engineering departments of Warwick University. I should like to thank the technical staff of both these departments for their high standard of work. Special thanks go to my supervisors Keith Bowen and Evan Parker, for supporting me throughout this work, and to the research staff in both departments particularly Richard Kubiak, Simon Newstead, Bob Barlow, Jarda Bradler, and Graham Cooke.

I should also like to acknowledge BEDE scientific for the loan of their reflectometer, and VG Semicon for financial support in the form of a CASE award

Final thanks go to Fiona for support and continual reading of this work from its inception to completion.

Declaration

The work presented in this thesis was carried out either by the author or at the instigation of the author. It is presented according to the guide-lines laid down in the regulations of the University of Warwick, see document Phys/PG3 (1988)

Several Parts of this study are in the process of being published. These are:

1 X-ray characterisation of a V90S SiGe MBE system. A.R.Powell et al, Proc Mat Res Soc **208** (1991) 161. Incorporated into chapter 5

2 X-ray diffraction and reflectivity characterisation of SiGe superlattice structures. A.R.Powell et al , Semiconductor Science and Technology 7 (1992) 627. Incorporated into chapter 5

3 Characterisation of interfaces in SiGe superlattices by combined grazing incidence X-ray fluorescence and reflectivity. A.R.Powell et al, Proc. Mat. Res. Soc. **238** 653. Incorporated into chapter 5

4 Residual Strain and defect analysis in as grown and annealed SiGe layers. A.R.Powell et al, Proc. Mat. Res. Soc. **220** 277. Incorporated into chapters 6 and 7

5 Elemental boron and antimony doping of MBE Si and SiGe structures grown at temperatures below 600°C. A.R.Powell et al, J.Cryst.Growth, **111** (1991) 907. Incorporated into chapter 8

6 Structural and electrical properties of B delta layers in Si. A.R.Powell et al, Semiconductor Science and Technology **6** (1991) 227. Incorporated into chapter 8

7 X-ray diffraction characterisation of Sb delta doping in Si. A.R.Powell et al, J.Phys.D:Appl.Phys **23** (1990) 1745. Incorporated into chapter 8

8 X-ray characterisation of boron delta layers in Si and SiGe. A.R.Powell et al, Proc. Mat. Res. Soc. **220** 115. Incorporated into chapter 8

Chapter 1

Introduction

1.1 Importance of Si and SiGe Technology

Silicon technology is highly developed when compared to alternative materials systems such as III-V semiconductors. However III-V materials offer higher carrier mobilities and hence the possibility of significantly faster device operation, and in addition the direct band gap of some of the III-V materials allows production of optical devices such as lasers. The possibility of growing high mobility / direct bandgap materials on Si substrates offers the advantages of the developed Si technology with the superior electrical properties of III-V and Ge materials.

Early work on the growth of GaAs on Si [Tsaur et al 1981] demonstrated the possibility of combining the materials systems. However there are major problems, first, Si is a dopant in III-V materials and vice versa and second the large lattice mismatch between Si and appropriate III-V materials leads to poor material quality.

The use of SiGe alloys allows heterostructures to be produced without any cross-doping, and low Ge content alloys provide low lattice mismatch systems. As the lattice mismatch is reduced (from ~4% for pure Ge) layers can be grown to useful thicknesses (100nm at 1% mismatch) before the relaxation of strain causes a

catastrophic increase in the number of dislocations. SiGe offers the possibility of high mobility material [Manasevit et al 1982] and a range of bandgaps (from 1.1eV to 0.7eV) depending upon the alloy composition and the strain present in the commensurate growth of this lattice mismatched material. The ability to alter the bandgap, by altering composition and strain, offers the possibility of improving many devices and producing novel devices [Jain and Hayes 1991, People 1985, Kasper and Bean 1988] such as;

a) the Heterojunction Bipolar Transistor, which is improved through the ability to suppress the reverse injection of carriers from base to emitter due to the inherent valence band offset [Shur 1986].

b) Modulation doped FETs; these produce a two dimensional gas of high mobility as the channel region, which improves gain and switching speeds [Pearsall and Bean 1986].

1.2 Why MBE ?

There are several growth techniques available for the growth of Si and SiGe epitaxial material, including Liquid Phase Epitaxy, Chemical Vapour Deposition and Molecular Beam Epitaxy. The major advantage inherent in the MBE growth technique is its relatively low growth temperatures. As growth temperature can be maintained below 850°C the smearing of dopant profiles due to diffusion is reduced and high resolution doping structures can be produced. MBE provides an additional advantage from the research viewpoint in that the use of elemental sources by-passes any complicated surface chemistry, and therefore theoretical models of the growth

mechanisms become practical: The commercial disadvantage of MBE is the fact that the sources are contained within the growth system consequentially the system must be opened to air to replace the Si and Ge sources periodically thus limiting wafer throughput.

1.3 Material Characterisation

As semiconductor device sizes have been reduced characterisation techniques have had to continually improve their resolution in order to provide information on the structures grown. Thus for the growth of low dimensional structures, techniques with sub-monolayer resolution are required for the structural characterisation. The material characterisation can be considered to divide into in four main areas:

i) The crystalline quality. This is particularly significant, with information on defects such as dislocations of particular importance when device production is to be considered. The presence of contaminants, eg metals, within the material must also be detected and controlled as this can lead to device degradation.

ii) Layer Characterisation. To calibrate the growth systems the structure must be assessed to find the alloy layers composition, thicknesses and dopant levels.

iii) Interface quality. If structures are to be grown with sharp interfaces between regions of either different alloy compositions or doping levels then a knowledge of the abruptness and electrical properties of the interfaces is essential in order to optimise the growth conditions.

iv) Electrical characteristics. The electrical properties of the structures is of paramount importance; carrier concentrations, mobilities, and leakage currents require measurement.

1.4 Aims Of This Work

This thesis reports research in two major areas. Firstly the general characterisation of MBE grown SiGe material and in particular the relaxation properties of SiGe, and secondly the development of the X-ray characterisation techniques. X-ray diffraction has enabled the characterisation of very narrow delta layers of dopant in Si, and X-ray reflectivity and fluorescence have been investigated as techniques for the structural characterisation of SiGe layers.

A limitation of SiGe technology is the inability to produce thick layers of high crystalline quality $Si_{1-x}Ge_x$ alloy. This generally restricts device structures to compositions with $x < 20\%$. When SiGe layers become too thick and exceed the critical thickness they relax, and a large density ($10^{10}cm^{-2}$) of threading dislocations is created, which prevents the material being used in device fabrication.

In this work the relaxation behaviour of SiGe material is examined, which leads to a study of methods of producing relaxed SiGe material with lower threading dislocation densities due to the elongation of the misfit dislocations. This should open the way to producing thick high quality, high Ge content, SiGe alloy layers and superlattices. Recent work in this area [Powell et al 1991, Fitzgerald et al 1991, LeGouges et al 1991] have shown major reductions in threading dislocation densities and show promise for the production of threading dislocation free buffer layers. The growth of material on limited areas is also considered as an approach to

producing relaxed SiGe layers without the presence of threading or misfit dislocations by allowing elastic relaxation of the material.

A second area of interest in Si technology is the production of atomically thin layers of dopant for delta Field Effect Transistors and doping in SiGe superlattices. It is for these structures that the low temperatures involved in MBE growth are critical in preventing dopant diffusion. Characterisation of these doping layers has, however, proved difficult as few characterisation techniques have sufficient resolution to determine the width of these layers.

The problem of thin layer characterisation has been addressed in this work by optimising the double crystal diffraction technique through improvement of the beam conditioner optics. This has allowed, for the first time, determination of the true width of the delta doped layers along with their depth and the strain induced by the dopant atoms. The ability to measure the layer width to ± 0.5 nm has enabled the investigation of the resilience of the delta layers to the anneals associated with device processing.

X-ray reflectivity and glancing incidence X-ray fluorescence have been considered as characterisation techniques for the SiGe material. As there is a large electron density difference between Si and Ge, high quality rocking X-ray reflectivity curves can be obtained with SiGe structures, even for very thin layers and relaxed material. The reflectivity technique gives information on layer widths and compositions along with surface and interface roughnesses. X-ray fluorescence is examined as a prospective technique for providing information on the concentration depth profiles of matrix materials along with dopant profiles for materials with concentrations above $10^{17}cm^{-3}$ (provided that their atomic numbers are higher than ~ 10).

Chapter 2

Background of Si MBE

2.1 Introduction

Molecular beam epitaxy, MBE, is essentially the deposition of material onto a clean substrate under ultra high vacuum, (UHV), conditions. In order to achieve this there are three basic requirements.

i) A clean UHV system, to reduce contamination of epitaxial deposits from residual gas species.

ii) Evaporation of sources to provide molecular fluxes of matrix and dopant atoms.

iii) A clean heated substrate which promotes 2 dimensional growth.

The MBE technique offers the possibility of producing high quality material in structures in which the layer thicknesses can be controlled to monolayer accuracy [Powell et al 1991d]

2.2 Si MBE

In this work Si and SiGe material has been considered. This material was grown in two similar MBE growth systems, a VG Semicon V80 and a V90S. In the following three sections the growth system required for the Si MBE process is described.

i The UHV system

In order to produce high purity MBE material deposition must take place in ultra high vacuum. Fig 2.1 shows a schematic of the V90S deposition chamber.

The vacuum within the deposition chamber is maintained avoiding the use of oil pumps to reduce hydrocarbon contamination; initial rough pumping is achieved with oil-free rotary pumps and liquid nitrogen cooled sorption pumps. The UHV is obtained with a helium closed-cycle cryopump [Bradwell and Rodes 1985] and a Titanium sublimation pump [Roth 1979]. These pumps provide a background pressure at or below the limit of the vacuum gauges. After thorough degassing pressures in the 10^{-9} mbar range can be maintained during the deposition of material. The deposition chamber is attached to a preparation chamber where wafers can be stored under UHV conditions prior to and post deposition. Wafers are transferred in and out of the system via the load lock (pumped here with an ion pump [Roth 1979]) so that the system may be maintained under UHV conditions for the whole of a growth series.

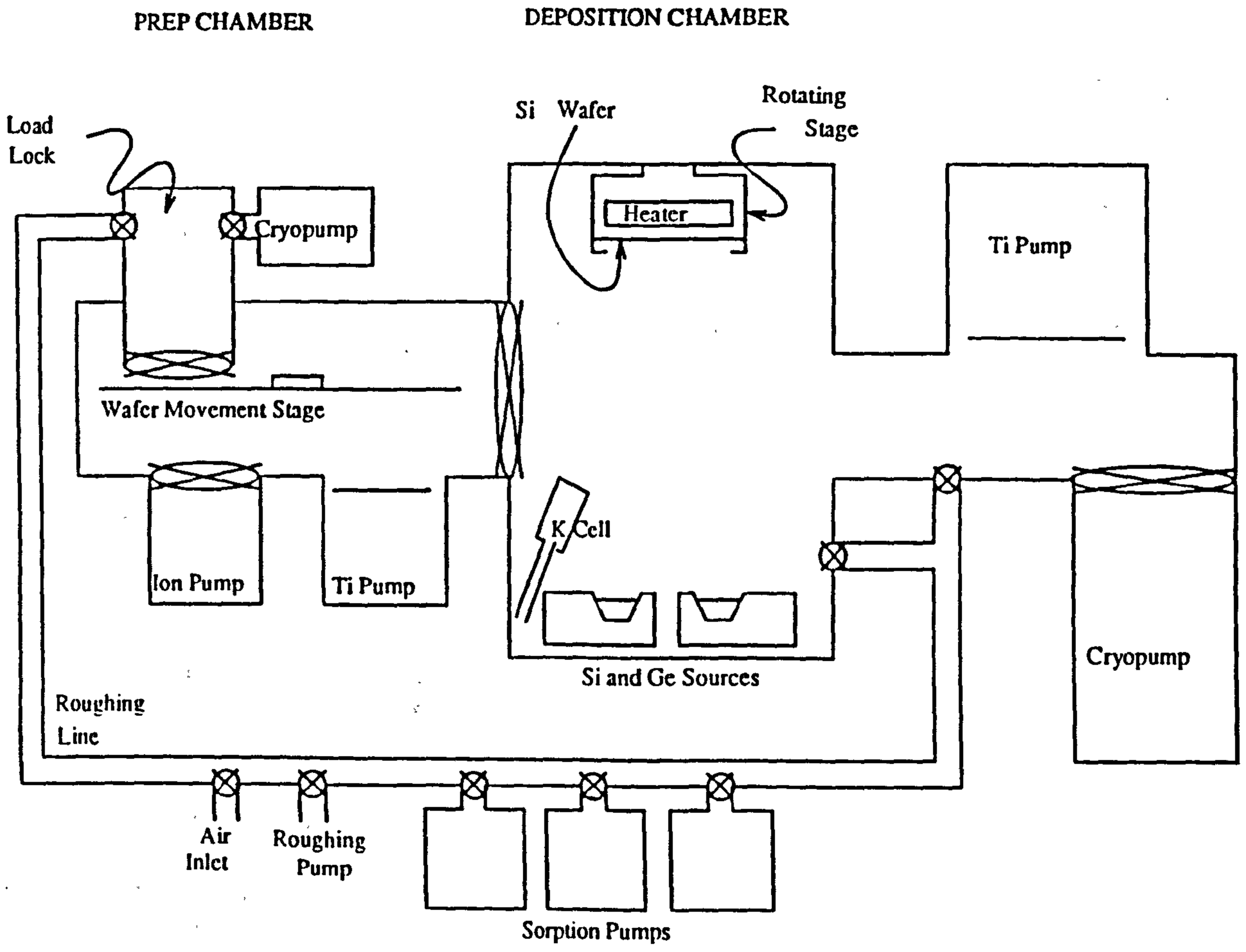

Fig 2.1 Schematic of the V90s MBE growth System

ii Flux Sources

Both Si and Ge require high temperatures in order to emit sufficient flux to provide a useful growth rate, of the order of 1 Å/sec. Since it is difficult to heat these elements to sufficiently high temperatures in a standard effusion cell [Kasper and Bean 1988] electron beam evaporation is used. Fig 2.2 shows a cross section of a Si source.

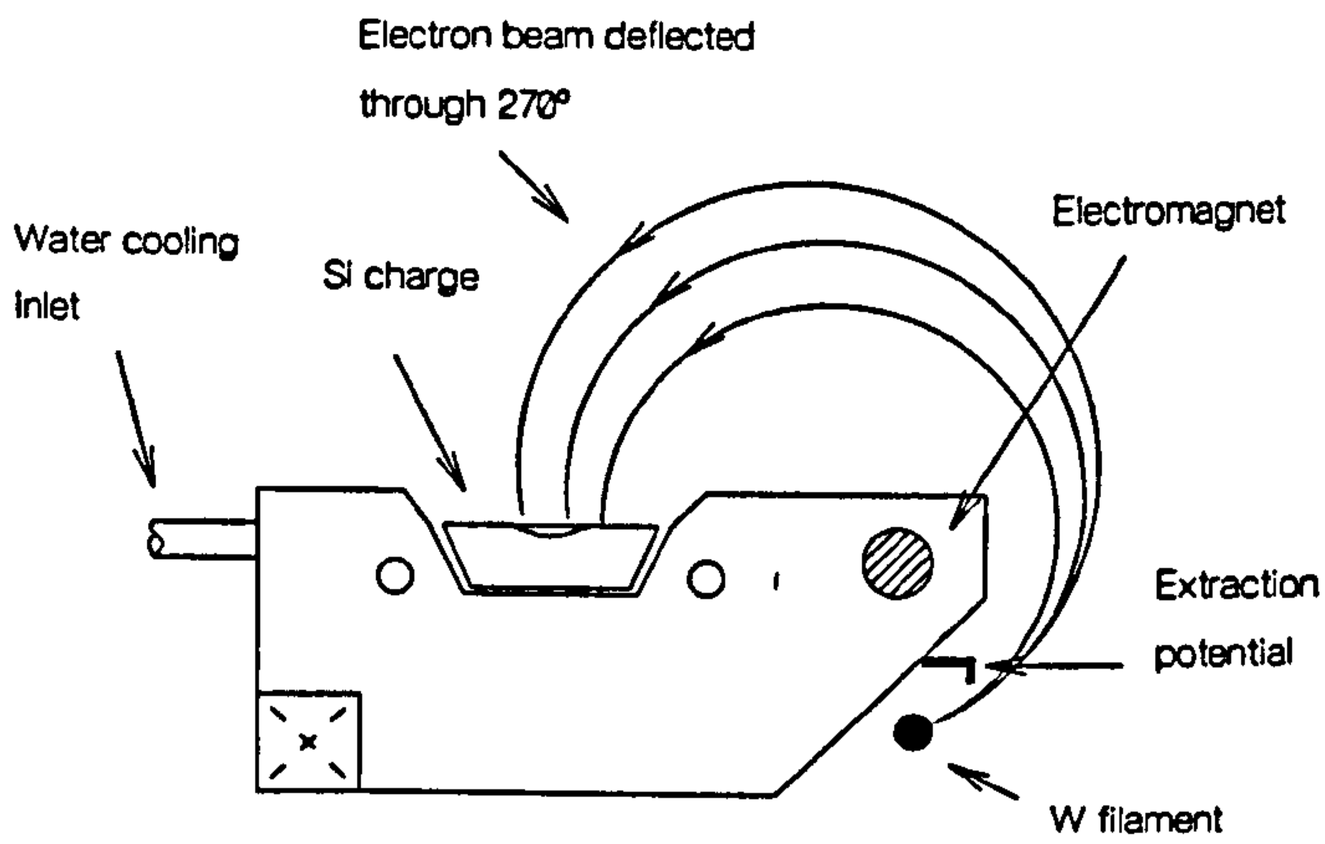

Fig 2.2 Schematic of the Si Electron beam evaporator.

In the electron beam evaporator, electrons are generated from a heated tungsten filament below the charge, and then magnetically bent through 270° to heat the source material. The electron flux is scanned across the central region of the matrix charge, which melts, and evaporation takes place from this region. In practice it is found that the emitted Si and Ge fluxes are highly variable and the fluxes were monitored using Sentinel III controllers, and altered via the current in the tungsten filament. The Sentinels sample a region of evaporated flux by exciting the atoms

with low energy electrons and measuring the infra-red radiation emitted. Finally a mechanical shutter is used to block the flux to the substrate when only one matrix flux is required during a growth run.

Dopant sources need to provide lower fluxes, most dopants including antimony can be evaporated from effusion (Knudsen) cells. Here the dopant material is contained within a cell which has a single orifice, facing towards the substrate, the whole cell is heated, (either radiatively or resistively) to a temperature where a sufficient flux is obtained from the material within the cell. The cell temperature controls the dopant flux in a repeatable manner so no flux monitoring is required, instead a calibration sample is grown in each growth series. Again mechanical shutters are employed to turn the doping on and off with atomic layer precision. Boron doping however requires higher temperatures (up to 2000°C) in order to provide sufficient flux for doping. The source for this [Kubiak et al 1985c] consists of a pyrolitic graphite tube enclosing the boron which is resistively heated to the high temperatures required. The boron then evaporates through a hole in the side wall of the graphite tube.

iii Substrate Conditions

During growth the Si substrate is positioned facing down at the top of the system. The cleanliness of the wafer surface is of critical importance for two dimensional growth and if high densities of defects nucleated from impurity precipitates are to be avoided. To achieve this the substrate undergoes an in-situ clean. Ex-situ cleans of a substrate can also be carried out using RCA cleans or Ozone reactive etches, however, the samples in this work either received no clean or a hydrogen passivation (a dip in hydrofluoric acid) as a previous study [Houghton 1989] demonstrated the manufacturers clean to be superior to that obtainable in our

laboratory. The in-situ clean consisted of heating the wafer to 850°C, under a low Si flux which provides a reactive ion etch to remove the surface oxide. The heating was achieved by radiatively heating the reverse side of the substrate. Care must be taken to avoid temperature gradients across the wafer, which cause slip lines to form. Wafers were then cooled to the growth temperature, generally between 850°C and 400°C and deposition carried out. A typical growth rate for this system is 0.1 nm/sec.

2.3 Crystal growth

In general in MBE two dimensional layer-by-layer growth is required as described by the BCF theory [Burton et al 1951]. In this we consider a substrate where there are more atoms arriving in the atomic flux than leaving by the process of desorption, thus there must be a net incorporation of atoms into the epitaxial layer. This growth takes place as shown in Fig 2.3 by

i) Arrival of atom on surface of layer. At Si and SiGe MBE growth temperatures, < 850°C, the probability of an atom desorbing again before incorporation is insignificant

ii) Diffusion of atom across surface to a step where incorporation takes place.

iii) Possible diffusion along the step edge to a kink site.

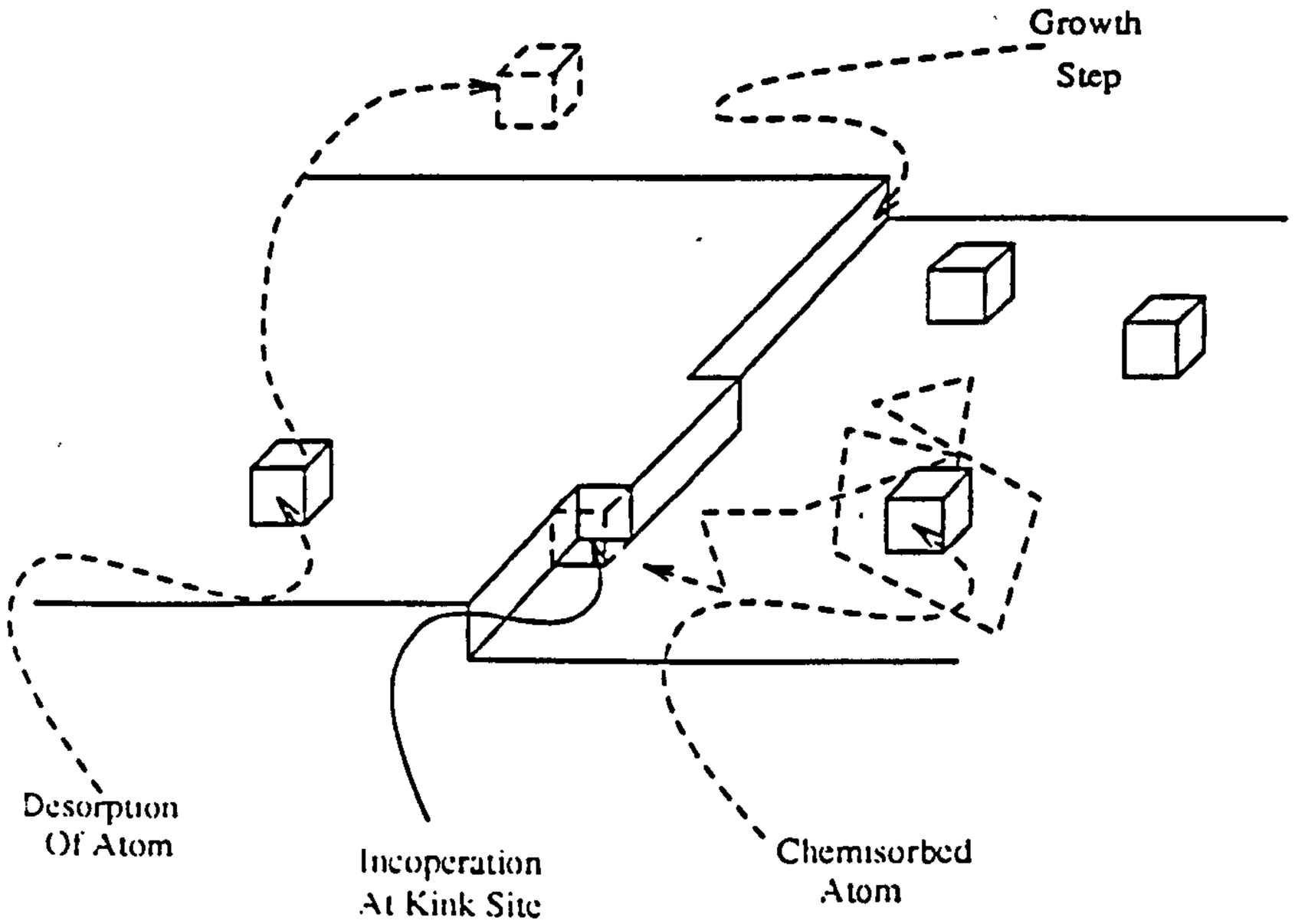

Fig 2.3 Arrival of atoms at a growing surface. Atoms will land and diffuse around on the surface until either desorbing or being incorporated at a kink site.

The distance between steps, L_s on a slightly misorientated substrate is simply calculated from a knowledge of the step height, for (100) Si, h = 0.271 nm and the misorientation angle, i.

$$L_s = h/\sin i$$

For wafers where the misorientation is small a step edge will form due to a number of atoms clustering together to form a monolayer high island and hence a new step edge [Kasper and Bean 1988]. These cluster-nucleated steps destroy themselves as a monolayer is completed and new clusters nucleate steps to form the next monolayer.

At usual growth temperatures, (450°C to 850°C) the diffusion distance of the atoms is so great that they will reach a step edge. Either a step edge due to wafer misorientation, or where wafer orientation is good, a step edge due to monolayer formation. In MBE the arrival rate of atoms is so high that describing the movement of atoms in terms of diffusion may no longer be correct, However, near a step edge the surface density of atoms will be considerably reduced due to incorporation at the step edge [Mullins and Hirth 1963] and thus the diffusion model can be used in the region close to the step edge. This growth mechanism has been directly observed with Scanning Tunnelling Microscopy [Horn et al 1987] during MBE growth.

At temperatures below 450°C the arriving atoms require more time to reach a step edge and be incorporated into a proper lattice site [Jorke et al 1989]. If this incorporation time becomes longer than the time required for a monolayer to form then the atoms bond to the surface - not in their correct lattice sites but frozen in as defects within the crystal. Each crystal defect creates disorder in the atoms above it and hence as more monolayers of Si are deposited the number of defects increase until a point is reached where the epitaxial layer can no longer be considered to be single crystal. This thickness depends upon the temperature and the growth rate and hence low temperature growth of single crystal material requires reduced growth rates. For the growth of Si on a Si substrate epitaxial growth can be achieved at temperatures down to room temperature [Eaglesham et al 1991].

2.4 Growth of SiGe

Growth of SiGe requires that consideration is given to lattice mismatch. Ge has a lattice parameter which is 4.17% larger than that of Si. This means that in order

to grow commensurately (ie with the SiGe planes of atoms aligning directly above those of the Si substrate) the unit cell of the SiGe epitaxial layer will be tetragonally distorted. Fig 2.4 shows SiGe both commensurately and incommensurately deposited on a Si substrate.

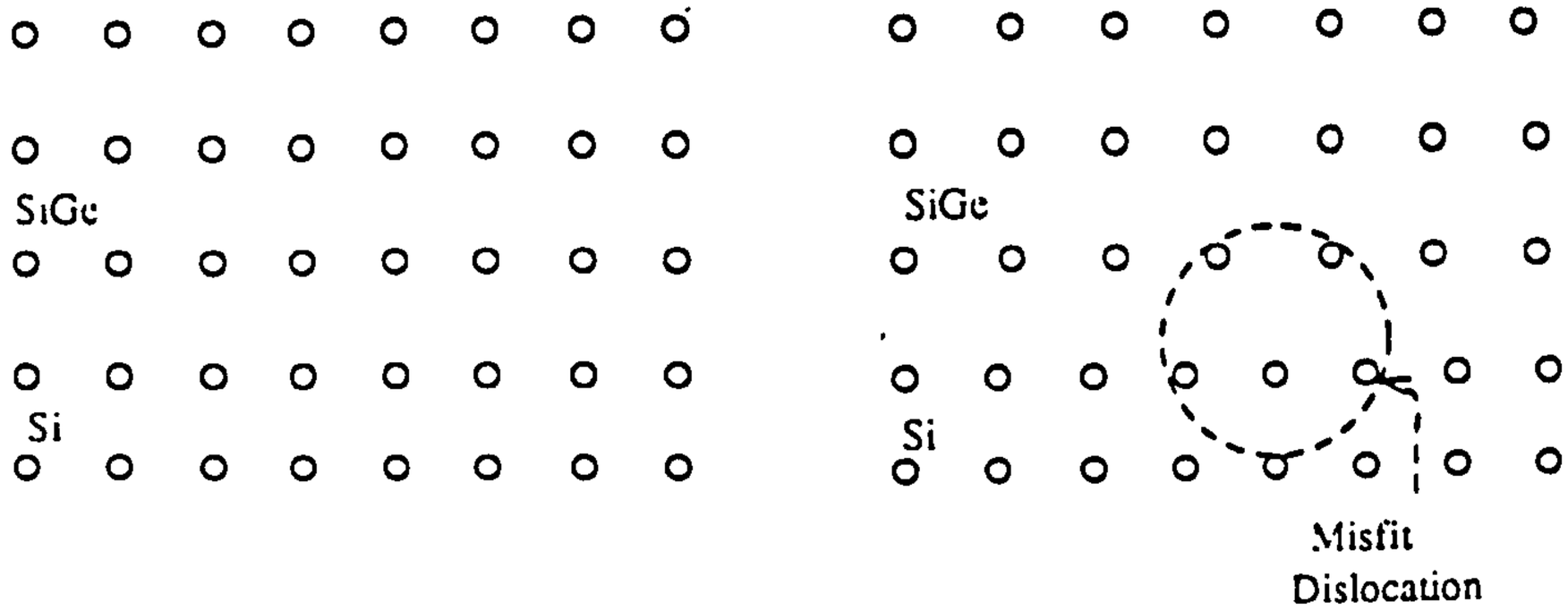

Fig 2.4 a) SiGe grown commensurately on a Si substrate. b) Incommensurate growth where plastic relaxation has occurred giving rise to a misfit dislocation going into the page.

As the thickness of a commensurate epitaxial layer increases the strain energy within the layer will increase. At some point, the equilibrium critical thickness, $t_{c\ equ}$, it will become energetically favourable for the layer to form misfit dislocations along the substrate/layer interface. Growth of commensurate material into a metastable region is possible beyond this thickness provided that growth temperatures are kept low; consequently most SiGe material is grown at ~ 550°C.

2.5 Doping Of Si and SiGe

The selection of the dopant species from groups III and V of the periodic table to dope Si and SiGe will be influenced by whether it is possible to evaporate the species satisfactorily. Ideally a reasonable flux rate should be obtained with an effusion cell temperature of ~ 1000°C. The magnitude of the flux required depends upon the sticking coefficient of the dopant species; for instance for B the sticking coefficient is 1, whereas for Sb the sticking coefficient varies by three orders of magnitude depending upon the substrate temperature. If the vapour pressure of the dopant source is too high then 'memory' doping effects will be seen. These are due to the dopant deposition on the system wall during doping and then later desorbing from the walls and contaminating the epitaxial layer. Too low a vapour pressure leads to the requirement to raise the effusion cell temperature in order to achieve a reasonable flux and can cause contaminants to be released from the components of the effusion cell. The dopant should also have suitable ionisation levels in the band gap, not diffuse significantly at growth temperatures, and incorporate easily into the growing surface. The sources used in this work were elemental Sb and B [Patel 1990]. Other sources tried have been B_2O_3 [Tuppen et al 1988], P [Patel 1990] Ga, Al [Becker and Bean 1977], and GaAs [Kubiak et al 1985 a]. Most of these sources have some associated problems usually being surface segregation or memory effects and the two used in this work are outlined below.

B has proved to be an excellent dopant which has few problems in incorporation [Parry 1991] allowing doping concentrations up to 10 atomic percent, At% [Powell 1991a] to be achieved. The B dopant can also be evaporated in its elemental form from an effusion cell at temperatures up to 1600°C.

Sb is not as ideal a dopant as at higher temperatures its sticking coefficient is poor and surface segregation occurs. Surface segregation is a serious problem if sharp doping profiles are required. This problem can however be avoided by interrupting growth to deposit the dopant and then continuing the growth at very low temperatures, <250°C, as is done for the growth of delta layers[Powell 1991a]. For bulk doping the problem of poor incorporation has been overcome with the use of Potential Enhanced Doping, PED. This consists of accelerating the ions normally present within the Si flux through a potential of up to 1.5 kV [Kubiak et al 1985 b] The Sb ions that are accelerated provide the energy required for incorporation of the Sb atoms present in the surface adlayer and thus doping levels of 10^{19} atoms/cm^{-3} can be achieved.

Chapter 3

Characterisation Techniques used by Author

In this chapter I shall discuss the techniques that I personally used to determine the quality and structure of Si and SiGe material. The following chapter will discuss characterisation techniques used to provide results for this thesis where the measurements were taken on my request by other workers.

3.1 X-Ray Diffraction-Introduction

In this work I am concerned with the characterisation of crystalline materials, these being materials where the constituent atoms form a regular periodic array in three dimensions. The use of X-ray diffraction to determine the positions of the planes of atoms within the crystal is well known, and when the reflected beam is considered it is called Bragg diffraction.

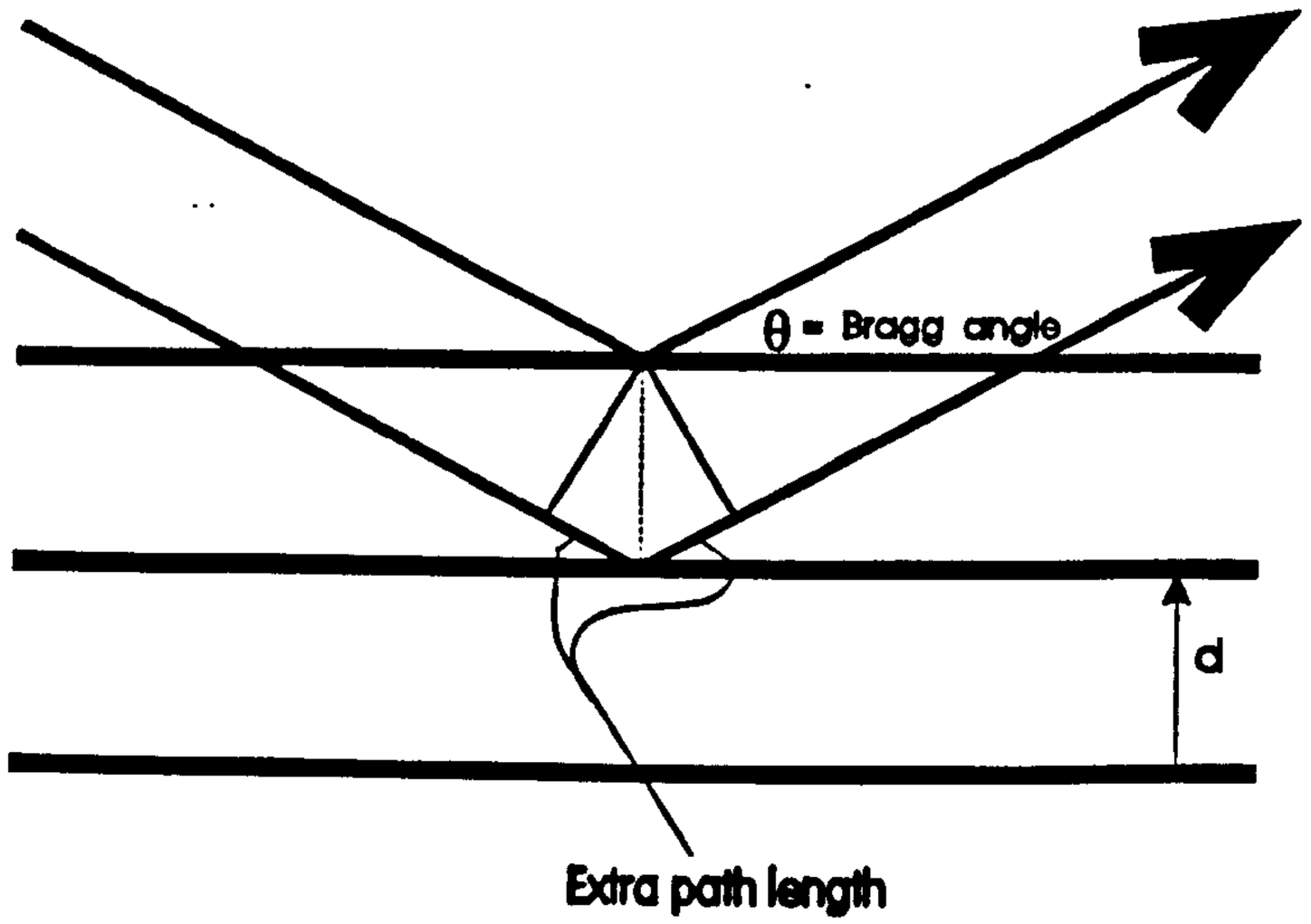

Fig 3.1 The orientation of crystal planes required to produce a Bragg reflection.

Bragg's law is expressed as

$$n\lambda = 2d\sin(\theta) \qquad (3.1$$

where

λ = wavelength

d = spacing of the atom planes

θ = Bragg angle

Having determined where Bragg peaks can occur the signal intensity at these angles must be considered. The diffracted intensity depends upon the strength of the reflection and the degree of absorption of the x-ray beam that occurs within the crystal. Let us first consider the strength of the reflection [Azaroff 1974].

The scatter from a single electron is described as

$$I_e = I_o (e^4/r^2m^2c^4)((1+\cos^2\theta)/2) \qquad (3.2$$

where

e = electron charge

I_o = incident intensity

r = distance from electron

m = electron mass

c = speed of light

This shows that the scattered intensity is greatest in the forward direction and falls off as the scatter angle increases. When an atom is considered which possesses Z electrons then it has a scattering factor of

$$f = \int U(r) \sin(kr) / kr \; dr \qquad (3.3$$

here

$U(r)$ = probability of finding an electron between r and dr

$k = 4\pi\sin\theta / \lambda$

This scattering factor is dependent upon the electron orbits occupied and values can be found in data books. Again the scattering factor is found to decrease with increasing scattering angle.

Finally a crystal unit cell has a structure factor

$$F_H = \sum f_n \exp[2\pi \mathbf{H}.\mathbf{r}] \qquad (3.4$$

here f_n = scattering factor of the n^{th} atom

$\mathbf{H}$ = incident wave vector

$\mathbf{r}$ = position of n^{th} atom in reciprocal space

This term again considers whether the atoms within the unit cell are scattering in or out of phase with each other, thus allowing for the situation where there is no net scattering from the unit cell at a Bragg reflection.

Once the structure factor for a reflection has been calculated then the effect of absorption of the x-ray beam within the crystal must be considered. The reduction of intensity, I, is given by

$$I/I_o = \exp[-\mu x] \qquad (3.5$$

Here

I_o = incident intensity

μ = linear absorption coefficient

x= distance travelled within the crystal

Thus by combining the reflection strength and the absorption in a numerical calculation the reflected intensity can be calculated for the Kinematical case.

3.2 Dynamical Theory

In order, accurately, to determine the structures giving rise to the rocking curves observed, it is necessary to use computer simulations to model the rocking curves. A simulation program can be based upon either the Kinematical or the Dynamical theory of X-ray diffraction. The Kinematical theory should be used where the diffraction is considered to be from many small regions of a size less than the penetration depth. In this case there is no significant interaction between the X-ray beams. Dynamical theory deals with the situation where there is a large highly perfect crystal and within the crystal there is significant interaction between the incident and diffracted beams. A number of reviews are available [Hart 1971, Batterman and Cole 1964, Tanner and Bowen 1980, James 1948, Pinsker 1978] on general dynamical theory and consequently in this work I shall only give a brief consideration of the dynamical theory underpinning the simulation programe used in this work.

In the region near to a Bragg diffraction peak the refractive index is influenced by the incident and diffracted beams and can not be considered as uniform. In dynamical theory the refractive index is taken as both periodic and anisotropic and thus the incident and diffracted wavevectors, k_o and k_h, may have slightly different values. Dynamical theory therefore sets out to find solutions which will satisfy both Bragg's law and Maxwell's equations.

Determination of Susceptibility

A crystal is periodic in all three dimensions and therefore its electron density, $\rho(r)$, can be described as a Fourier series

$$\rho(r) = {}^{1}/_{V} \sum F_{H} \exp[-2\pi i \mathbf{H}.\mathbf{r}] \qquad (3.6$$

here V = unit cell volume

$H = hb_1 + kb_2 + lb_3$, h,k,l = miller indices

b_1, b_2, b_3 = reciprocal lattice vectors

F_H = Structure Factor for h,k,l, reflections

Through a Fourier transformation the structure factor coefficients can be expressed as

$$F_H = \int \rho(r) \exp[2\pi i \mathbf{H}.\mathbf{r}] \, dv \qquad (3.7$$

If the atoms are considered to be independent scattering sources then one can consider the scattering from the individual atoms

$$F_H = \sum f_n \exp[2\pi i \mathbf{H}.\mathbf{r}] \qquad (3.8$$

here

f_n = scattering factor of the n^{th} atom

Now the refractive index can be expressed as

$$n^2 = \kappa = 1 - (4\pi e^2/m\omega^2)\,\rho(r) \qquad (3.9$$

here κ = dielectric constant

m = electron mass

ω = radiation frequency

The electric susceptibility can be expressed as

$$\chi = n^2 - 1 \sim (4\pi e^2/m\omega^2)\,\rho(r) \qquad (3.10$$

The susceptibility is periodic in real space, as it is a function of $\rho(r)$ and therefore it can be expressed as a Fourier series

$$\chi = \sum \chi_H \exp[-2\pi i \mathbf{H}.\mathbf{r}] \qquad (3.11$$

By comparison of equation 3.5 with 3.8 the relationship between the Fourier coefficients of the susceptibility and the structure factor can be found;

$$\chi_H = -1/V\,(4\pi e^2/m\omega^2)\,F_H \qquad (3.12$$

In practice for X-ray radiation χ is found to be $\sim 10^{-6}$. The path of the internal wave is slightly altered due to refraction, and as the refraction is periodic a number of

solutions to the Bragg condition can exist. These wavevectors which are solutions of the Bragg condition originate from what is termed the Dispersion Surface.

Allowed Wave Vectors

In addition to satisfying Bragg's law a satisfactory solution must also obey Maxwell's equations

$$\nabla \Lambda E = -\partial B/\partial t \qquad (3.13$$

$$\nabla \Lambda H = \partial D/\partial t \qquad (3.14$$

The wave equation can then be obtained from equations 3.13 and 3.14

$$\kappa \partial^2 D/\partial t^2 = (1/\mu_0 \varepsilon_0) \nabla^2 \Lambda D \qquad (3.15$$

A plane wave solution to the wave equation is a Bloch wave and this can be expressed in terms of the electric field as written below

$$D = \sum D_n \exp[-2\pi i \mathbf{k}.\mathbf{r}] \qquad (3.16$$

Now in the situation where only one reciprocal lattice point falls near the Ewald sphere there will only be two waves within the crystal with appreciable amplitude, these being the incident beam and the diffracted beam. Therefore, 3.16 may be written in terms of these two waves;

$$D = D_0 \exp[-2\pi i K_0.r] + D_H \exp[-2\pi i K_H.r] \qquad (3.17$$

Batterman and Cole (1964) show that the amplitudes of the two waves can be expressed as shown in the equations 3.18 and 3.19. Included in these equations is a polarisation factor "C". For σ radiation (perpendicular to the plane of incidence defined by the incident and diffracted beams) **C = 1**. With π polarised radiation, where the initial radiation is in the plane of incidence and normal to the incident beam, when the beam is diffracted through an angle of 2θ the amplitude is reduced by a factor of $\cos 2\theta$

$$\{k^2(1+\chi_0) - K_0.K_0\}D_0 + k^2C\chi_{H^*} D_H = 0 \qquad (3.18$$

$$k^2C\chi_H D_0 + \{k^2(1+\chi_0) - K_H.K_H\}D_H = 0 \qquad (3.19$$

In equation 3.18 χ_{H^*} represents the complex conjugate χ_H and it can be considered to represent scattering of the diffracted beam back into the direction of the incident beam. For non-trivial solutions to these equations the determinant of these combined equations must equal zero.

$$\begin{vmatrix} k^2(1+\chi_0) - K_0.K_0 & k^2C\chi_{H^*} \\ k^2C\chi_H & k^2(1+\chi_0) - K_H.K_H \end{vmatrix} = 0 \qquad (3.20$$

In order to simplify this equation "difference parameters" ξ_0 and ξ_H can be substituted into equation 3.20.

$$2k\xi_0 = K_0.K_0 - k^2(1+\chi_0) \quad (3.21$$

$$2k\xi_H = K_H.K_H - k^2(1+\chi_0) \quad (3.22$$

These represent the difference between the actual wave vector inside the crystal and what would be expected if an average value for the refractive index were used. They enable equation 3.18 to be simplified to;

$$\xi_0\xi_H = 1/4\, k^2C^2\chi_H\chi_{H*} \quad (3.23$$

This equation essentially allows the dispersion surface to be drawn out in reciprocal space. The dispersion surface represents the locus of the origins of the allowed wave vectors in reciprocal space and its properties will be considered in the next section.

The Dispersion Surfaces

When considering ξ_0 and ξ_H for the dispersion surfaces only the real parts are taken, as the complex component represents absorption. Fig 3.2 shows the Laue and Lorentz points.

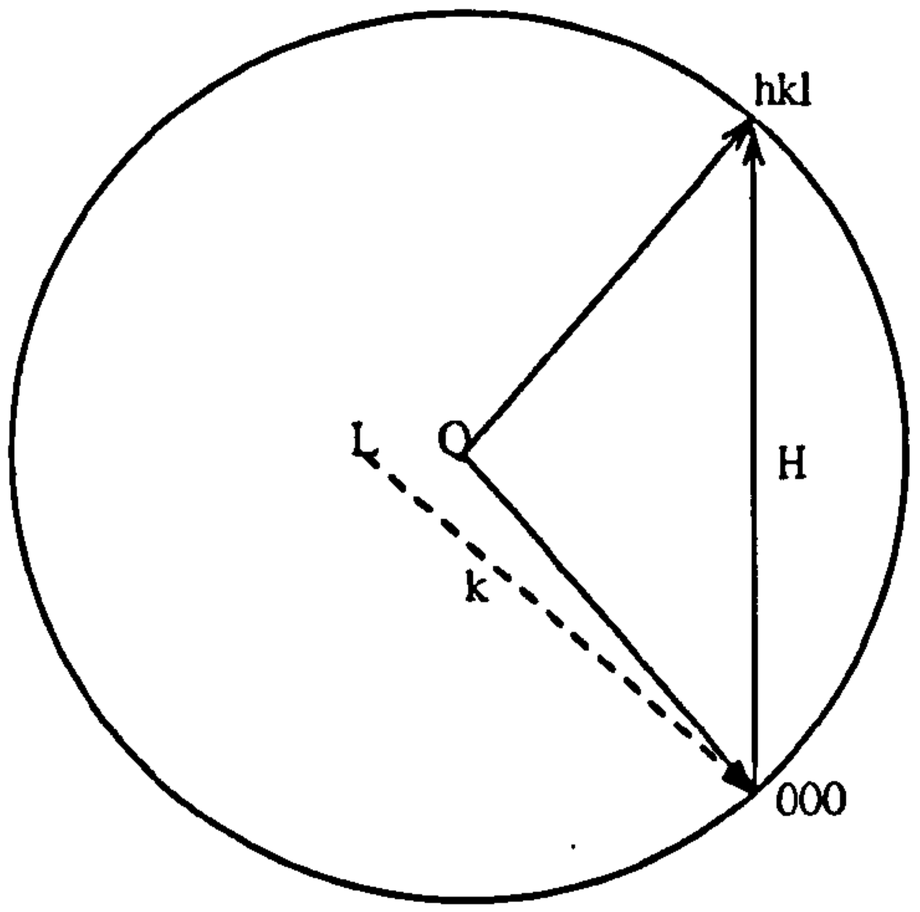

Fig 3.2 Lorentz,Q, and Laue, L, points in reciprocal space, k represents the external wave vector and H represents the reciprocal of the separation of the diffracting planes.

The Laue point, L, would be the centre of the Ewald sphere if the susceptibility within the crystal were equal to zero. The Lorentz point, Q, is where the Ewald sphere is centred.

In Fig 3.3 the region about the Lorentz point is expanded and circles of radius equal to k and $k(1-1_{/2}\chi_0)$ have been drawn about the reciprocal lattice points. The dispersion surfaces can then be considered as hyperbolic sheets whose asymptotes are defined by O"O' and H"H'. The distance of the dispersion surfaces from the spheres around O and H is defined by the difference parameters ξ_0 and ξ_H.

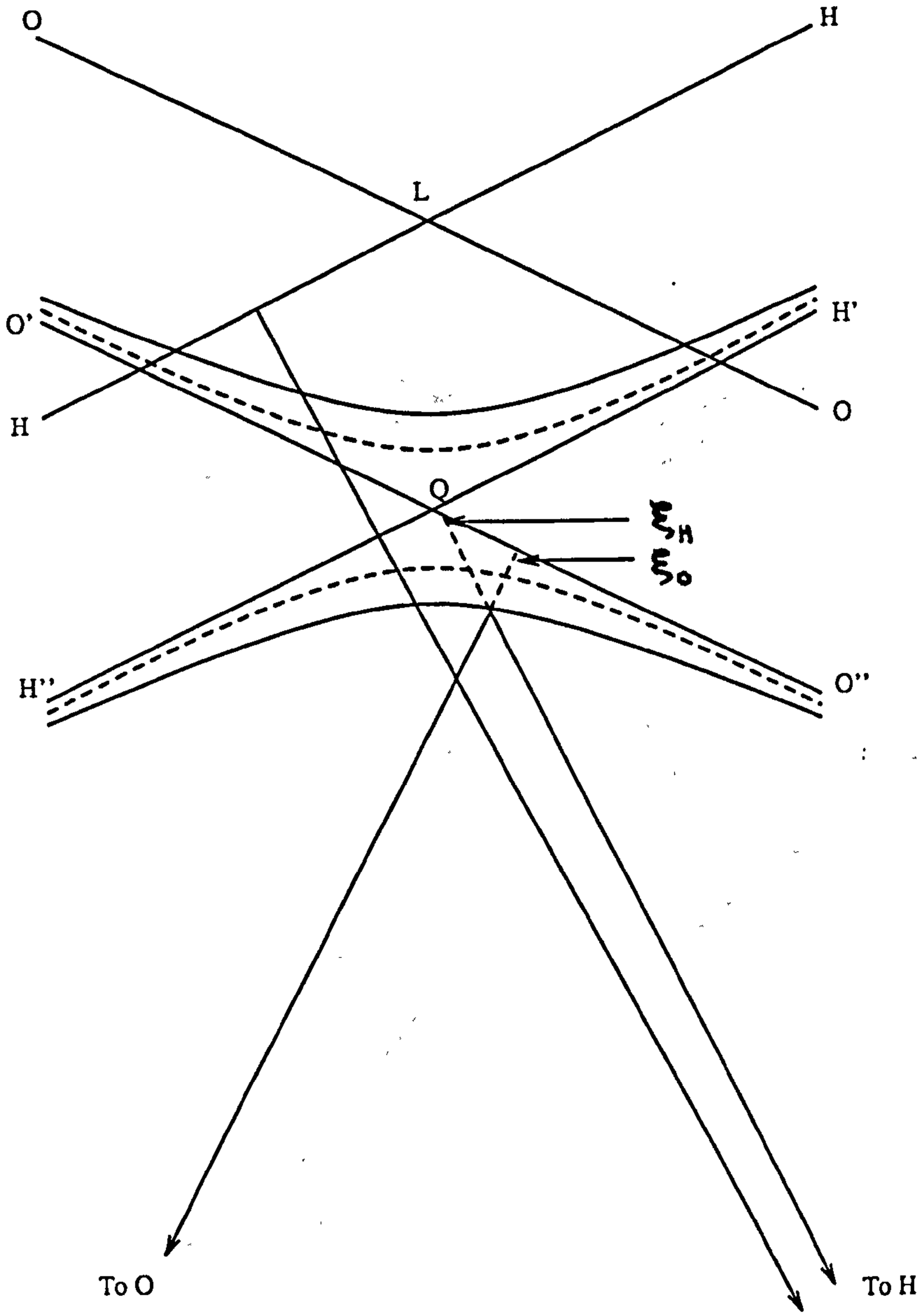

Fig 3.3 The dispersion surface

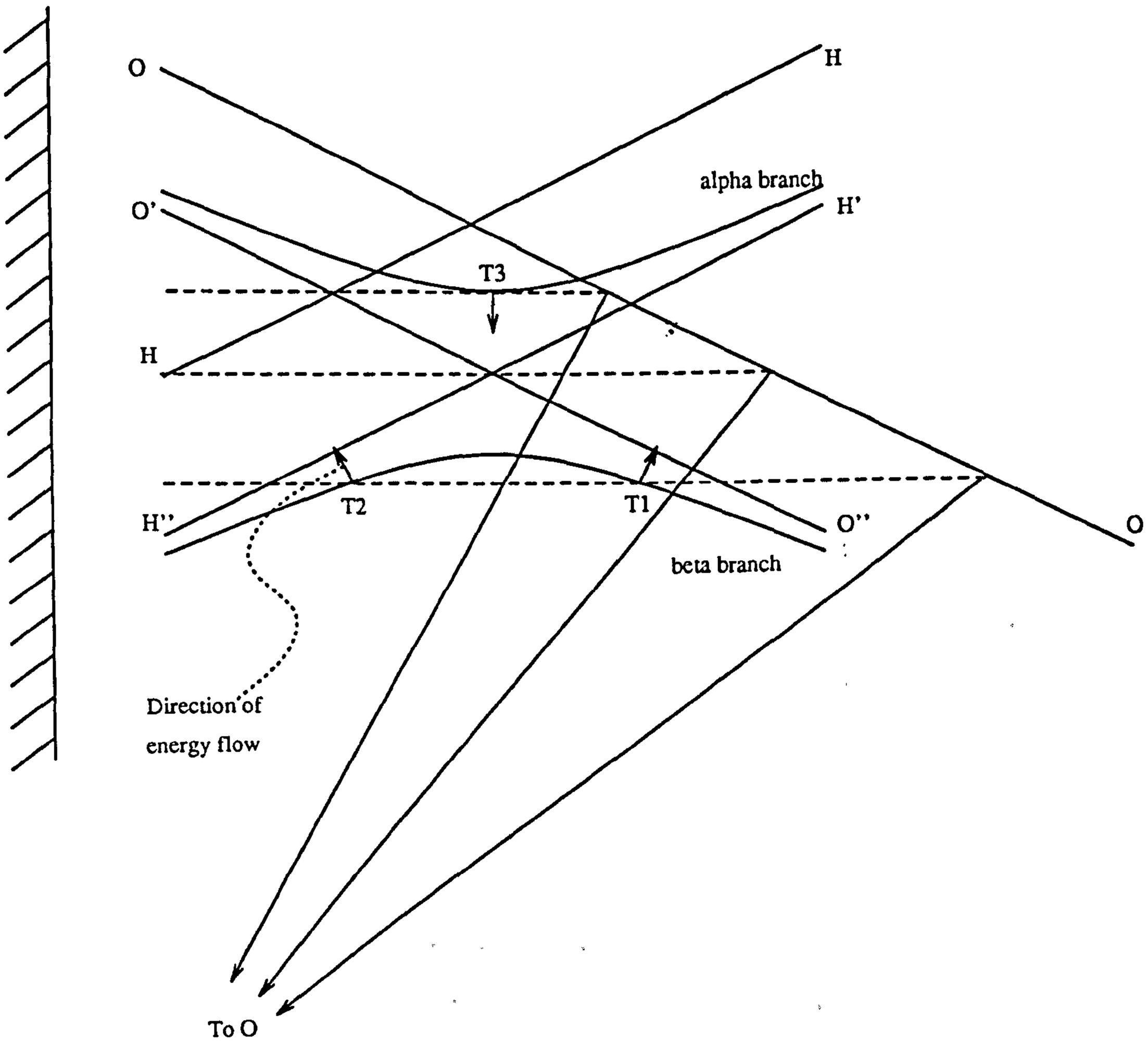

Fig 3.4 The Dispersion surface and boundary construction

Having found that the dispersion surface defines which wavevectors are allowable let us consider the amplitudes of the wave vectors associated with each "tie point" on the dispersion surface. We are concerned with the amplitude of the diffracted beam with respect to the incident beam ie D_H/D_0. By substituting equations 3.21 and 3.22 into equations 3.18 and 3.19 D_H/D_0 is found to be;

$$D_H/D_0 = 2\xi_0/C\chi_{H^*}\, k = C\chi_H\, k/2\xi_H \qquad (3.24$$

In Fig 3.3 the amplitude ratio is shown for various parts of the dispersion surface. The regions where D_H/D_0 is greater than 1 require a power source within the crystal thus for thick crystals allowable tie points lie in the regions where $D_H/D_0 \leq 1$.

Let us now consider how the dispersion surface can be used to produce rocking curve data. If a wave is incident on the crystal surface the component of the wavevector parallel to the surface must remain unchanged in order to match the phase fronts and the change in the wavevector must be in the direction normal to the surface. Thus the wavevector undergoes a slight change in direction. In Fig 3.4 the dispersion surface for a symmetric Bragg diffraction is shown along with three possible wavevectors with differing incident angles. If only the σ polarisation is considered wave 1 could excite two tie points, T_1 and T_2, however, if a thick crystal is assumed then only T_1 is excited and the intensity of the diffracted beam is found from comparing the difference parameters. Wave 2 however excites no tie points thus implying that only evanescent waves can exist within the crystal hence total external reflection is obtained, except for the effect of absorption on the evanescent wave. Wave 3 excites one tie point T_3 in a manner similar to wave 1 however this tie point

is on the opposite branch of the dispersion surface. Consideration of the diffracted intensity allows the zero absorption, Darwin, curve to be drawn as in Fig 3.5.

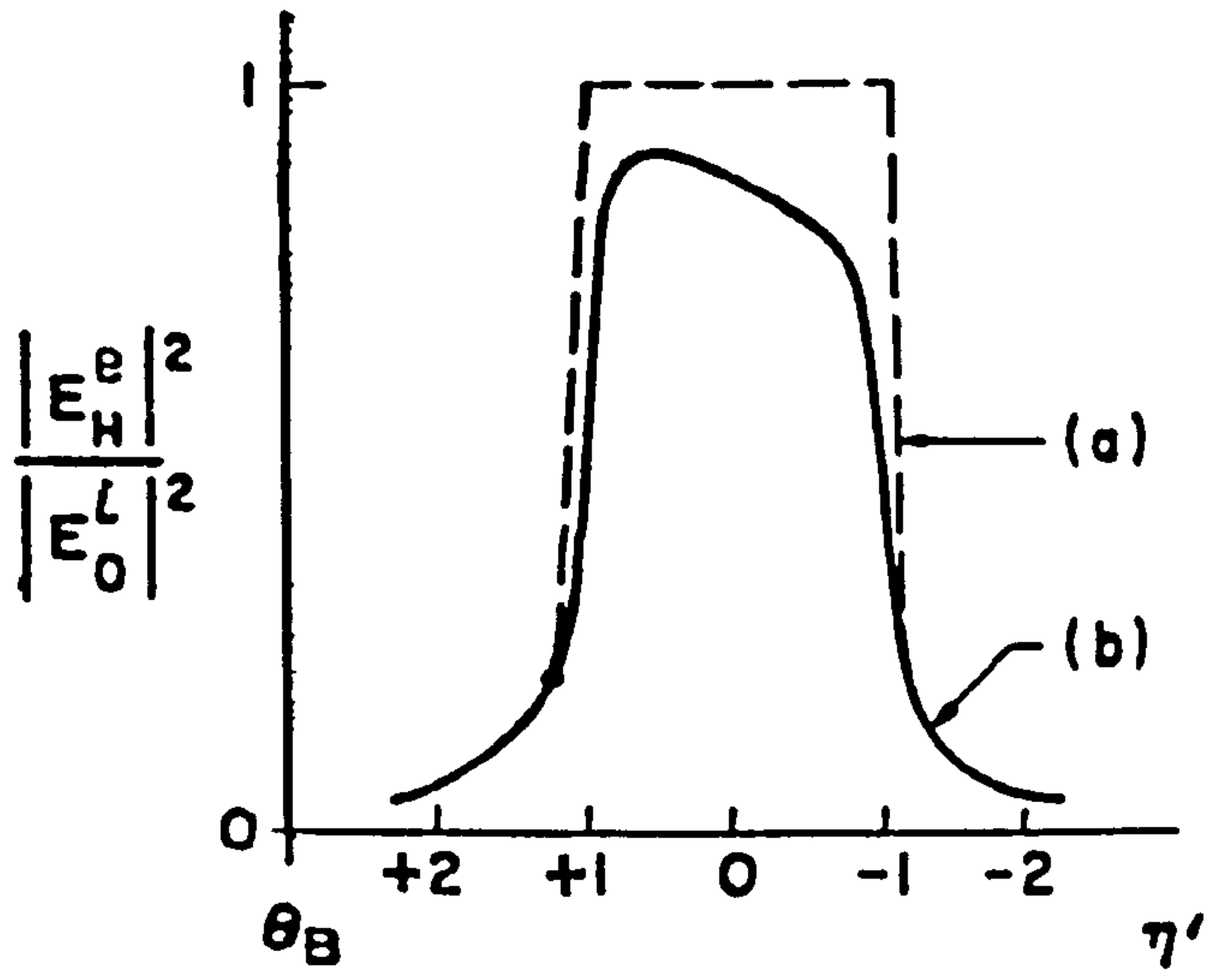

Fig 3.5 Shape of the Bragg reflection from a perfect crystal. The upper dotted curve is for zero absorption(Darwin curve) and the lower curve is with absorption (Darwin-Prins curve). [Batterman and Cole 1964]

If the case of a thin epitaxial layer on top of a thick substrate is considered there exists the possibility of diffracted energy from the underlying crystal and hence tie points in the region $D_H/D_0 > 1$ can be excited in conjunction with points in the region $D_H/D_0 \leq 1$. As two tie points are excited there exist within the crystal two diffracted waves travelling in very similar directions and hence interference effects are expected to be seen as indeed is the case for thin layers and superlattices.

Dispersion and Absorption

So far the effects of dispersion and absorption have been ignored. However, both these effects can be phenomenologically accounted for by considering susceptibility as a complex quantity and including correction terms within the structure factor. A real term $\Delta f'$ represents dispersion and a complex term $\Delta f''$ accounts for absorption.

$$F_H = \sum (f + \Delta f' + i\Delta f'')_n \exp[\, 2\pi i \mathbf{H}.\mathbf{r}] \qquad (3.25$$

The effect of this can be seen in the lower curve of Fig 3.5 where absorption effects have been included. It may be noted that the curve is asymmetrical. This is due to the fact that on the α branch of the dispersion curve the antinodes of the standing wave field within the crystal are between the atom planes. However, on the ß branch the standing wave nodes fall on the atom planes and, therefore, suffer higher absorption thus leading to a reduction of diffracted intensity on the high angle side.

The extinction depth of the wave at the Bragg condition is found from considering the separation of the two branches of the dispersion surface and the inclination of this vector with the incoming and exiting beams. Substitution of equation 3.12 in to 3.26 gives the equation in terms of the structure factor.

$$d_{exp}^{-1} = \frac{\lambda \sqrt{(\gamma_h \gamma_o)}}{c \sqrt{(\chi_H \chi_{H^*})}} = \frac{m_e c^2 \pi \sqrt{(\gamma_h \gamma_o)} V}{e^2 \lambda |F_h|} \quad (3.26$$

here

$\gamma_h = \sin(\theta+\phi)$

$\gamma_o = \sin(\theta-\phi)$

ϕ = angle between diffracting planes and the crystal surface

3.3 Simulation program

The computer simulation program used is based on dynamical theory and uses equations put forward by Takagi and Taupin in order to describe reflections in material where the susceptibility varies due to variable strain and composition. The Takagi-Taupin equations allow calculation of the amplitude of the incident and diffracted beams as a function of depth.

$$(i\lambda/\pi)\, \partial D_o/\partial u_o = \chi_o D_o + C\chi_{H^*} D_H \quad (3.27$$

$$(i\lambda/\pi)\, \partial D_H/\partial u_H = (\chi_o - \alpha_H) D_H + C\chi_H D_o \quad (3.28$$

here

$\alpha_H = -2\Delta\theta \sin 2\theta_v$

$\Delta\theta$ = local variation from the vacuum Bragg angle

θ_v = vacuum Bragg angle

$u_o\, u_H$ = incident and diffracted unit vectors

Consider a sample with varying strain and composition within the epitaxial layer. This can be split into a number of lamina with uniform susceptance within the individual lamina. Then one needs to determine how the amplitude ratio, $X = D_o/D_H$, changes between the bottom and the top surfaces of the lamina.

In order to achieve this one must differentiate the amplitude ratio with respect to depth

$$dX/dz = d(D_o/D_H)/dz = (1/D_H)\partial D_o/\partial z - (D_o/D_H^{\,2})\partial D_H/\partial z \qquad (3.29$$

here

$$z = K_o\gamma_o + K_H\gamma_H$$

γ_o, γ_H are the direction cosines of the incident and diffracted beams.

Substitution of equations 3.27 and 3.28 gives

$$dX/dz = (i\pi/\lambda\gamma_o)(C\chi_{H^*}X^2 + ((1-\gamma_o/\gamma_H)\chi_o + \alpha_H\gamma_o/\gamma_H)X - C\chi_H\gamma_o/\gamma_H) \qquad (3.30$$

Use of the substitutions below allows simplification of equation 3.30

$$A = C\chi_{H^*} \qquad 2B = (1-\gamma_o/\gamma_H)\chi_o + \alpha_H\gamma_o/\gamma_H$$

$$D = \pi/\lambda\gamma_o \qquad E = -C\chi_H\gamma_o/\gamma_H$$

Thus

$$dX/dz = iD(AX^2 + 2BX + E) \qquad (3.31$$

Hence for a lamina with constant susceptibility the amplitude ratio can be expressed as a function of the height, Δz, above the base of the lamina, where the amplitude ratio at the bottom surface is known to be X_o

$$X_{top} = \frac{X_o(BB\text{-}EA)^{0.5} + i(BX_oE)\tan(D(BB\text{-}EA)^{0.5})\Delta z}{(BB\text{-}EA)^{0.5} - i(AX_o+B)\tan(D(BB\text{-}EA)^{0.5})\Delta z} \qquad (3.32$$

For a computer simulation (in this work RADS was used [Bowen et al 1991]) one first considers the amplitude ratio expected from a perfect semi-infinite substrate where the component of the electric field exiting from the base is zero and hence $X_o = 1$ for this semi-infinite layer. Then one can build up to the surface by taking one lamina at a time and working out the amplitude ratio at the top surface of the lamina and then considering the next lamina.

3.4 X-ray Reflectivity

In addition to the use of X-rays to provide information on the atom plane positions, information on the electron density can be obtained from low angle scattering or reflectivity. The essential theory for the reflectivity of x-rays from a material in which the electron density changes as a function of depth was put forward by Parratt [Parratt 1954] using the Fresnel reflectivity formulation. Here the sample is considered to consist of a number of lamina each of which has a constant electron

density. The reflectivity, R, at the top of each lamina is then given in terms of the value of R at the top of the previous lamina by the recursion formula below:

$$R_{n-1,n} = a_{n-1}^{4} \quad \frac{R_{n,n+1} + F_{n-1,n}}{R_{n,n+1}F_{n-1,n} + 1} \qquad (3.33$$

Here $a_n = \exp[-i\pi f_n d_n/\lambda]$

$$F_{n-1,n} = \frac{f_{n-1}-f_n}{f_{n-1}+f_n}$$

$$f_n = (\varphi^2 - 2\delta_n - 2i\beta_n)^{0.5}$$

where the refractive index, n is given by

$$n = 1 - \delta_n - i\beta_n$$

φ = angle of incidence

This is solved by working up from the substrate, which is considered to be semi-infinite in depth.

Roughness at the interfaces, including the surface, is considered as a Gaussian distribution [Nevot and Croce 1980, Sinha et al 1988] and thus the Fresnel

coefficient may be expressed as;

$$F_{n-1,n} = \frac{f_{n-1}-f_n}{f_{n-1}+f_n} \exp[-1/2\, \sigma_{n-1,n}{}^2 Q_n Q_{n-1}] \qquad (3.34$$

Here σ = root mean square of the roughness

$Q = 4\pi f_n/\lambda$

Expression 3.34 is then used in equation 3.33 to provide the basis of a simulation program that can vary layer composition, density and thickness, along with roughness at the surface and at the interfaces. This program (REFS) created by Wormington [Wormington 1991] is used in section 5.5 where the modelling parameters are considered.

3.5 Experimental Double Crystal Diffraction

In this work I am primarily working with thin epitaxial layers grown on a highly crystalline substrate with well-characterised material properties. Double crystal diffraction allows the epitaxial layer to be compared to the substrate and hence its plane spacings can be found and as the plane spacings of Si are well known, the true structure of the epitaxial layer can be found. Fig 3.6 shows a typical rocking curve obtained from a single SiGe epitaxial layer on Si. For the characterisation of epitaxial layers the distances from the epitaxial diffraction peaks to the substrate peak need to be measured to an accuracy of a few seconds of arc. From these distances

layer compositions, structures, and tilts can be calculated. However in order to achieve this a plane wave source is required.

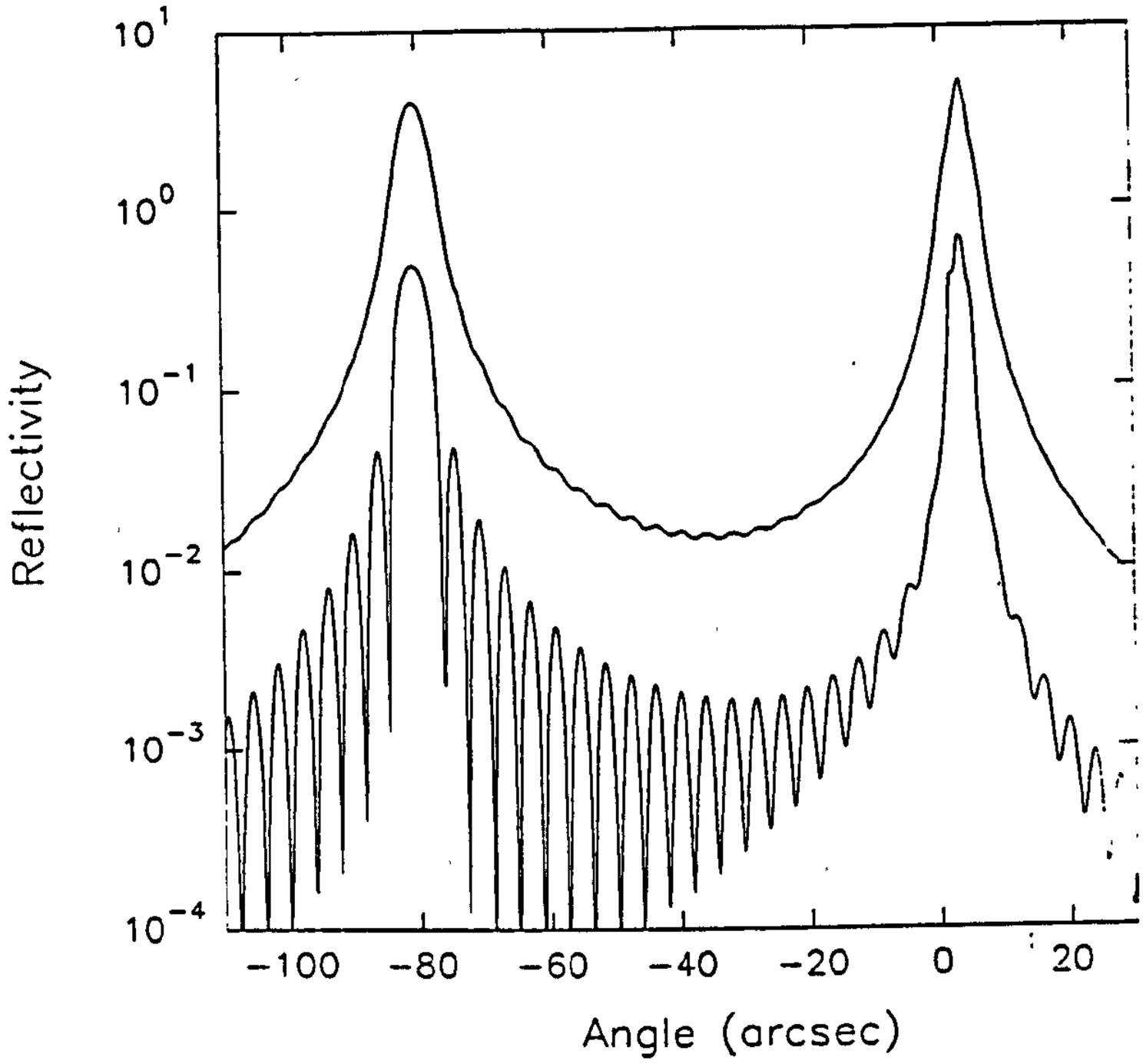

Fig 3.6 Two simulations are shown of a 8%, 6 micron SiGe layer; the upper curve is obtained using a single bounce beam conditioner(and multiplied by 10) and the lower curve is the ideal rocking curve with planar illumination.

In reality planar monochromatic sources are hard to come by and single or multiple bounce beam conditioners are used. If a standard tube source is considered it is not strictly monochromatic, ie a Cu source contains both Kα and Kß characteristic lines along with bremsstrahlung radiation. Also if a rocking curve is taken with this source the width of the diffraction peak obtained is essentially the angular dispersion defined by the width of any slit present divided by the distance from the slit to the

source which is generally several thousand arc seconds. Therefore if high angular resolution is required we must remove the detrimental effects of angular and wavelength divergence.

DuMond

In order to remove both the angular and wavelength dispersion an idea put forward by DuMond [DuMond 1937] is to cross correlate the rocking curve using a reference crystal of the same material. If we consider the wavelength passed as a function of Bragg angle, Fig 3.7a , we have a DuMond diagram for the first crystal. In the DuMond diagram the band of allowable transmission is not a delta function but has the width and shape of the characteristic Bragg reflection for the crystal in question. This pass band from the first crystal is correlated with the pass band of the second crystal which, if both crystals are identical, results in a pass band approximately 1.4 wider. Thus in practice the sample peak width can be accurately determined provided that the first crystal is of high crystalline quality.

Consider the situation where there are two similar crystals, where the first rotates the beam in a positive sense ie,'+' and the second rotates the beam in the opposite negative sense ' - 'Fig 3.7b. The first crystal and hence its DuMond curve is fixed. As the second crystal is rotated the curve moves to the left and over a narrow range of angle the two transmission conditions are satisfied and the X-ray beam is able to pass and what is termed a "rocking curve" is obtained which provided that the first crystal is of high quality is very similar to that obtained using a plane wave source. As implied above it is the cross correlation of the plane wave curves from the two crystals.

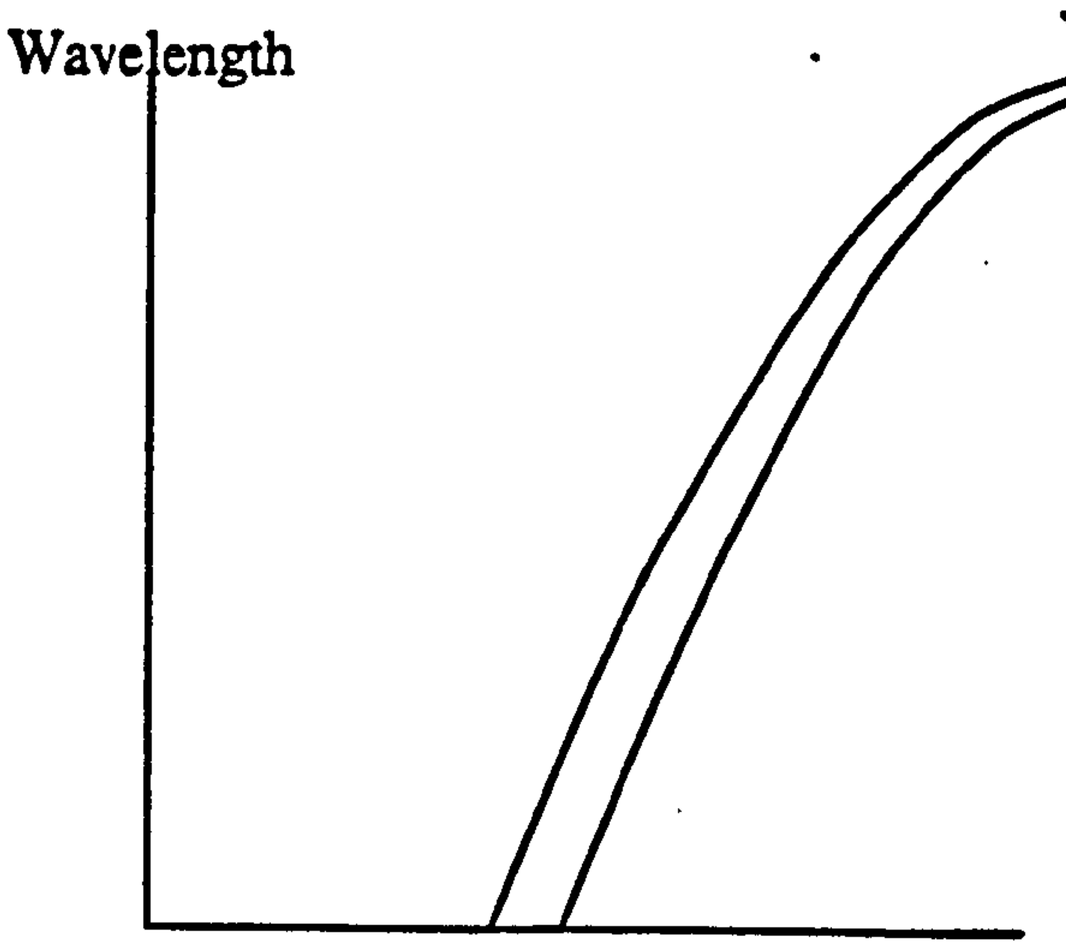

Fig 3.7a DuMond curve for a single crystal.

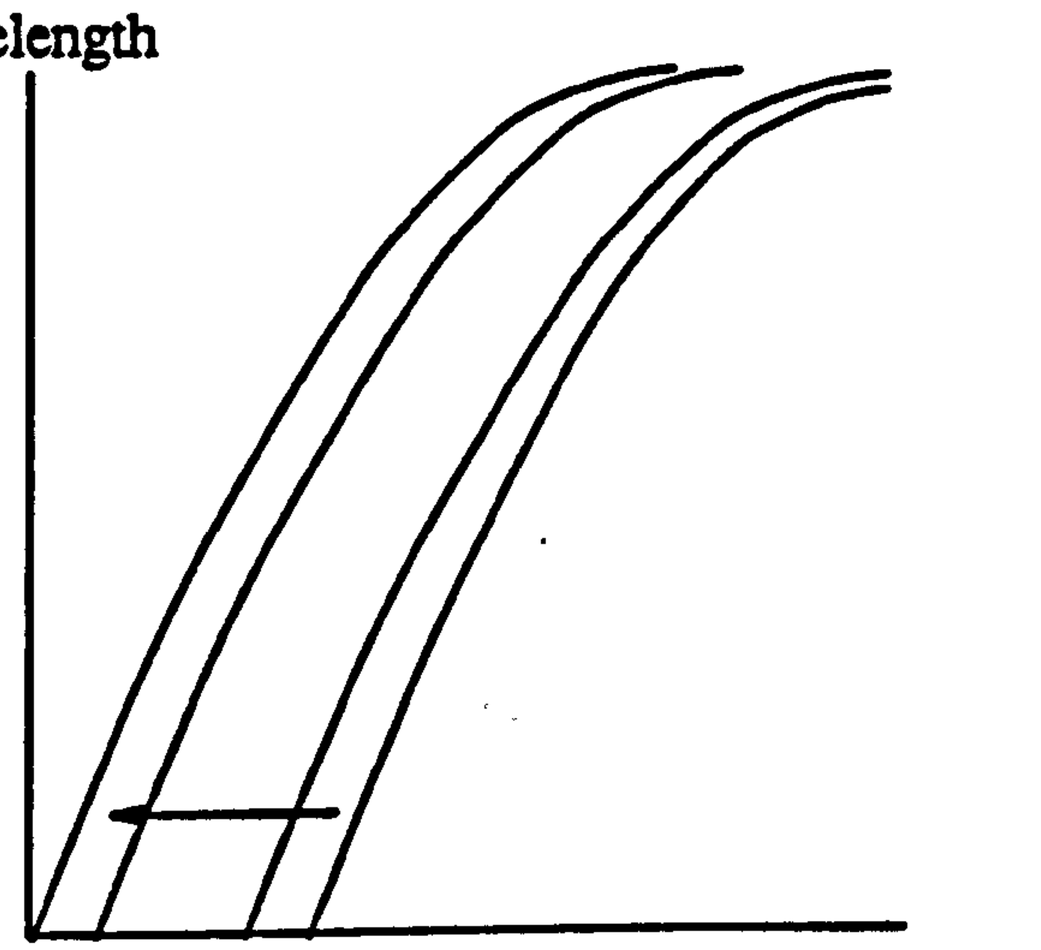

Fig 3.7b (+–) Curve for two crystals with one crystal rotating with respect to the other.

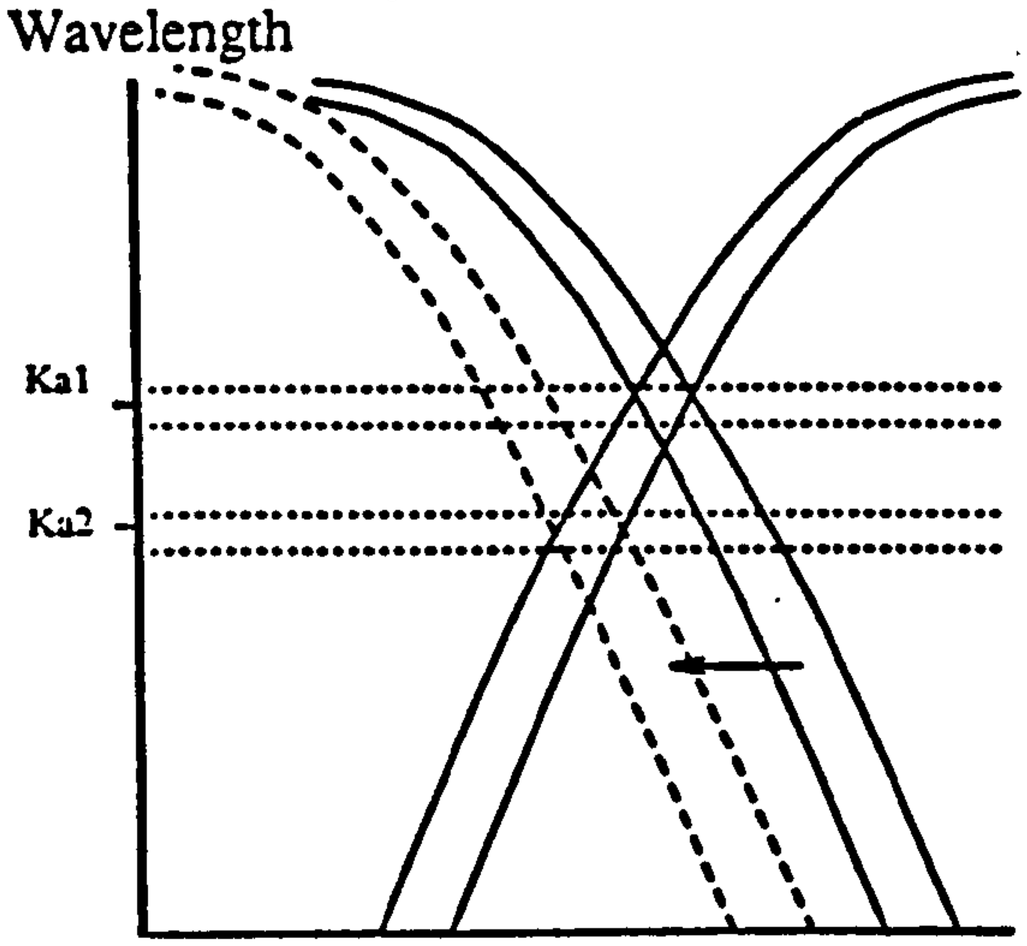

Fig 3.7c The (++) set-up for two similar crystals showing the passing of the of the $K\alpha_1$ line, solid line and at a different angle the $K\alpha_2$ line

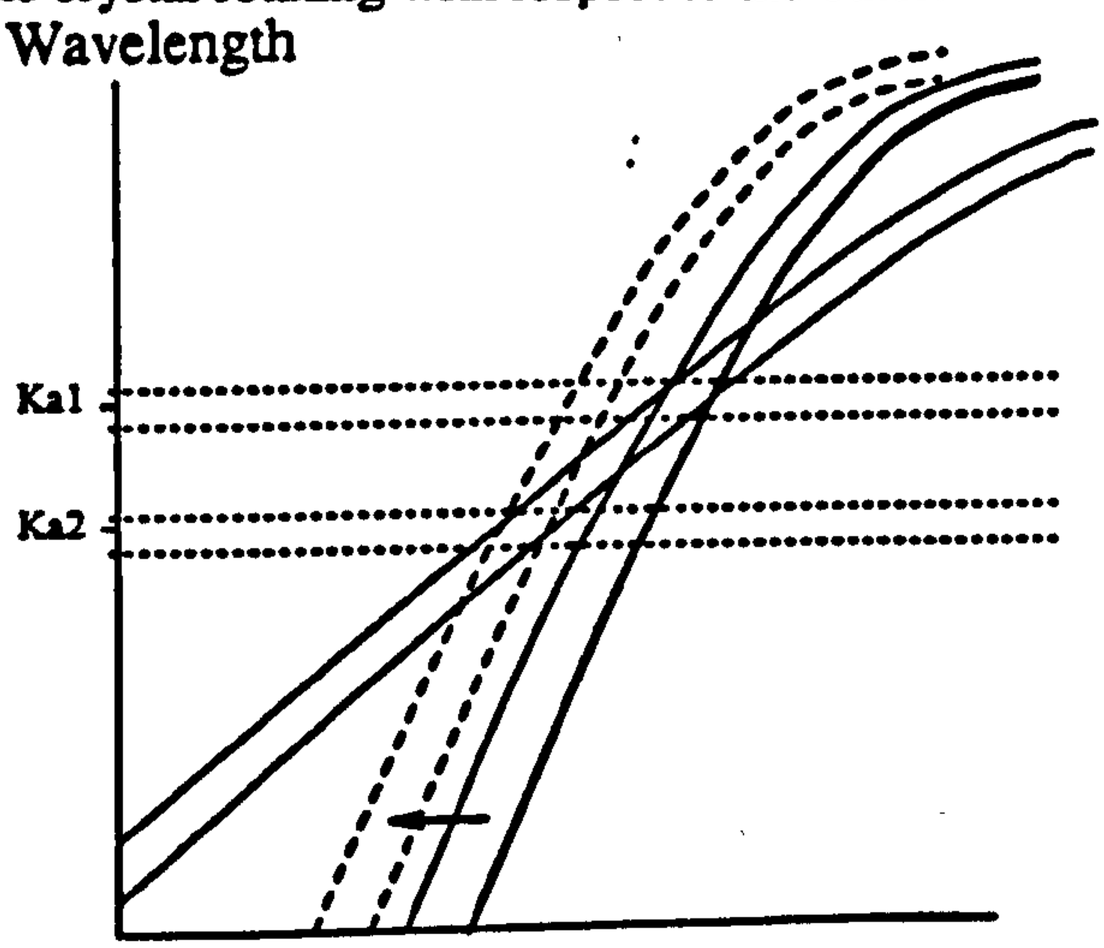

Fig 3.7d The (+-) setup for two dissimilar crystals showing the passing of the $K\alpha_1$ line, solid line, and at a different angle the $K\alpha_2$ the $K\alpha_2$ line, dashed line.

Dispersion

Dispersion occurs where the two DuMond curves for the first and second crystals are not identical, ie either a (++) set-up, or where the two Bragg reflection angles are different. The effect of dispersion can be shown by considering a source emitting two radiations λ and $\lambda - \Delta\lambda$ ie $K\alpha_1$ and $K\beta_1$.

Fig 3.7c shows the (++) set-up where the x-ray beam is rotated in the same direction by both reflections. One peak of transmitted intensity is seen in the position shown, and a second peak is seen due to the $K\beta_1$ radiation after a further rotation of the second crystal by $\delta\theta$ to the position indicated by the dotted line . Fig 3.7d shows the second situation where the set-up is (+ -) but the Bragg reflections are different. Here again it can be seen that a rotation of the second crystal brings it to a point where the $K\beta_1$ is passed.

3.6 Experimental set up of a double crystal diffractometer

Sources

The sources generally used for X-ray diffraction are

i) A synchrotron radiation source.

The fluorescence and some of the reflectivity work in this thesis was carried out at the synchrotron source at Daresbury. The source relies upon the fact that charged particles emit radiation when accelerated. In a synchrotron high energy particles, eg electrons at 2 GeV at Daresbury, are confined to a circular orbit and the radiation emitted is used. The characteristics of this radiation are

1, White radiation , a typical spectrum can be found in Tanner 1980.

2, High intensity throughout spectrum

3, Non divergent beam, the experiment may be 80 m from the ring.

4, Polarised radiation in the plane of the synchrotron ring

This type of source is however considerably more expensive than laboratory sources and hence is generally used when necessary for work such as white radiation topography and fluorescence.

ii) A standard sealed tube source.

This type of source was used for all the diffraction and some of the reflectivity work in this thesis. A tube source essentially works by impacting highly energetic electrons ~ 50keV on a metal target. A tube source emits both the characteristic lines of the target metal and a lower intensity of Bremsstrahlung radiation. The output intensity is however limited by the heat transfer properties of the metal target.

iii) Rotating anode source.

This is similar to a standard sealed tube except that in these sources the target metal is rotated so that each area has time to dissipate heat energy whilst it is not illuminated with the electron flux. This enables the electron beam currents to be increased and an order of magnitude increase in emitted intensity can be achieved.

Diffractometer

The modified set up for a double crystal diffractometer is shown in Fig 3.8. Here the beam from the source Bragg diffracts from the first crystal (shown here as a four bounce crystal, which gives higher angular resolution as will be discussed in chapter 8) through a pair of slits to remove scattered radiation. This "conditioned " beam then falls on the second crystal which is "rocked" through a range of angles

which includes the Bragg angle for the specimen. This provides a rocking curve for the crystal which shows the main diffraction peak along with any diffraction peaks nearby.

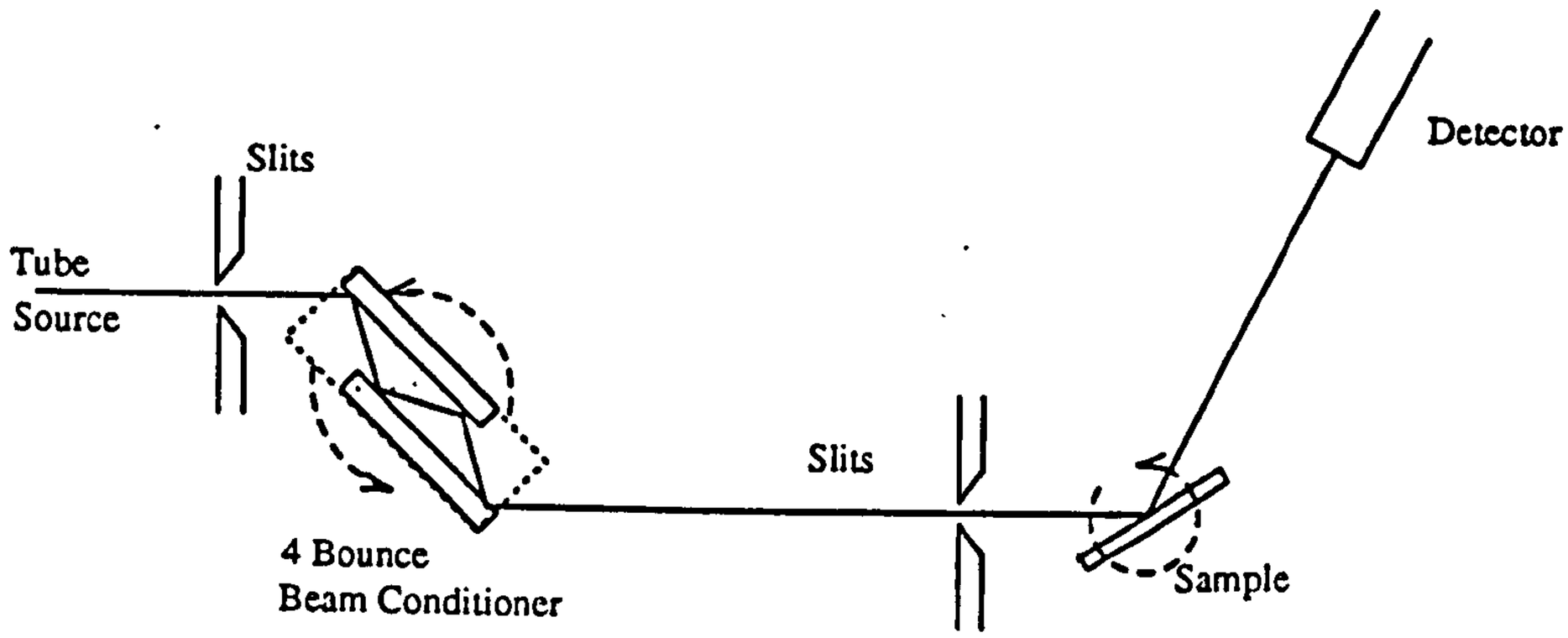

Fig 3.8 A standard X-ray diffractometer with a four bounce beam conditioner.

Dislocation broadening

The presence of dislocations induces strain fields and micro tilts around the central dislocation cores. this in turn means that the diffracting planes are distorted and the diffraction peak broadened. Equation 3.35 allows an estimate to be made of the dislocation density from the degree of this broadening.

$$\text{Peak Width (in radians)} = 9b^2/h^2 \qquad (3.35$$

where

b = Burgers vector

h = Dislocation separation

Thus for crystals with high densities of dislocations a rough measurement of the dislocation density may be made from the rocking curve width.

Asymmetric reflections

The use of symmetric reflections can only give information on the lattice parameters perpendicular to the surface of the sample. However if an asymmetric reflection is used then information about the lateral lattice parameters can be determined. Use of an asymmetric reflection can also enable a higher degree of surface sensitivity, Table 1 shows the penetration depth for various reflections with Cu Kα and Mo Kα radiation on [100] silicon.

The penetration of the X-rays can be calculated using the Kinematical theory, $d[exp^{-1}] = \sin(\theta-\varphi)/\mu$. This is valid where there is no strong interaction between the incident and diffracted beams, ie for mosaic crystals and for perfect crystals away from the main diffraction peak. Dynamical theory gives an extinction depth for perfect crystals when on the Bragg angle. This extinction is due to the incident beam being first diffracted and then re-diffracted back in the original direction but 180° out of phase, see section 3.2. In considering penetration depths when considering the SiGe fringe peaks the Kinematical extinction depth should be used as these peaks occur well away from the main substrate peak.

Table 3.1

Penetration of X-Rays into Silicon

Reflection		Incidence Angle (Degrees)	Penetration depth (μm) Kinematical	Dynamical(σ radiation)
004	Cu K_α	34.55	40.1	15.74
004	Mo K_α	15.14	177.1	11.46
113	Cu K_α	2.81	3.47	6.86
113	Mo K_α	-	-	-
115	Cu K_α	31.7	37.2	44.44
115	Mo K_α	4.04	47.0	24.67
224	Cu K_α	8.73	10.7	10.48
224	Mo K_α	-	-	-
044	Cu K_α	8.32	10.2	9.04
044	Mo K_α	-	-	-

In this thesis the most commonly used reflections are the [004] and both glancing incidence and glancing exit [113] with Cu K_α radiation.

Composition and strain measurement

As stated earlier Ge has a larger lattice constant than Si and thus when SiGe alloys are grown on Si Substrates tetragonal distortion occurs. Fig 3.9 shows the effect of this on the [004] and the [113] planes within the epilayer.

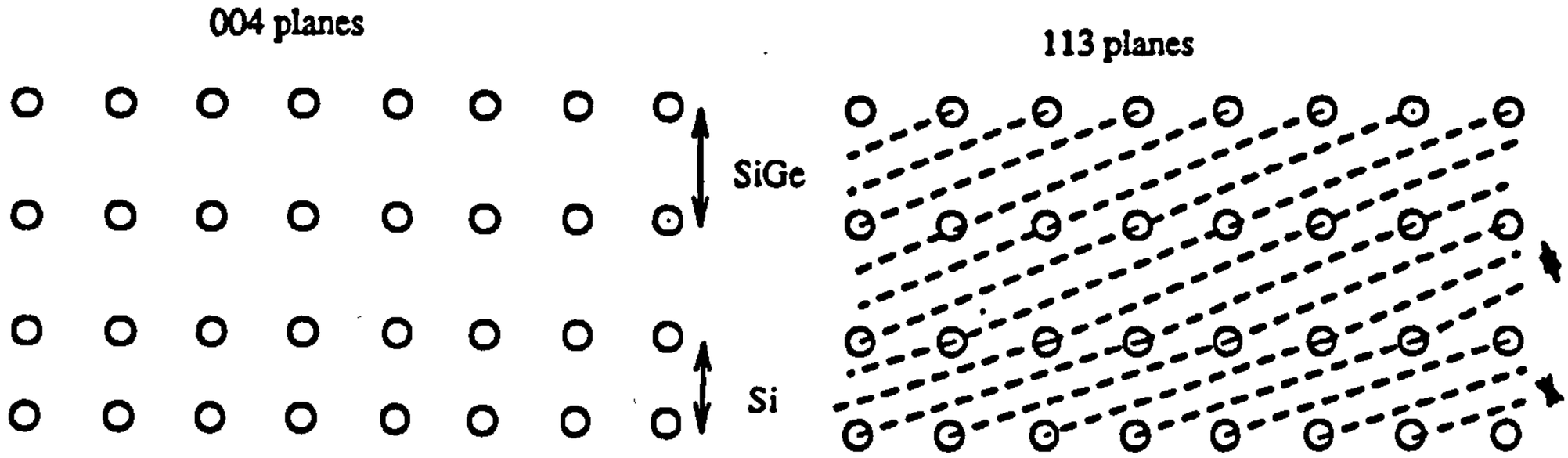

Fig 3.9 Plane spacings for SiGe grown commensurately on a Si substrate. The 004 spacing is expanded as is the 113 spacing. The 113 planes are also tilted relative to the 113 planes in the Si.

The fact that these planes now have different spacings, and for asymmetric reflections, a tilt relative to the same planes in the substrate means that the diffraction peak from the epilayer is displaced from the substrate peak. This displacement depends upon the change in plane spacing, d_{004} may be found with one 004 reflection and d_{113} requires both glancing incidence and glancing exit 113 reflections.

For material epitaxially grown on exact 001 substrates there is no tilt between the epitaxial layer and the underlying substrate. However, for samples where there may be some tilt present, as is normal if the substrate is cut off the exact 001 orientation, three measurements of the same Bragg reflection are made with the

sample at 0, 90 and 180° of rotation about the normal to the sample then any misorientation can be calculated and corrected for.

3.7 Interference fringes

Diffraction from thin epitaxial layers is now being considered as opposed to diffraction from effectively infinite substrates. In the dynamical theory fringes are produced owing to the interference of the two Bloch waves present within the crystal. However, if we initially consider the situation using Fourier analysis then the effects of the limited thickness of the epitaxial layer can be seen.

Single Layer fringes

Consider a SiGe layer on a Si substrate as in Fig 3.10a. The Fourier transform of this layer gives the profile shown in reciprocal space.

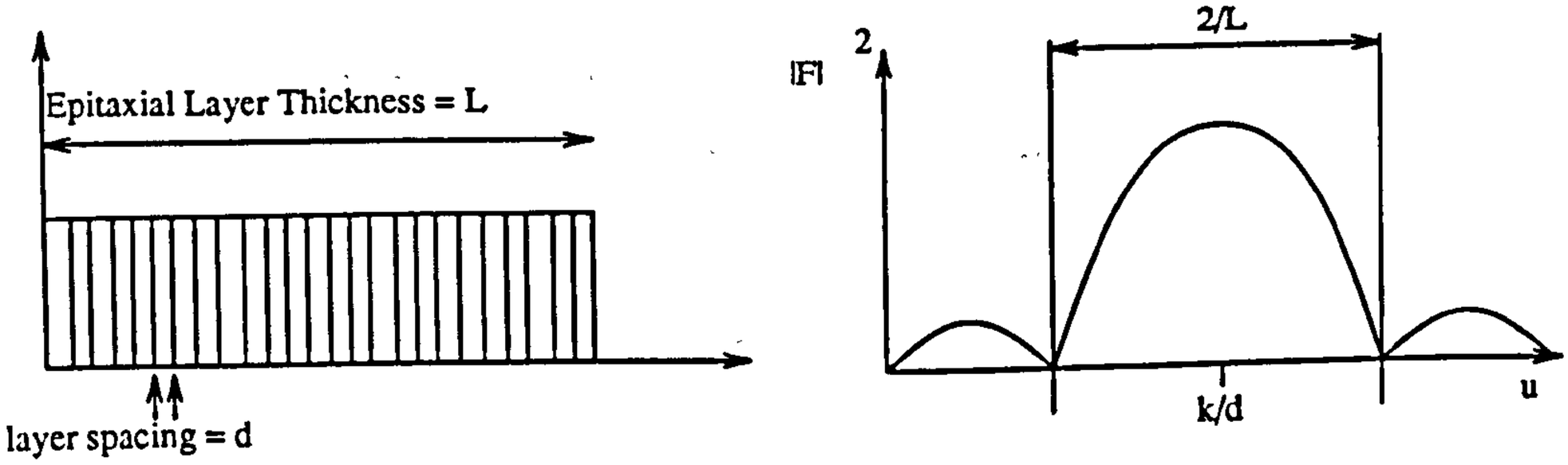

Fig 3.10a (left) This shows a representation of SiGe epitaxial layer. (right) Fourier transform of the representation of the SiGe layer.

As only a few degrees of angle is being considered, this reciprocal space can be equated to the angular measurement taken in a rocking curve. The reciprocal space

space axis can be converted to an angular axis (in radians) by multiplication using conversion factor 'x' as below

$$x = d \sin^{-1} (\lambda/2d) \qquad (3.36$$

As Fig 3.10a shows the width of the primary layer fringe gives the layer thickness, in addition the side fringes also arise from the limited thickness of the layer.

$$t_e = 2x / \text{peak width} \qquad (3.37$$

here

t_e = epitaxial layer thickness

Superlattice structure determination

In a manner similar to that just discussed if a SiGe superlattice is now considered as in Fig 3.10c

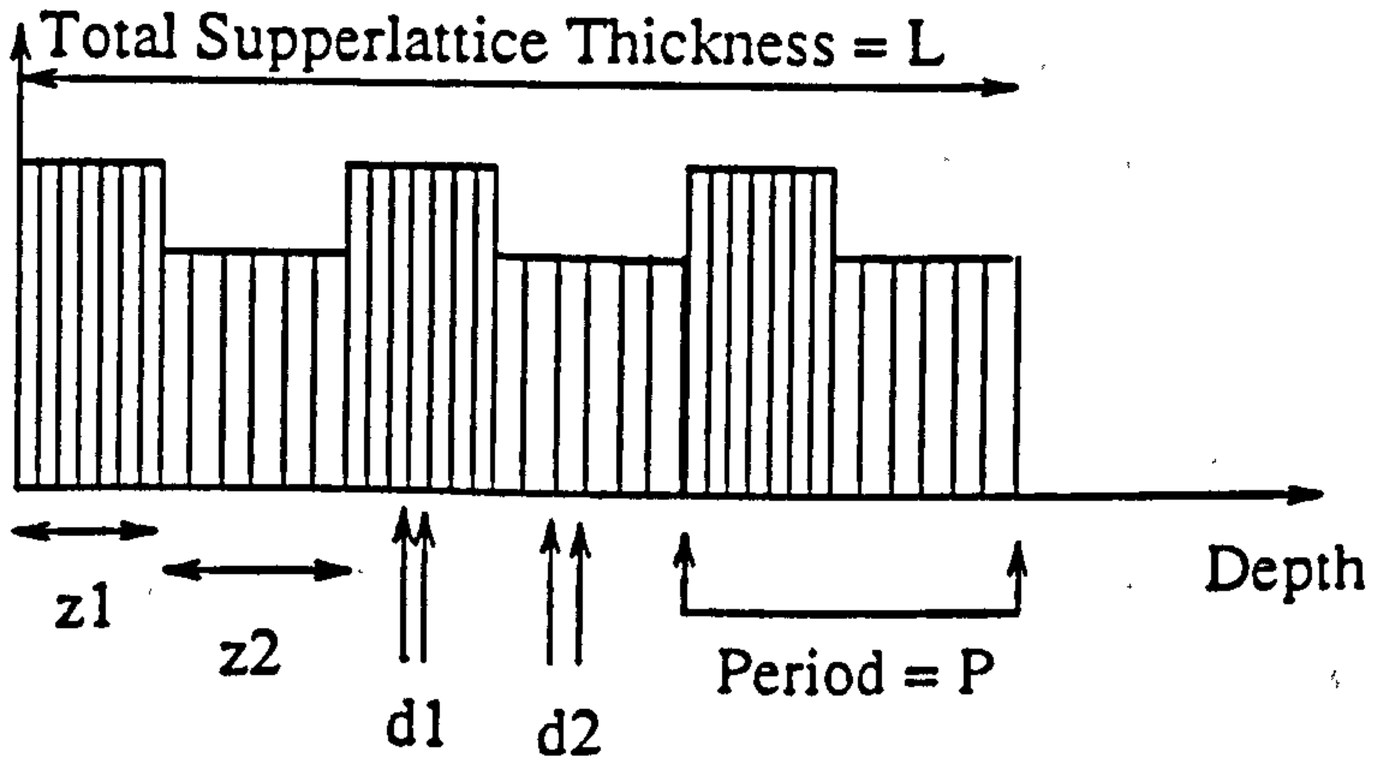

Fig 3.10c representation of a Si/SiGe superlattice showing the layer thicknesses z1,z2, the period P, the total layer thickness L, and the plane spacings in the alternate layers d1,d2.

This now undergoes a Fourier transform.

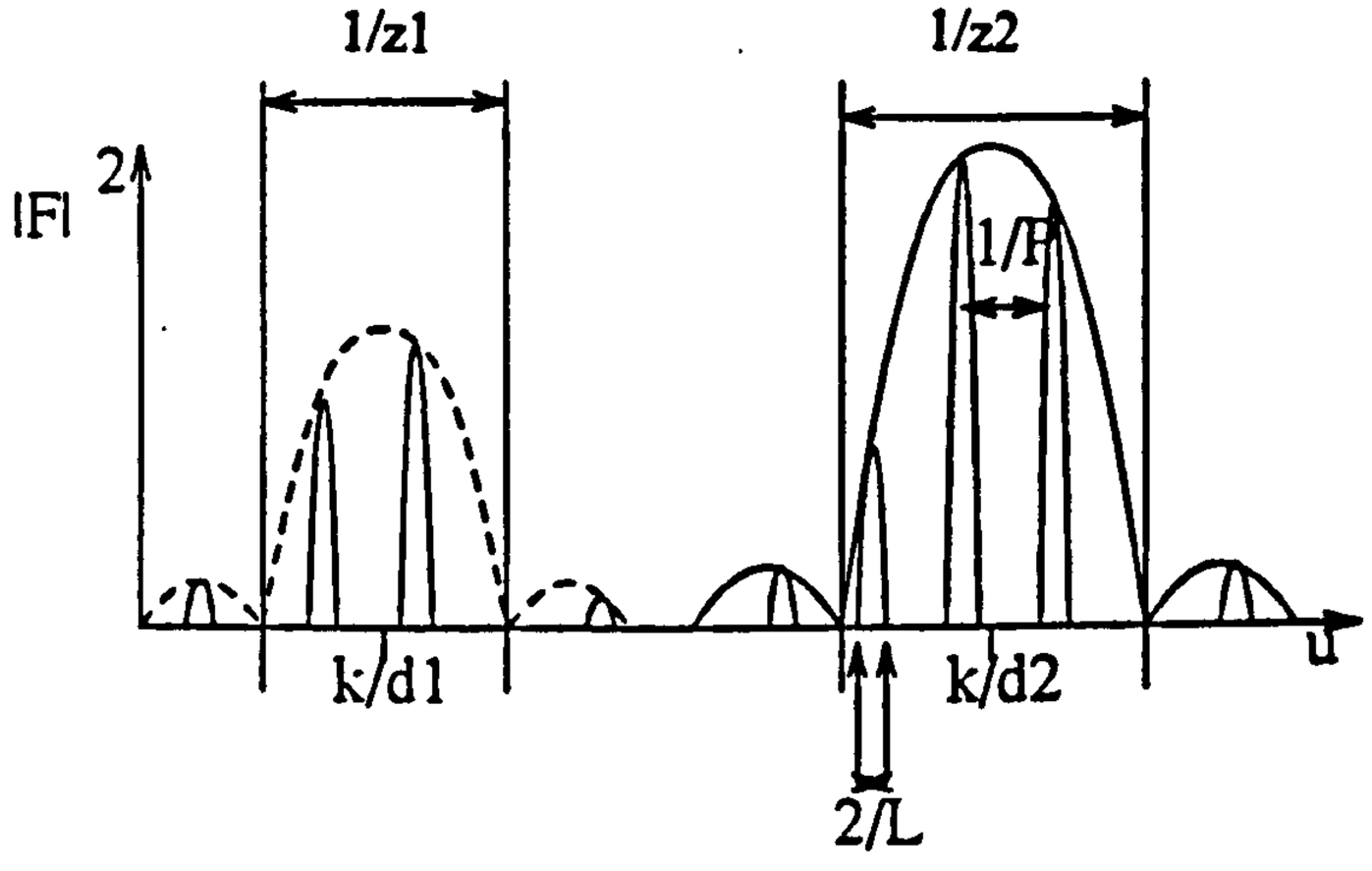

Fig 3.10d fourier transform of 3.10c

The total width of the superlattice stack determines the width of the fringes seen in a manner identical to the calculation of the peak width in the previous section. The period of the superlattice controls the fringe peak separation and the width of the individual layers determines the shape of the intensity modulating envelope. Finally the lattice spacing of the diffracting planes within the superlattice layers determines the positions about which the modulating envelopes will be centred. Thus from a rocking curve it is possible to find 1) structure thickness, 2) superlattice period, 3) layer thickness, and 4) layer composition

The above analysis as stated only is an approximation. This lack of accuracy can be clearly demonstrated if thin layers are considered where the peaks are not well separated then significant errors occur due to interaction between the substrate and epilayer peaks [Fewster and Curling 1987]. In practice this thickness below which large errors occur is dependent on layer composition as well as thickness and in order to achieve a 1% accuracy in layer thickness with the Fourier approach equation 3.3 must be satisfied:

$$t_e > 10 / x \qquad (3.38$$

where

x = Ge composition

and

t_e = epilayer thickness in microns

3.8 X-Ray Reflectivity-Experimental Introduction

X-ray reflectivity can be carried out on the same equipment as X-ray diffraction, although in this work a dedicated machine was used. The technique of X-ray reflectivity relies upon the fact that materials with different electron densities have differing refractive indices. Thus if the region where reflectivity is dominant, ie near the critical angle, is considered then the reflectivity signal at an angle φ is dependent upon the refractive index of the sample. For layered samples such as superlattices the refractive index changes with depth thus different layers will reflect more or less strongly, and interference can take place. X-ray reflectivity can be carried out in two modes;

i) Energy dispersive, where the sample is held at a fixed angle and illuminated with white radiation. The differing energies within the white radiation reflect with different intensities dependent upon the sample's reflectivity at that wavelength and this is measured with a solid state detector and a multichannel analyser.

ii) Wavelength dispersive, here monochromatic radiation is used and the sample is rocked from 0 degrees to ~ 2 degrees and the reflectivity signal measured with a single channel device.

3.9 Experimental Procedure

The X-ray reflectivity measurements were carried out in the angular dispersive mode using a Bede GXR1 with a CuK_{α} tube source. A schematic of this is shown in Fig 3.11.

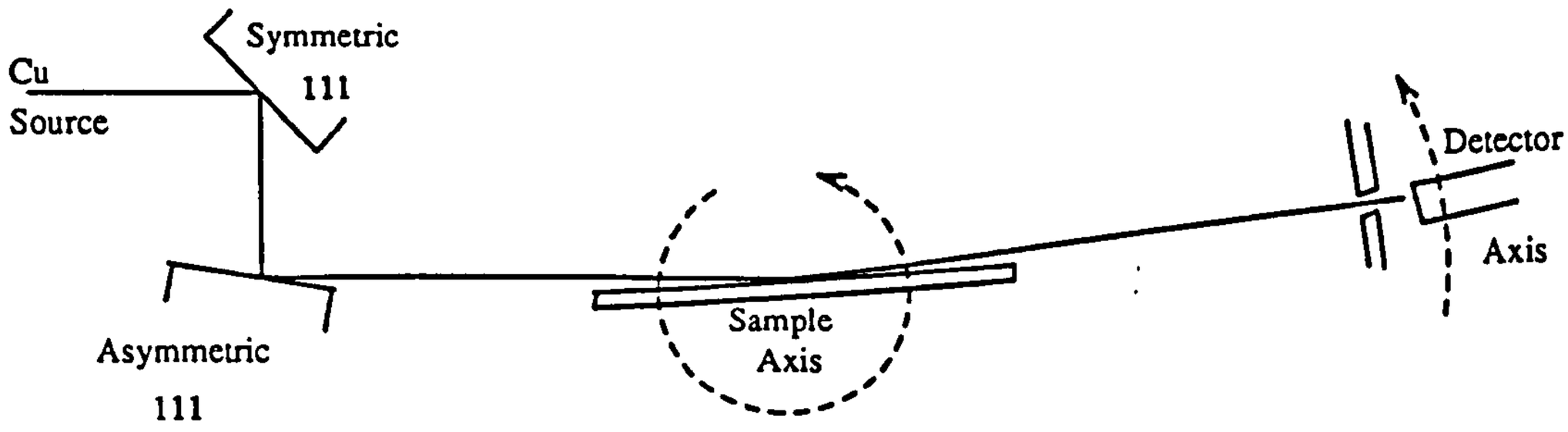

Fig 3.11 Schematic of the GXR1 reflectometer.

The beam conditioner consisted of two crystals the first being a symmetric 111 Si and the second an asymmetrically cut 111 Si crystal which reduces the beam height to ~ 50μm and increased the brightness by a factor of ~ 5 to give a maximum intensity of $3x10^5$ counts per second. This also gave a beam divergence of approximately 30 arcsec. This beam is then used to illuminate the sample. The sample is initially set up at 0° to the direction of the incident radiation and at this point it should be blocking half of the radiation. The sample is then rotated in small

steps to allow a reflectivity curve to be taken. The detector is positioned beyond this behind a pair of slits that rotate at twice the speed of the sample so that only the reflected beam is considered as oppose to scattered radiation from the sample.

3.10 X-ray fluorescence

It is well known that any element will emit characteristic radiation when excited with high energy X-rays. This is used in X-ray fluorescence to determine which elements are present within an irradiated sample.

Considering first the efficiency of the emitted fluorescence, for maximum absorption the exciting radiation should be slightly higher energy than the emission line. However, Compton-Raleigh Scattering of the excitation radiation produces scattered radiation at energies at and just below [Willams 1987] the excitation energy. As a consequence of this the optimum energy to excite fluorescence is ~ 10% higher that of the characteristic line under examination. In general, unless the type of impurity is already known, several measurements at different energies are required to ensure that any elements present have a suitable excitation radiation.

Having chosen which radiation to use consider now which part of the sample is receiving the radiation. If the incoming radiation is below the critical angle then no x-rays penetrate into the sample and any fluorescence signal must be from the surface of the sample. As the incidence angle increases the penetration depth of the X-rays increases and fluorescence can originate from deeper regions of the sample.

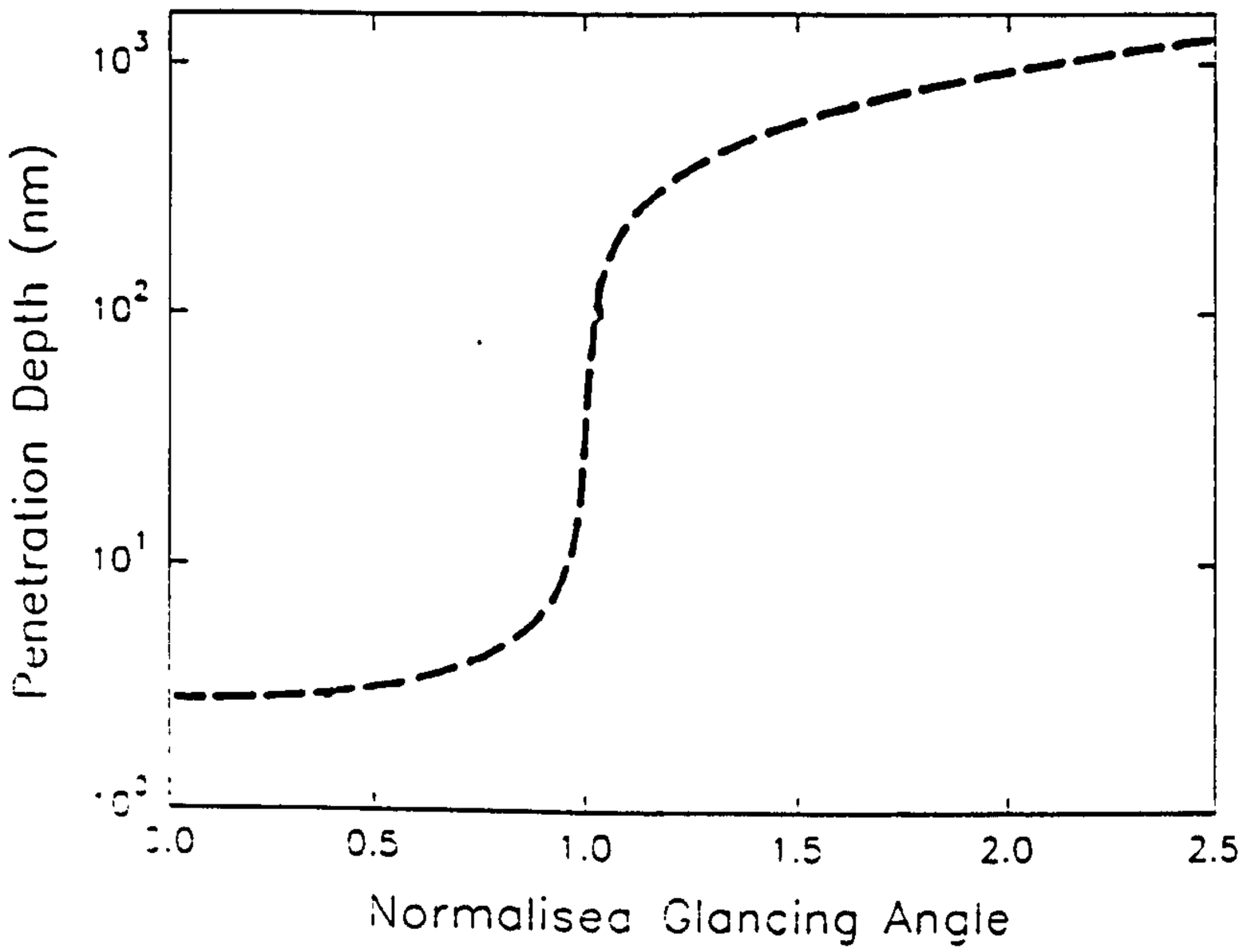

Fig 3.12 Penetration depth of X-rays at angles normalised to the critical angle.[Iida et al 1986]

Hence by rocking the sample through the critical angle fluorescence may be obtained from different depths within the sample and a depth profile of the fluorescing element obtained.

In this work glancing angle fluorescence was carried out. This involves a similar experimental stage as to that used in X-ray reflectivity and this is shown in Fig 3.13.

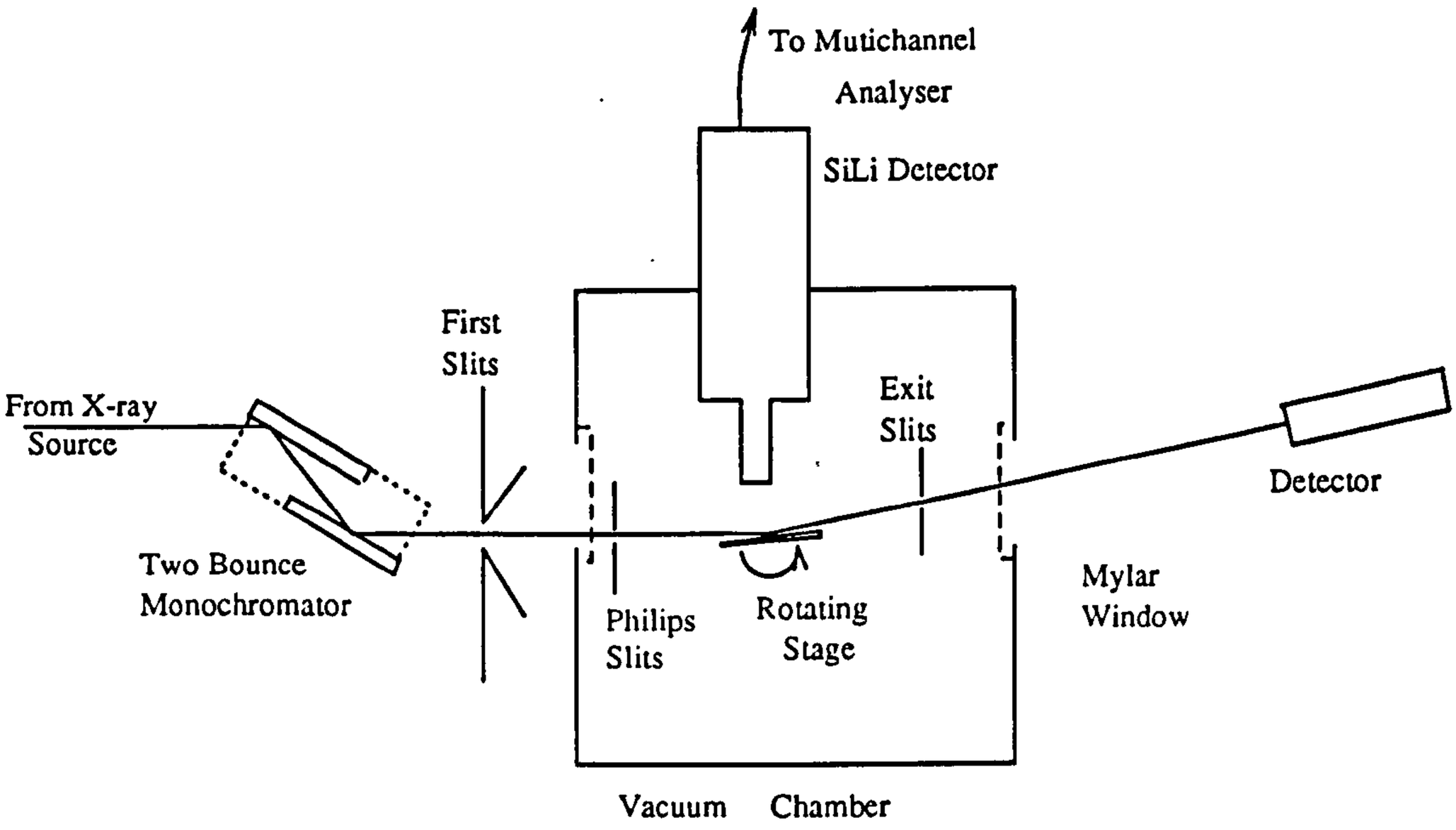

Fig 3.13 X-ray fluorescence and reflectivity stage used at Daresbury.

The X-ray fluorescence stage is similar to the reflectivity stage except that the experiment is carried out under vacuum conditions. The fluorescence is detected with a lithium drifted silicon detector and this gives an energy dispersed spectrum in 1024 channels. This allows the characteristic fluorescence from differing elements to be determined at each measuring position, the sample is then rotated to its next position and another energy dispersive spectrum taken. By this method the fluorescence at a range of angles is built up and a fluorescence rocking curve can be obtained for each element present. The curve was simulated using a development of the REFS simulation program [Wormington 1991,Powell et al 1991f] to calculate the electric field present within the crystal as a function of depth. This information was then combined with the Ge concentration at that depth and the absorption of the

fluorescence signal that would occur before it reached the sample surface. An integration of all the layers considered then provided the fluorescence signal as a function of incidence angle. Thus the fluorescence rocking curves can be simulated to produce the required depth profile.

3.11 Defect Etching

The previous two techniques provide information on the average quality of the crystalline material. Defect etching provides a method of examining the individual defects within the structures investigated. In this technique a chemical etch is used which will etch at differing rates dependant upon the crystalline quality of the material under examination. Thus in regions associated with defects, such as dislocations, where the crystalline structure is strained and a high density of dangling bonds is expected, pits will be formed on the surface of the layer being etched. These pits can then be seen with an optical microscope. In this work a diluted Schimmel etch is used.

Dilute Schimmel = $3H_2O : 2CrO_3(0.75M) : 4HF$

The hydrofluoric acid is present to remove the oxide as it is formed, chromium trioxide oxidizes the Si or SiGe material, it is this oxidation rate that is dependent upon the electrical activity of the material, and water to slow down the reaction to a manageable rate. As the etch progresses, hydrogen is evolved due to the reaction of hydrofluoric acid with the oxide. This hydrogen adheres to the surface as

bubbles and can cause non-uniform etching, therefore vigorous agitation is required during etching.

In this work I have been primarily concerned with the presence of threading dislocations and misfit dislocations. As threading dislocations generally run from the surface to base of the epitaxial layer the etch depth is not particularly important.

However, misfit dislocations run along the interfaces where there is a change of matrix material. In order to see a misfit dislocation the etch must reach the interface but go no significant depth beyond it. If the sample is overetched the pits will become smeared out.

In order to achieve this the etch rate must be known. For doped Si calibration curves have been produced [Pindoria 1990] in which an increase in etch rate with dopant concentration is shown. For the majority of this work SiGe layers with low Ge contents have been considered and the etch rate for these is found to be similar to that of Si material with the same dopant level. The temperature of the etch also has a strong effect on etch rate. Thus if knowledge of the depth of the etch is required then part of the layer must be masked, with black wax, during the etch and then the step edge created can be used to determine the thickness of material that has been etched away.

In order to determine the etch pit density differential interference contrast or Nomarski microscopy is used. This enables features – 3nm in depth to be resolved which is sufficient for most etched samples. The field of view in an optical microscope allows defect pit densities in the range from 10 cm^{-2} to 10^7 cm^{-2} to be measured with a good statistical confidence.

In Figs 3.14 and 3.15 the features observed on SiGe layers can be seen.

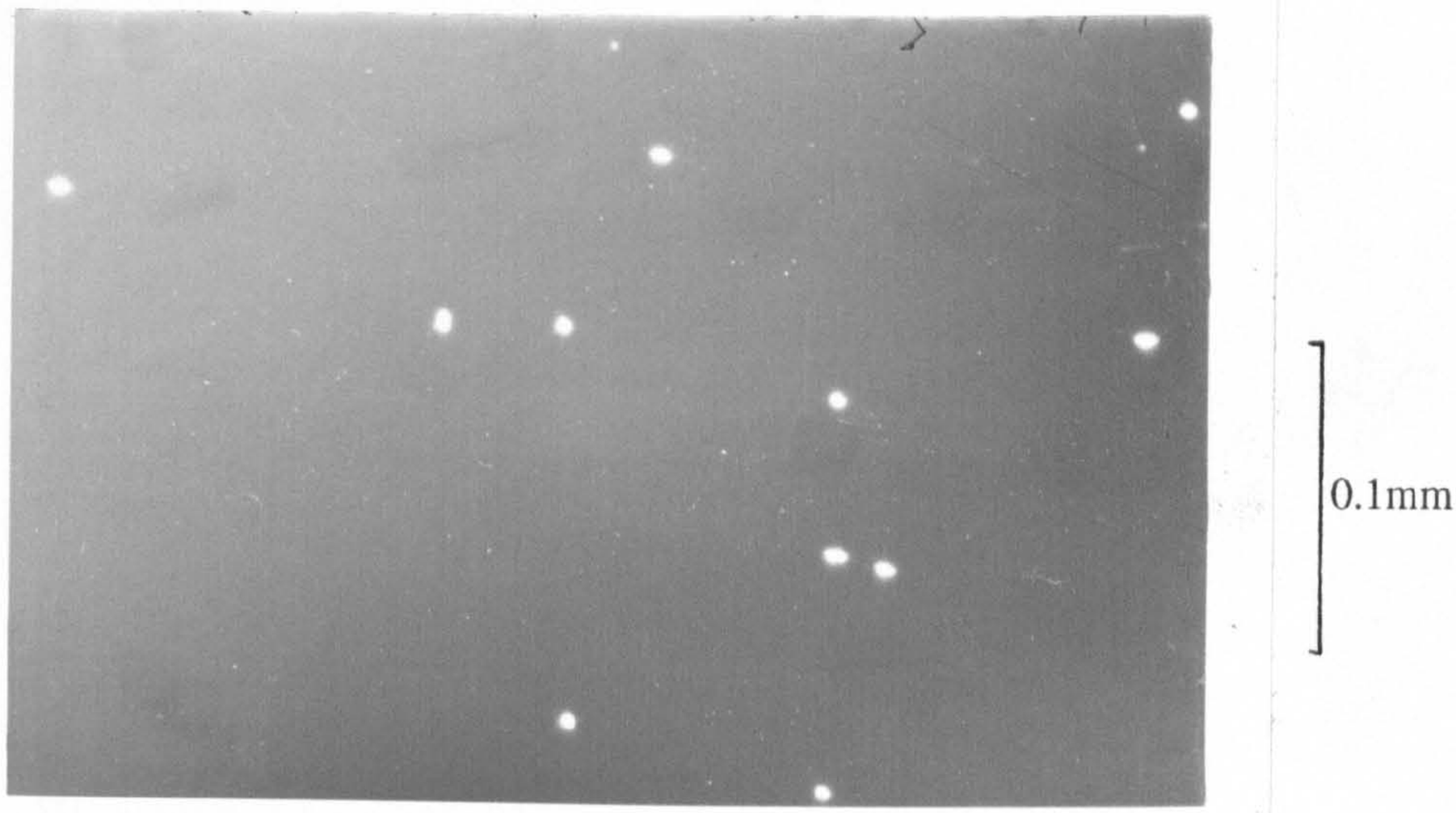

Fig 3.14 Threading dislocation pits seen after a Schimmel etch

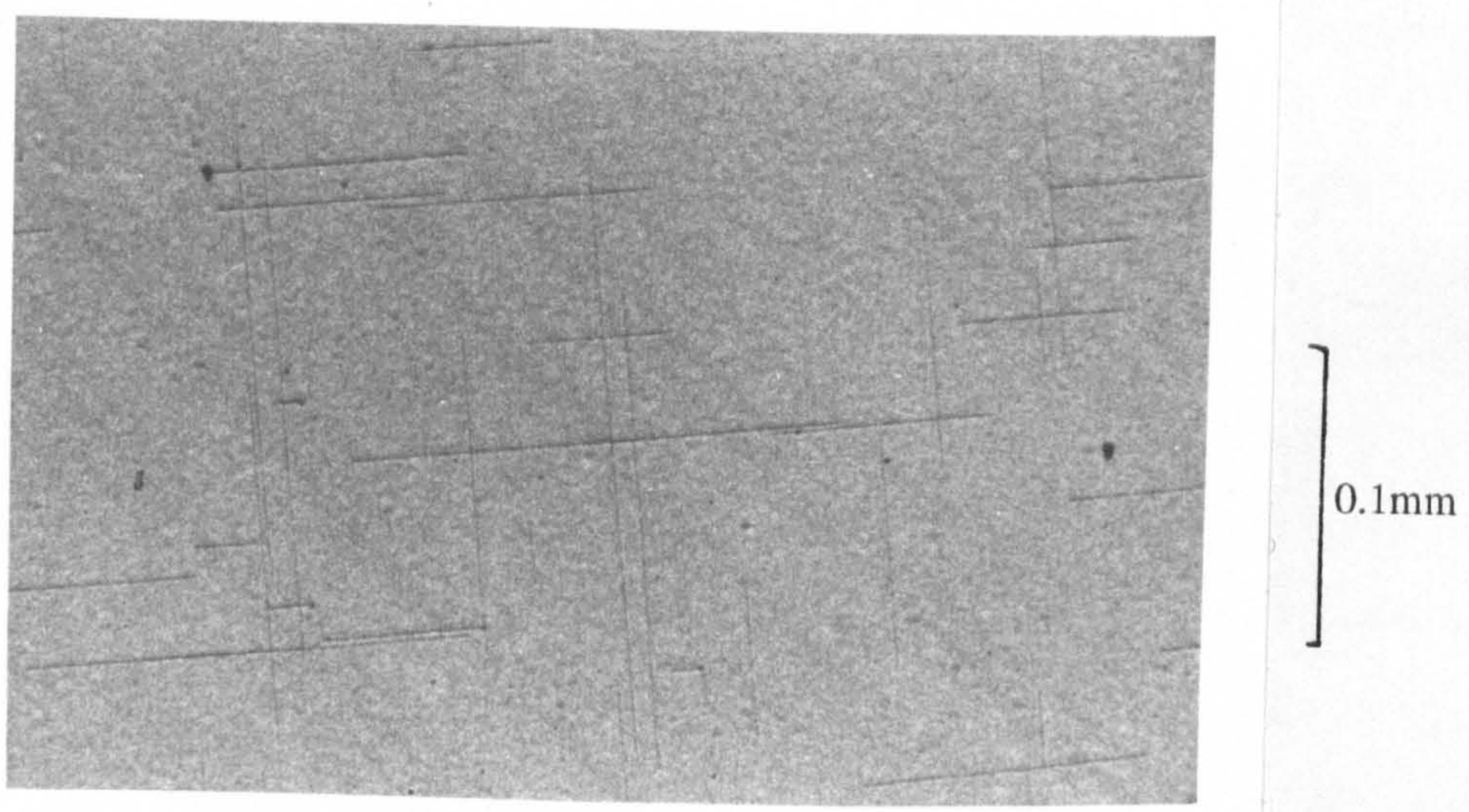

Fig 3.15 Misfit dislocations lines seen after a Schimmel etch of a SiGe layer in the first stages of relaxation.

Chapter 4

Characterisation Techniques Used On The Author's Behalf

4.1 SIMS

This work was carried out at, Warwick University, and, at Cascade (Loughbough University).

Secondary Ion Mass Spectrometry is a technique for determining the material composition of the top few microns of a sample. It can provide a depth profile for any element with a lateral resolution of 10 μm. In SIMS the sample is placed within a high vacuum system and an ion beam made to strike the surface. The ions within this beam either backscatter from the surface or penetrate the material and lose their energy to the surrounding atoms. Atoms can in this way receive sufficient energy the leave the surface, those that have also been ionised (secondary ions) can subsequently be detected and analysed using a mass spectrometer. As a consequence of the sputtering process the surface is etched away, and if the beam is rastered in a set pattern then a uniform crater can be produced and thus a depth profile obtained for the element under examination.

Depth Resolution limits

The fact that the primary beam ions impact upon the surface with several keVs of energy means that they able to impart a considerable amount of energy to

those atoms with which they collide, not only at the surface but for a considerable depth into the material. The energy imparted to the sample atoms means that they are either able to escape from a region below the surface, or move to a new site at a distance from their original position. This second effect is called cascade mixing, this generally limits depth resolution to 3→10 nm [Briggs and Seah]. Fig 4.1 illustrates the effect of this cascade mixing on a delta layer buried within a silicon matrix.

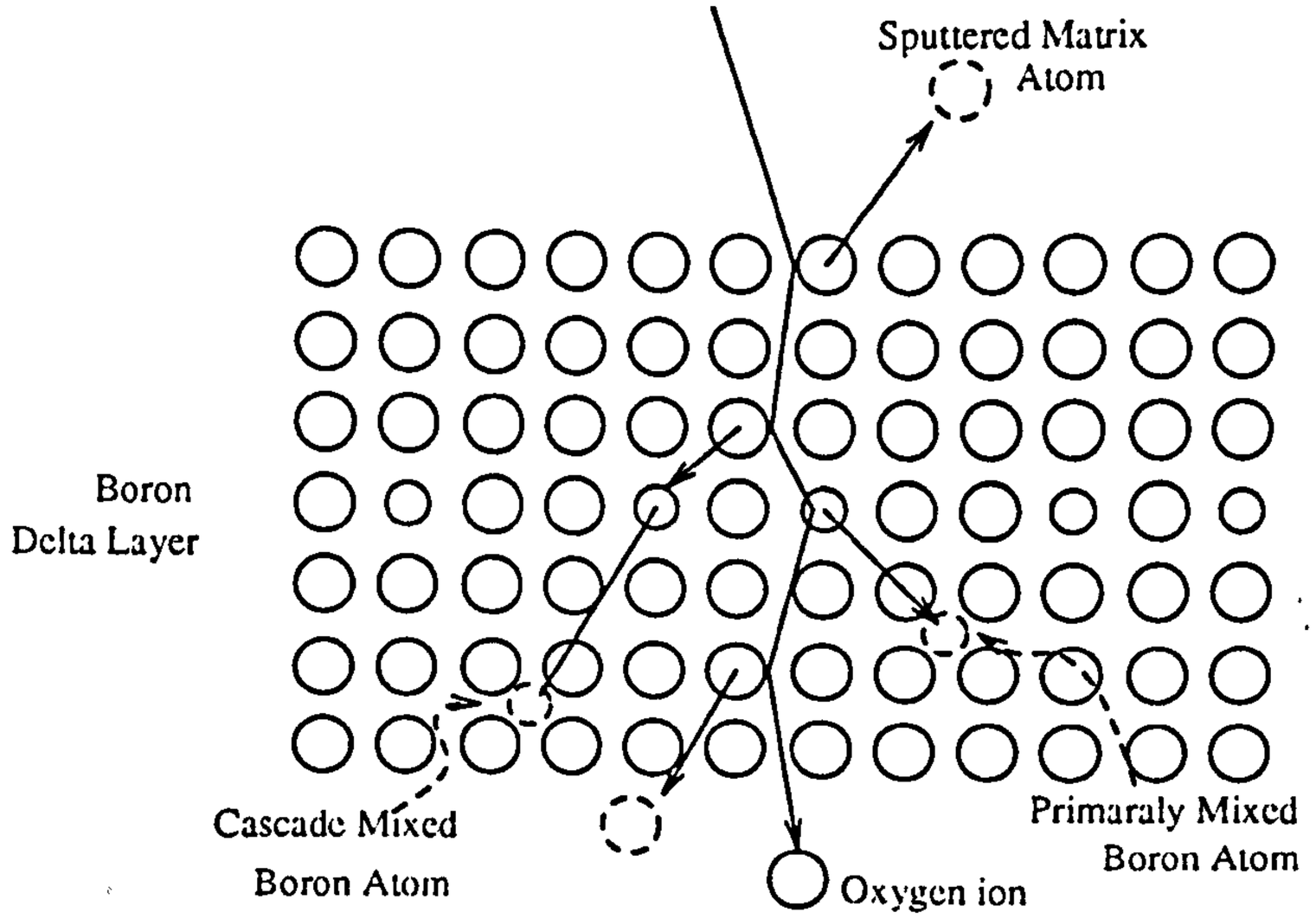

Fig 4.1 An incoming oxygen ion is shown to have many collisions with the atoms present in the top 100 monolayers leading to primary and cascade mixing of the layer under examination.

If the energy of the primary ions is reduced then the penetration and hence the cascade mixing due to the primary ions is reduced. However, reduction of the acceleration voltage applied to the ion source gives a corresponding reduction in the ion current and thus in the sputtered ion count. One way to overcome this problem is

to initially pull the ions from the source with a high potential but then slow them down prior to their impact with the sample by holding the sample at a similarly high potential [Barlow priv. comm.].

Concentration Resolution

SIMS measures the sputtered ions from the surface and hence the fraction of ionised to unionised sputtered atoms (secondary ion yield) is critically important. In order to maximise the signal this ratio should be maximised. It is found in practice [Williams 1979] that electronegative atoms have a higher ion yield if bombarded with oxygen ions. However electropositive species of atoms give a larger yield if electropositive ions are used, usually caesium. Thus in SIMS the nature of the probe beam, O or Cs is determined by the element under examination. An example of the concentration resolution obtainable is boron in a silicon matrix where concentrations down to $10^{16}cm^{-3}$ can be measured with the uncertainty limited by statistical precision to 30%.

Concentration Calibration

The secondary ion yield varies with differing measurement conditions, ie beam energy and inclination. In addition emission profile may not be homogeneous. Thus for accurate concentration determination calibration using a known standard for the relevant element should take place each time the measurement conditions are changed. The assumption is also made that the secondary ion yield remains unchanged as the concentration varies, this appears to be valid where concentrations are below $10^{21}cm^{-3}$ [Barlow priv. com.].

4.2 Berlin Topography

This work was carried out at the Institute for Electrophysics, East Berlin [Jenichen et al 1988]

The basic principle of a Bragg reflection topograph is to illuminate an area of the sample crystal with radiation, with the sample set so that a Bragg reflection occurs. In this situation the bulk material (usually unstrained) will diffract strongly. However, in regions of the crystal where the lattice parameter is different to the bulk, or where tilts are present then this material will not be at the Bragg condition and dark regions will appear in the image plane. Thus dislocations can be imaged on photographic film or X-ray cameras.

This method of dislocation imaging works well for crystals with little curvature. However the samples of interest in this thesis include strained SiGe epitaxial layers which produce significant curvature. This prevents the taking of standard topography as only a small region of the material satisfies the Bragg condition at any angle. However, if the incident radiation is first reflected off a collimator crystal which is distorted to the same shape as the sample then topography can again be taken over the whole area of the X-ray illumination.

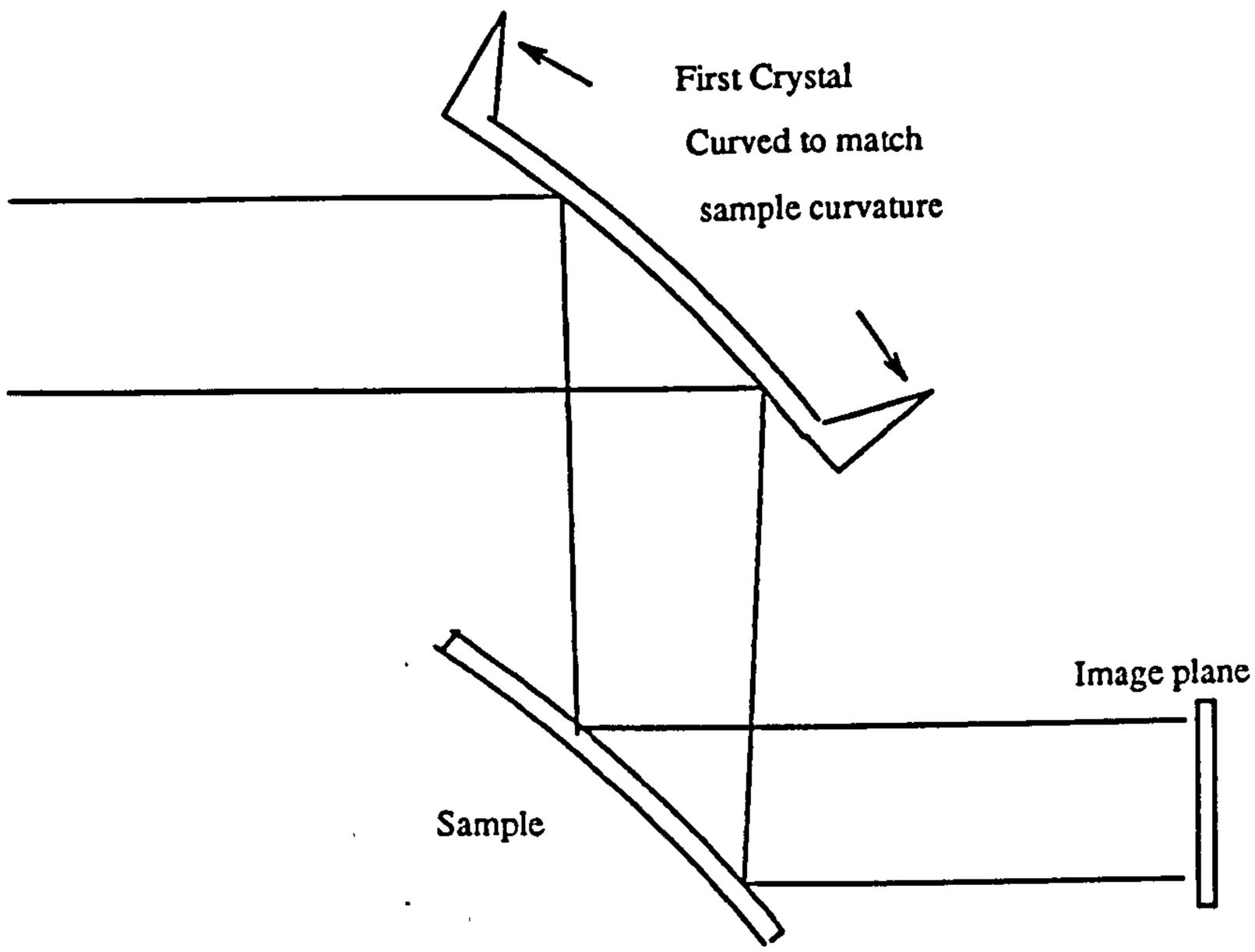

Fig 4.2 shows a schematic of the double crystal topograph camera

4.3 TEM

This work was carried out by P.Augustus at Caswell

Transmission Electron Microscopy, TEM, provides direct method for examination of strain present within a structure whether it is due to dislocations or compositional variations. For TEM imaging of material a high energy, 100→2000 KeV, beam is focused onto the sample and the electrons exiting from the reverse side of the sample are then focused by an objective lens system onto an image plane. Two types of imaging are generally used these being bright field and dark field.

In the bright field case, unscattered electrons are imaged. The sample is set up near but not on a Bragg reflecting orientation, thus for unstrained material the

electrons pass through the sample with little scatter. However, for material near a defect or with a different lattice parameter the bragg condition may be satisfied, in this case enhanced scattering will take place and a dark line or area will appear in the bright field image.

The dark field image is the reverse of the bright field case as the scattered electrons are imaged rather than the unscattered electrons

The strong interaction of electrons with material requires that for transmission of an appreciable number of electrons the sample must be fairly thin ie 100→400nm. This is generally achieved by mechanical thinning followed by ion beam thinning to remove any surface damage.

TEM as stated has the ability to image the strained regions associated with dislocations,in addition to this the Burgers vector $\underline{b}$ of the dislocations may be found. If the lattice is considered in the plane perpendicular to the burgers vector of the dislocation then it appears to be a perfect lattice. Thus by finding two diffracting vectors $\underline{g}_1$ and $\underline{g}_2$ lying on this plane where $\underline{g}.\underline{b} = 0$, $\underline{b}$ is then found from $\underline{b} = \underline{g}_1 \Lambda \underline{g}_2$.

In general TEM is used to show the presence of strain, ie a dark or lighter area in a micrograph. However from use of Kikuchi lines a quantitive measure of the strain present may be obtained. Kikuchi lines arise due to bragg reflection of scattered radiation, deficit lines are due to Bragg reflections reducing the scattered intensity in directions close to the incident beam and excess lines are the positions to which these electrons are reflected. These lines allow strains of the order of 0.0001 to be measured from the relative positions of the Kikuchi lines.

4.4 Microdiffraction with STEM

This work was carried out by Tom Pike at the Cavendish Laboratories [Pike et al 1991a].

This technique allows diffraction information to be obtained from small regions of a sample. The STEM probe is 0.5 nm in diameter and hence layers of this thickness may be examined, see Fig 4.3. The electron probe hits the sample and a number of transmitted diffraction spots can be imaged in the detector plane.

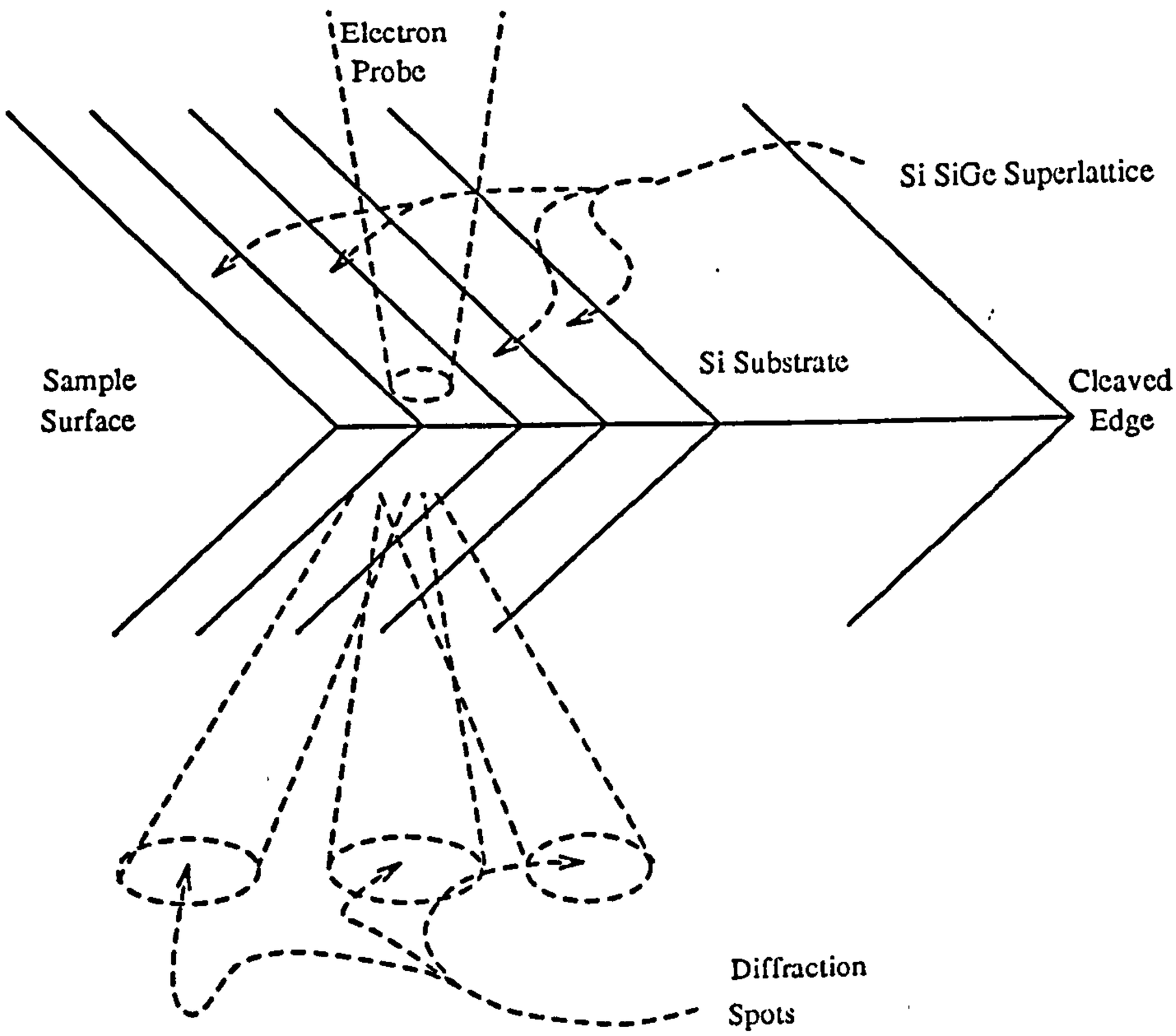

Fig 4.3 The geometry of the sample with respect to the incident STEM beam.

Consider now the diffraction spots, superimposed on these spots are deficit high order Laue zone (HOLZ) lines, dark lines due to the electrons diffracted towards the spot undergoing a second Bragg reflection out of the direction of the primary diffraction spot. The positions of the HOLZ lines depend upon the three lattice parameters, a_x, a_y, a_z, of the material under examination and on the energy of the incident electrons. Thus from consideration of the relative positions of the HOLZ lines the composition and state of strain in the material may be found. Similarly to TEM the strain resolution of this technique is limited to ~ 10^{-3}. However it does provide a direct measurement of strain from layers buried within a structure. In addition it allows this measurement to be performed on thicker layers than usually used in TEM analysis and hence surface strain relaxation effects are less prominent.

4.5 Hall Measurements

This work was carried out at Warwick University

When considering measuring the carrier concentration and mobility for epitaxial layers the first concern is to remove the effect of the substrate. Thus to take a Hall measurement the substrate must be of opposite carrier type to the epitaxial layer. Provided that this is so a Hall cross is made from the epitaxial layer. To do this a cross is marked out on the sample surface with acid resistant black wax. This is then used as a mask to produce a cross shaped mesa structure by etching the uncovered material down to the substrate. Electrical contacts are then made to the end of each arm of the cross with an amalgam of indium gallium metals and gold leaf. The contacts must be ohmic and this is checked by ensuring that the Hall

voltage varies linearly with the applied current. Having produced the cross the sample is placed within a magnetic field and the Hall voltage measured in all four possible orientations. This is then averaged in order to reduce errors due to non uniformity of the cross structure.

Depending upon the sample, measurements can either be taken at room temperature (for highly doped samples) or as is the case with delta layers, at low temperatures so that all other possible carriers have been frozen out. The errors associated with this technique are of the order of 5% but it does provide a reasonably quick method of measuring epitaxial layer carrier concentrations. It should be noted that the hall coeficient is converted to the carrier concentration by multipling it by a scattering factor which depends upon the scattering mechanisms occurring.

4.6 Electrochemical Profiling

This work was carried out at Warwick University

Electrochemical capacitance/voltage, eCV, measurement provides a rapid method for determining carrier profiles of samples. The technique is related to the standard C/V technique where a Schottky barrier is created at the surface. In the eCV technique a voltage V_1, typically 0.2V is applied and a depletion region is set up of width d1 which depends upon the carrier concentration within the depletion region. If a 1 KHz ac voltage is then applied on top of V_1 the change in depletion width is dependant upon the carrier concentration at the edge of the depletion region. Application of a high frequency ac signal of ~ 30 KHz enables the capacitance to be measured which in turn allows calculation of the depletion width (similarity to a flat plate capacitor is used). Thus the carrier concentration in the region adjacent to the

edge of the depletion region can be determined. The Schottky barrier itself is created using an electrolyte which both provides the "metallic " side of the Schottky barrier and enables a controlled etching of the sample to provide a depth profile.

A typical cell is shown in Fig 4.4. This cell is brought up to the sample and the electrolyte pumped in, a constant supply is circulated to reduce the build up of bubbles on the sample surface. A measurement cycle is then carried out which consists of a capacitance measurement followed by an etch which is induced by application of a dc voltage of ~ 2V. This cycle is repeated until the sample has been profiled.

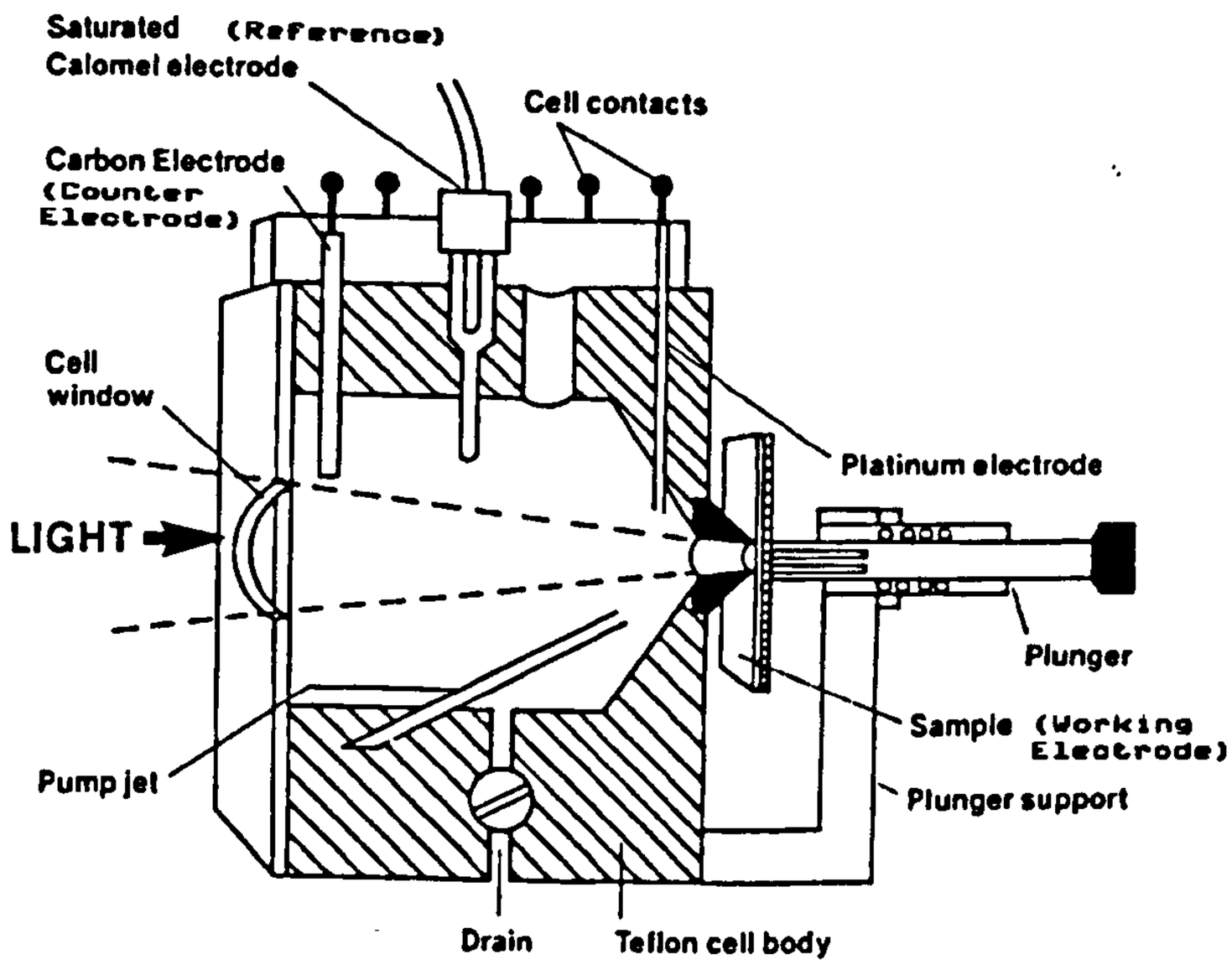

Fig 4.4 Cross section of an electrochemical cell [Bio-Rad manual]

Chapter 5

Characterisation of SiGe Matrix material

5.1 Introduction

The structural characterisation of epitaxial layers is of critical importance. In general a fast characterisation is required so that the growth system calibration can be corrected for the remainder of the growth series. Fast turn-around techniques include electrical measurements for the characterisation of dopant profiles, however these can give little information on the Ge concentrations within the structure.

For the characterisation of Ge profiles a number of techniques, SIMS , TEM, and X-ray Diffraction, are at present used. SIMS can give information on the Ge compositions although there are problems associated with the segregation of the Ge at the altered layer created due to the etching of the surface with the oxygen ion beam [Dowsett priv com]; in addition SIMS is too expensive to use for a standard characterisation technique. Cross sectional TEM gives excellent information on SiGe layer thicknesses, however, sample turn around is of the order of weeks and again it is an expensive technique. X-ray Diffraction is widely used for SiGe characterisation as it enables accurate determination of layer structure, with fast turn-around times of a few hours.

In this chapter the use of X-ray techniques to characterise SiGe single and multilayer structures is described. X-ray diffraction is used for the standard characterisation of x-y uniformity, layer thickness and composition. X-ray diffraction has also allowed determination of the growth direction uniformity from consideration of high order superlattice peaks. X-ray reflectivity is also considered as a new technique capable of offering additional information on the layer structures, and interface roughnesses, under examination, particularly for thin epitaxial layers and layers with high defect densities. Finally the use of X-ray fluorescence in conjunction with X-ray reflectivity is investigated as a method of determining matrix and contaminant concentration profiles.

5.2 Double Crystal characterisation

Section 3.2 showed how by use of X-ray diffraction the lattice plane spacings could be measured and hence how the perpendicular and parallel lattice parameters could be determined. SiGe deposited commensurately with a Si substrate will be tetragonally distorted. Any relaxation that takes place will allow the SiGe unit cell to revert back towards its cubic state.

The use of two reflections ie 004 and 113, can allow the lattice parameters in the z and x,y directions to be measured ie a_z and a_x,a_y respectively. Thus if equation 5.1 is considered and the known values for a_z and a_x inserted then the relaxed lattice parameter a_r may be found.

$$\frac{\Delta a}{a_r} = \frac{1-\upsilon}{1+\upsilon}\frac{\Delta a}{a_z} + \frac{2\upsilon}{1+\upsilon}\frac{\Delta a}{a_x} \qquad (5.1$$

. From a knowledge of the relaxed lattice parameter the composition, x, may be immediately found from

$$a_r = (1-x)a_{Si} + xa_{Ge} \qquad (5.2$$

The degree of strain remaining in the epitaxial layer after partial relaxation, S, is similarly found from

$$S = \frac{1-\upsilon}{1+\upsilon} \frac{a_z - a_r}{a_r - a_{Si}} \qquad (5.3$$

Thus once the lattice parameters have been determined and assuming that Vegards law is valid for SiGe [Dismukes et al 1964] the composition and state of strain can easily be calculated. In fact for SiGe Vegards law may not be strictly obeyed, however the deviations are small [Cembali et al 1991]. As stated earlier in practice a simulation program is used to model the curves obtained.

5.3 X-Y lateral uniformity

For the production of device structures on SiGe wafers it is essential that the layer has high lateral uniformity so that device structure does not alter in different positions on the wafer. Similarly if various characterisation techniques are to be used uniformity is vital so that results can be directly compared.

In order to obtain this uniformity, the substrate is positioned above and slightly to the side of the matrix sources. In this way the substrate is located where the flux cross-section is reasonably uniform. Additionally, by rotating the substrate at

about one revolution for every monolayer grown, the small gradient in flux cross section can be further reduced.

As the wafer is rotated during growth the only lateral variation should be in a radial direction from the centre of the substrate. Thus in order to find the lateral uniformity several diffraction measurements were taken at different radii, on a number of SiGe epitaxial layers grown on 4 and 6 inch substrates in the V90S system. Fig 5.1 shows three almost identical rocking curves obtained from different positions on a 4" wafer.

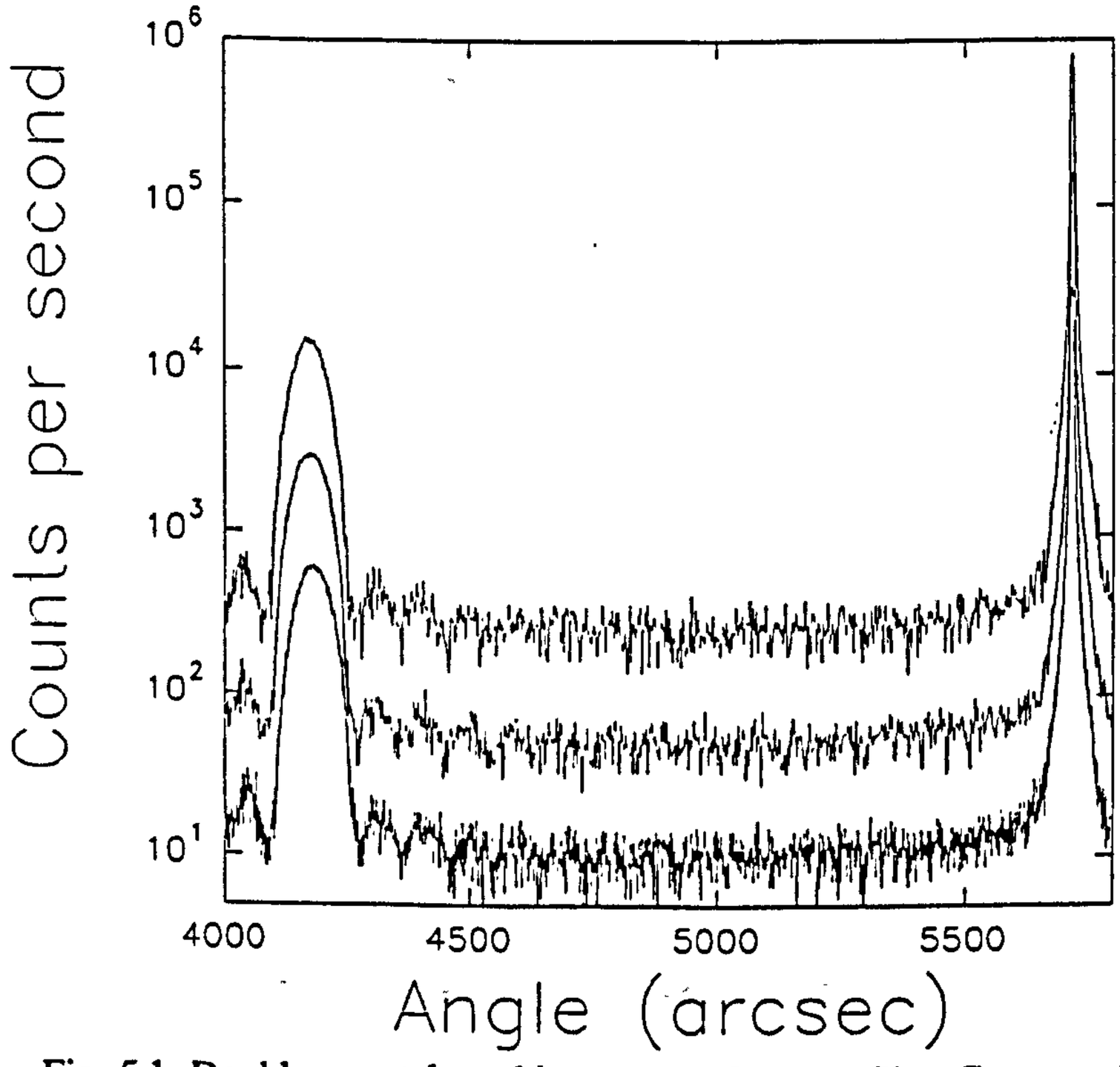

Fig 5.1 Double crystal rocking curve from a $Si_{0.85}Ge_{0.15}$ epilayer 004 reflection. Three curves are shown; (lower curve) centre of wafer,(middle curve) 2cm from centre, (upper curve) edge of wafer.

The results from four samples are summarised in Table 5.1. The small variations in peak separation correspond to a composition variation which does not exceed 0.6% of the total composition, for the V90 material.

Table 5.1

X-Y uniformity of SiGe Layers

Average Composition	Peak Separation At x cm From Centre (arcsec) ±3			
% Ge	0	2	4	7
16.5	1706	1716	1710	-
14.9	1538	1542	1544	-
12.3	1272	-	1267	1272
7.7	796	-	794	797

In addition to determining the compositional uniformity the thickness uniformity has been assessed from measurements at differing radii of superlattice structures and considering the spacing of the superlattice fringes. From these measurements the thickness uniformity of the two growth systems was found to be 0.6 % for the V80 over the 3" wafers used and 0.3 % for the V90S.

5.4 Z, Growth Direction Uniformity

The uniformity in the growth direction is dependent upon the stability of the matrix flux sources. The sources are, as discussed in section 2.2, evaporated from Cu hearths by an electron beam, the current in this beam is controlled by a feedback

circuit which uses an Inficon Sentinal III to sample the matrix flux [Kubiak et al 1991]. The arrangement of the source and flux monitor is shown in Fig 5.2.

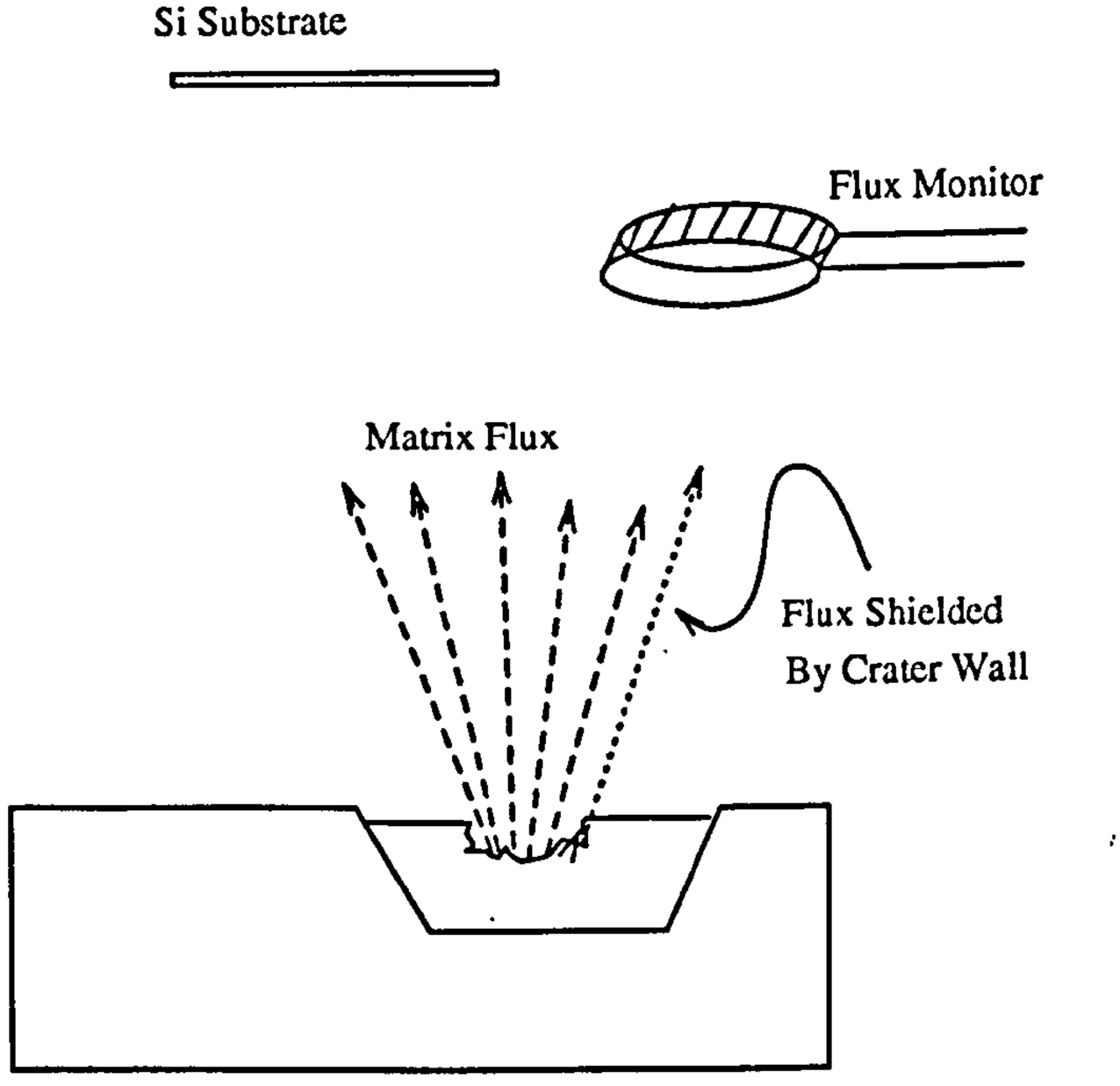

Fig 5.2 Schematic of a matrix flux source. The arrangement of the flux monitor is such that shadowing of matrix flux by the crater wall can cause an incorrect determination of the emitted flux.

The monitor is in fact not measuring the flux going direct to the substrate, but only a sector of flux leaving the source. Thus, as it is possible that the flux profile leaving the source does not remain constant, perhaps due to shadowing effects from the crater walls, irregularities may occur in the epitaxial layer composition and thicknesses.

Superlattice structures were grown in order to determine the flux uniformity during a single growth. In these structures any flux irregularities should show as variation in period length within the superlattice structure. Two samples were grown one in a VG V80 machine and the second in the VG V90S machine. The rocking curves obtained from these layers are shown in Figs 5.3 and 5.4.

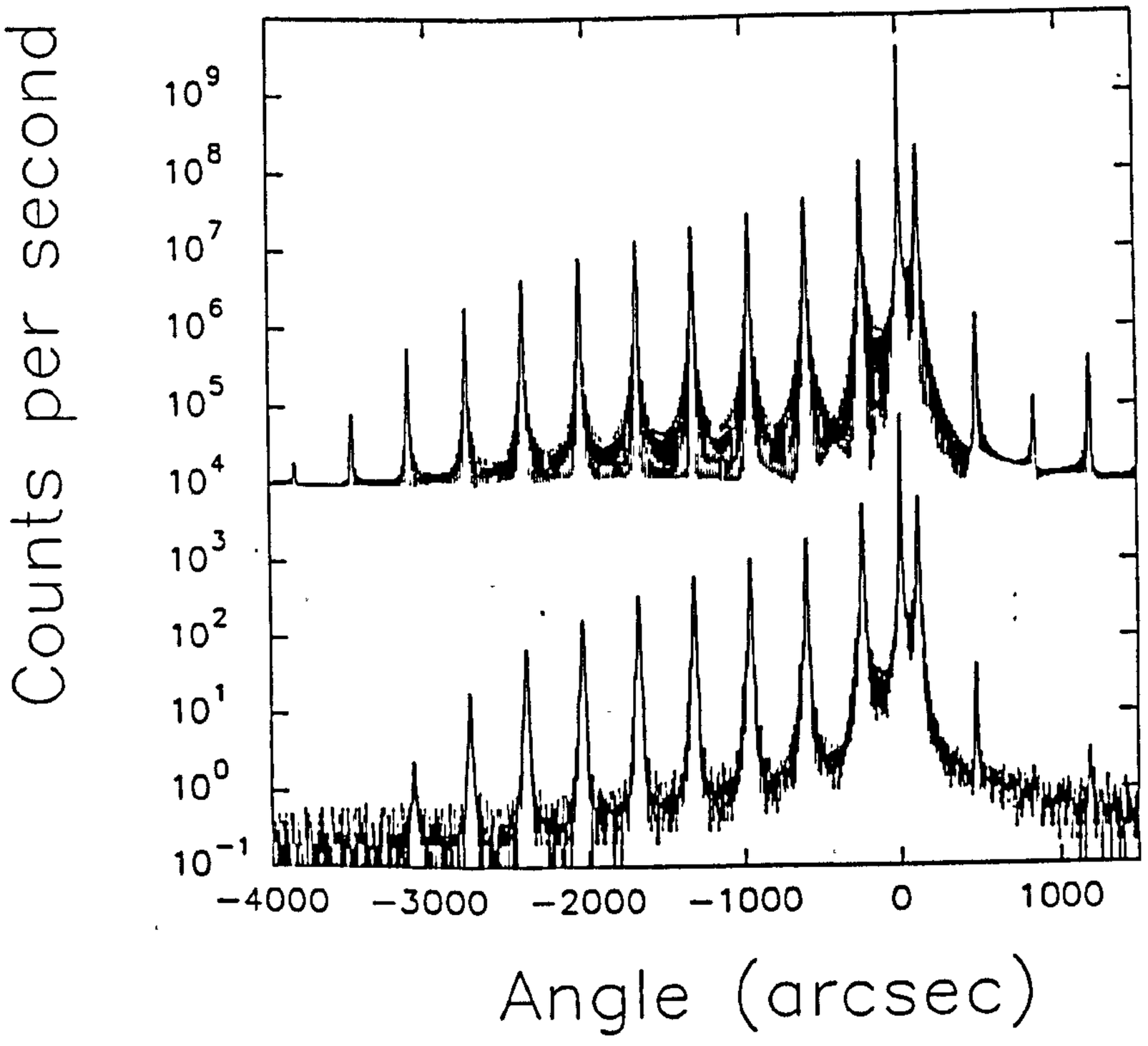

Fig. 5.3. (lower curve) Double crystal rocking curve from a (nominal) Si - 15% Ge 20-period superlattice structure grown in the V90 machine using an 004 reflection. (upper curve) RADS simulation using 20x(8.7 nm 14.7 At% Si-Ge + 45.0 nm Si).

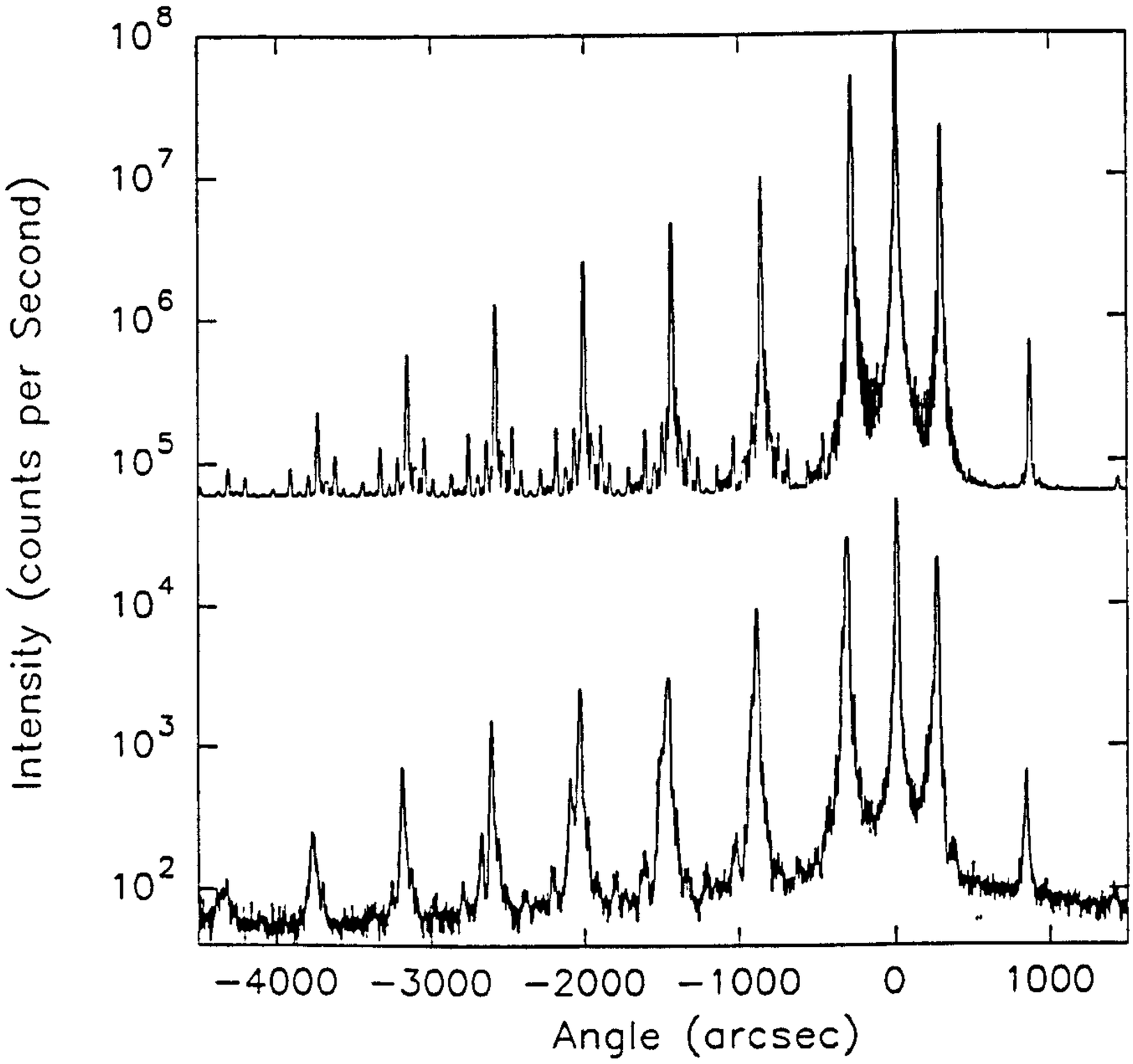

Fig 5.4 (lower curve) Double crystal rocking curve from a (nominal) Si - 15% Ge 30-period superlattice structure grown in the V80 machine using an 004 reflection. (upper curve) RADS simulation using 30x(5.8 nm 15.8 At% Si-Ge + 27.8nm Si) and a period dispersion of 3%.

Consider the superlattice grown in the V90S system. This structure consists of a 20 period superlattice with nominally 8 nm $Si_{0.85}Ge_{0.15}$ and 45 nm Si layers. Both TEM and X-Ray analysis were carried out and simulation of the rocking curve carried out with the dynamical theory simulation. From this the structure is found to

be 14.7 At% SiGe layers 8.7 nm wide separated by 45.0 nm of Si. Figs 5.5 and 5.6 show the superlattice grown in the V90S in more detail.

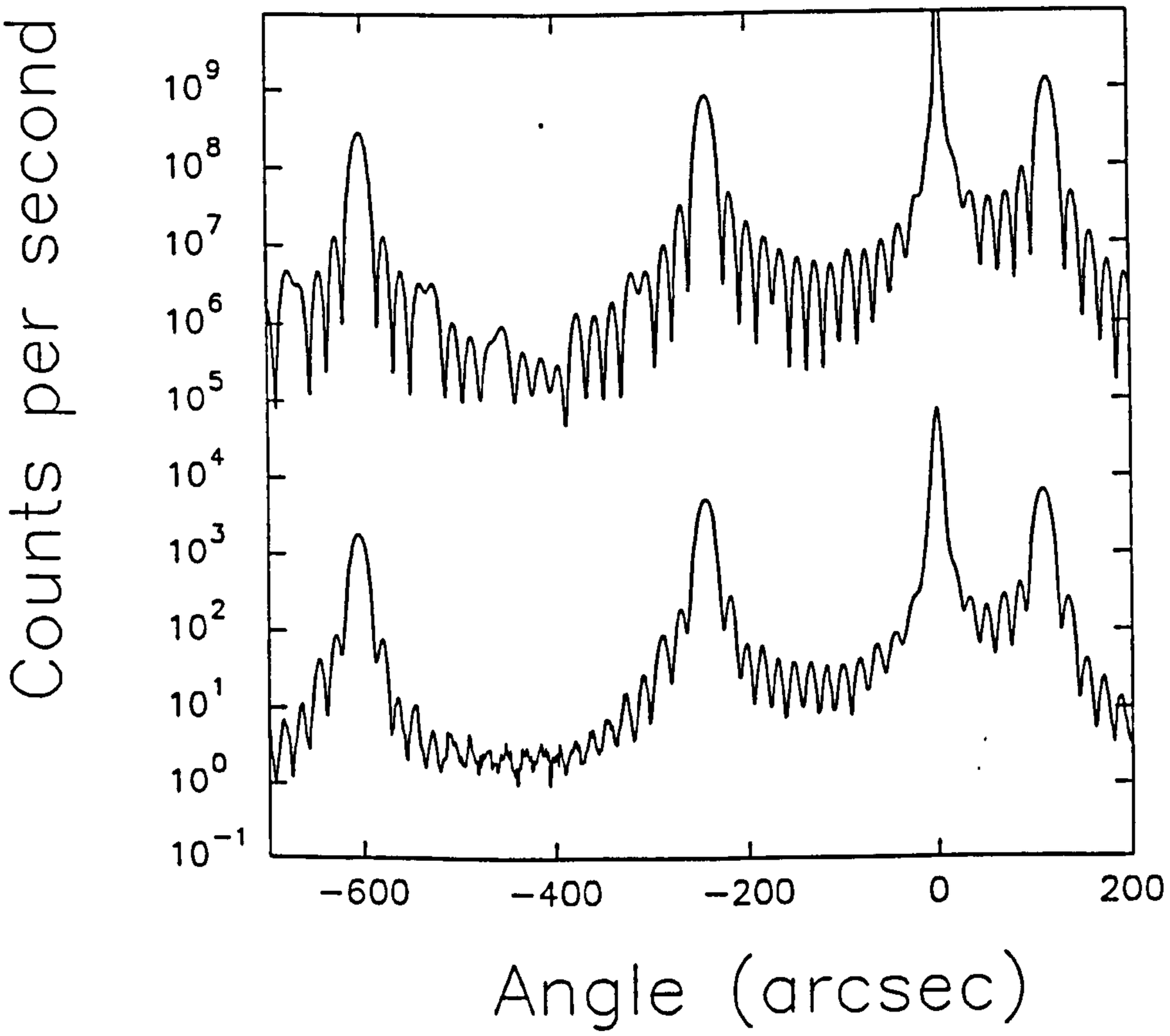

Fig. 5.5. (lower curve) Detail from Fig. 5.3, showing the Pendellosung fringes between the +1 and -2 satellite peaks in the measured rocking curve; (upper curve) simulation of the superlattice structure with 2% period dispersion introduced, showing irregular changes in the amplitude of the Pendellosung fringes.

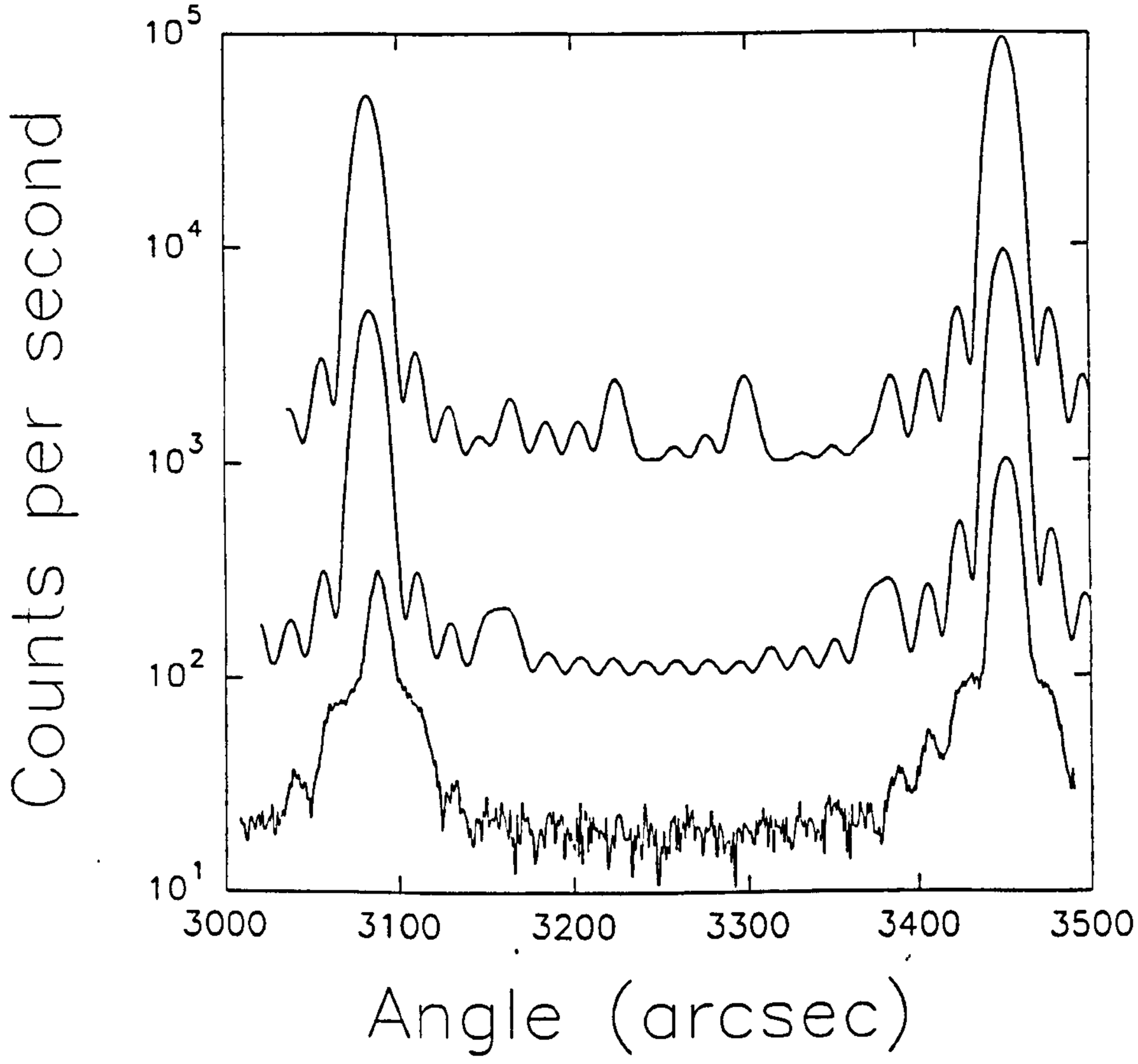

Fig. 5.6. (lowest curve) Detail from Fig. 5.3, of the fringes between the -5 and -6 satellite peaks in the experimental curve; (middle curve) simulation of the superlattice with 0.5% period dispersion; (upper curve) simulation with 1% period dispersion.

The region of Fig. 5.3 between the +1 and -2 satellite peaks is expanded in Fig 5.5. This shows that in between each pair of superlattice fringes there are 18 Pendellosung fringes, indicating that there are 20 periods in this superlattice structure. If these fringes are clear and regular then the superlattice has good periodicity. However if the superlattice has a 2% variation in period as in the simulation also shown in Fig 5.5 then these fringes become irregular in height. Fig

5.6 shows higher order peaks, -5 and -6 where the effects of period dispersion should be more pronounced; the lower curve is the experimental result and above it are two curves the first with a period dispersion of ± 0.3 nm and the second with a dispersion of ± 0.6 nm. As can be seen the experimental sample has less apparent variation in the pendellosung fringes than even the ± 0.3 nm simulation, which corresponds to a short term flux stability of better than 0.6 % over the one micron thick structure. The simulation is not intended to be a match to the experimental structure, but a demonstration of the sensitivity that can be achieved in the modelling and measurement of period dispersion. It should be noted that the width of the high order peaks do not in fact vary with non uniformity as has been proposed in studies of a superlattice using a powder diffractometer [Fewster and Curling 1987]. Although the latter technique is useful for rapid measurement of peak positions, its resolution is inadequate to distinguish between peak broadening and an increase of the intensity of the Pendellosung fringes immediately adjacent to the superlattice reflection.

Superlattice reflections can be thought of as a constructive interference between Pendellosung fringes from successive units of the superlattice, as is easily seen by modelling a series of superlattices with increasing numbers of repeat units on a simulation program. Such modelling shows that the individual reflection widths change little with the introduction of period dispersion but that relative intensities of individual maxima in the Pendellosung oscillations are very sensitive to irregularities in the period [Powell et al 1991c]. Often, a small period dispersion transfers intensity from the superlattice peak to the immediately adjacent Pendellosung fringes, giving the impression of peak width increase if resolution is not sufficient. However, the individual peak widths of both superlattice and intermediate Pendellosung fringes must be determined by the total thickness of the superlattice structure. It is by

examination and simulation of the intensities of the fringes in between the higher order superlattice reflections that we may determine period dispersion.

5.5 Interface roughness

Double crystal x-ray diffraction gives excellent characterisation of epitaxial layer composition and layer thicknesses, but, its ability to give information on the interface quality is limited. In order to investigate the abruptness of the SiGe interfaces x-ray reflectivity was used.

The aim of this experiment was to determine if the interface roughness was measurable with x-ray reflectivity, and then if so to consider how the interface quality is affected by the composition of the SiGe layers. To this end five superlattice structures were grown. The samples were grown in the V90S, the substrate temperature during deposition was 550°C and a matrix flux deposition rate of ~ 0.1 nm/s was used. The structures consisted of a five period superlattice with 24 nm of Si and 8 nm of $Si_{1-x}Ge_x$ capped with 10 nm of Si. Five similar structures were grown with nominal SiGe layer compositions of x_{nom} = 0.1, 0.2, 0.3, 0.4, and 0.5. The measured values for these layers is shown in Table 5.2.

TABLE 5.2

Comparison of X-Ray Diffraction And Reflectivity Period Measurements

Nominal Ge Composition	X-ray Diffraction		X-ray Reflectivity
	SiGe Composition	Period(nm)	Period(nm)
0.1	0.100	30.8	30.8
0.2	0.206	33.1	32.8
0.3	0.325	32.2	31.9
0.4	0.432	33.3	33.4
0.5	0.57 ± 0.5	-	32.3
	± 0.005	±0.1	±0.1

Double Crystal Characterisation

Double crystal x-ray diffraction was used, along with the simulation program, to determine the exact Ge compositions of the layers with good precision, and two of the rocking curves obtained are shown in Figs 5.7 and 5.8.

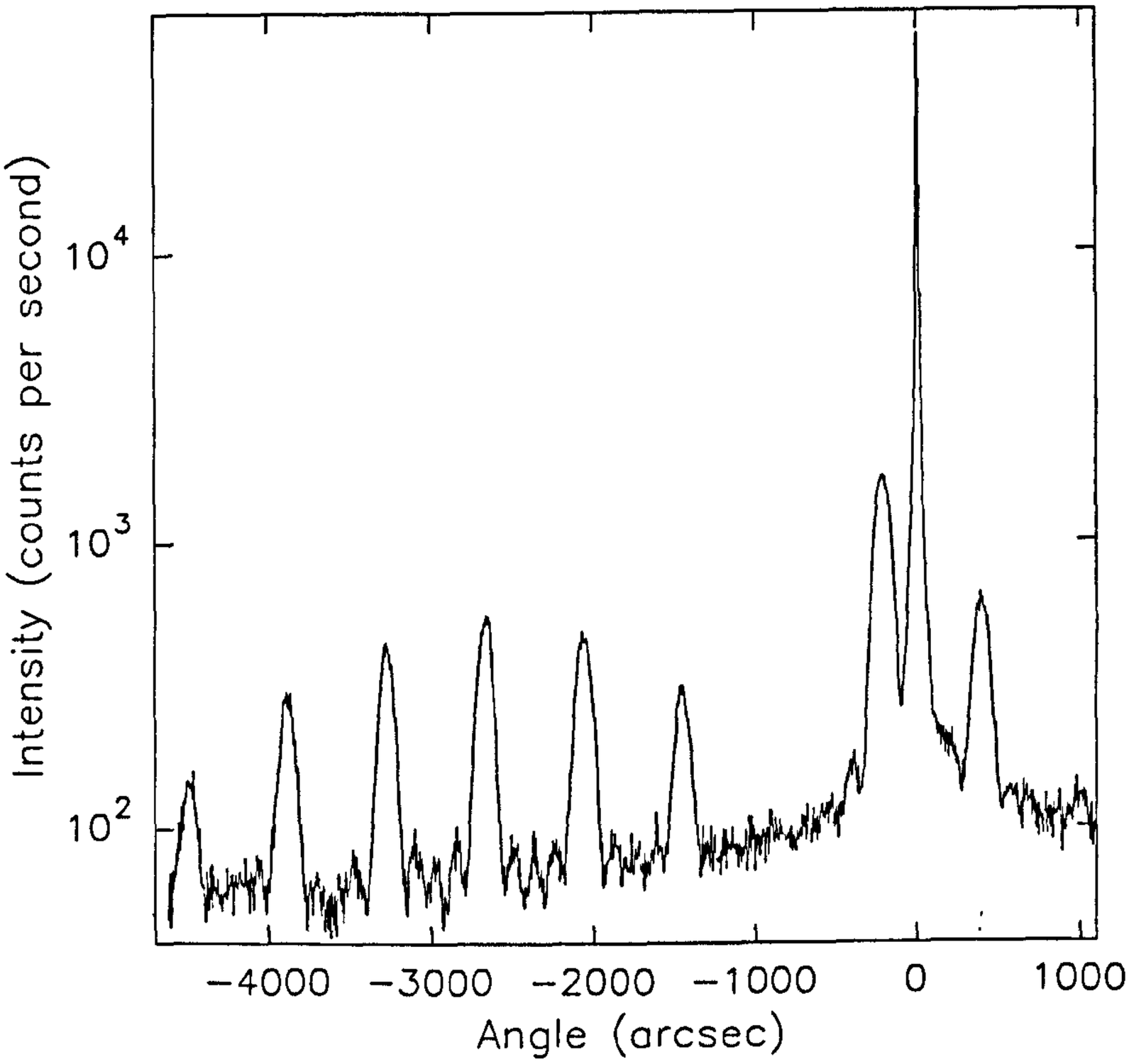

Fig 5.7 Double crystal rocking curve, (004) reflection, of the five period $Si_{0.68}Ge_{0.32}$ superlattice structure.

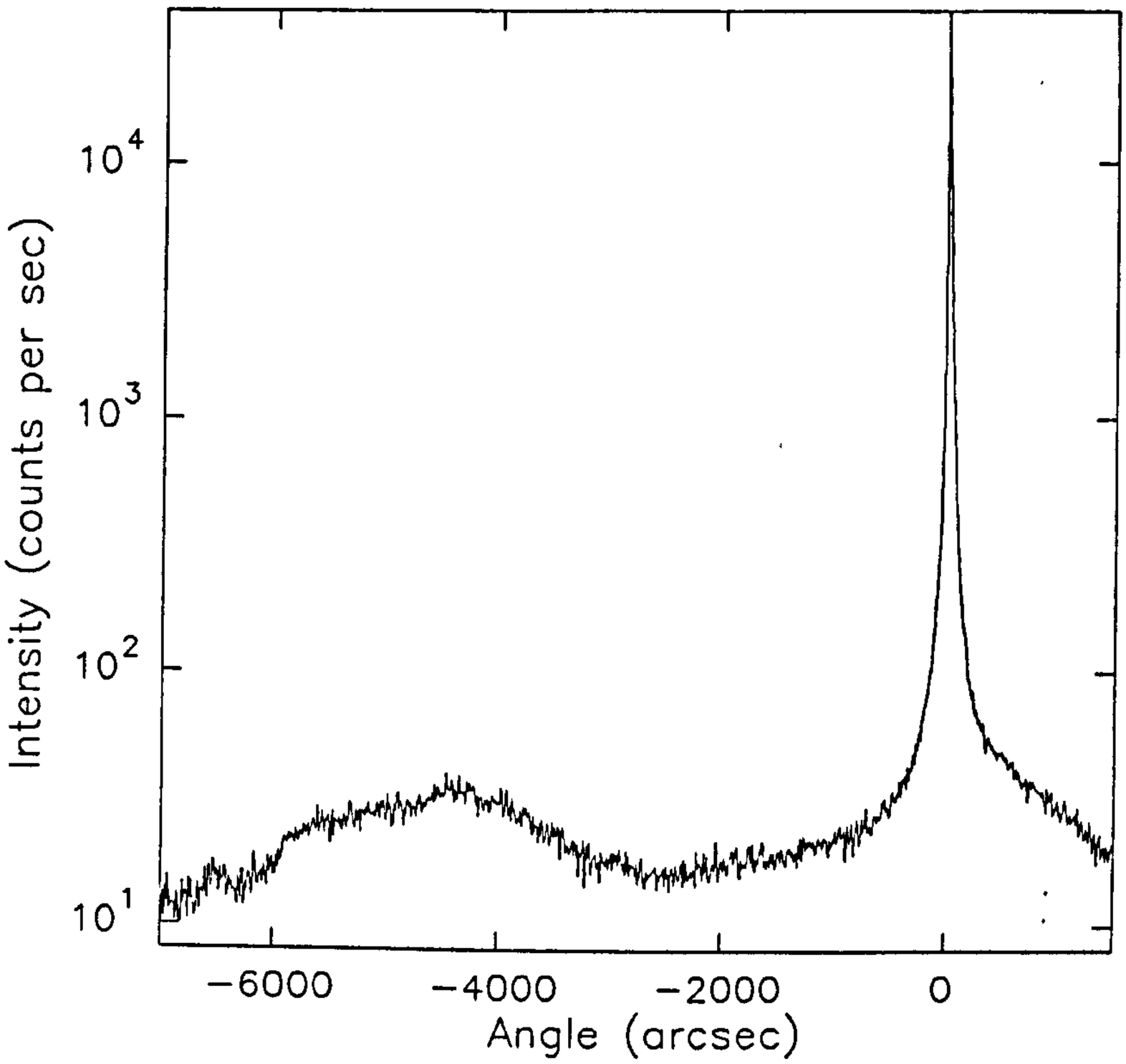

Fig 5.8 Double crystal rocking curve, (004) reflection, of the five period $Si_{0.43}Ge_{0.57}$ superlattice structure.

The degradation of the $x_{nom} = 0.5$ structure is quite apparent, this is due to the presence of dislocations producing variable strain fields within the layer (although it may also be an effect related to the factors that cause the roughness of the SiGe to Si interface). However, even though the individual X-ray diffraction superlattice peaks have been broadened beyond recognition in Fig 5.8, the composition of the SiGe layers can still be measured from their average position. It should be noted that since this layer has started to relax a second asymmetric reflection was also required to

calculate the composition. The periods of the superlattices was also measured and the results can be compared to those obtained from x-ray reflectivity in Table 5.2

Reflectivity Measurements

The reflectivity measurements of the samples provided curves such as those shown in Figs 5.9. and 5.10. It is immediately apparent that no degradation of the reflectivity signal has been caused by the threading dislocations present in the x_{nom} = 0.5 sample and hence a measurement of the period of this superlattice may be made. It is worth noting that reflectivity offers the possibility of examining epitaxial layers with high densities of defects and in fact even amorphous films can be characterised.

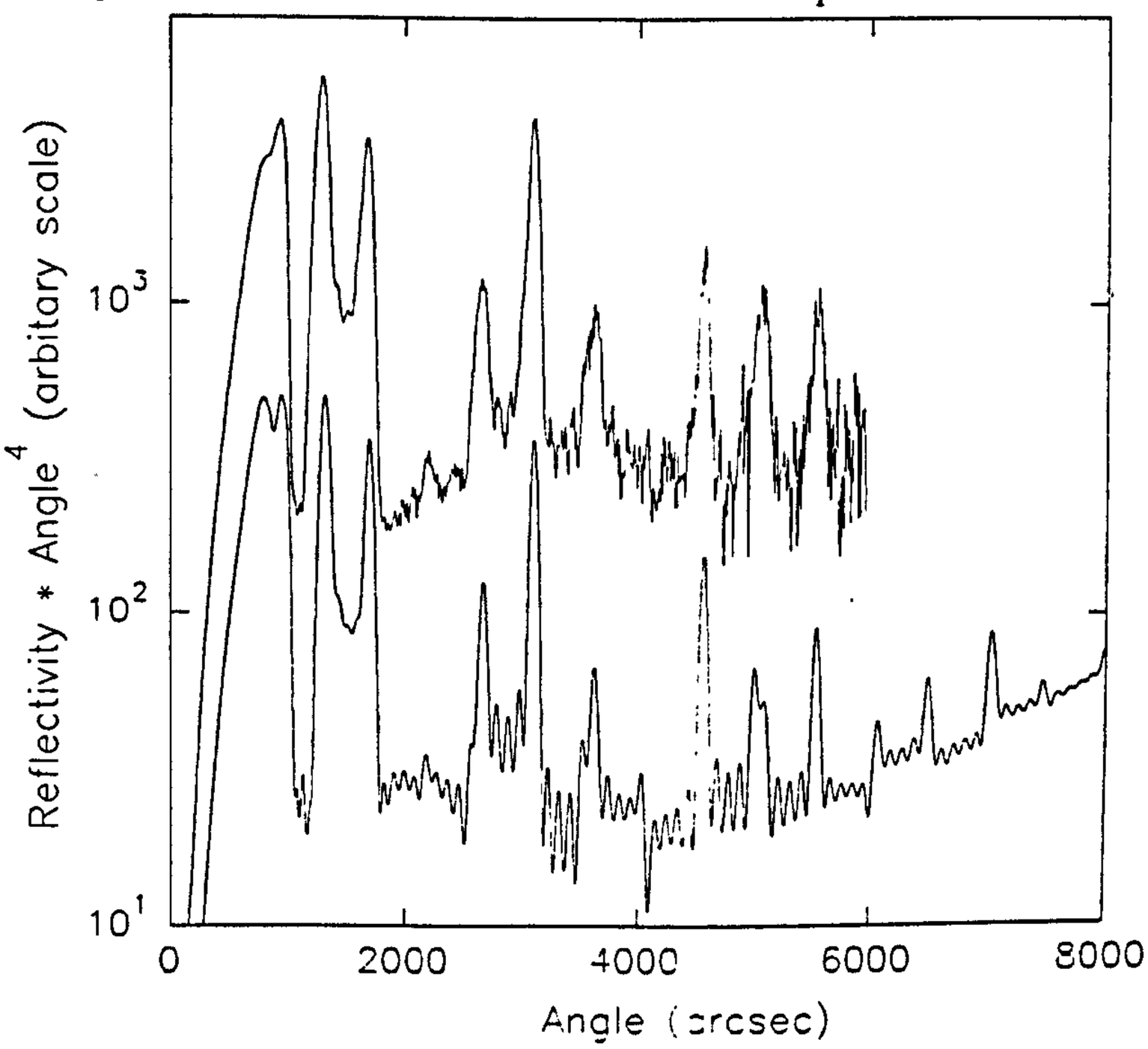

Fig 5.9 Reflectivity of the five period $Si_{0.68}Ge_{0.32}$ superlattice. Upper curve experimental, Lower curve simulation using the values given in Table 5.3

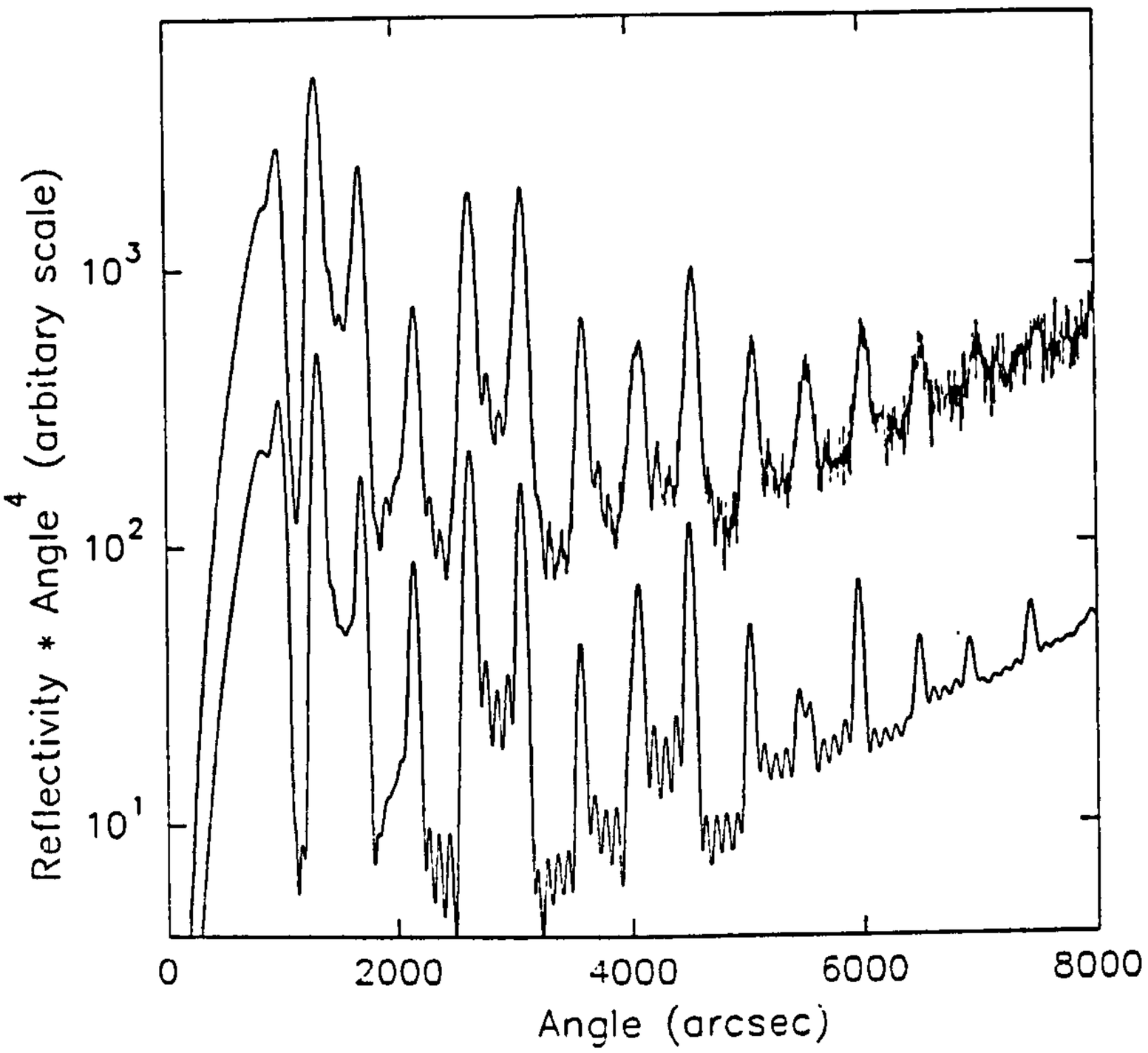

Fig 5.10 Reflectivity of the five period $Si_{0.43}Ge_{0.57}$superlattice structure. Upper curve experimental, Lower curve simulation using the values given in Table 5.3

Modelling Parameters

When the modelling of these reflectivity curves is considered a large number of parameters can be considered;

i) Si and SiGe layer widths within the superlattice

ii) Period uniformity of the SiGe/Si structure

iii) Capping layer width

iv) Surface oxide layer width

v) Surface roughness

vi) Si→SiGe interface roughness

vii) SiGe→Si interface roughness

viii) Ge composition in SiGe layers

ix) Sample curvature

With this number of variables simulation of the curves becomes extremely difficult, therefore attempts must be made to reduce the number of parameters. To do this a number of assumptions must be made;

i) The flux from the Si and Ge sources are reasonably constant, as indeed is indicated from the results of section 5.4. This means that the Si SiGe superlattice layers and the Si capping layer are related directly to the time for which the source shutters were open. In addition the period uniformity is assumed to be < 0.5%, i.e. too small to have a significant effect on the reflectivity. A small effect can be seen in that the apparent width of the high order Kiessig fringes is greater than the simulation due to excitation of the 'pendellosung ' fringes either side of the main peaks.

ii) The oxide layer thickness was not measured in this work, however, measurements [Philipp and Tafft 1982] have shown that a Si surface will form an oxide layer which reaches a thickness of 2.5 nm after a period of a few weeks (the time delay between growth and x-ray reflectivity characterisation for this work was ~ 6 months. The oxide formed will be a mixture of SiO and SiO_2 however in the simulation SiO_2 was assumed. It should also be noted that a 2.5 nm oxide layer will reduce the Si capping layer width by ~1 nm.

iii) The composition of the SiGe layers have previously been measured by double crystal diffraction.

Thus having reduced the variable parameters to the six considered below the simulations were carried out.

i) Sample curvature broadens the fringe peaks but gives no net loss in signal intensity. The effect reduces as the reflectivity angle increases thus it is simple

to model as consideration need only be given to the region where the 'pendellosung fringes become visible.

ii) Superlattice period is the variable that determines the spacing of the main peaks. It should be noted that the peak separation changes as one goes from the low angle peaks to the high angle peaks.

iii) The ratio between the Si and SiGe layer thicknesses determines the modulation envelope superimposed on the main superlattice fringes.

iv) Roughness on one of the two types of interface has the effect of reducing the degree of modulation of the main superlattice peaks by the mark space ratio.

v) Roughness on both types of interface reduces the intensity of all the superlattice fringes.

vi) Surface roughness is the controlling factor on the rate at which the whole curve falls off with increasing angle. A high roughness results in a rapid reduction in signal with increasing angle.

The x = 0.21 layer simulation gives an interface roughness of 0.5±0.3 nm and a surface roughness of 0.5±0.3 nm. Outside of these error limits, differences between simulation and the experimental result become significant. The situation with the x = 0.57 sample proves to be more complicated. The best fit simulation is obtained with a surface roughness of 0.5±0.3 nm. However, one of the two types of interface is found to have a roughness of 1 ± 0.3 nm and the other a roughness of 0.5 ± 0.2 nm. It is not possible to tell directly with the X-ray techniques which is the rougher of the two interfaces although the quality of the surface suggests that the Si provides the smoother of the two interfaces, and is able to "planarise" the rough interface found at the top of the SiGe layer.

Table 5.3 gives values of the roughness at the Si on SiGe interface as the SiGe composition varies. This roughness is seen to be stable up to x ~ 0.3.

Above x = 0.3 the roughness at the Si on SiGe interface increases. TEM analysis (Fig 5.11) was used to confirm that the Si on SiGe interface has the greater roughness. By direct measurement of the long range (~ 70 nm) roughness visible in the TEM micrograph the r.m.s. roughness was found to be 1.0 ± 0.3 nm. However, when the SiGe on Si interface is considered, the TEM shows this interface to be relatively smooth as opposed to the reflectivity measurement of 0.5 ± 0.2 nm. This may be accounted for by assuming that it is either a short range roughness too small to be observable in TEM where the sample thickness is ~100 nm or a grading of the interface.

Table 5.3

X-Ray Reflectivity Measurements of Layer Thickness and Interface Roughness

Ge composition (At%) ±0.005 At%	10	20.6	32.5	43.2	57
SiGe layer thickness (nm)	7.3±0.3	8.0±0.3	7.9±0.2	8.7±0.2	9.4±0.2
Si layer thickness (nm)	26.2±0.3	24.8±0.3	23.4±0.2	24.4±0.2	22.9±0.2
Si→SiGe Interface roughness (nm)	0.5±0.3	0.5±0.3	0.5±0.2	0.5±0.2	0.5±0.2
SiGe→Si Interface roughness (nm)	0.5±0.3	0.5±0.3	0.7±0.3	1.0±0.3	1.0±0.3

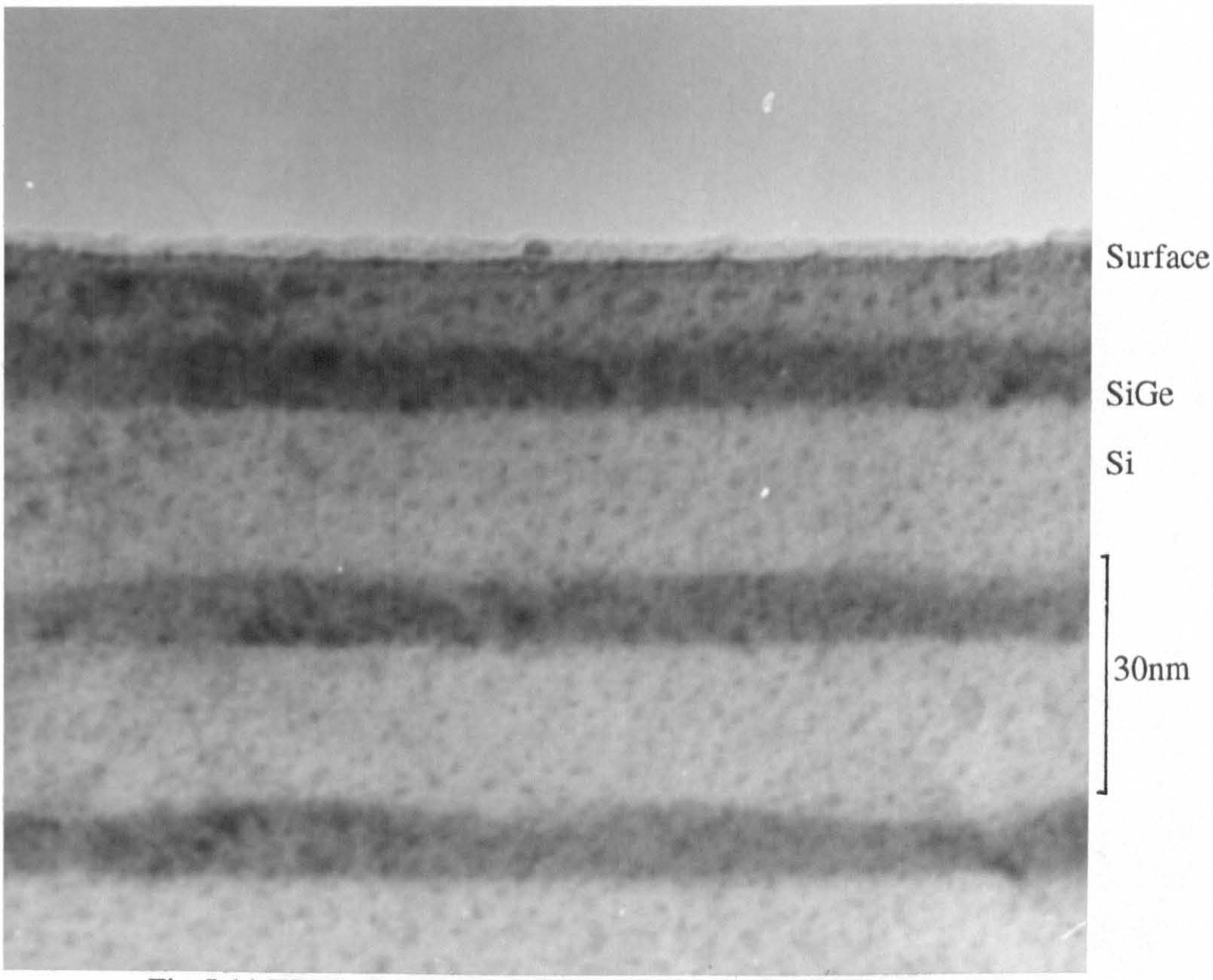

Fig 5.11 TEM micrograph of the $Si_{0.43}Ge_{0.57}$ superlattice.

As there is a short range roughness at the SiGe on Si interface it is reasonable to propose that a similar short range roughness is present at the Si on SiGe interface which would be superimposed upon the long range roughness. Reflectivity measures the total roughness which can be considered as the root mean square of both the short and long range roughness present [Braslau et al 1988]. This, in effect, suggests that for the x = 57% sample the Si on SiGe interface has a short range roughness of 0.5 ± 0.2 nm and a long range roughness of 0.9 ± 0.3 nm. Long range roughness will continue to affect the peak intensities until the wavelength of the roughness exceeds the coherence area of the X-ray probe, typically several μm [Born and Wolf 1970]. In

this work diffuse scattering has been ignored, however, consideration of the diffuse scattering should provide additional information on the interface roughnesses.

5.6 X-Ray Fluorescence

In addition to characterising the position of the matrix elements of the epitaxial layers the depth profiles of dopants and contaminants within the layer is of interest to the crystal grower. In this section the usefulness of glancing incidence x-ray fluorescence is considered.

The experiment carried out, considered a 5 period superlattice consisting of 22.9 nm Si layers and 9.4 nm $Si_{0.43}Ge_{0.57}$ layers with a 87 nm Si cap, a structure already well characterised with TEM and x-ray reflectivity in the previous sections. As discussed in section 3.6 the fluorescence signal obtained from an element is dependent upon which excitation lines are under observation and the energy of the exciting radiation. For this reason one must either know which element is present or scan at two or three different energies. In this experiment 0.1 nm radiation was used as this gave a reasonable fluorescence signal for Ge along with likely contaminants such as Cu and Fe. The primary aim of the experiment was to determine the depth resolution obtainable in the fluorescence profile. Initially a reflectivity curve was taken over the range from which fluorescence measurements were to be taken, this is shown later in Fig 5.14. This reflectivity curve enables any backlash in the stage to be corrected for as reflectivity measurements may also be taken during the fluorescence measurements. The fluorescence measurements required a counting time of 10 minutes at low angles reducing to 1.5 minutes at angles well above the critical angle. This results in a total measurement time of several hours and consequently

corrections must be made for the reduction of the incident X-ray intensity, as measured by an ionization chamber.

In Fig 5.12 a typical fluorescence curve taken from the region well below the critical angle is shown, in addition to the Ge fluorescence peaks, Cu fluorescence peaks are seen. However these Cu peaks remain at approximately the same intensity as the incident angle progresses past the critical angle indicating that the Cu contamination is located in the surface layer and not as a bulk contaminant [Iida et al 1986].

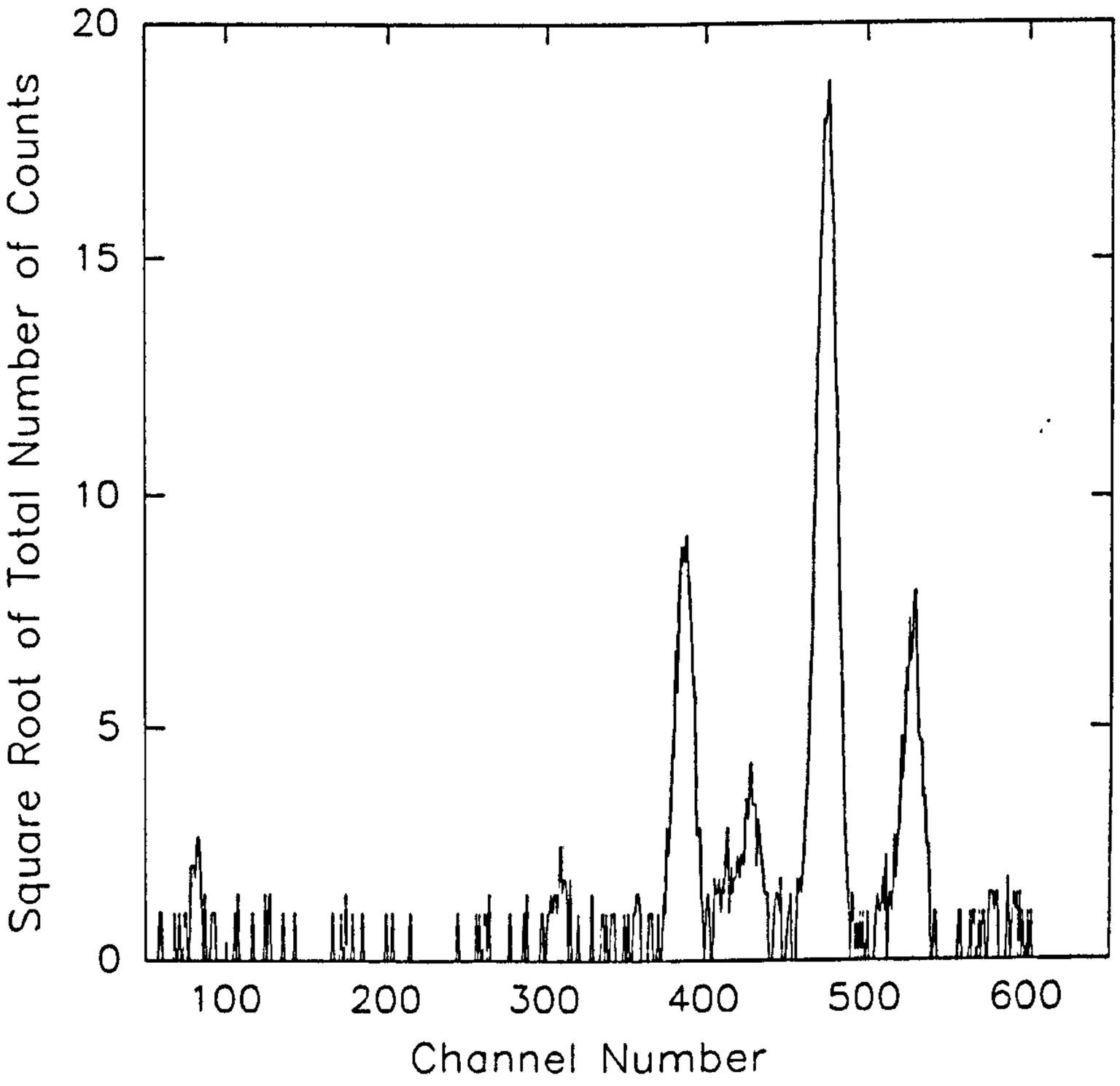

Fig 5.12 Glancing angle X-ray fluorescence from a $Si_{0.43}Ge_{0.57}$ superlattice where incidence angle =0.083° and count time = 600 seconds.

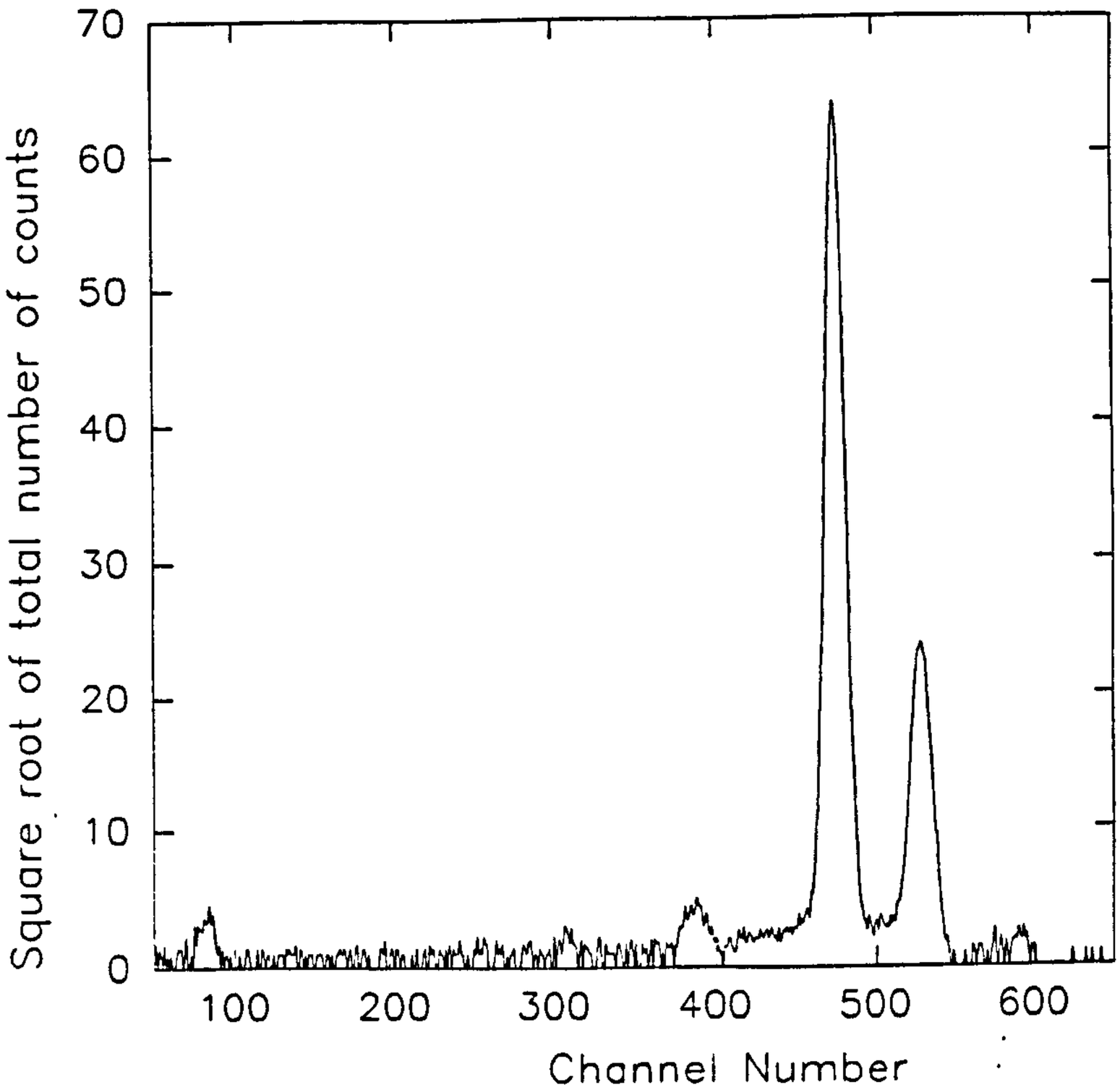

Fig 5.13 Glancing angle X-ray fluorescence from a $Si_{0.43}Ge_{0.57}$ superlattice where incidence angle = 0.153° and count time = 150 seconds.

The integrated area of the Ge Kα peaks as a function of incidence angle is shown in Fig 5.14. It can be seen the troughs in the fluorescence response correspond to the peaks in the reflectivity signal.

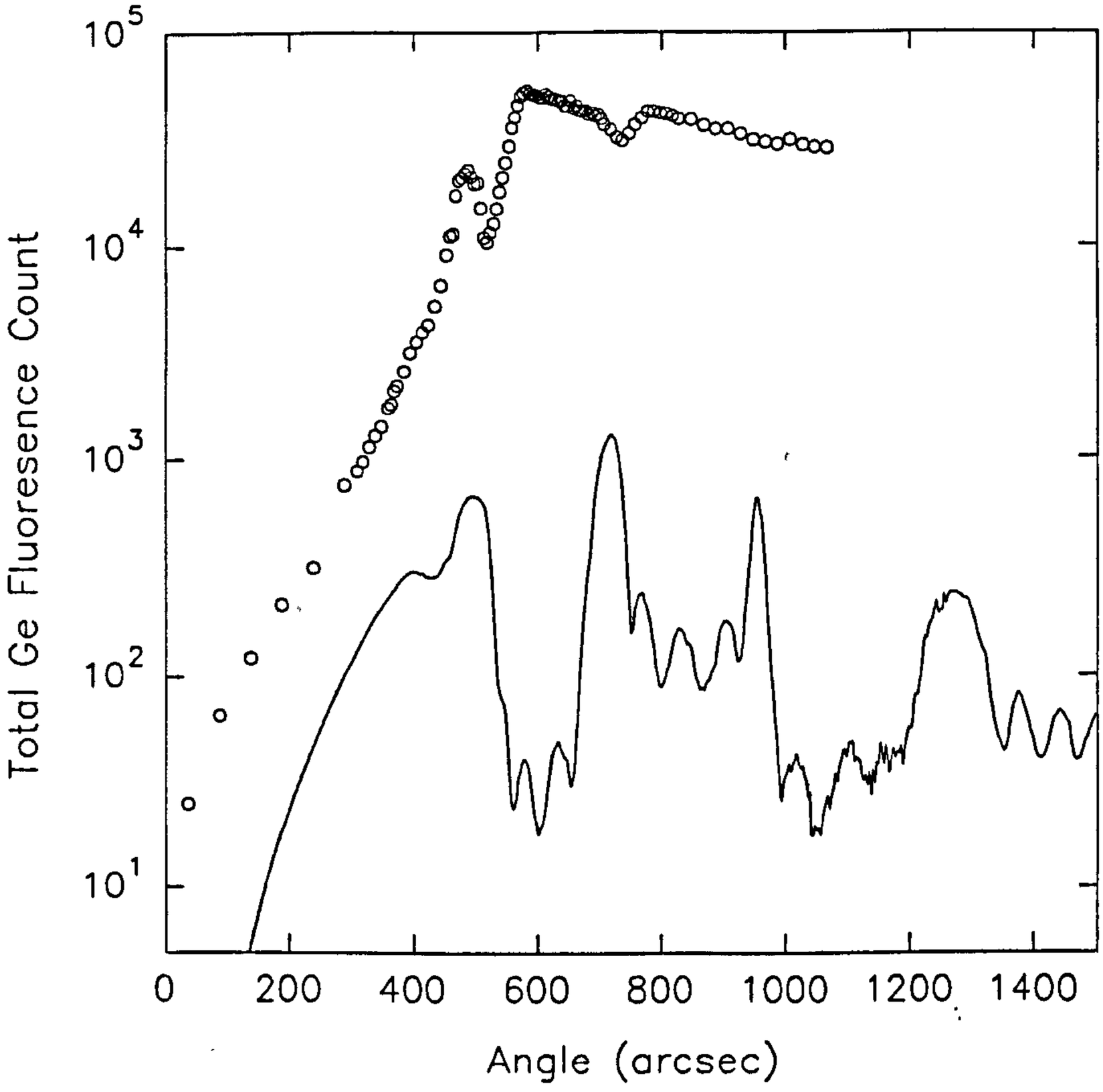

Fig 5.14 Ge fluorescence (top) and reflectivity (lower) curves for a $Si_{0.43}Ge_{0.57}$ superlattice. The reflectivity curve has been multiplied by the angle^4 and thus has an arbitrary scale

The structure of the rocking curve can be explained by considering the electric field standing wave which is created within the superlattice structure, as the incident angle changes the maxima of this standing wave move. Thus when the maxima is within a SiGe layer the Ge fluorescence is seen to peak and when the standing wave maxima fall in Si layers a trough is seen in the Ge fluorescence signal. This fluorescence rocking curve has been modelled using the simulation discussed earlier. A calibration of the fluorescence signal was obtained by consideration of a

15% SiGe layer which was fully strained and therefore could be well characterised with X-ray diffraction. With this calibration the composition of the SiGe layers within the superlattice was found to be 57 ± 2 At% which is comparable with the X-ray diffraction results of 57 ± 5 At%.

5.7 Fluorescence Conclusions

The fluorescence technique has proved capable of providing compositional information with a high degree of accuracy, ± 1%, for matrix materials. It is also capable of providing depth profiles for impurity elements (with atomic numbers > 11) with concentrations down to $10^{17}cm^{-3}$. The present experimental system uses equipment designed for the Daresbury SRS X-ray microprobe [Langevelde 1990] and in this work we were primarily demonstrating the technique. Consequentially there are a number of improvements available to increase the sensitivity of the technique.

i) The use of a condensing crystal as the beam conditioner can give a five fold increase in beam intensity. The disadvantage of a condensing crystal is that it will work over a small angular range only, and consequently several such crystals would be required to cover the energy range 5 to 20 keV

ii) A larger fluorescence detector (a 4 mm square detector was used here) would give a substantial increase in collection efficiency.

iii) A bending magnet source was used, with the station 80m from the tangent point. There is an increase of at least two orders of magnitude in the beam intensity available from the wiggler line station that is close to the source.

Thus by the use of these improvements a reasonable estimate of the sensitivity of the fluorescence depth profiling technique would be $10^{15}cm^{-3}$.

Chapter 6

Relaxation Of SiGe

6.1 Why do we want to know about relaxed material ?

One of the main stumbling blocks preventing SiGe technology from achieving its full potential is the inability to produce high quality substrates with lattice parameters between Si and that of Ge. The ability to chose substrates with varying lattice parameters would open up new possibilities in device design, two such ideas are discussed later in this section. The production of these substrates has however proved difficult, no SiGe substrate wafers are available, therefore the idea of producing relaxed SiGe on Si substrate wafers has been considered. Until recently [Powell et al 1991e] the growth of relaxed SiGe on Si involved the creation of very high densities of threading dislocations – $10^{11}cm^{-2}$. Defect densities as high as these would prevent devices grown on the layer from operating. This chapter therefore initially considers the standard growth of SiGe on Si substrates and uses this information to produce buffer structures showing a significant reduction in defect densities of the relaxed buffer layers. The reduction in threading dislocation densities is not yet sufficient for VLSI however the improvements obtained suggest that it may well be possible to produce buffers of sufficient quality in the future.

Heterojunction Band alignment

Consider the Si lattice grown commensurately on a Ge substrate. The lattice will be tetragonally distorted, compressed in the z direction and expanded in the x and y directions. This distortion means a loss of cubic symmetry and thus the band alignments are different for the different orthogonal directions. Fig 6.1 shows the band structure obtained [Gell 1988]

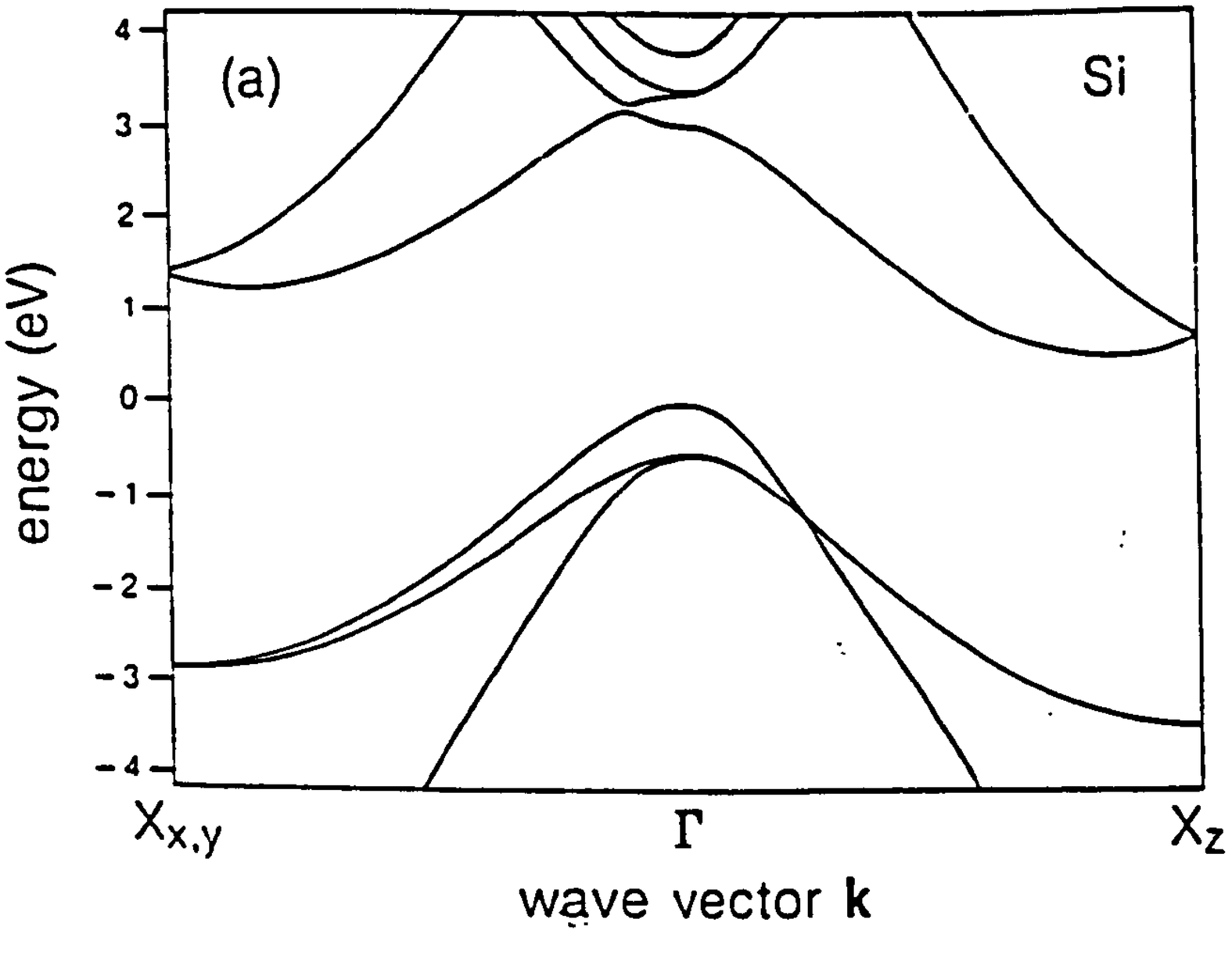

Fig 6.1 Band structure of Si grown commensurately on a Ge substrate. The left hand side shows the bands in x,y directions and the right-hand side gives the band structure in the growth direction.[Gell 1988]

It can be seen that the Si compressed in the z direction has both a lower valence and conduction band as one approaches the X band edge. The change in band positions with the degree of strain allows the band offsets at the heterojunctions to be

altered as the designer wishes. For example consider Fig 6.2a and b [People and Bean 1985] in Fig 6.2a $Si_{0.5}Ge_{0.5}$ is grown commensurately on cubic (unstrained) Si, a type I alignment of the bands is obtained where both electrons and holes prefer to be in the SiGe material.

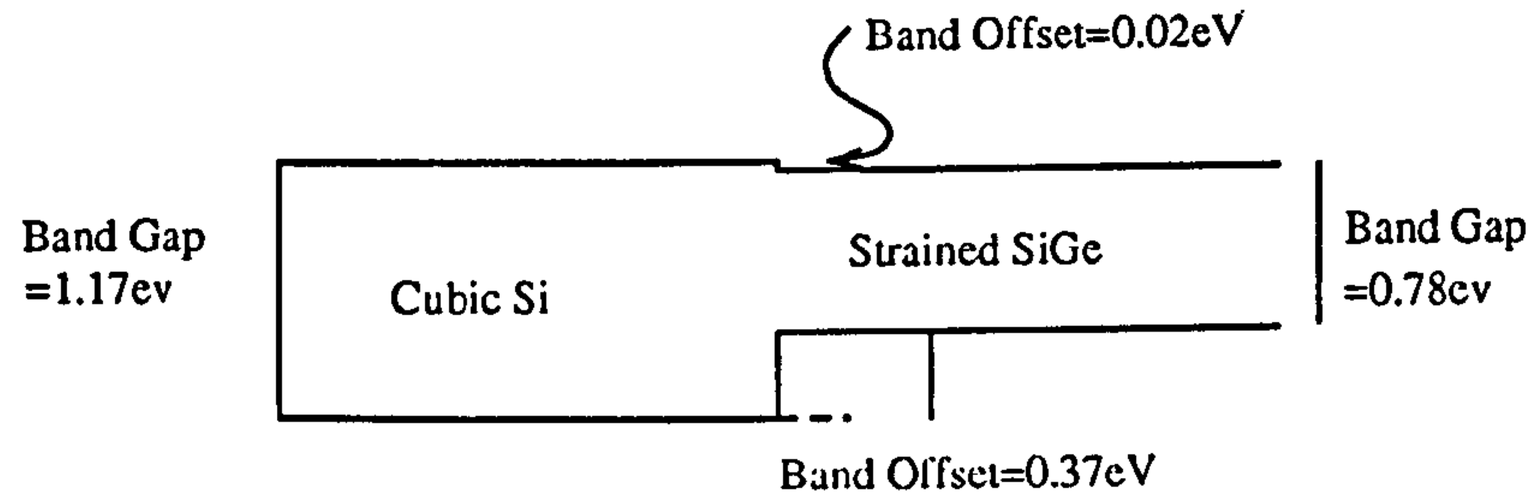

Fig 6.2a $Si_{0.5}Ge_{0.5}$ material grown commensurately on a Si substrate

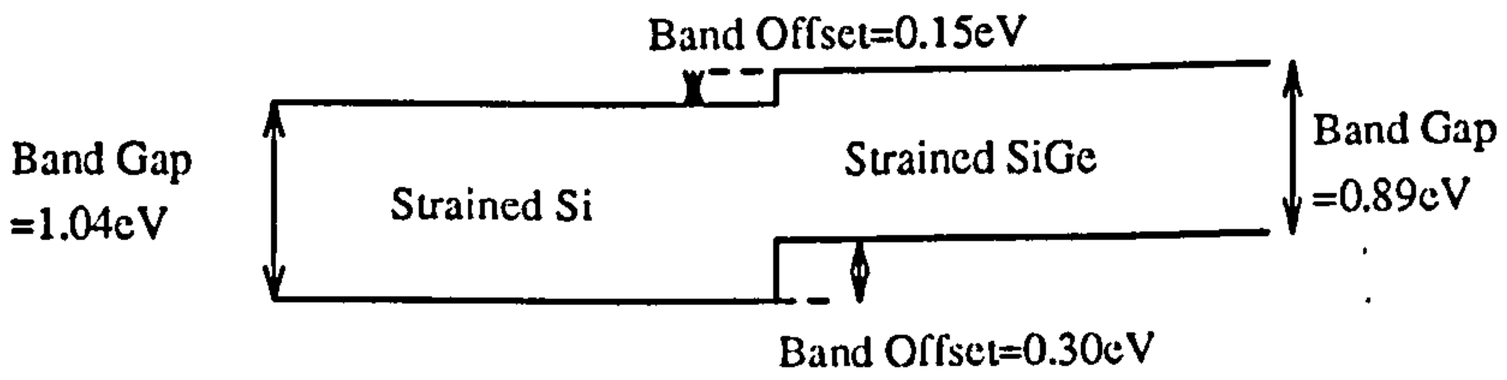

Fig 6.2b $Si_{0.5}Ge_{0.5}$ material grown commensurately on a relaxed $Si_{0.75}Ge_{0.25}$ buffer layer.

However, if Fig 6.2b is considered where the same junction is grown on a relaxed $Si_{0.75}Ge_{0.25}$ buffer then the band alignments within each material have changed and the heterojunction becomes type II where the discontinuity at the conduction band has been reversed from -0.02 eV to 0.15 eV.

Zone Folding

The ability to produce light from a material compatible with Si VLSI technology is in great demand. The problem is simply that Si has an indirect band

gap and there is no direct bandgap material which can be grown commensurately with Si to any significant thickness. A solution to this may be to produce an artificial crystal with an additional periodic modulation of the electric field. Consideration of the band structure of Si shows that the conduction band minimum falls 4/5 of the way to the X zone edge [Pearsall et al 1989, R.Zachai 1991]. If a Si type crystal could be produced where there is an additional periodicity with five times the Si crystal period then new Brillouin zone boundaries would be produced which would fold the conduction band back towards the Γ centre. Fig 6.3 shows how this produces a quasi direct bandgap for the material.

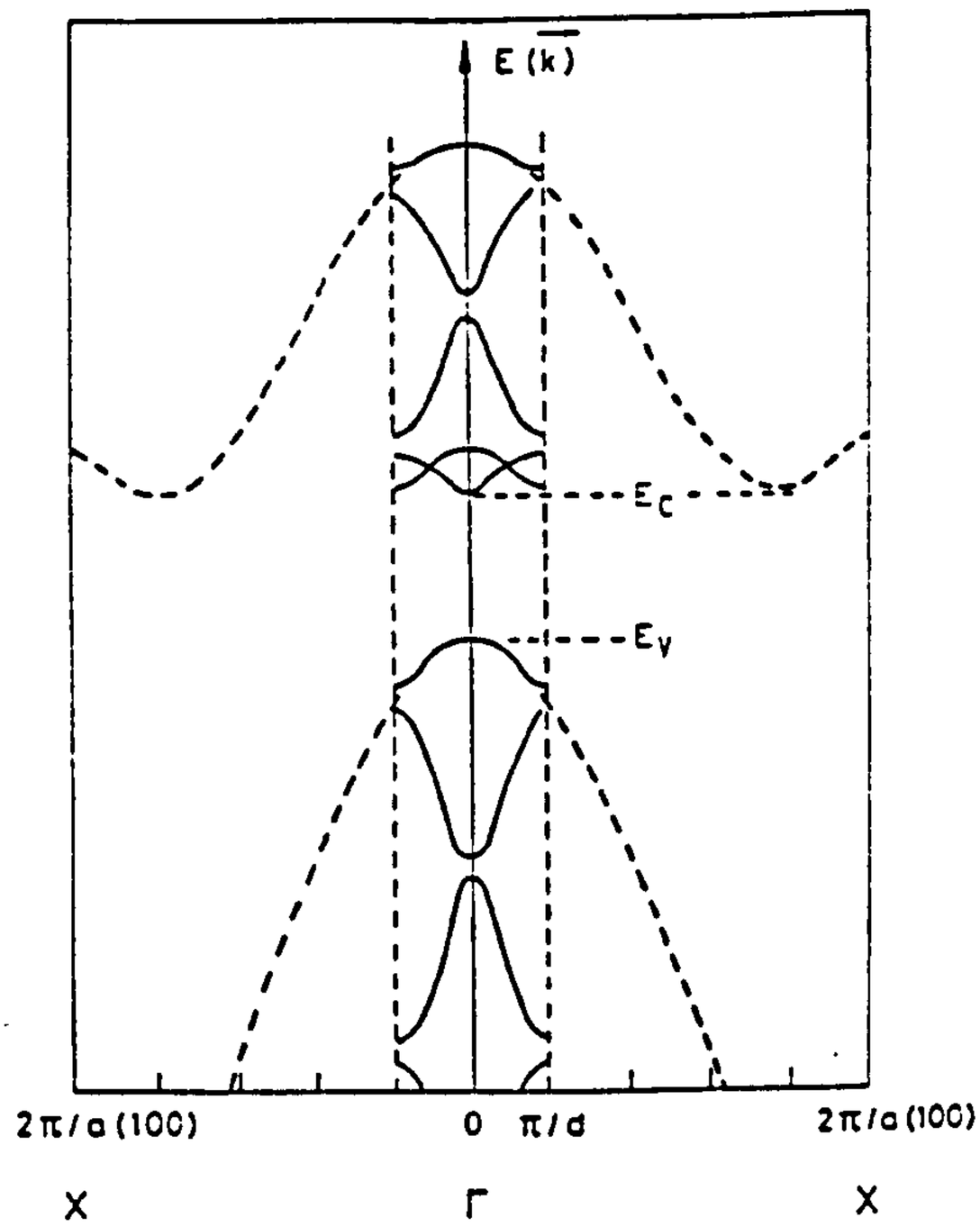

Fig 6.3 Band diagram for Si_5Ge_5 [Jain and Hayes 1991].

In order to formulate this new crystal a superlattice structure can be grown consisting of a repeated layer structure; 5 monolayers of Si followed by 5 monolayers of Ge. Thus in the z direction there is the required periodicity. However there is still the problem that this superlattice can only be grown to a thickness of 10 nm before the strain present in the layer causes it to break down. In order to overcome this the superlattice can be equilibrium strained by growth on top of a relaxed $Si_{0.5}Ge_{0.5}$ buffer layer as in Fig 6.4. In the equilibrium strain state the superlattice structure can be grown to any desired thickness.

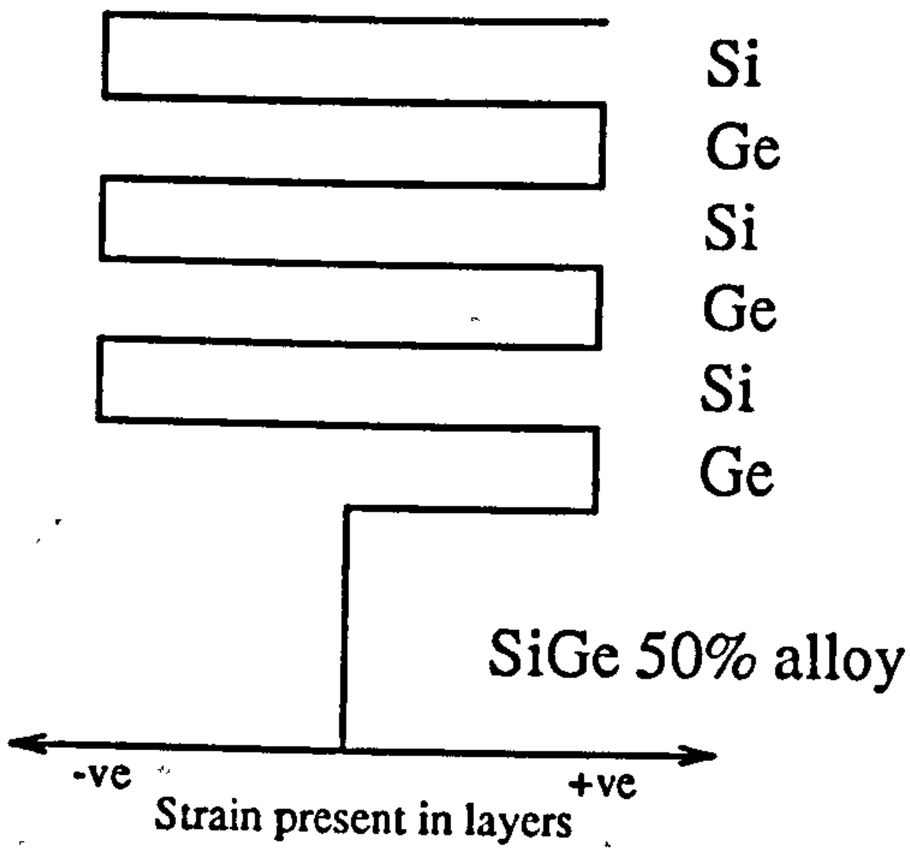

Fig 6.4 Schematic of equilibrium strained structure.

For both these applications a relaxed SiGe buffer layer is required with a low density of dislocations and it is towards this end that this chapter considers relaxation in SiGe.

6.2 Processes of plastic relaxation

As discussed earlier SiGe material when grown epitaxially on a Si substrate initially deposits commensurately with the substrate. This requires that the unit cell of the SiGe material to be tetragonally distorted and consequently there is a strain energy associated with this distortion. As the SiGe epitaxial layer grows thicker the strain energy of the layer increases. When the epitaxial layer reaches the equilibrium critical thickness the strain within the layer is equivalent to the strain required in order to make an existing threading dislocation glide along the interface between the Si and SiGe layers to create a misfit dislocation. Fig 6.5 shows how a misfit dislocation represents a missing (111) plane of atoms which allows the strain in the layer to be reduced.

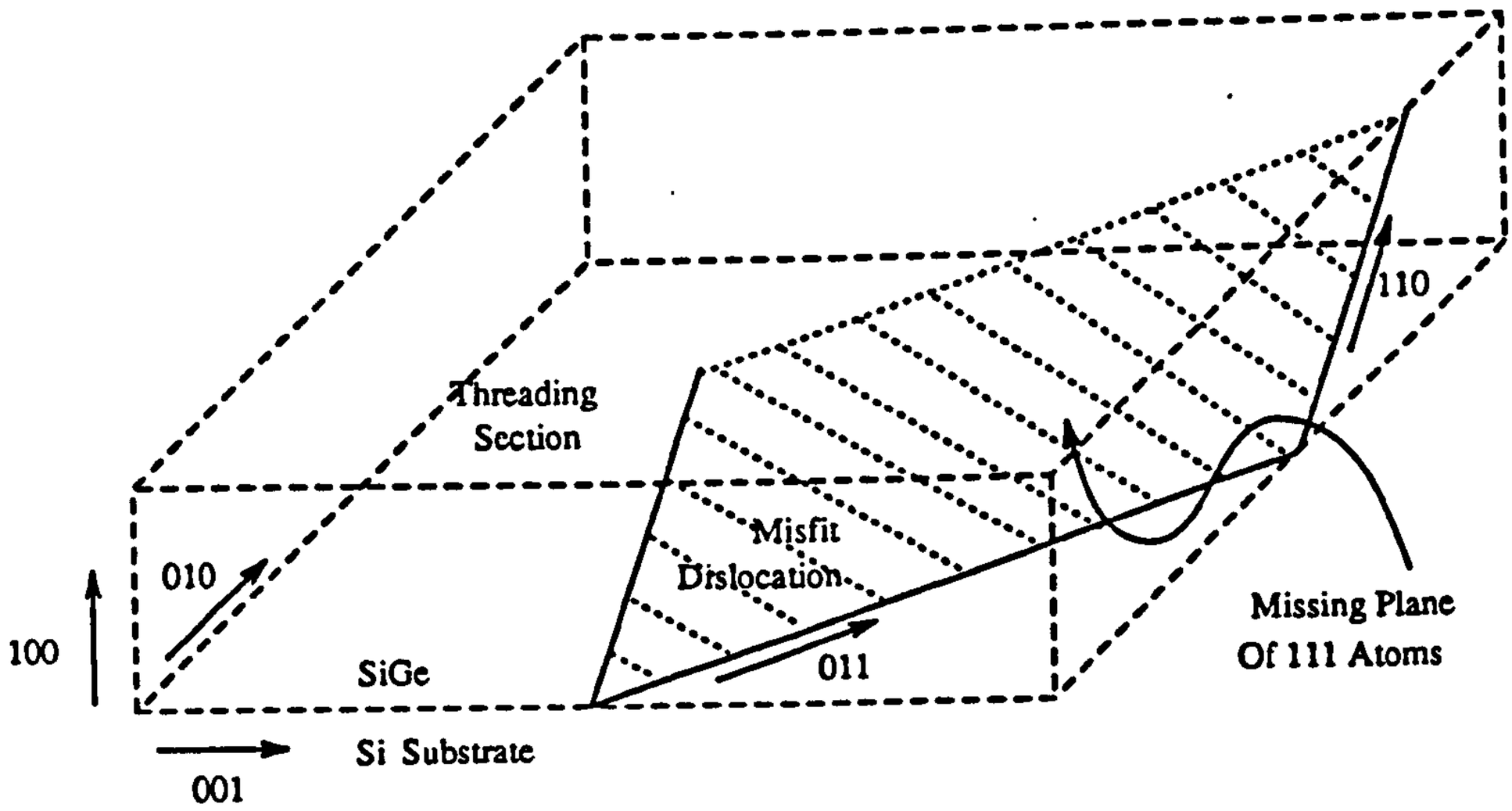

Fig 6.5 To relieve the strain of a SiGe layer on Si missing (111) planes of atoms occur, in the case shown this missing plane is bounded by a misfit dislocation along the interface and two threading dislocations in the SiGe material.

This equilibrium state is described in Equation 6.1 [Matthews and Blakeslee 1974]

$$h_c = \frac{b}{2\pi f} \frac{(1-\nu\cos^2\alpha)}{(1+\nu)\cos\lambda} \left(\ln h_c/b + 1\right) \qquad (6.1$$

This equation however only describes the state at which the creation of misfit dislocations becomes energetically favourable. However if layers are grown to beyond this thickness and annealed at high temperatures then relaxation can be observed [Houghton.D.C et al 1990]

For a misfit dislocation to extend, the threading dislocation which terminates the misfit dislocation must move in the direction of the misfit dislocation, ie along a [110] direction. Thus the threading dislocation must jump over the 'Peierls barrier' from the 'lattice valley' in which it is to the next lattice valley. The energy required for this is called the glide activation energy, E_g. This can be considered as the combination of two terms, these being the energy to form a kink in the dislocation, E_k, and the energy for the kink to move along the dislocation, E_m, as is shown in Fig 6.6.

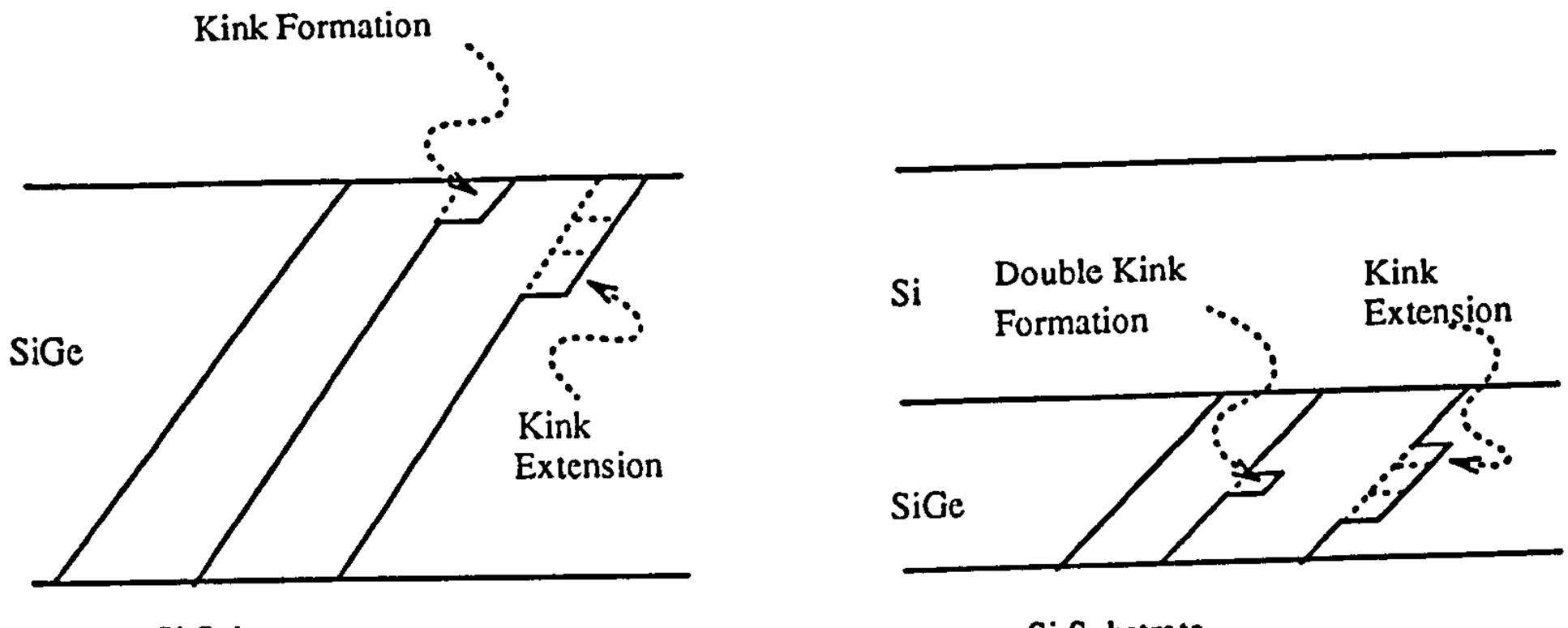

Fig 6.6 Kink formation in single and buried SiGe layers

For single layers of SiGe a kink may start at the surface of the layer, which in turn implies that the surface quality may effect E_k. For capped SiGe layers a double kink must be formed at some point along the threading dislocation; the formation of a double kink requires more energy [Hull et al 1989] and thus buried layers are found to be more stable.

$$E_g = E_k + E_m \qquad (6.2$$

The glide activation energy has been measured for bulk Si and Ge and values of 2.2 and 1.6 eV respectively have been determined. In SiGe layers however values of E_g have been found to vary from 2.5eV [Houghton.D.C 1990] 2.2eV for 5At% and 13At% layers [Tuppen and Gibbins 1989] and 1.1 eV for a 25At% layer [Hull et al 1989]. An explanation for this [Dodson 1988] is that the glide activation energy may be dependent upon the excess stress σ_{excess} present within this layer.

$$E_g(\sigma) = E_g(0)(1 - \sigma_{excess}/\sigma_p) \quad (6.3$$

where

σ_{excess} = layer stress - dislocation line stress

σ_p = Peierls stress , believed to be > 2 GPa

Equation 6.3 shows that as the layer thickness approaches the metastable critical thickness the glide activation energy is reduced.

Having considered the glide activation energy the velocity of a threading dislocation is given by

$$v = v_0\sigma_{excess}\exp[-E_g/kt] \quad (6.4$$

where

v_0 = constant

Thus once the epitaxial layer thickness is beyond the equilibrium critical thickness, misfit dislocations will begin to be formed. However, in order to produce significant relaxation one requires either,

i) High excess stress, ie thick layers so that the misfit dislocations nucleated from suitable sources have sufficient velocity to cause significant relaxation.

ii) High temperature so that their glide activation energy can be surmounted and the misfit dislocations present can extend at high speed

iii)A large density of nucleation sites. With enough nucleation sites ~ 10^9 misfit dislocations need only extend for a few μm in order to relax the layer.

6.3 Nucleation Sites

The initial work on strain relaxation using MBE considered threading dislocations to be the nucleation sources. In Si MBE material the threading dislocation density is ~ 10^3 cm^{-2} . However, if a SiGe layer is examined after growth to beyond its metastable critical thickness then the dislocation density can be as high as 10^{10} cm^{-2}. Clearly there must be additional nucleation sites available although their nature is unknown. A number of possibilities exist.

i) Dislocation half loops propagating down from the surface. Consideration of the nucleation energy required [Eaglesham et al 1989, Freund et al 1989] shows that where the misfit is < 1% the nucleation activation energy required is unreasonably high. Thus these dislocations need only be considered in high strain systems.

ii) Defects in the crystalline matrix may provide an additional source for the propagation of defects. Defect etching of relaxed layers [Gibbins et al 1989] show many misfit dislocations nucleated from a central defect. As multiple dislocations can be generated from a single source a reasonable density of these sources could lead to the 10^{10} cm^{-2} density of threading dislocations seen in some relaxed layers. Possible candidates for the nucleation sources are the 'diamond defects'[Eaglesham 1989] and SiC precipitates [Perovic et al 1989]. Alternatively additional sources can be produced from surface damage[Tuppen et al 1991a]. The supposition that nucleation sites are required is also supported by the lower nucleation rates seen upon annealing material grown by room temperature CVD [Perovic and Houghton 1991]

The activation energy associated with dislocation nucleation from each type of source should be considered. A pre-existing threading dislocation requires no additional nucleation energy. However, diamond defects, half loops, SiC precipitates and any other defects may require further stress in order to become energetically viable nucleation sites. Thus one will have the situation where as the stress is increased by growing the epitaxial layer to greater thickness more nucleation sites become active. This is considered further in section 6.5.

6.4 Growth To Beyond Metastable Critical Thickness

In order to produce the symmetrically strained structures, considered earlier in this chapter, relaxed buffer layers are required. The simplest method of achieving a relaxed SiGe buffer layer is to grow to beyond the metastable critical thickness. However complete relaxation is not achieved and in this section the degree of residual strain is considered. A number of SiGe layers , shown in Table 6.1, with Ge compositions varying from x = 0.22 to 0.9 were grown, with a substrate temperature of 550°C, to a thickness well beyond the metastable critical thickness.

Table 6.1

Relaxation of Thick SiGe layers

Sample Composition (% Ge)	Layer Thickness (nm)	Residual Strain (% of total)
90	300	0.02
77	350	0.04
64	300	0.06
45	350	0.23
33	2070	0.06
29	350	0.32

The composition and strain of each layer was determined with x-ray diffraction using the 004 and 113 reflections. By considering a $\text{normalised}_{\text{metastable}}$ thickness - this being the layer thickness/ metastable critical thickness, an empirical relationship between the degree of residual strain and the $\text{normalised}_{\text{metastable}}$ thickness can be obtained. This relationship is shown graphically in Fig 6.7. It is found that even high temperature anneals, 800°C for 1 hour, gave no significant movement in the residual strain of the upper four points, with the lower points showing a small effect. Thus it appears that the relaxation has reached some equilibrium state where dislocation interaction is limiting the relaxation of the layer.

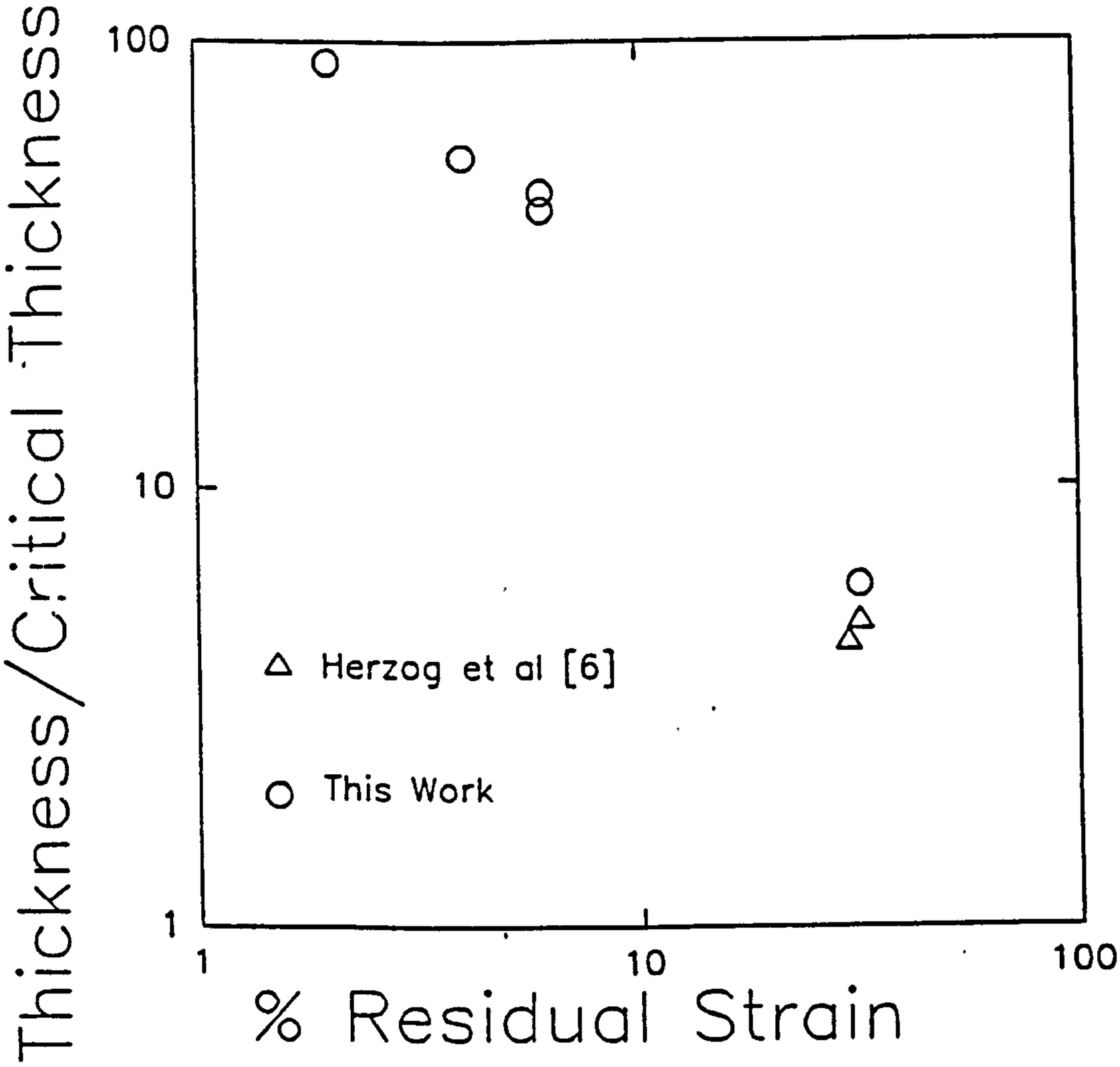

Fig 6.7 Plot of (thickness)/(metastable critical thickness) vs. residual strain for a number of layers.

The curve in Fig 6.7 provides the crystal grower with a method of predicting the X-Y lattice parameter prior to growth of a buffer layer. For example, to achieve a buffer layer comparable to a fully relaxed 50At% SiGe layer one could either grow 250 nm of 55At% SiGe or 90nm of 60At% SiGe.

6.5 Metastable Layers

An alternative method of producing a relaxed SiGe layer is to anneal a structure in the metastable region, ie $t_{c\ meta} < t < t_{c\ equilibrium}$

In this work a range of $Si_{1-x}Ge_x$ samples were considered, with x varying from 0.05 to 0.3, and either annealed at 850°C for 1 hour or given a RTA at 950°C for 6 sec. The 850°C anneals were carried out in a tube furnace with a constant flow-through of nitrogen gas to prevent the formation of an oxide layer. Rapid Thermal Annealing of the same sample set consisted of a 5 second ramp up to 900°C a 6 second stay and then a 5 second ramp down, (this was carried out on my behalf at Imperial College). X-ray diffraction was again used to determine the composition and strain of the epitaxial layers and a defect etch was used to examine the defect structure.

Again a normalised form for layer thickness was used, this time we considered $normalised_{equilibrium}$ thickness = layer thickness/ equilibrium critical thickness. Fig 6.8 shows the misfit dislocation density in the SiGe layers after annealing.

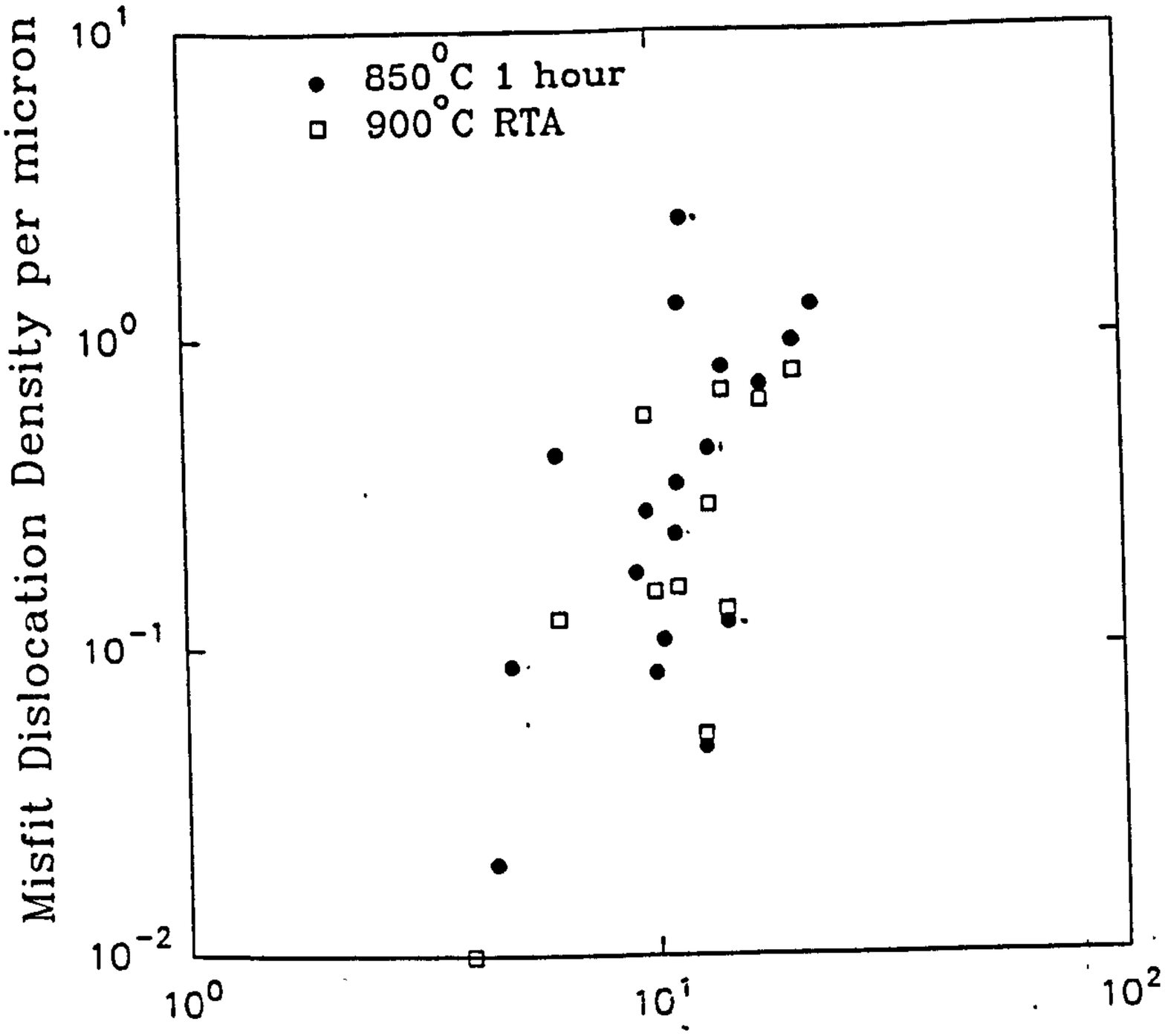

Fig 6.8 Plot showing the post anneal misfit line density plotted against the normalised$_{\text{equilibrium}}$ thickness for metastable SiGe layers.

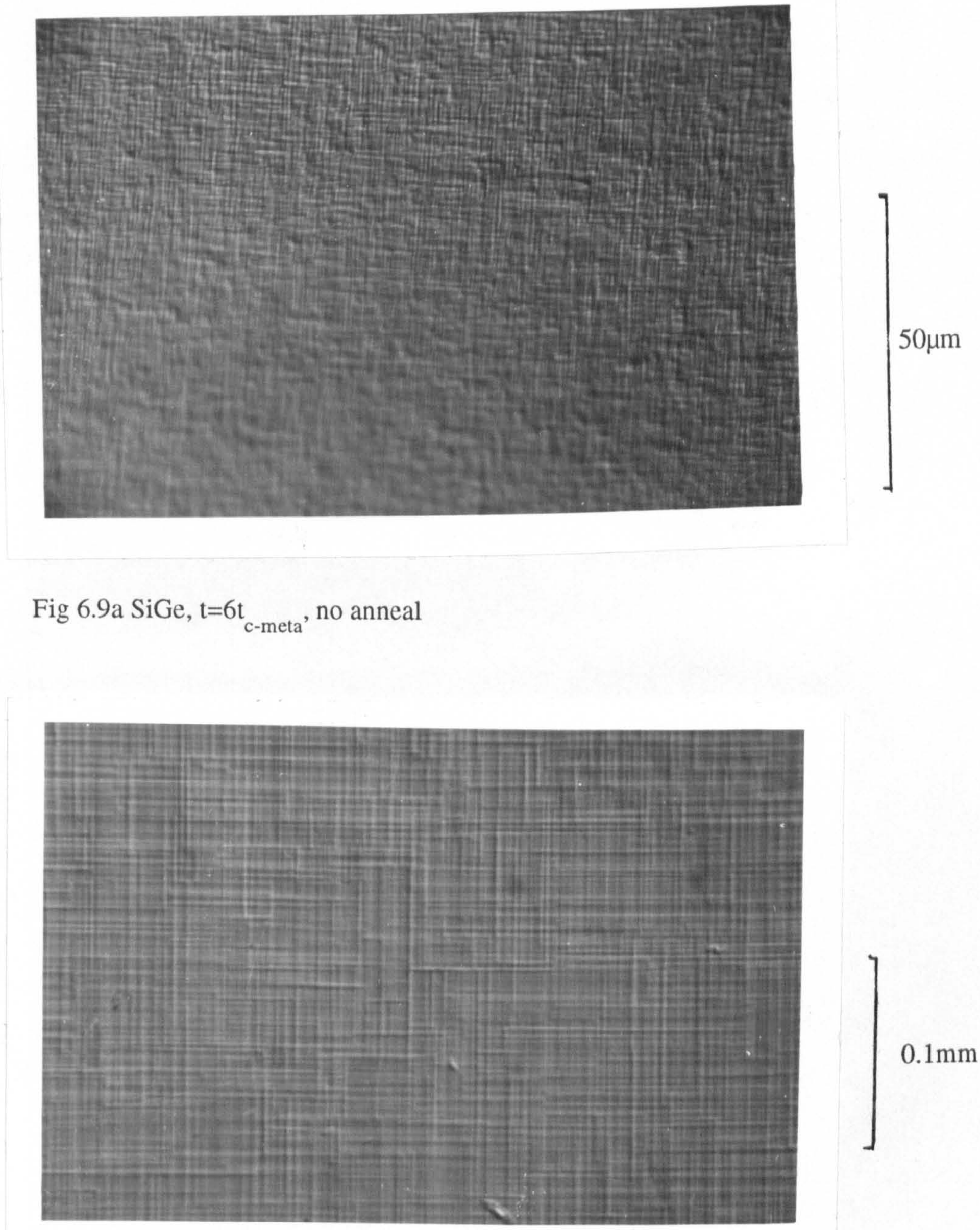

Fig 6.9a SiGe, t=6$t_{c\text{-}meta}$, no anneal

Fig 6.9b SiGe, t=0.62$t_{c\text{-}meta}$, annealed

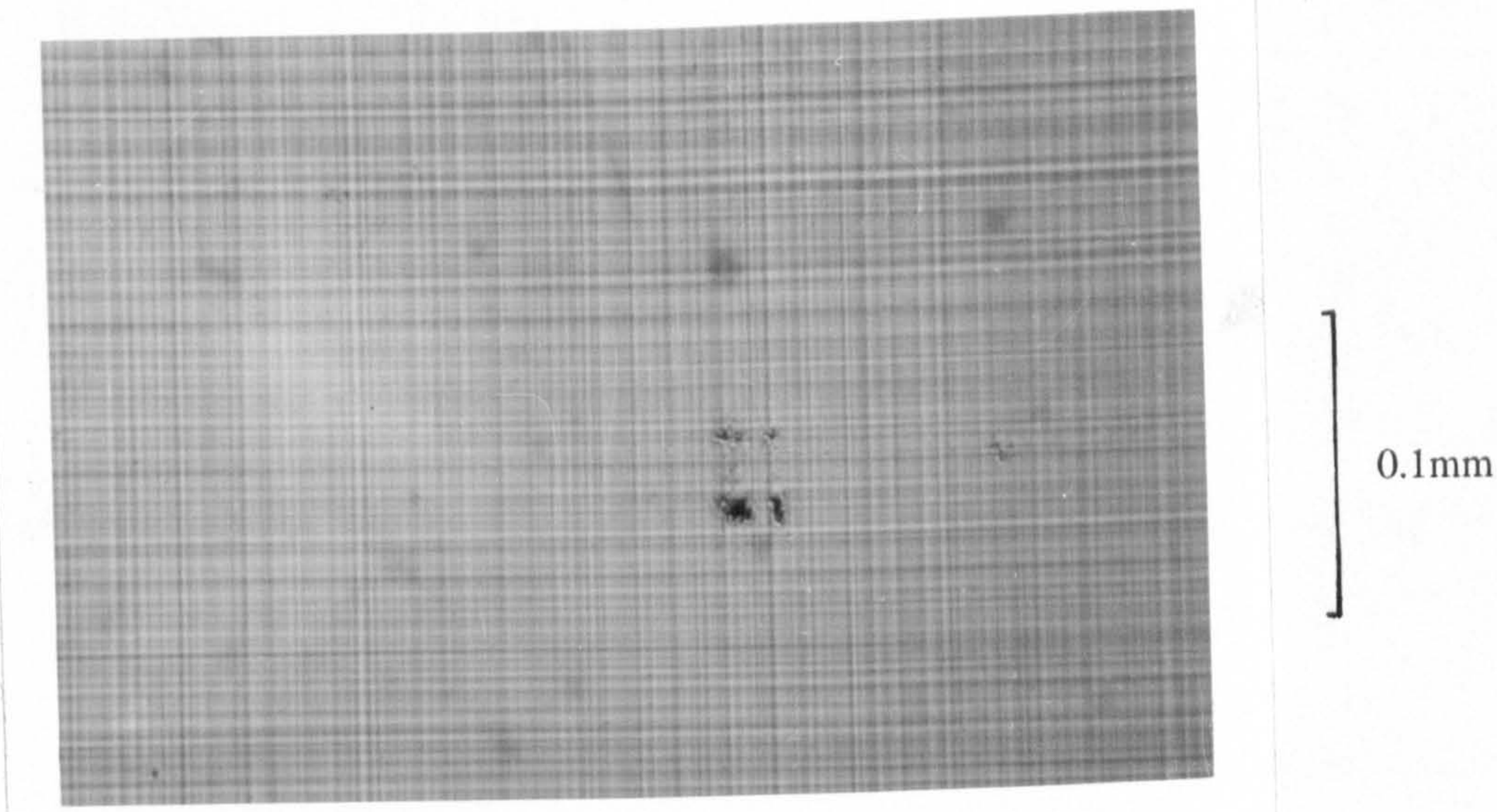

Fig 6.9c SiGe, $t=0.38t_{c\text{-}meta}$, annealed

If the graphs are considered from a device fabricators point of view then very low defect densities and low strain relaxation are required. If defect levels of $< 10^3$ cm^{-2} are required and assuming the length of a typical misfit dislocation to be ~ 2 mm the degree of relaxation must be < 0.1%. In order to achieve this for $x < 0.3$ material the SiGe layers should only be grown to three or four times the equilibrium critical thickness to ensure that significant relaxation does not occur during processing.

Consideration of Fig 6.8 from a relaxed buffer layer perspective shows that in order to achieve significant relaxation upon a 850°C anneal a layer must be grown to 10-20 times its equilibrium critical thickness. Having determined how to effectively

relax the layer, the nature of the misfit dislocations created should be considered. Fig 6.9 shows Normaski photographs of three defect etched samples. The first Fig 6.9a is of a $Si_{0.7}Ge_{0.3}$ layer grown to beyond its metastable critical thickness; very short misfit dislocations can be seen < 2μm and as a consequence there is a very high density of threading dislocations, ~ $10^9 cm^{-2}$. Consider now the misfit dislocations associated with the two annealed samples. The $Si_{0.85}Ge_{0.15}$ grown to 0.62 $t_{c\text{-}meta}$ has misfit dislocations ~ 0.1 mm and the $Si_{0.88}Ge_{0.12}$ sample grown to 0.38 $t_{c\text{-}meta}$ has even longer misfit dislocations, > 2 mm. Measurement of all the annealed samples showed that for layers where the layer thickness was less than half the metastable critical thickness, then the misfit dislocations obtained were longer than could be measured with the defect etch technique, ie > 2mm.

This relaxation by very long misfit dislocations in the SiGe layers with a lower degree of strain suggests that there are fewer nucleation sites available in these layers. Thus we have experimental support for the hypotheses that as the strain within the layer increases more of the possible defect nucleation sites become active.

6.6 Step Graded Buffer Layers

As seen in the previous section if the strain in SiGe layers can be kept small then few of the nucleation sites will become active. In addition if high temperatures are applied then the misfit dislocations nucleated from the few active sites can travel at high speed and relax the epitaxial layer. To maintain the condition of low strain throughout the growth of a buffer layer the structure shown in table 6.2 was grown.

Table 6.2

Low Growth Temperature Buffer

Composition % Ge	Thickness microns	850°C Anneal
Nominal	Nominal	
13	0.35	Yes
22	0.2	Yes
31	0.2	Yes
40	0.2	Yes
45	0.2	No

The first SiGe layer was deposited at 550°C in the standard growth manner. However this first layer was then subjected to an 850°C in-situ anneal for 20 minutes after which it was allowed to cool down to 550°C for the growth of the following layer. The SiGe layer should now in principle be relaxed with long threading dislocations and consequently a low density of threading dislocations. The second lamina of the buffer structure is now grown to about the same level of stress. As the first lamina is predominantly relaxed the 0.2 μm $Si_{0.78}Ge_{0.22}$ layer will have a strain roughly equivalent to a 15At% layer of the same thickness. This process was then repeated for each of the following lamina except for the final layer. This layer would in practice be given an in-situ anneal if a further structure were to be deposited on top of it. However in this experiment an ex-situ anneal was carried out on the final lamina to reduce the in-system growth time.

Double crystal diffraction was initially used to determine the residual strain in the layers. However as can be seen in Fig 10 the microtilts present in the layer due to the dislocations, broadened the peaks such that all the epitaxial layer peaks merged into one. In order to overcome this problem triple crystal X-ray diffraction was used. This is similar to double crystal work, except that a third crystal is introduced between the sample and the detector (in this work a 111 Ge crystal). This crystal will only pass radiation originating from a set direction from the second axis. Thus by rotation of this third crystal radiation reflected in different directions can be scanned. This directional sensitivity allows a θ 2θ scan to be taken where as the second axis is rotated by an angle θ the third axis is rotated by 2θ which means that the crystal will only pass radiation which has Bragg reflected in a perfectly symmetrical manner from the sample. This means that the radiation Bragg reflected from slightly tilted planes is not passed and hence a rocking curve can be taken which examines only those planes parallel (to within 15 arcsec, the width of the 111 Ge reflection) to the substrate. The effect of the third crystal can be seen in Fig 6.10 where the 113 glancing incidence double crystal and θ 2θ triple crystal curves are shown.

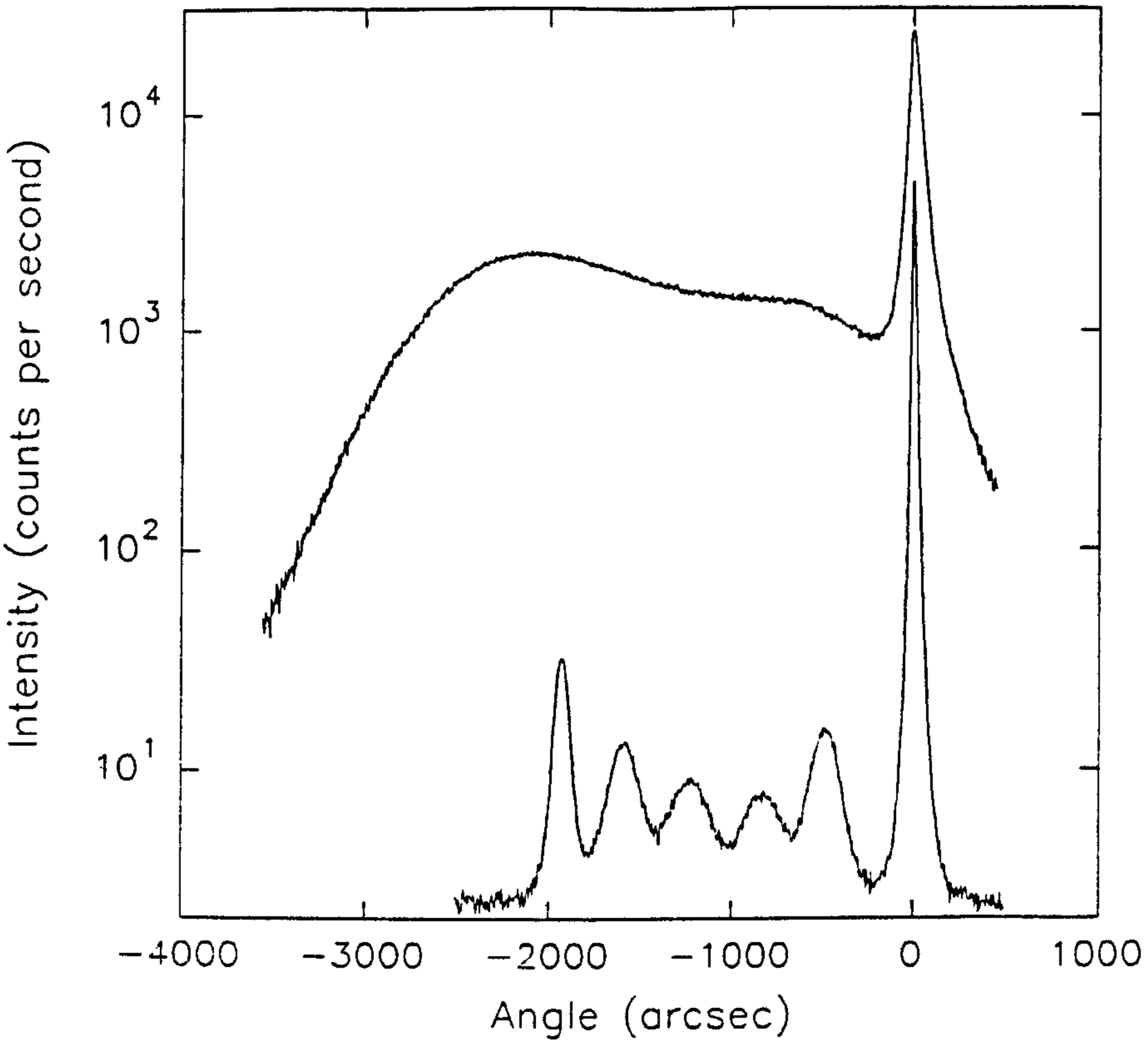

Fig 6.10 (upper curve) 113 glancing incidence double crystal rocking curve (lower curve) same reflection with 111 Ge third crystal in position.

Table 6.3

Relaxation of Low Growth Temperature Buffer

Composition % Ge ±2At%	Thickness microns Nominal	Layer Strain % ± 5%
11	0.35	1
20	0.2	-2
29	0.2	-3
38	0.2	-3.5
45	0.2	-2

As is shown table 6.3 the buffer structures layers are fully relaxed. In fact several of the lamina have a negative strain, this can be explained if one considers that the relaxation took place at 850°C. At this high temperature the lattice mismatch is 4.42% as opposed to the 4.17% value obtained at room temperature thus differential contraction on cooling leaves the SiGe layer with a negative strain. In addition to the triple crystal measurements Electron Microdiffraction has been carried out on my behalf on a similar structure and shown that the layers are fully relaxed ± 10% after the in-situ anneals [Pike et al 1991b].

Defect etching of the structure of table 6.2, shown in Fig 6.11 shows that the misfit dislocation length for the upper lamina is ~0.2 mm which suggests a threading dislocation density of 5 x $10^6 cm^{-2}$ Determination of threading dislocation densities on the sample was complicated by the high density of misfit dislocations, however a threading density of $4x10^6 cm^{-2}$ was found from direct observation.

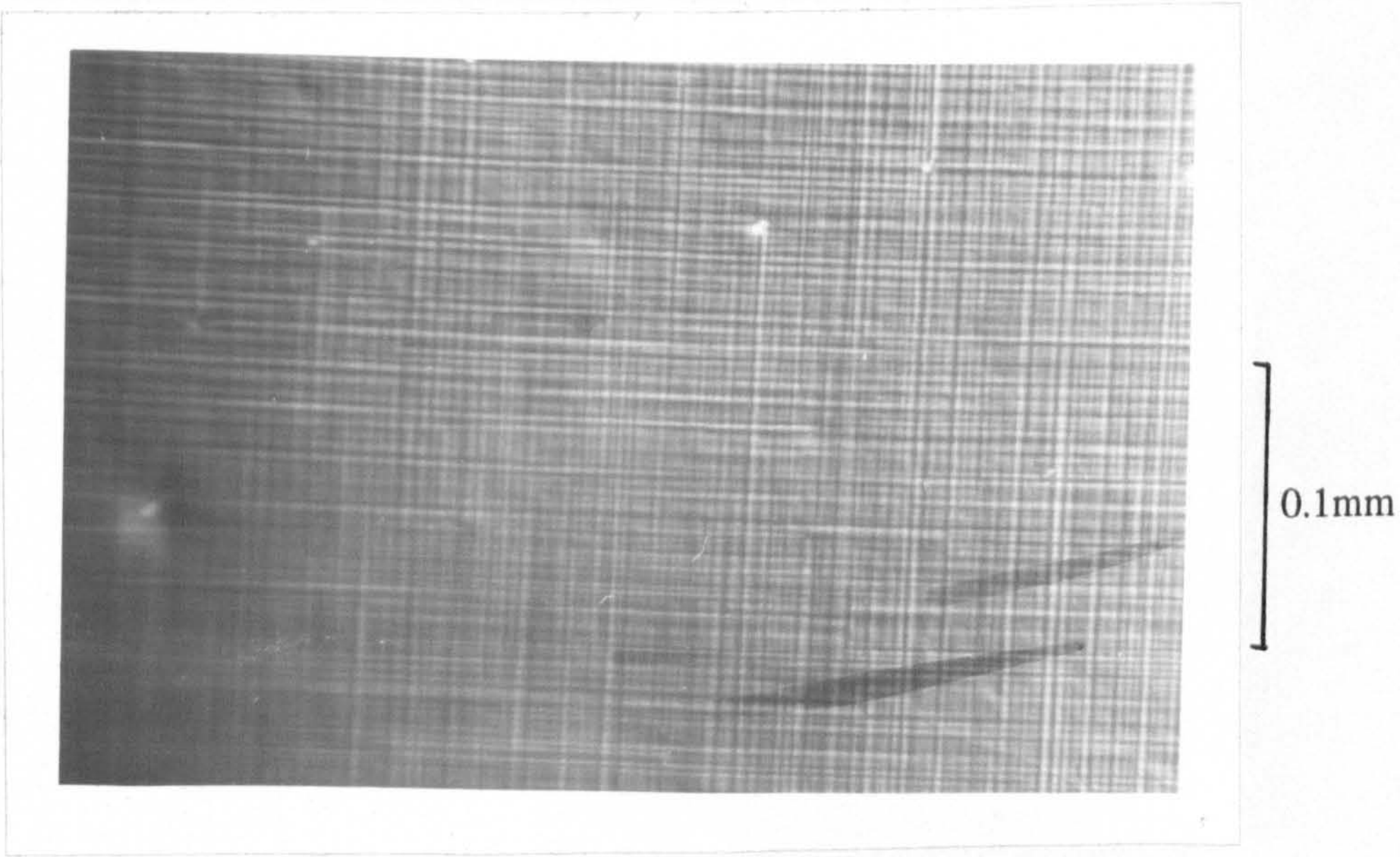

Fig 6.11 Defect etch of the relaxed buffer structure given in Table 6.2

Cross sectional TEM analysis was also carried out on this layer, prior to the ex-situ anneal, as shown in Fig 6.12.

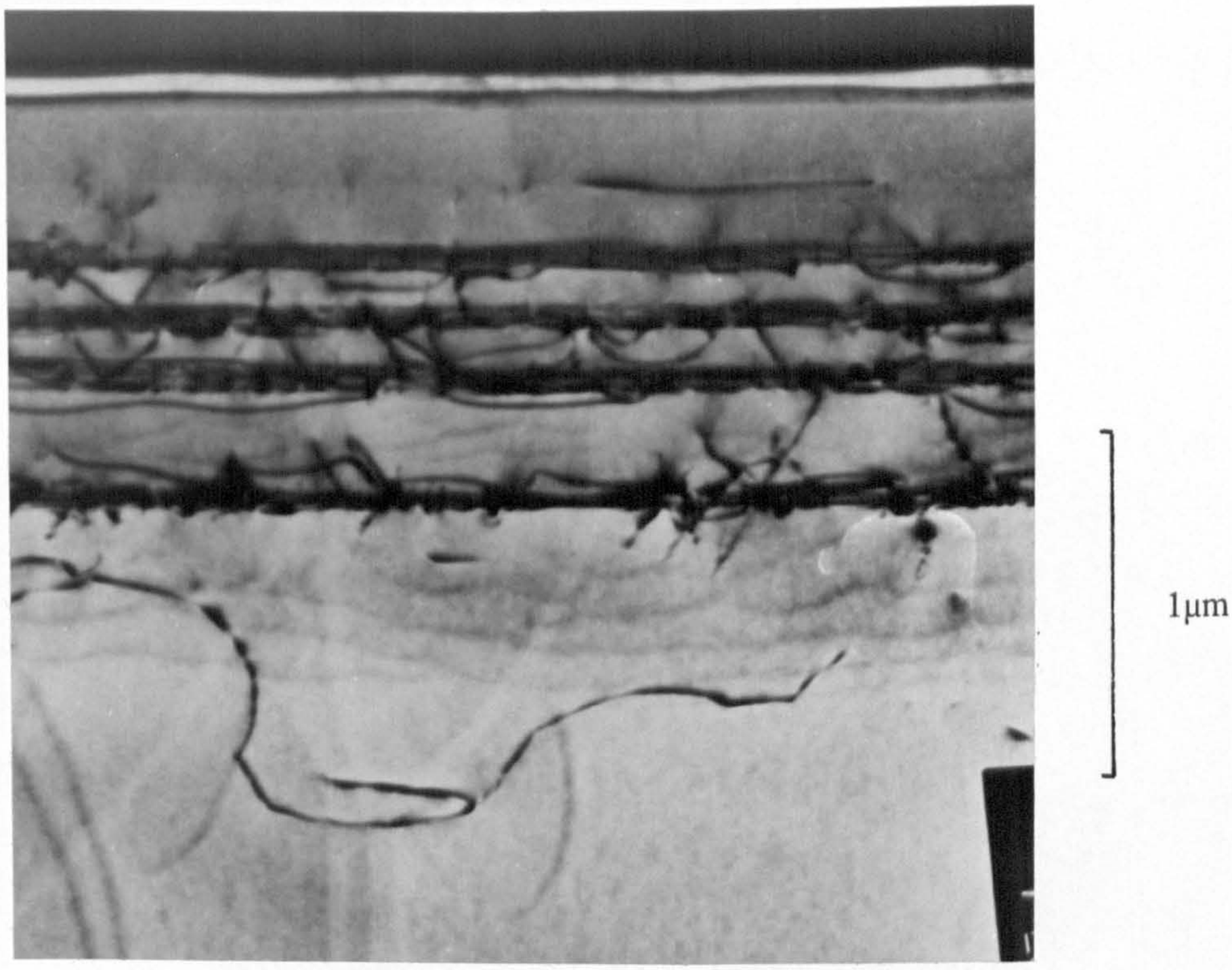

Fig 6.12 XTEM of the relaxed buffer structure given in Table 6.2

The high density of misfit dislocations at the interfaces between SiGe lamina of differing compositions can be clearly seen. Also visible are dislocation loops which appear to have been pushed down into the Si substrate. The top layer appears to have a low density of threading dislocations somewhere in the $10^7 cm^{-2}$ level, this is slightly higher than that observed from the defect-etch results. However

considering the difficulty in determining etch pits in the etched material and the problem with statistical significance of the small region examined with the TEM this difference is not significant. From the TEM analysis the long range (>50 nm) surface roughness of the buffer layer can be directly measured and for this structure it is found to have a root mean square roughness of 1.5 nm.

Growth of a relaxed buffer layer with a lower level of threading dislocations has been achieved, nevertheless there are still problems. The threading dislocation density is high for device fabrication, however [Ravi 1981] , it is suggested that decoration of dislocations by impurities within the material is the factor which causes device deterioration. Consideration of the dislocations present within this layer show that there are three orders of magnitude more length of dislocation at the SiGe lamina interfaces than there is threading up to the top layer. It would be hoped therefore that the SiGe lamina interfaces would act as gettering sites for the impurities within the epitaxial layer and thus reduce decoration of threading dislocations. The second difficulty with this technique is the time required for growth, about 6 hours, this is due to the slow heating and cooling rates required to prevent slip plane formation. It is to reduce the growth time that higher growth temperatures are considered in the next section. However it should be noted that the amount of material required ~ 1 μm is a reasonable requirement for an MBE layer.

6.7 Continuously Graded Buffer Layers

An alternative to annealing a layer at high temperature and then cooling down to the standard growth temperature of 550°C is to attempt to grow material at the high temperatures required for fast dislocation movement.

Table 6.4

850°C Growth Temperature Buffer

Layer thickness	Composition	Growth Temperature
0.5 μm	0 - 30%	850°C
0.2 μm	30%	850°C
0.1 μm	30%	550°C
20 period Superlattice	20% 5nm/40% 5nm	550°C

Table 6.4 shows the initial high temperature structure grown.

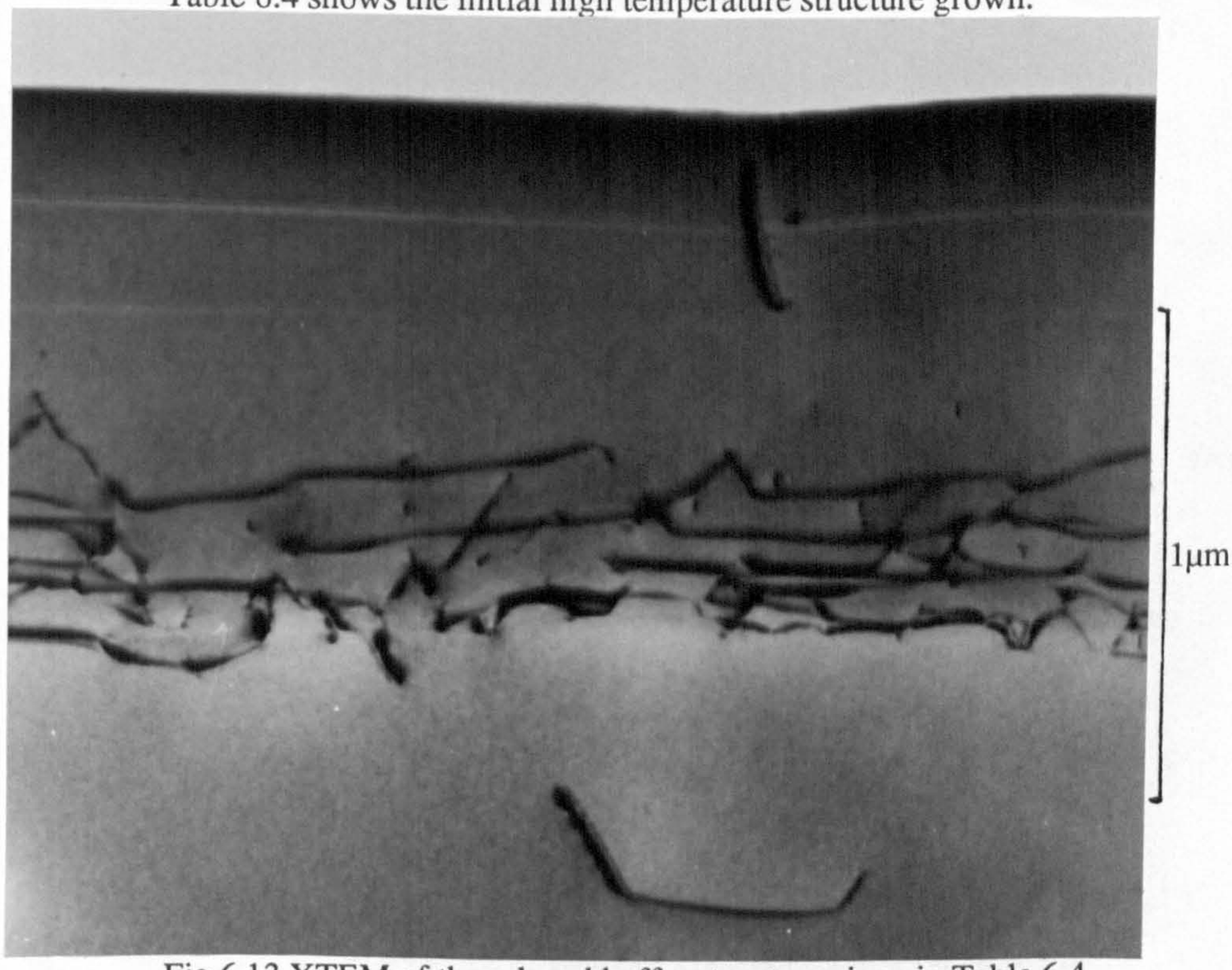

Fig 6.13 XTEM of the relaxed buffer structure given in Table 6.4

Defect etching of this layer again showed misfit dislocations ~ 0.2 mm long, However, the surface showed severe roughness which prevented direct measurement of the threading dislocations. TEM analysis of this layer gives a threading dislocation density of ~ $10^7 cm^{-2}$. Fig 6.13 also shows a severe surface roughness of the order of 1μm in wavelength and with an r.m.s. amplitude of 5 nm. This roughness appears to be a factor associated with the high growth temperatures used. Similar work involving the growth of SiGe with CVD, at temperatures of ~ 1150°C has also produced layers with rough surfaces [Kubiak priv com]. The second structure was subsequently grown with the growth temperatures shown in table 6.5 to try to avoid this problem. Consideration was given to the melting point of the SiGe material [Landolt-Bornstein 1987] as the composition changes. The growth temperature was kept to 400°C below this temperature.

Table 6.5

Graded Growth Temperature Buffer

Layer thickness	Composition	Growth Temperature
0.3 μm	0 → 20%	850°C
anneal		850°C for 20 min
0.2	20 →30%	850→790°C
anneal		850°C for 20 min
0.1	30%	790→750°C
anneal		850°C for 20 min
20 period Superlattice	20% 5nm/40% 5nm	550°C

This structure was also found to have severe surface roughness and further work is required in optimising the growth temperature to produce the low threading dislocation buffer without this associated surface roughness.

6.8 Future Buffer Layers

Two ideas are at present under investigation which may improve the buffer layer performance.

It has been demonstrated[Gibbings, Tuppen and Higgs 1991] that the presence of arsenic at high concentrations in SiGe material increases the velocity at which the misfit dislocations extend, with a density of $10^{19}cm^{-3}$ an 80 times increase in velocity was observed. The effect of antimony may be similar, we intend to dope SiGe material with antimony using potential enhanced doping with the hope that the dislocations will be able to move with high velocities at lower growth temperatures, hence avoiding the surface roughness effects seen in the latter two buffer structures grown.

The second consideration is to provide a large number of the lowest activation energy nucleation sources in specific areas. This is done by scoring, with a diamond tipped scribe, lines on a Si substrate, the pattern shown in fig 6.14 is scored.

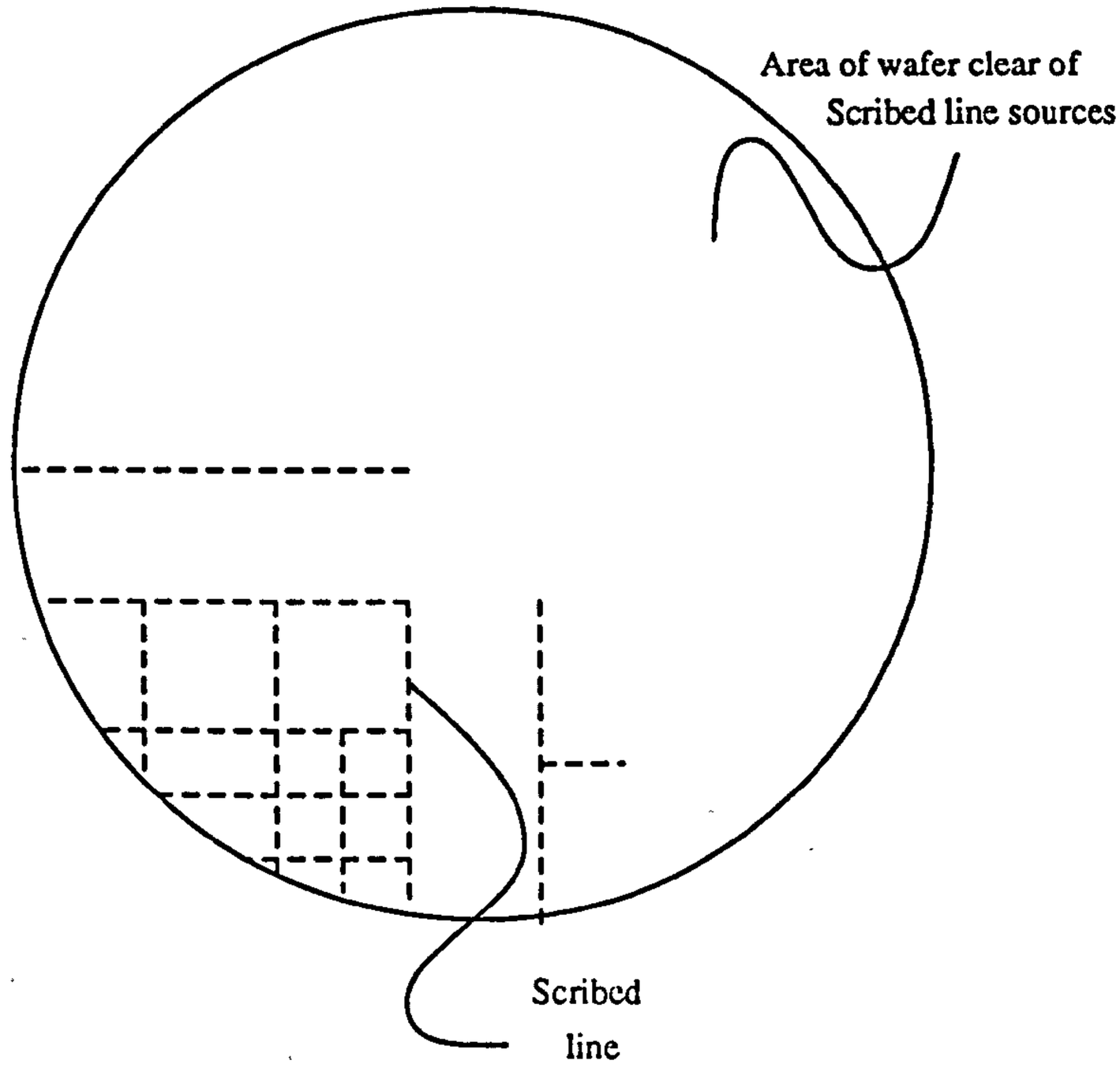

Fig 6.14 Scoring pattern on a Si wafer to produce threading dislocations in localised areas to act as misfit dislocation nucleation sites.

When the initial Si layer is grown on this substrate a large number of threading dislocations will be present above the scored lines and these will act as nucleation sites for misfit dislocations. In principle as SiGe is deposited and the equilibrium critical thickness is exceeded then a front of misfit dislocations will move perpendicularly away from the scored lines. Thus in the region close to a scored line the strain in the layer should never exceed the equilibrium strain as there is a supply of misfit dislocations which will form misfit sections and move away from the scored line. As the strain never significantly exceeds the equilibrium strain

condition no other nucleation sites will be excited. Therefore, as the predominant source of nucleation is the scored lines, misfit dislocations emitted from these lines should not experience a reduction in their driving strain, until they reach either the edge of the wafer or, a dislocation front coming from a different scored line.

6.9 Discussion

The examination of relaxed buffer layers has provided a pointer to a method of producing relaxed buffer layers with low threading dislocation densities. Two approaches have been considered. The first of these being to grow material at the standard SiGe epitaxial temperature of 550°C and carry out in-situ anneals. The second approach was to grow the material at higher temperatures. Both these approaches have produced relaxed material with dislocation densities of ~ 10^6 cm^{-2} in the top layers, a major advantage of these buffer structures is that they require only one micron of epitaxial material as oppose to the ten microns structures reported elsewhere [Tuppen et al 1991b, Fitzgerald et al 1991]. In addition by converting the 20 minute 800°C anneal to a Rapid Thermal Anneal at 1000°C it may be possible to reduce the buffer growth time to less than one hour. Consideration of the top surfaces of these layers however shows that the material grown at high temperatures has high surface roughness (~ 5 nm) which would cause problems for the growth of superlattice structures. However the 550°C growth/850°C anneal structure shows significantly better surface roughness (1.5 nm) and therefore more promise as an effective buffer layer.

Chapter 7

Mesa Island Growth

7.1 Introduction

In general MBE epitaxial growth is carried out on single crystal planar substrates several cm in diameter. However in this section the effect of reducing the area upon which the epitaxial layer is grown is examined. The reduction of growth area should provide information on two different aspects.

i) As has been suggested previously the formation of misfit dislocations in epitaxial layers grown to beyond the equilibrium critical thickness requires nucleation sites where the energy of formation of the defects is reduced. If the area upon which material is to be grown can be reduced to a size such that there is a finite probability of no nucleation sites being present then it may be possible to grow the material to well beyond the metastable critical thickness until the strain in the layer is sufficient to produce dislocations without the presence of nucleation sites. Similar work to this has been carried out with GaAs material[Fitzgerald et al 1988]

ii) As the growth area is reduced it can no longer be assumed that there is no lateral expansion of the epitaxial layer. As the growth area dimensions are reduced to approach the same magnitude as the epitaxial layer thickness the strain in a layer

may be reduced by lateral expansion of the epitaxial layer. This limited area growth has been theoretically considered [Luryi and Suhir 1986] for growth on flat Si substrates as in Fig 7.1

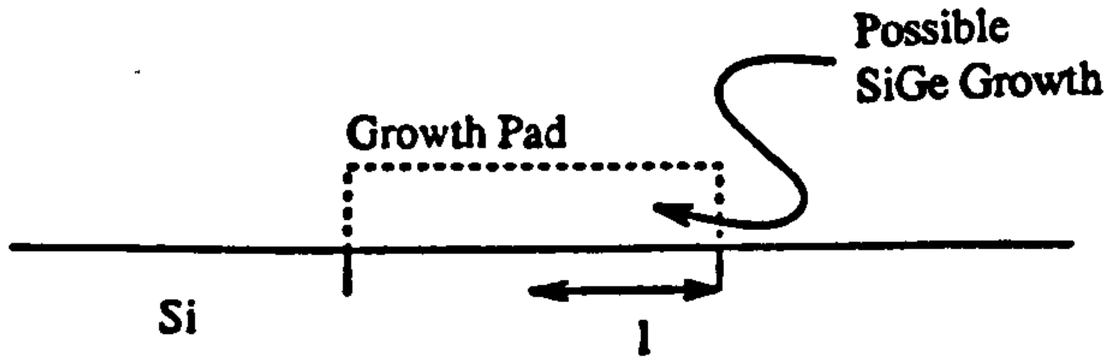

Fig 7.1 Area for Luryi and Suhir's consideration of limited area growth.

Luryi and Suhir give a graph showing the size of pad required to enable epitaxial layers to be grown to any thickness, this is reproduced in Fig 7.2

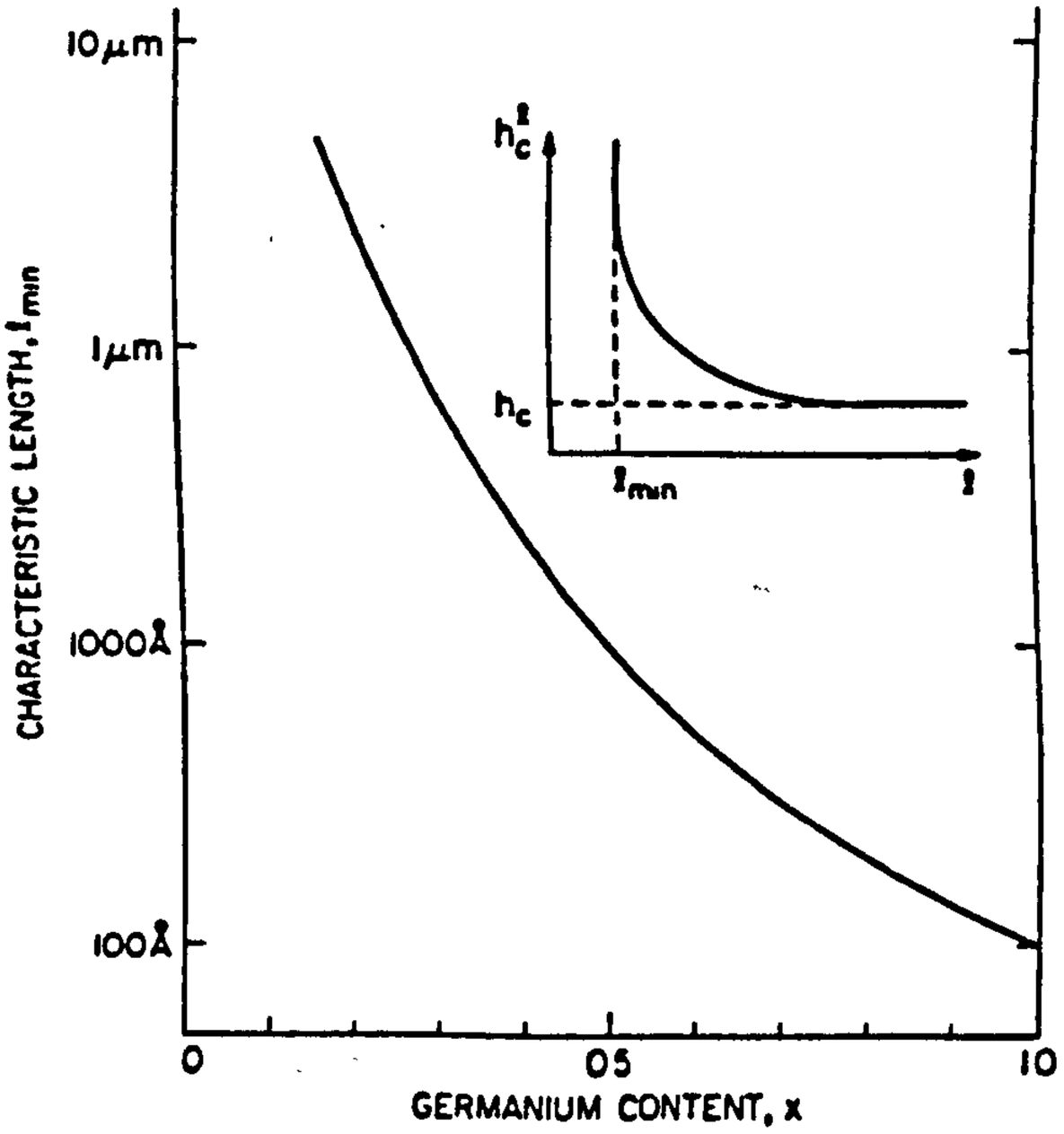

Fig 7.2 This shows the maximum pad half length for which the effective metastable critical thickness is infinite for varying compositions of SiGe.

As can be seen, for pure Ge to be grown to any thickness commensurately on Si, a pad size of r=10 nm is required. This is the same order of magnitude as the expected separation of misfit dislocations for a 4.17% mismatch structure ie 8 nm (assuming a Burgers vector of 0.38 nm along the [110]).

7.2 Production of Mesa Structures

In order to produce regions of SiGe epitaxial growth independent of the surrounding area mesa islands were produced on the Si substrates. The aim was to produce islands as in Fig 7.3 which have a planar top and steep, almost vertical sides.

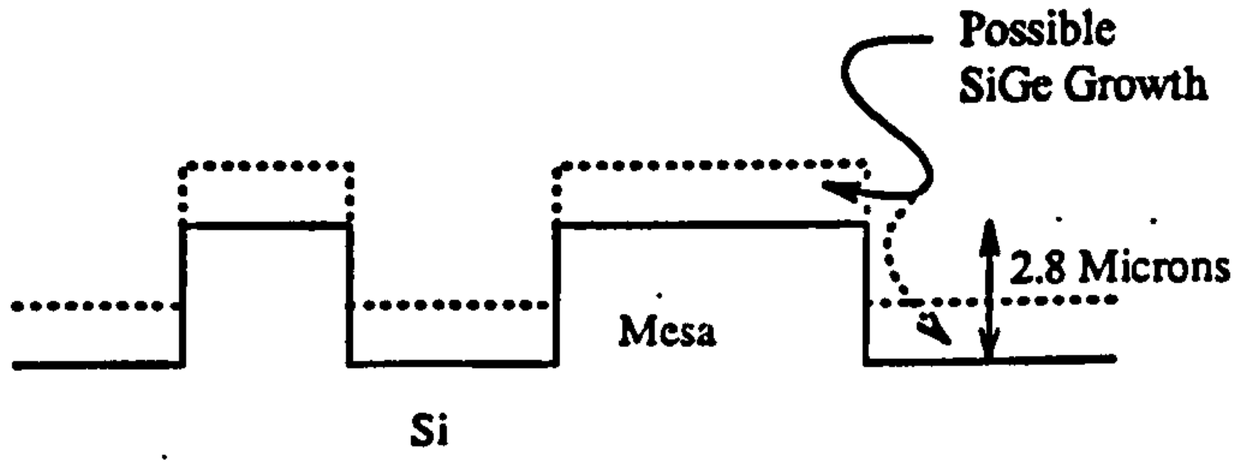

Fig 7.3 Cross section of Si mesa island substrate

Thus during growth of the epitaxial layer, material will be deposited upon the tops of the mesas and on the valley floors, but no significant growth should take place on the mesa sides. This leaves the SiGe deposited on top of the mesa with no connection to that on the valley floor and hence limited area growth should be achieved.

The initial approach to producing these mesa structures was to produce small dots of black wax on the Si wafer to act as a mask during wet etching. This was

achieved by dissolving the black wax in xylene and using a pin to deposit small drops of wax upon the surface, it was found to be possible to produce dots of 100 μm diameter by this method. These samples were etched in diluted CP_4A, (5 Nitric acid, 5 Hydrofluoric acid, 3 Acetic acid). However examination of these islands with a surface profilometer showed that the island walls were significantly non-vertical. Therefore growth of MBE material would occur on the island walls connecting the tops to the valleys and limited area growth would not have taken place.

In order to produce vertical sides a plasma etch was used. Plasma etch facilities are routinely used at the Edinburgh Microfabrication Facility along with photolithography, hence this technique was chosen for the mesa production. This enabled the production of a complicated test structure with various sized and shaped islands.

7.3 Design of Test Structure

The mask design was carried out on a commercial design package ,CIF , which allows direct drawing of the mask onto the screen and hence to computer disk. The design was then sent to the Rutherford Appleton Labs to be made into an optical mask. Fig 7.4, an X-ray topograph of the finished structure, allows the mesa island design to be seen. The mask is a 3mm square in which were put a number of square islands ranging from 1500 to 1 μm across, these enable the dependence of misfit dislocation density with area to be examined. In addition to this a number of rectangular islands were created 300 microns long and ranging in width from 5 to 150 μm, these were aligned in the [110] [101] and [010] directions. The aim of the rectangular islands was to determine the effect of any elastic strain relaxation present

as for an island 5 μm wide and 300 μm long the elastic relaxation would differ in the two different directions.

7.4 Production of mesa islands

The processing of the substrates involves the creation of a thick oxide layer on the Si. This was removed at the last possible stage so as to reduce contamination that might have occurred prior to growth. Hydrofluoric acid was used to strip the oxide layer, however, the pits seen on the surface of the mesas suggest that some contamination may have occurred. The substrates were then inserted into the MBE system and growth carried out in the usual fashion. Three structures have been grown upon these substrates as shown in table 7.1.

Table 7.1

SiGe Layers Grown On Patterned Substrates

SiGe Composition (At%)	SiGe Thickness (nm)	Beyond Metastable Critical Thickness
10	700	No
20	7500	Yes
20	7500	Yes

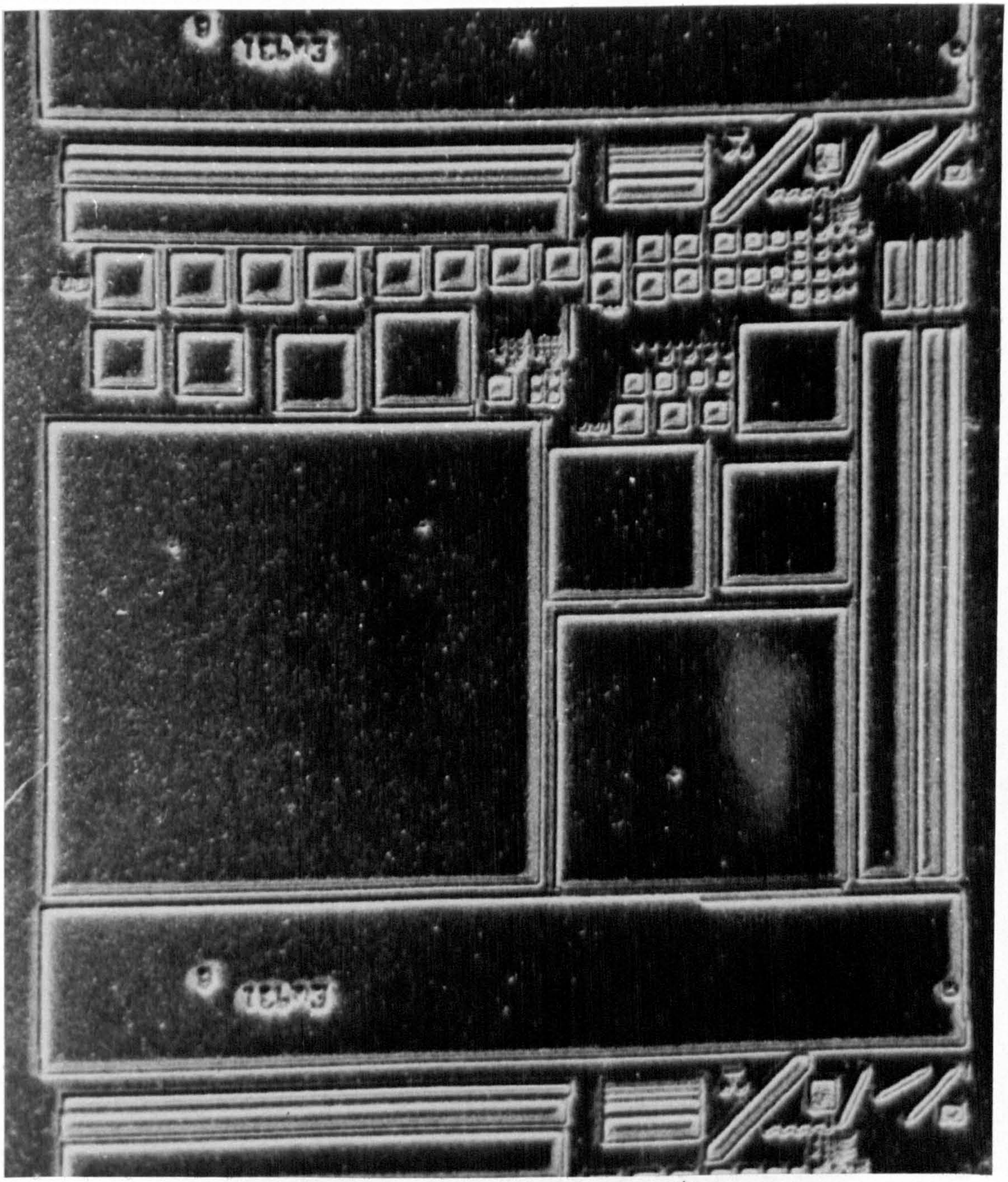

Fig 7.4 Double crystal topograph of mesa island structures.

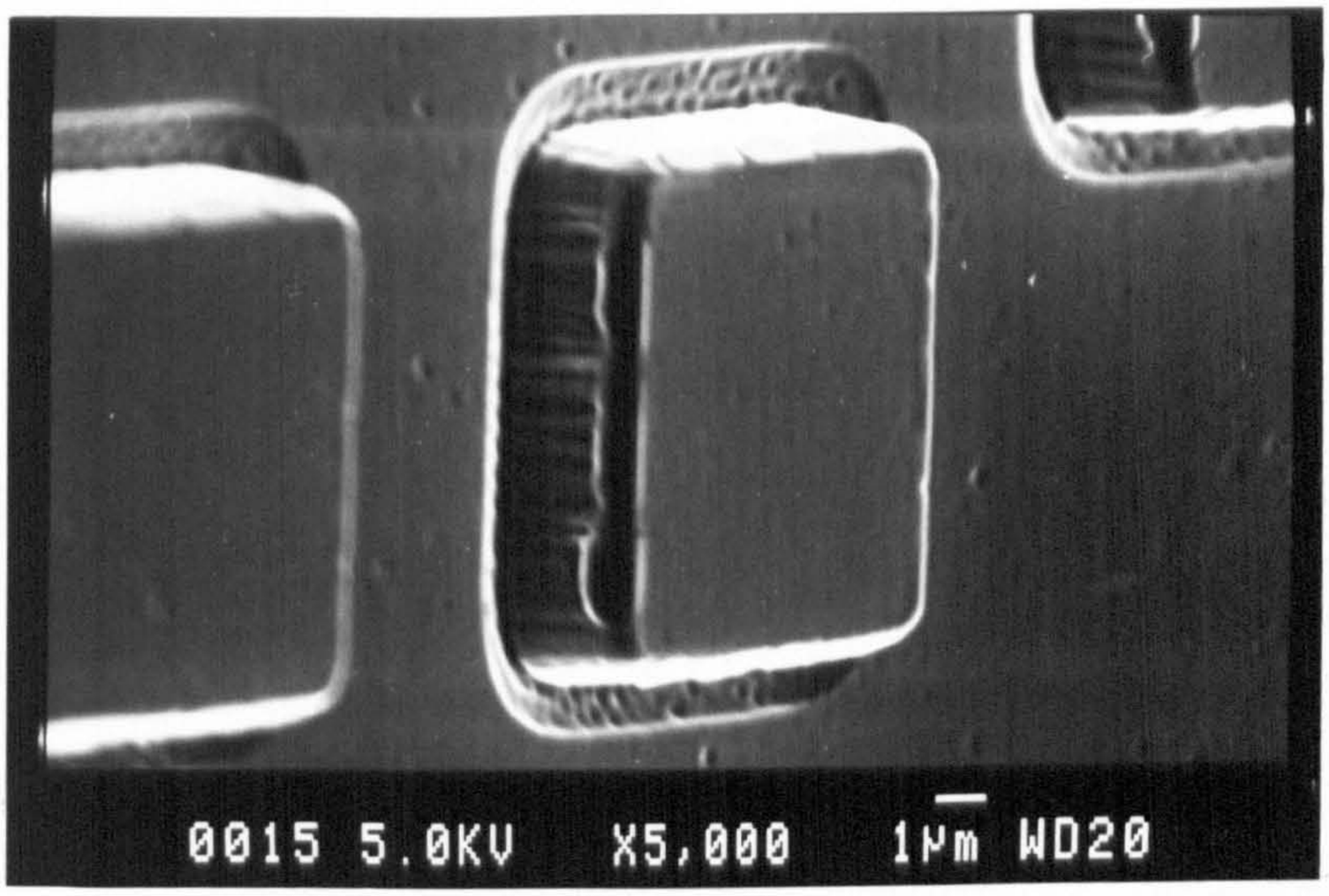

Fig 7.5 shows a SEM photograph of a 10 µm island after deposition of 0.75µm of SiGe.

In Fig 7.5 the SiGe layer can be clearly seen and hence no significant SiGe deposition on the mesa walls can have taken place. However, some shadowing effects can be seen at the base of the mesa structure. In addition to this small pits can be seen on the surface of the material which may be indicative of defects caused by poor cleanliness of the Si substrate prior to growth.

7.5 Characterisation

The characterisation of the state of strain in the epitaxial layers on top of the mesa islands has proved not to be a trivial problem. As the mesa islands of most

interest are so small ~ 10μm it is almost impossible to hit only the island in question with an X-ray beam, though it is hoped to overcome this problem later. Use of Kikuchi lines with an electron microscope may be possible, however the strain measurement possible with electron beams does not give sufficient sensitivity.

The fact that strain is present can be seen from use of X-ray topography as shown in Fig 7.4. Here an epitaxial layer is shown where the SiGe is below its metastable critical thickness and so no misfit dislocations are present. The topograph in Fig 7.4 was taken from the Si diffraction peak and hence the bright regions represent areas where the Si material is either strained or tilted. Clearly there is no strain in the centres of the larger islands. However, at distances up to 50 μm from the edges of the islands some degree of strain can be observed. As there are no dislocations seen it is assumed that the strain is due to the presence of the SiGe layer which forces the Si material to expand as in Fig 7.6. The same topography technique was used on the sample after an 850°C 1 hour anneal. However the resolution was insufficient to show the small, <15 μm, islands where the elastic relaxation is dominant. Thus these images merely showed the presence of a high density of misfit dislocations in the larger islands.

Elastic Deformation Of Mesa Structure

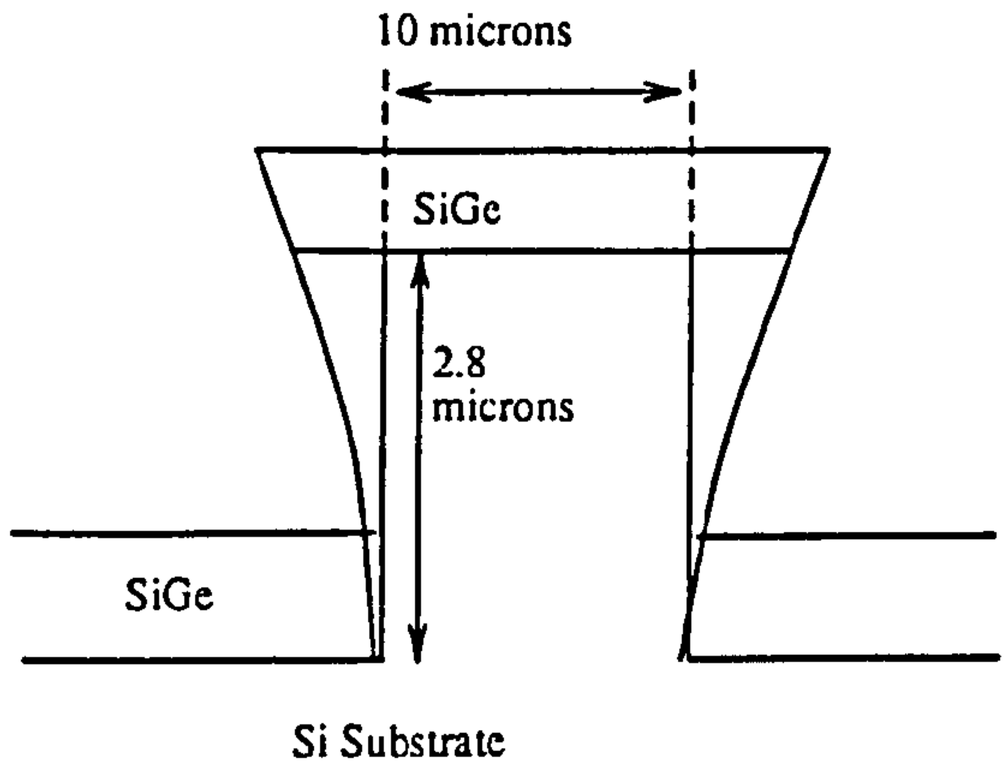

Fig 7.6 Cross section of mesa structure showing the suggested distortion of the Si mesa structures.

The samples were also defect etched before and after annealing so that the metastable SiGe layers would relax. Upon defect etching of the samples a high density of shallow etch pits ~ $10^7 cm^{-2}$ was found, these we believe must be due to contamination during some stage of the processing. The presence of the pits suggest that there is a large density of possible nucleation sites for misfit dislocations and hence any effect of limited area growth in the respect of removing nucleation sites is invalid. This was confirmed by the lack of a decrease in misfit dislocation density until the island size is reduced to under 30 μm where elastic relaxation effects become relevant.

In consideration of elastic relaxation the rectangular mesa structures give the most information. In Fig 7.7 a Nomarski photo of a SiGe epitaxial layer grown to well beyond the metastable critical thickness is shown.

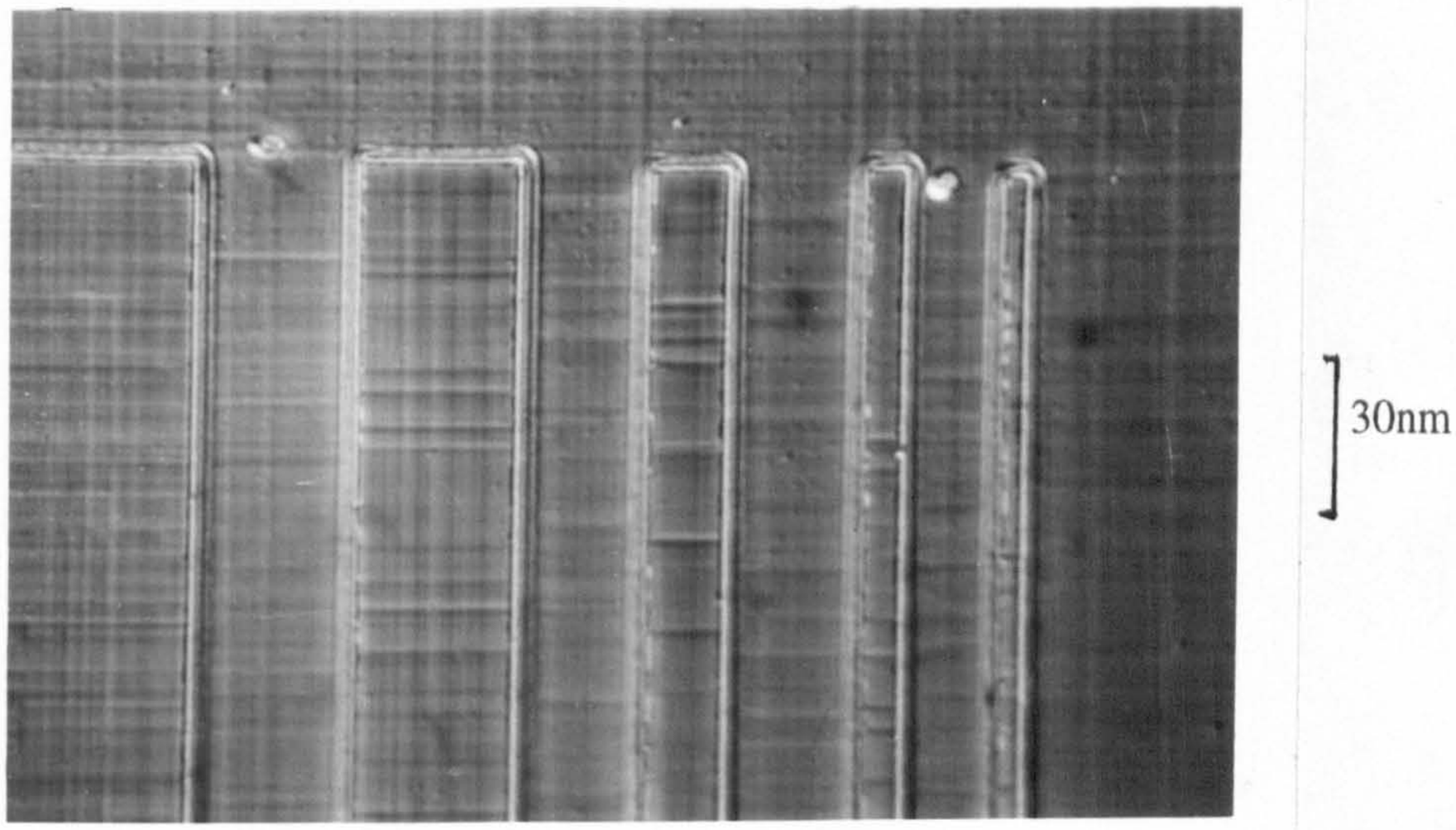

Fig 7.7 Defect etch of rectangular mesa islands showing misfit dislocations crossing but not running along the long islands

The rectangular islands range from 5 μm to 40 μm in width. On the narrower mesas misfit dislocations can be seen to cross the islands at intervals of ~ 10μm, however misfit dislocations running along the length of the mesas are not observed. The presence of misfit dislocations crossing the islands demonstrates that nucleation sites are present and that the degree of strain present in the direction parallel to the long sides of the islands is sufficient to create the misfit dislocations. It follows from this that the strain perpendicular to the long sides must have been reduced as no misfit dislocations have been created even though suitable nucleation sites are available. This reduction of strain must be due to elastic relaxation of the islands in a direction perpendicular to their long sides. Thus it has been shown that a reduction of

lateral dimensions to 10 μm has increased the effective metastable critical thickness and reduced the degree of strain in the SiGe layer.

7.6 Discussion

In this chapter the elastic relaxation of small mesa islands of SiGe has been demonstrated. The uses of this however are not immediately apparent, it may be possible to use the asymmetrically relaxed structures to examine the effects of asymmetric relaxation on the band structure and carrier mobilities.

Further characterisation of the elastic relaxation may be achieved by the design of a new mask. Production of a structure consisting entirely of one type of island, for instance a 5 x 300 μm rectangular mesa, would then enable bulk characterisation techniques such as double crystal diffraction to be used. In addition the use of triple crystal diffraction would allow the strain and lattice tilt to be separately measured.

If these structures were to be combined with the types of buffer layer considered in the previous chapter it may be possible to produce relaxed SiGe material where the threading dislocations associated with the relaxing misfit dislocations run off the edges of the mesa structures thereby giving plastically relaxed material with no threading dislocations

Chapter 8

Characterisation of Delta doping in Si

8.1 Introduction

Delta doping consists of the deposition of a thin layer of dopant atoms sandwiched between layers of the matrix material. A thin sheet of dopant is considered to be a delta layer if the electron or hole gas created exhibit two dimensional properties. For this to be so for Si a dopant sheet density of 10^{13} cm^{-2} (single carrier type dopants)[Koch and Zrenner 1988] must be present within the width of the potential created by confining the dopant to within a few atomic planes, ie approximately 3 nm. These delta layers can be used in a number of novel devices incorporating two dimensional electron or hole gases such as delta MOSFETS [Dohler 1978, Schubert 1990] where they should allow the channel length to be brought down to tenths of microns [Yamaguchi 1983]. Thin sheets of dopant can also be used for selectively doping SiGe superlattices where the Si and SiGe layers are often < 5 nm in width. In these structures the free carriers migrate to the adjacent SiGe potential wells where they can travel without any ionised impurity scattering [Powell et al 1991a].

In this work two dopants have been used for delta doping. Boron in P-type and antimony in N-type.

8.2 Calibration of strain induced by dopant atoms

Boron Doping

X-ray diffraction gives information on the spacing of the lattice planes and hence the strain present within the layer. In order to determine the strain induced by the dopant atoms when in activated, and unactivated states, we combined information from SIMS, Hall measurements and X-ray diffraction.

For boron a number of papers consider the induced lattice strain [Fukuhara and Takano 1977, Becker and Scheffler 1984, Cohen 1966], these however show disagreement about the degree of lattice strain induced by a boron dopant ion in Si. Therefore in order to determine the strain produced by boron in Si we took five highly boron doped layers which were grown at temperatures varying from 500 to 800 ^{o}C. Double crystal measurement using both the 004 and 113 reflections enabled the strain in the epitaxial layers to be found. This is achieved in a manner exactly analogous to the determination of strain in SiGe layers see sections - 3.9 and 5.2 - where the degree of strain is found from the separation of the substrate and epitaxial layer peaks. Then from a knowledge of the dopant density (SIMS), and the carrier concentration, the strain induced by activated and unactivated boron can be found.

Table 8.1

Strain Induced By Boron Doping At Varying Temperatures

Growth Temperature	Boron Density (SIMS)	Carrier Density (Hall Measurements)	Strain per Atom (X-ray Diffraction)
(^{o}C)	± 5% (cm^{-3})	± 3% (cm^{-3})	± 5%
500	5.6×10^{19}	5.6×10^{19}	-6.0×10^{-24}
600	1.3×10^{20}	1.3×10^{20}	-6.1×10^{-24}
670	1.4×10^{20}	4.1×10^{19}	-1.7×10^{-24}
760	1.3×10^{20}	2.8×10^{19}	-1.2×10^{-24}
800	2.0×10^{20}	3.5×10^{19}	-1.2×10^{-24}

From the above table the induced strain for one atom per cm^3 can be calculated by substituting the above numbers into equation 8.1;

$$S_a \times B_a + S_u \times B_u = \text{Strain per Atom} \qquad (8.1$$

where

S_a= Strain per activated B atom

S_u= Strain per unactivated B atom

B_a = Activated B i.e., Carrier Density

B_u = Unactivated B i.e., B Density (SIMS) - Carrier Density

The subsitution of values from Table 8.1 into equation 8.1 produces the results shown below;

$$\text{Activated boron} = -6.05 \pm 0.1 \times 10^{-24}$$

$$\text{Unactivated boron} = 0.03 \pm 0.1 \times 10^{-24}$$

This value for activated boron agrees with the values obtained by References [Fukuhara and Takano 1977, Becker and Scheffler 1984]. It also agrees with the value obtained from theoretical calculations considering the covalent radius. Unactivated boron can be seen to have little effect on the lattice constant as one might expect since there is neither the effect of replacement of Si on the lattice sites by a smaller atom or is there strain due to the presence of holes in the electron gas [Kavanagh priv comm]. As can be seen the growth temperature has a very marked effect on dopant incorporation [Parry 1991] and if one requires full activation of highly doped material as is present in the delta layers they must be grown below 600°C

Antimony Doping

Antimony is a larger atom than Si and this tends to expand the lattice. However it is also a n-type donor, which in effect means that there are more electrons present within the conduction band; this results in a strain for an electron per cm^3 of -1.8 $\pm$0.4 x 10^{-24} [Cargill et al 1988]. As I have not obtained a calibration set for antimony I have obtained the expansion coefficient from references [Becker and Scheffler 1984]. This gives a value of 2.9 x 10^{-24} for the induced strain per atom. This value agrees (to 10%) with the values obtained from considering the covalent

radius of the atom for an activated atom. In MBE growth of antimony doped layers at the usual growth temperatures 450 to 850 °C the antimony forms as an adlayer on the surface of the growing layer and antimony is only incorporated upon lattice sites. However this is not the case with the growth of delta layers, here the antimony is deposited followed with a Si capping layer at a substrate temperature of < 250°C. The growth of the Si cap at this low temperature is carried out specifically to avoid the formation of a dopant adlayer and hence profile smearing. However, this means that antimony may be present other than on lattice sites (ie in precipitates), this makes it difficult to determine the sheet density based solely upon the strain present within the layer.

8.3 How can delta layers be seen ?

The most common method for characterisation of delta layers is by SIMS. However, this is limited in resolution to a few nm owing to intermixing effects [Magee and Honig 1982]. This can be reduced by the use of very low energy ion probes [Dowsett et al 1991]; however the resolution remains poorer than 2 nm. In order to determine the widths of the delta layers more accurately double crystal X-ray diffraction was used. As the total sheet density of dopant present in the delta layers is of the order of one tenth of a monolayer it is not possible to characterise the delta directly from the signal diffracted from the delta layer itself.

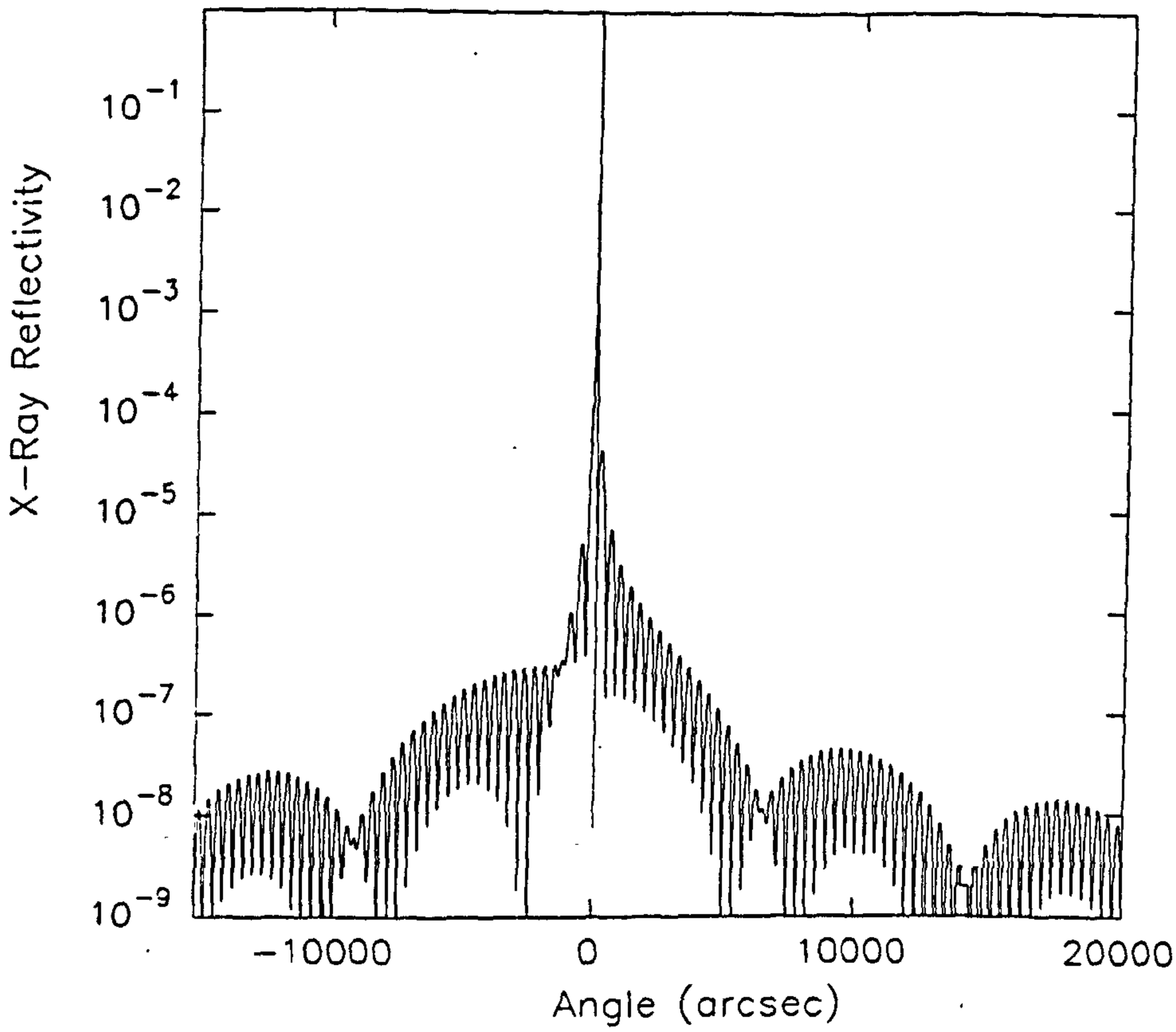

Fig 8.1 RADS simulation of a double crystal rocking curve obtained from a boron delta layer in Si with a sheet density of $2x10^{16}$ cm^{-2} buried at a depth of 50 nm.

Fig 8.1 shows the diffraction peak for a boron delta layer with a sheet density of $2 x10^{16}$ cm^{-2} ie 25 monolayers of 100% B, not only would determination of this peak require scanning for many thousands of seconds either side of the main Si diffraction but also the intensity of the peaks is 2 or 3 orders of magnitude below the level of noise ~ 5 counts per second. Since the directly diffracted signal is too small to measure I had to consider modulations of the main Si diffraction peak due to the strain induced by the delta layer.

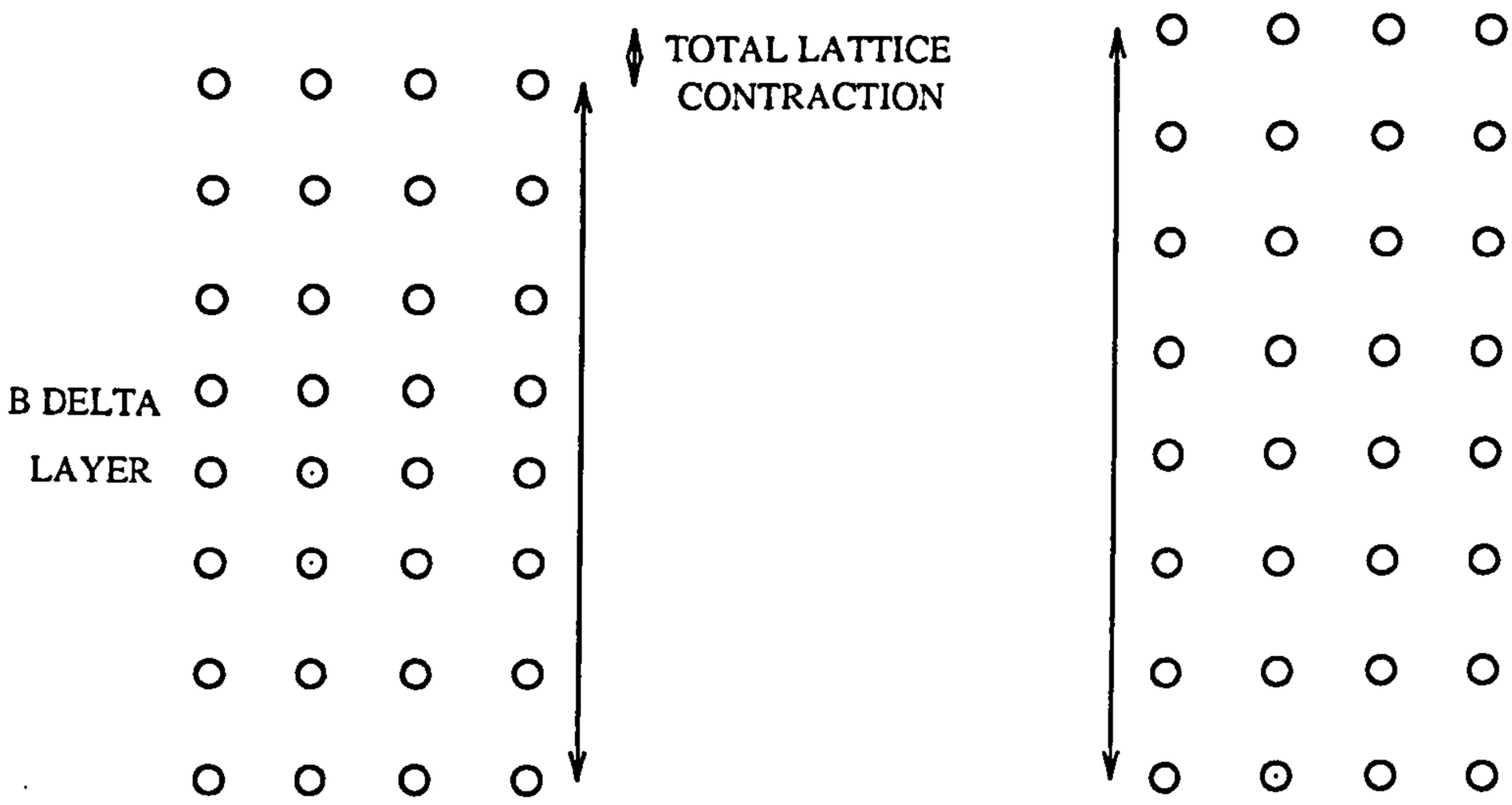

Fig 8.2 Representation of the shift in the upper Si layer with respect to the underlying Si due to the presence of the delta layer.

Fig 8.2 shows how the presence of boron dopant atoms on lattice sites causes the lattice planes in the capping layer of Si to be out of synchronisation with those in the underlying Si substrate and therefore the diffracted signal from the capping layer interferes with the diffracted signal from the substrate. This causes fringes to be seen on the flanks of the rocking curve. The period of the fringes seen depends primarily on the thickness of the Si capping layer as described by Kiessig [Kiessig 1931]. However the position of the peaks with respect to the main Si peak gives information on the degree of strain present and the relative intensity of the fringe peaks enables determination of the delta layer width. This is analogous to an optical heterodyne interferometer in which a carrier signal (the capping layer) is modulated by a weak

signal (the delta layer). In order to illustrate Delta layer characterisation let us consider the boron delta layer, 10-33, the rocking curve of which is shown in Fig 8.3.

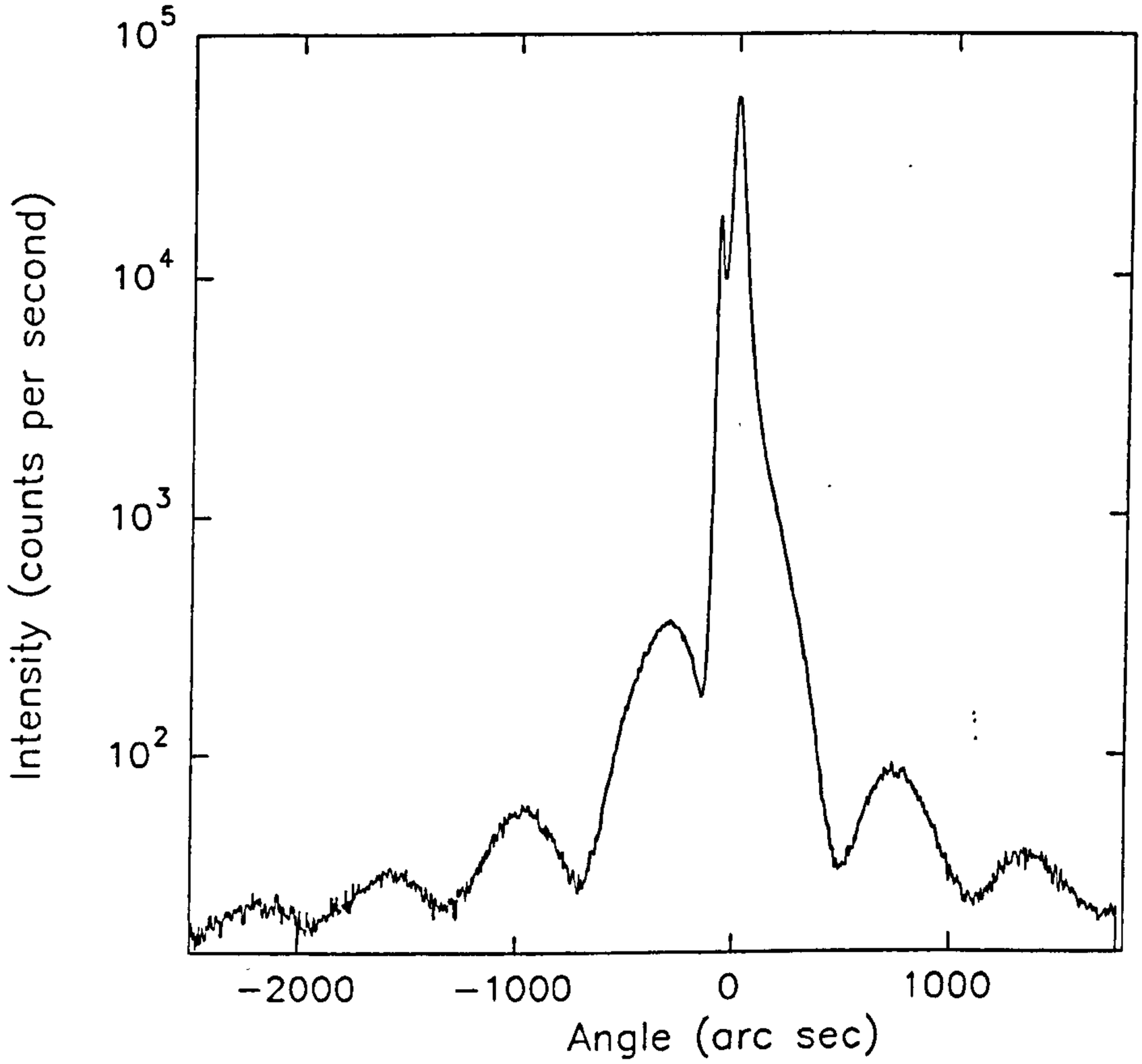

Fig 8.3 A typical 113 glancing incidence rocking curve obtained from a delta doped structure. In this case 3.6 x $10^{14}cm^{-2}$ at a depth of 52 nm.

The measurements were taken on a BEDE 150 diffractometer with a four bounce [Loxley et al 1991] 004 beam conditioner. The four bounce conditioner was required to reduce the intensity of the tails associated with the Si main diffraction peak so that the interference fringes could be seen. Both 004 symmetric and 113

glancing incidence reflections were used with the same beam conditioner, this leads to the subsidiary peak seen in the 113 reflections which is due to dispersion separating $K\alpha_1$ and $K\alpha_2$. The majority of the $K\alpha_2$ radiation has been cut off with slits and the remaining peak is two orders of magnitude down on the main peak. Thus its effect is negligible on the delta layer fringes. From examination of these fringes it is possible to determine a number of features of the delta layer.

i) capping layer width

The period of the fringes seen depends upon the combined width of the delta layer and the capping layer this is however complicated by the fact that the delta layer does not necessary have uniform doping and sharp interfaces. If one considers, as shown later, that the delta width is only a few angstroms then this is insignificant and we can talk about the delta layer depth 'd' by simply considering the reciprocal of the fringe separation.

Thus in 10-33 the boron delta is found to be at a depth of 52 ± 1 nm.

ii) strain

As the boron contracts the lattice in its vicinity it causes a phase difference between the diffracted signal from the capping layer and the signal from the underlying layer , Fig 8.4.

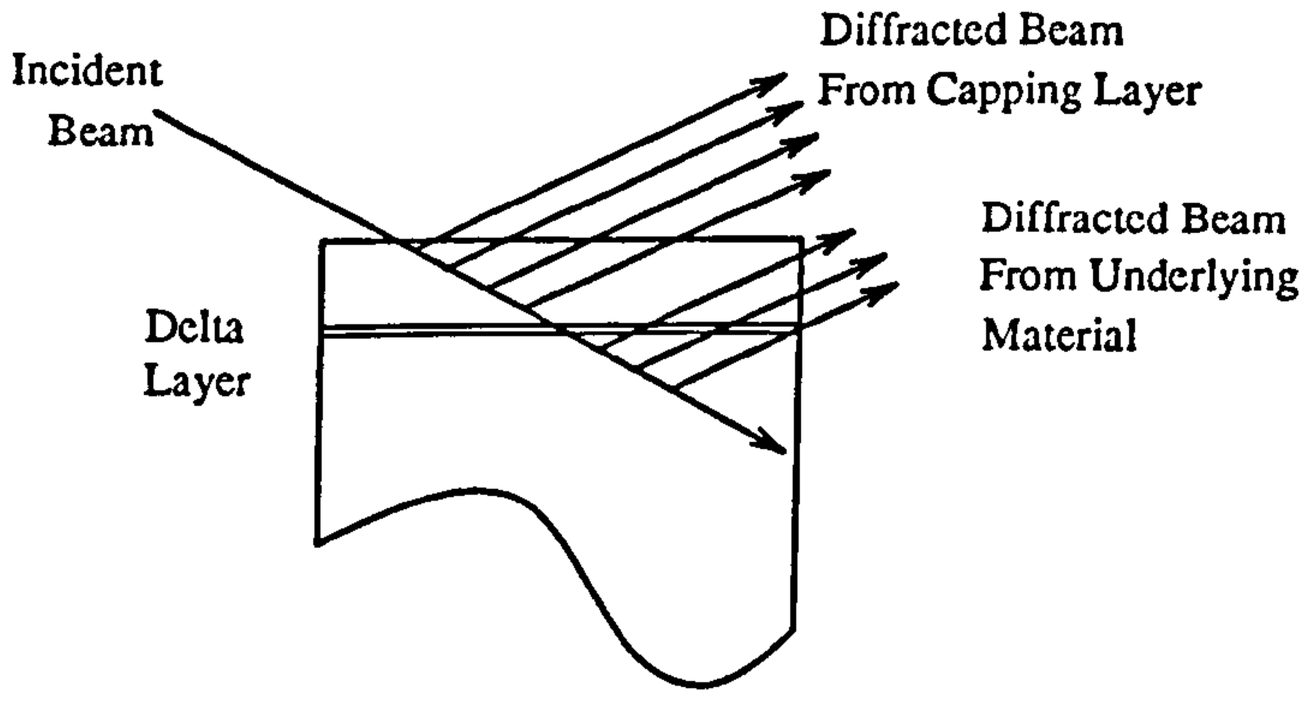

Fig 8.4 Illustration of the diffraction from capping and underlying Si layers.

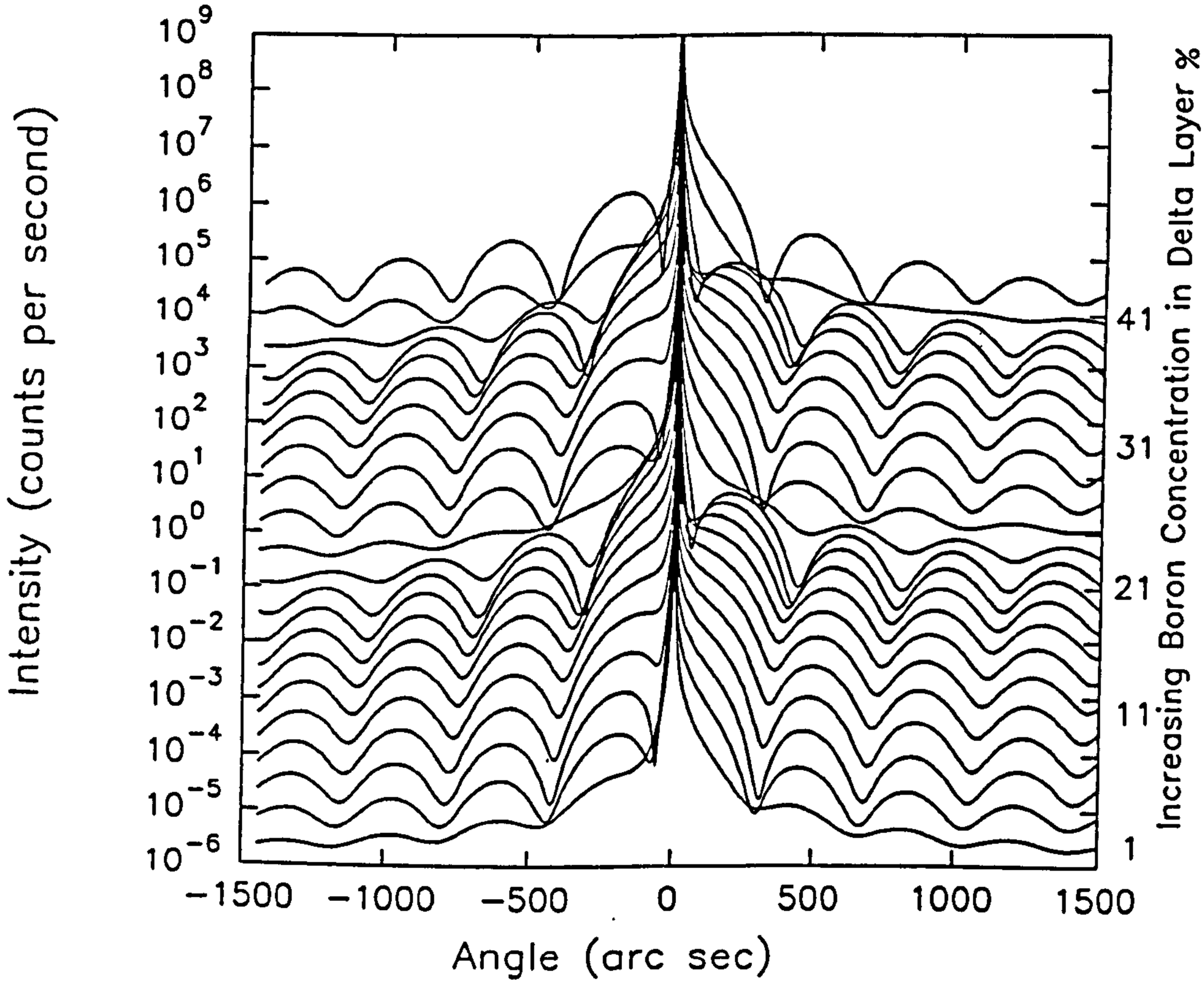

Fig 8.5 Simulations of the 004 rocking curve obtained from a 1 nm wide delta layer with boron concentration rising from 1 to 41 At%.

The phase difference between the capping layer and the substrate causes interference fringes which can be seen in the simulated rocking curves above. It can be seen that the interference fringes move to the right as the degree of compressive strain increases. Therefore from measurements of the spacing of the fringes from the Si peak the strain in the delta layer can be determined. However, there are discontinuities where the boron concentration is 25 At% and 41 At% these correspond to where the X-ray path difference between the diffracting planes of the capping layer and underlying material is equivalent to an integer number of wavelengths. The fringe pattern is seen to repeat itself and therefore it is necessary to take a second asymmetric reflection for example the 113 in order to uniquely determine the degree of strain present.

iii) delta layer width

The width of the delta layers can be found once the delta layer depth and dopant sheet density, (strain induced by the dopant), have been determined. If a sample is considered such as 10-33, a boron delta at a depth of 52 nm, and with a sheet density of $3.5 \times 10^{14} cm^{-2}$ the width can be determined through simulation. If one considers a uniformly doped layer of boron in which the sheet density is constant but the width of this layer is varied from 0.5 to 10 nm it is seen, Fig 8.6, that the relative heights of the peaks on opposing sides of the substrate peak change.

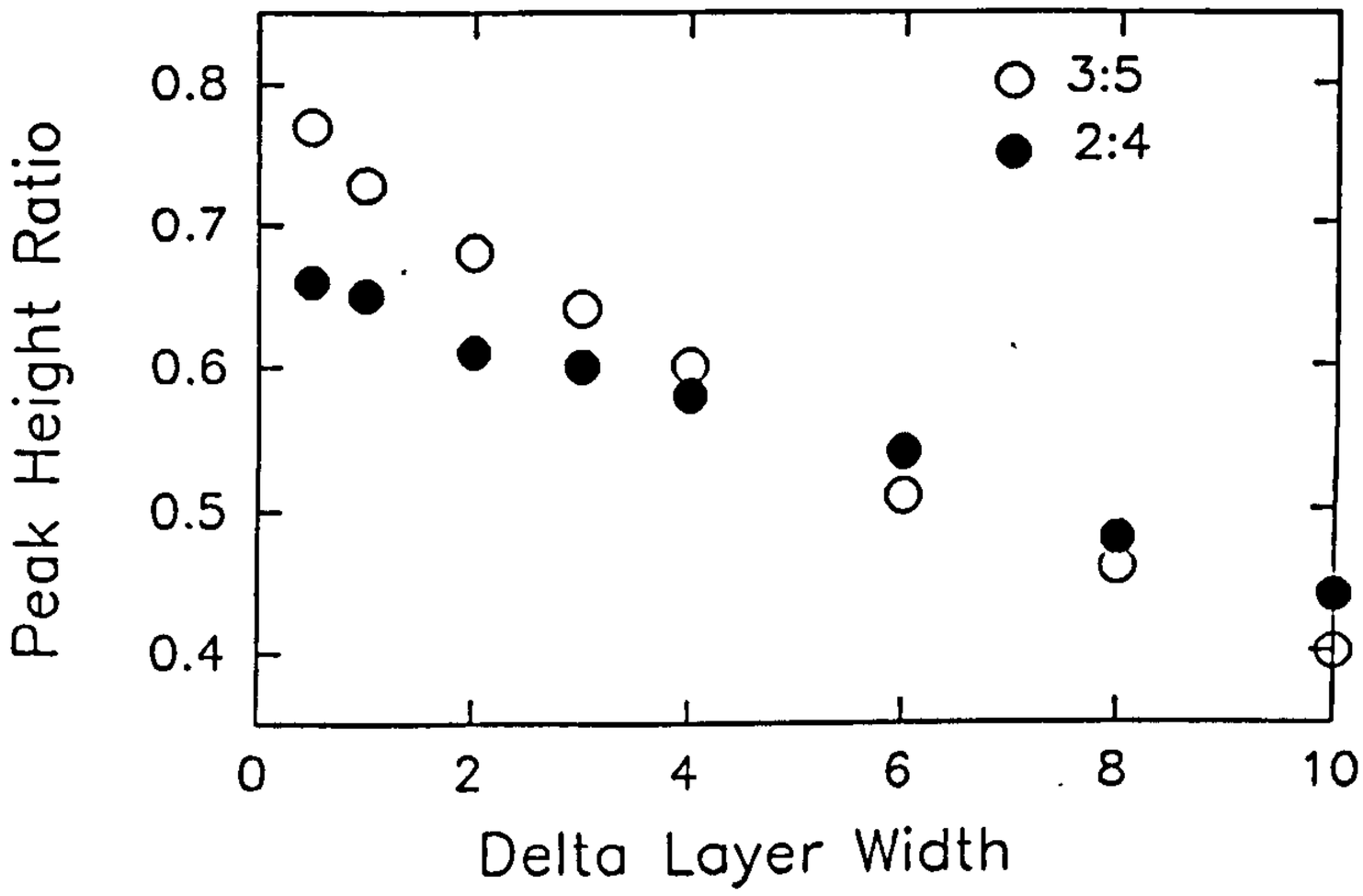

Fig 8.6 Peak height ratios for a boron delta layer with a sheet density of $3.5x10^{14}cm^{-2}$ are shown for increasing delta width, assuming a uniform doping profile.

The heights of the interference peaks is modulated by an envelope function, the shape of which is determined from the width of the delta layer itself, see section 3.7. This modulation envelope is centered at the angle corresponding to the state of strain in the delta layer itself and as the delta width increases the width of the modulating envelope will decrease. The consequence of this is that for a compressive dopant the fringes on the right-hand side of the main peak lose intensity with respect to those on the left hand side. Therefore, by considering this ratio of peak heights the width of the delta layer can be determined. For the delta layer considered here the 3:5 experimental ratio was found to be 0.8 ± 0.4 which corresponds to 0.3 ± 0.5 nm. Thus we have a technique capable of measuring down to the Angstrom level. However, it

is worth noting that this measurement provides information on the average position of the dopant and if a low composition tail were present in the doping profile then this technique would be unable to detect it.

8.4 Evaluation of Sb delta layers

Growth of Sb delta layers

The delta layers were grown in the V90S machine using an elemental antimony effusion source. A 300 nm Si buffer layer was first grown with a substrate temperature of 750°C and then the Si source was shuttered and the antimony source unshuttered allowing antimony to accumulate on the wafer surface. Then in order to overcome surface segregation effects [Mattey et al 1990, Zeindl et al 1987, Powell et al 1991a] the substrate temperature was lowered to below 250°C and a Si cap deposited. The structure was then annealed at 800°C in order to activate the antimony delta layer

Characterisation of Sb delta layers

The first delta layer examined was an antimony delta layer with a sheet density, determined by SIMS, to be 2 x 10^{14} cm^{-2} and with a Si capping layer of 50nm. Fig 8.7 shows the first rocking curve obtained for this sample using the 004 symmetric reflection and a single bounce beam conditioner.

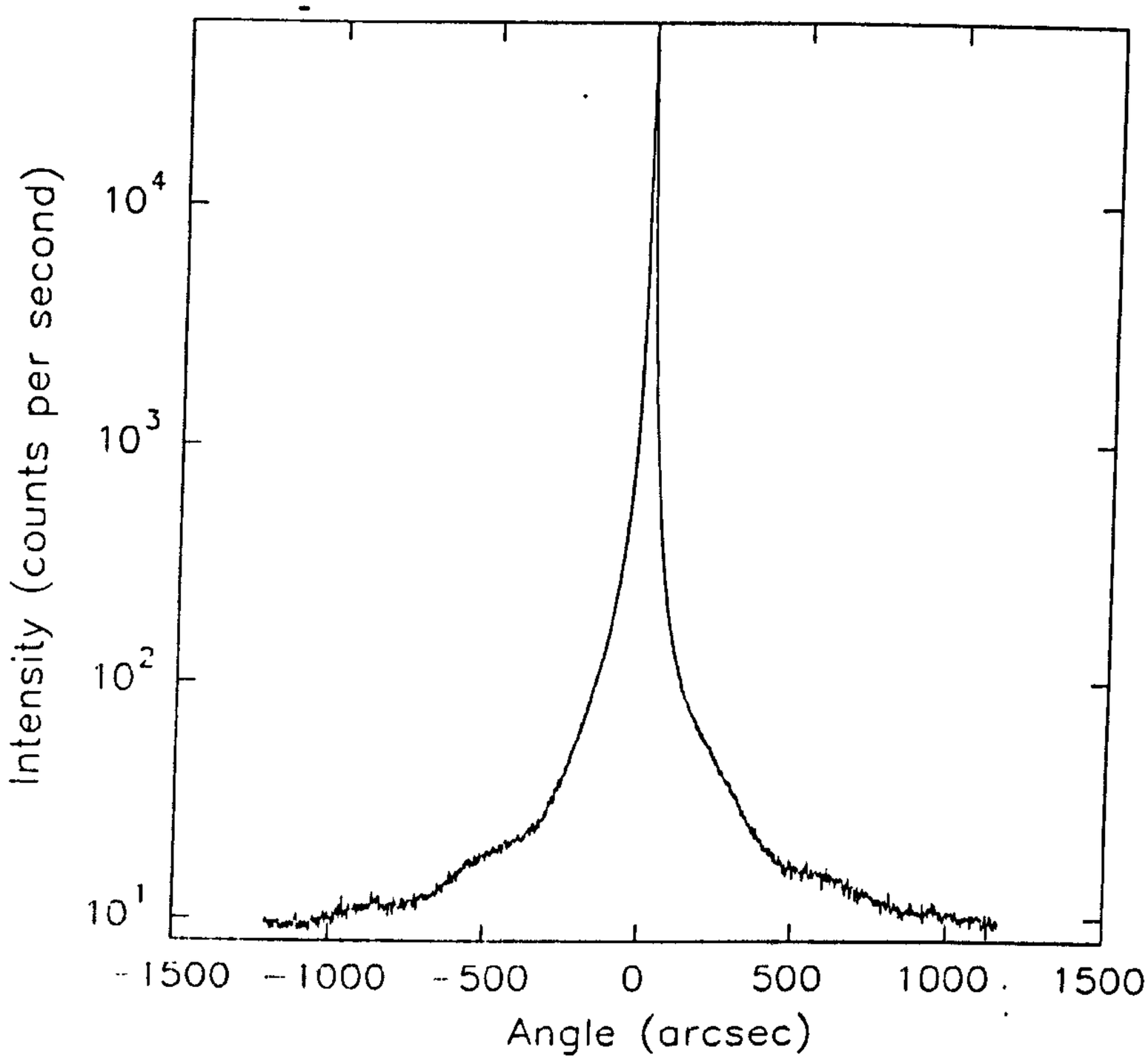

Fig 8.7 004 Double crystal rocking curve of $2x10^{14}cm^{-2}$ antimony delta layer with a single bounce beam conditioner.

The interference fringes can be seen on this curve, however they are not separated sufficiently from the main Si peak for good peak height measurements. In order to improve this two experimental improvements were made. The first one being the use of a four bounce beam conditioner which significantly reduces the tails associated with the main peak as seen in Fig 8.8.

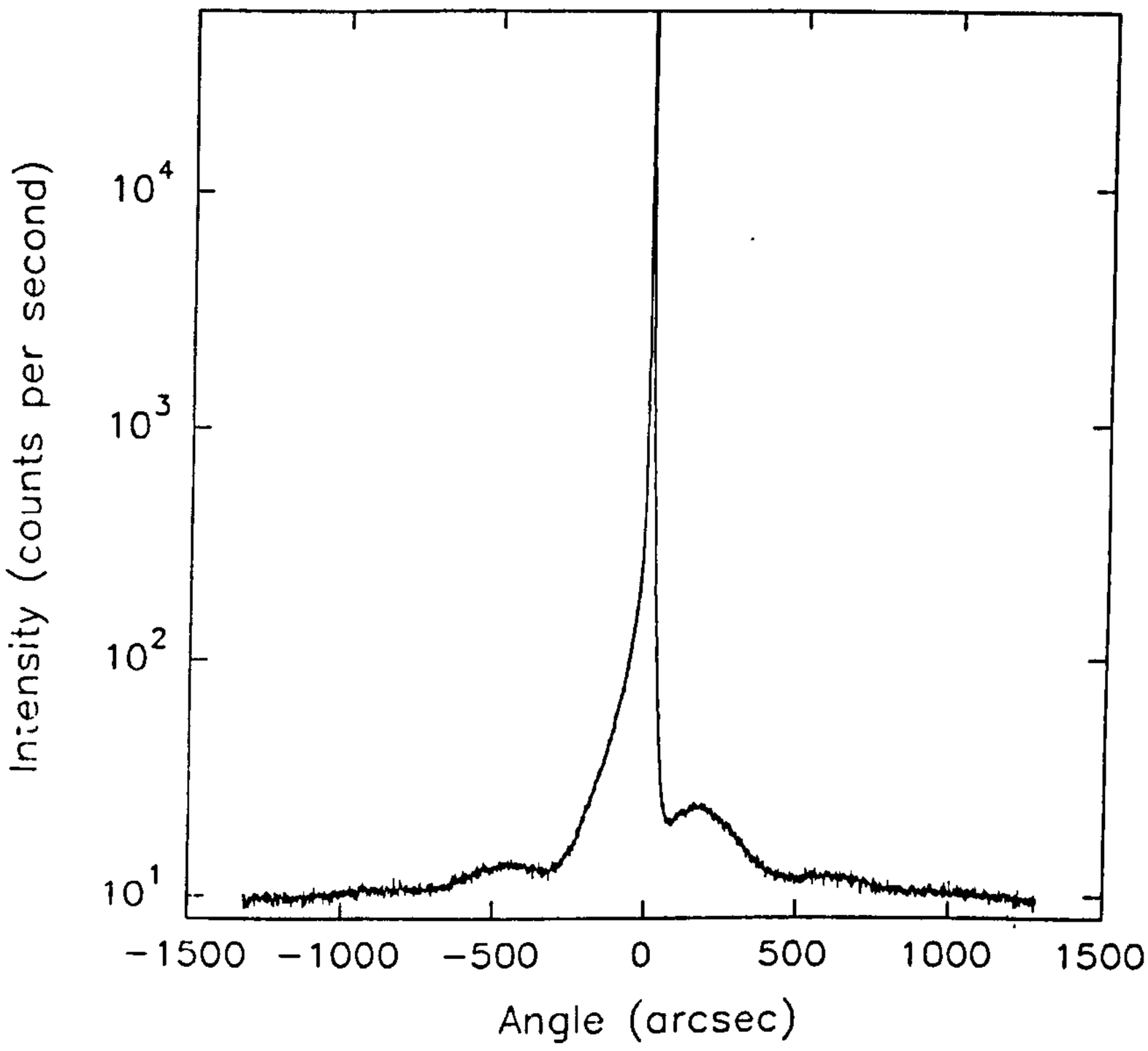

Fig 8.8 004 Double crystal rocking curve of $2x10^{14}cm^{-2}$ antimony delta layer with a four bounce beam conditioner.

The second improvement in signal to noise is to use the glancing incidence 113 reflection which will increase the diffracted signal from the top few microns of the structure thus enhancing the interference fringes, Fig 8.9. Even though the sheet density for the antimony dopant can not be found with X-ray diffraction the strain profile can be found and thus the width of this strain profile is calculated and thus the width of the delta layer can be inferred.

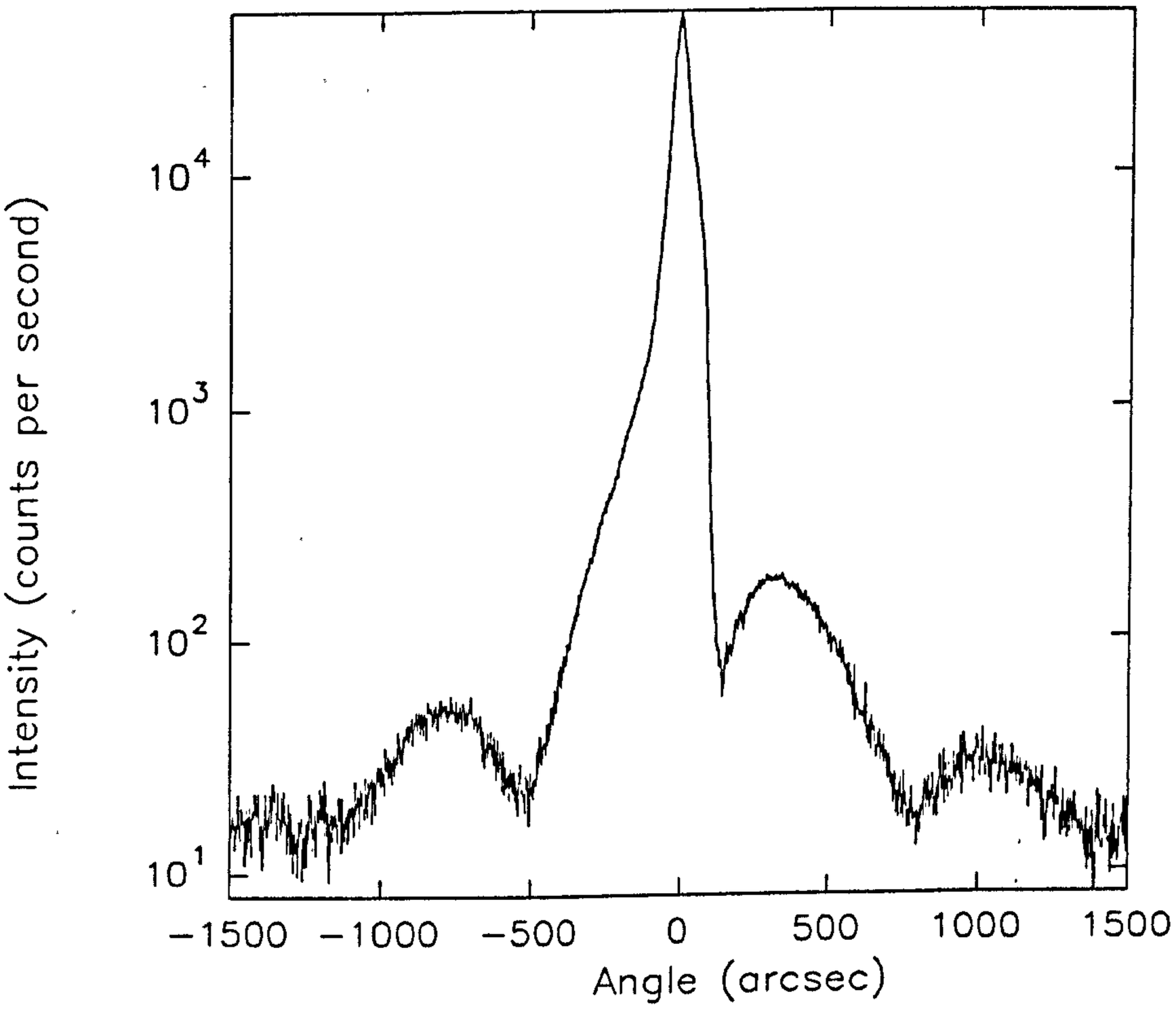

Fig 8.9 113 glancing incidence double crystal rocking curve of $2x10^{14}cm^{-2}$ antimony delta layer with a four bounce beam conditioner.

For the sample shown in Figs 8.6 to 8.9 the net expansion in the 004 direction was found to be 0.046 ± 0.005. Consideration of the modulation of the peaks enables an estimate of the delta layer width to be given as 1 ± 1 nm. X-sectional TEM analysis of this layer confirmed the thickness value and in addition shows the presence of precipitates in the antimony layer.

8.5 Boron delta layers

Growth of the Delta Layers

The growth of the delta layers was carried out in the V90S MBE machine using electron beam evaporated Si and Ge sources, and an elemental boron effusion cell. The Si substrates were given an in situ 850 ^{o}C anneal to remove SiO_2 and then a Si buffer deposited as the temperature cooled to the growth temperature of 480^{o}C to avoid dopant segregation [Jorke and Kibbel 1990] . Si was then grown to a thickness of 50 nm. The matrix fluxes were then shuttered off and boron was allowed to accumulate on the surface for up to ten minutes. This allows the surface to become saturated with B. This saturation is however limited to 1/2 monolayer ie $3.6x10^{14}cm^{-2}$ atoms [Headrick 1990]. Finally the capping layer was deposited. In section 8.3 the boron delta layer used as an example was shown to have a very sharp doping profile of only a few Angstroms. Fig 8.10 shows a TEM photograph of a single delta layer, as can be seen no precipitation is apparent and the layer is as sharp as the resolution of the micrograph.

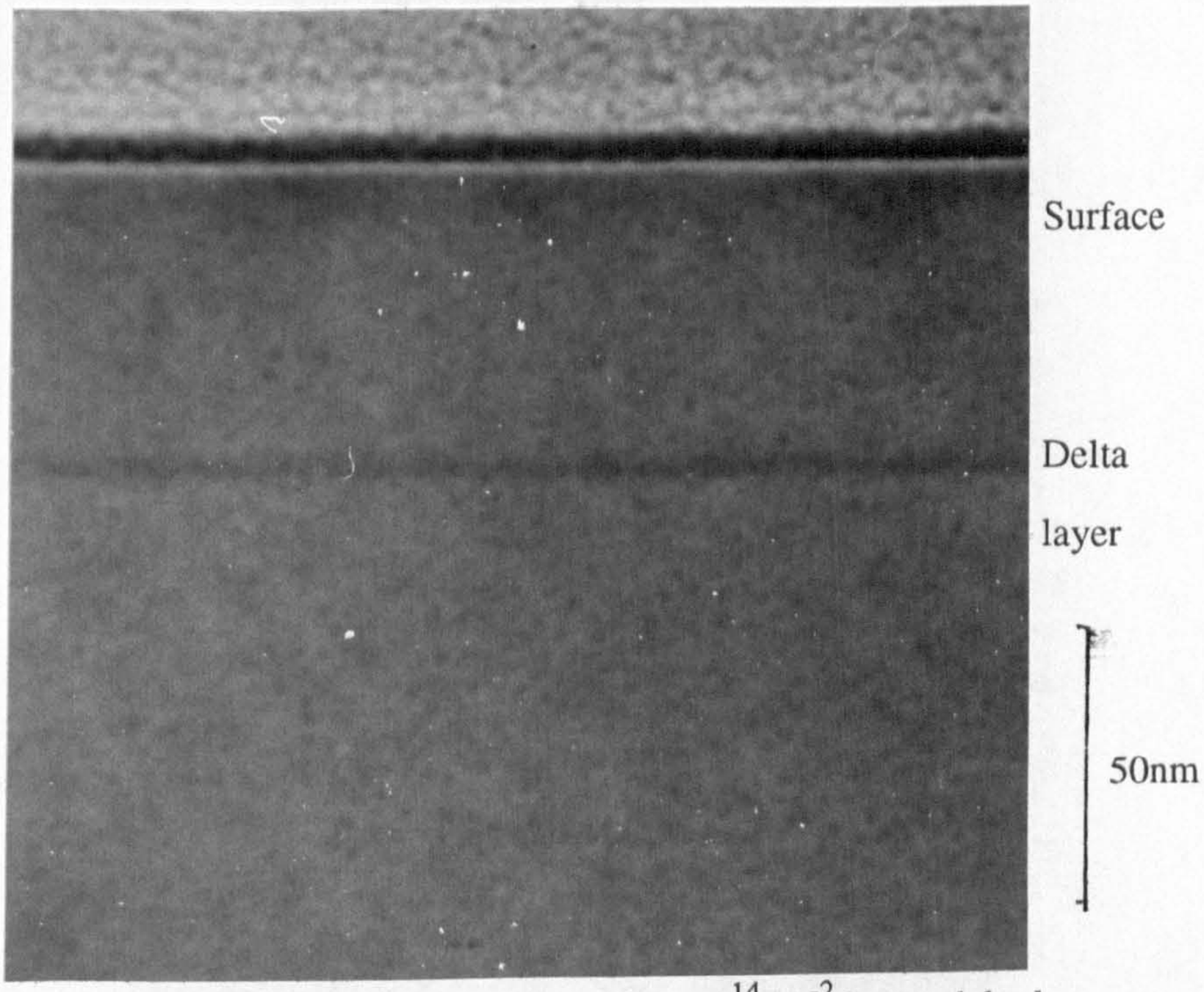

Fig 8.10 X-TEM micrograph of 10-33, a $3.5x10^{14}cm^{-2}$ boron delta layer

A large number of B delta doped structures were grown and rocking curves from three samples are shown in the next three figures. Fig 8.11 and 8.12 show the rocking curves obtained from two boron delta layers with cap thicknesses of 75 and 150 μm, the change in fringe spacing can be clearly seen. Fig 8.13 shows the rocking curve obtained from a five period superlattice structure consisting of 100 nm Si layers and $3x10^{14}cm^{-2}$ boron delta layers.

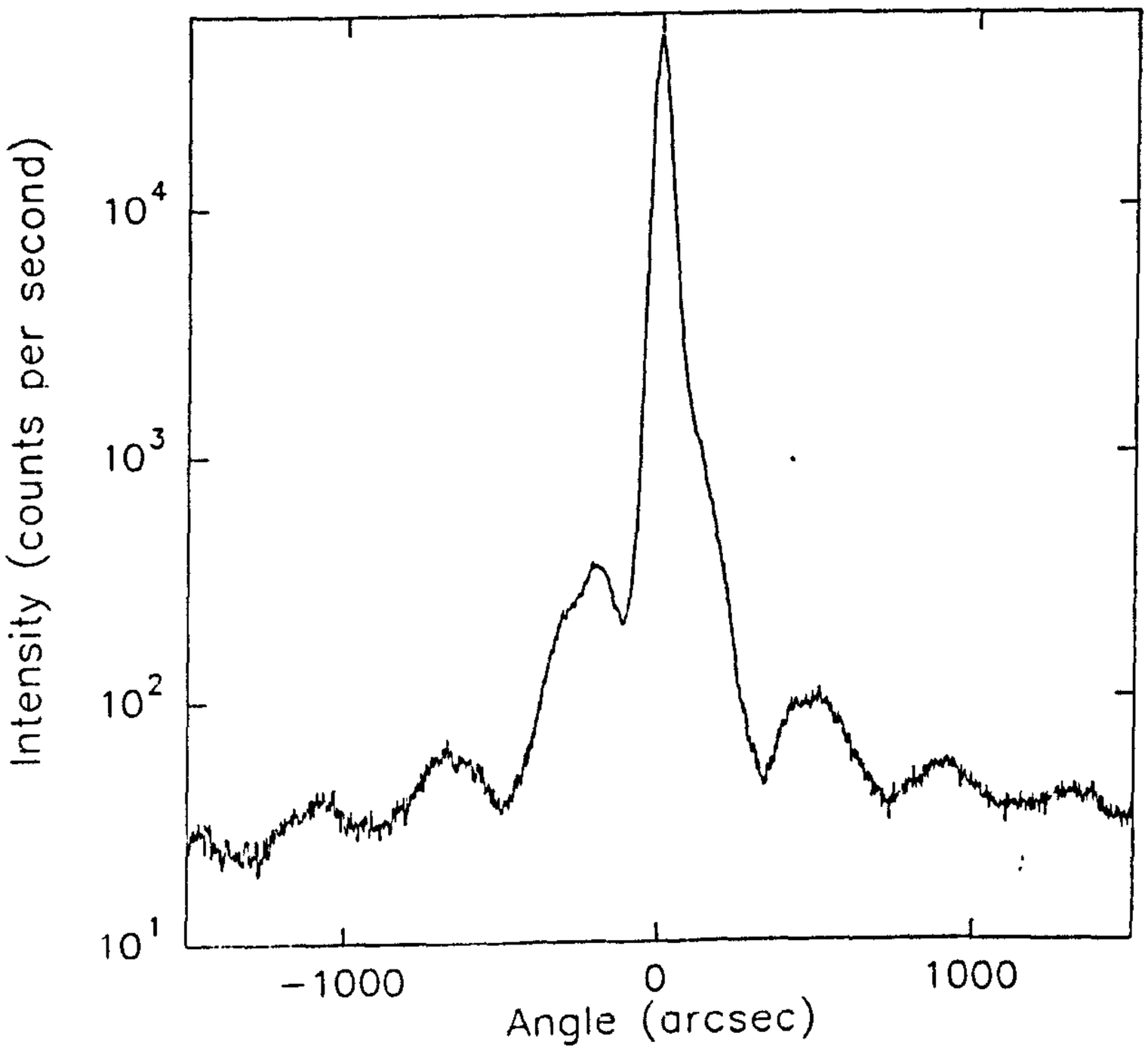

Fig 8.11 113 glancing incidence X-ray diffraction rocking curve of a 75μm deep $3x10^{14}cm^{-2}$ boron delta layer

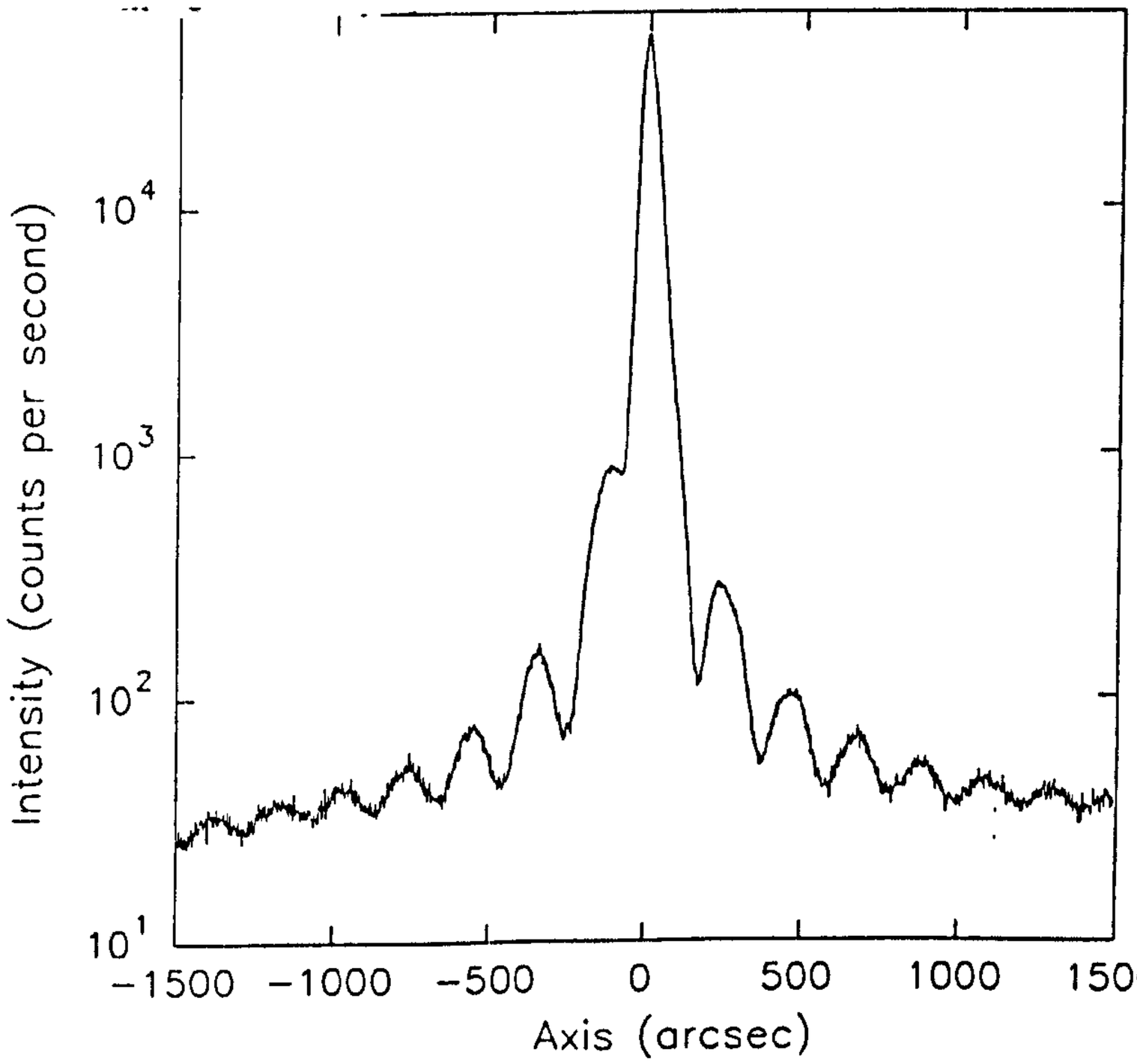

Fig 8.12 113 glancing incidence X-ray diffraction rocking curve of a 150μm deep $3x10^{14}cm^{-2}$ boron delta layer

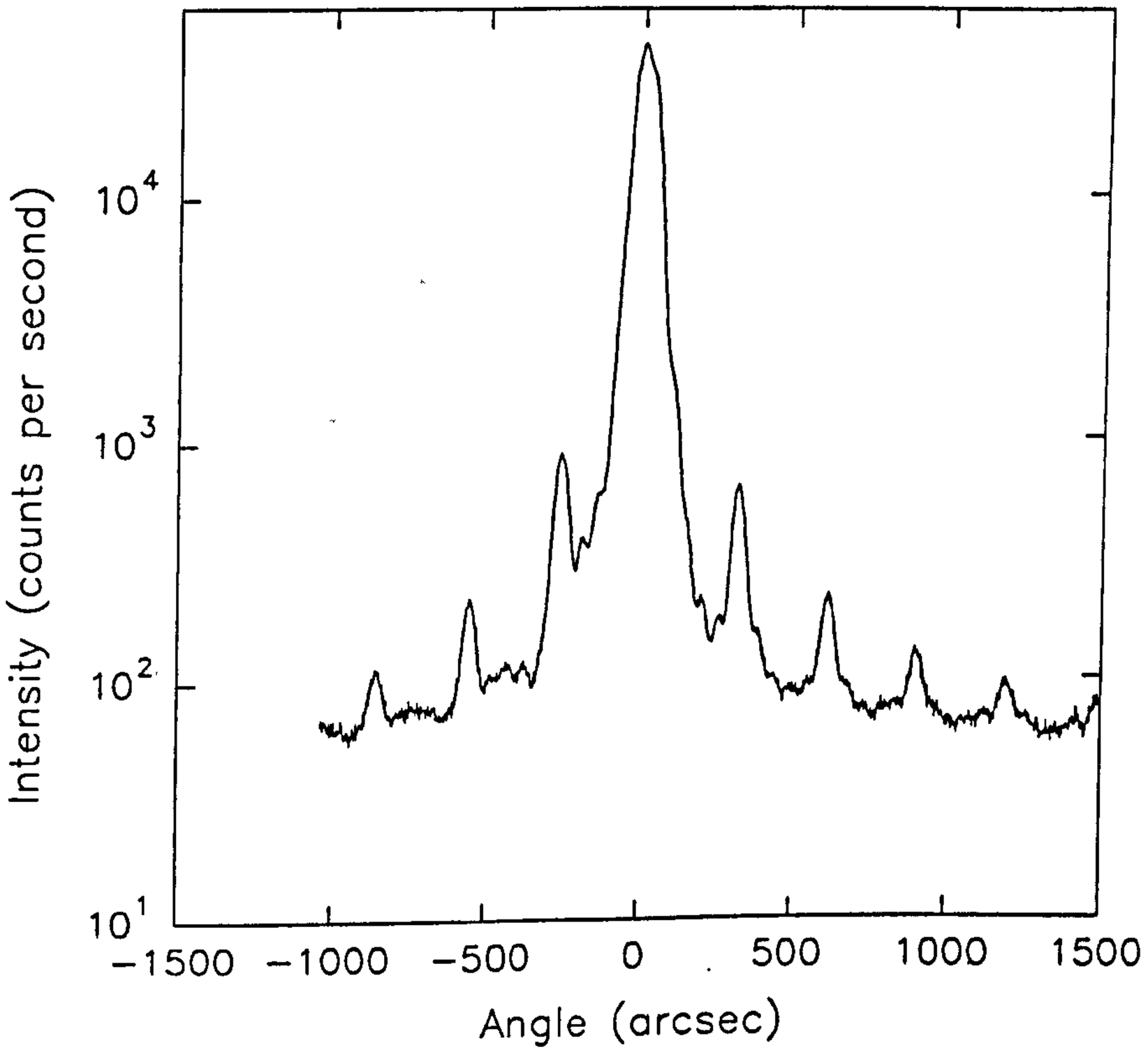

Fig 8.13 113 glancing incidence X-ray diffraction rocking curve of a superlattice structure consisting of 5 x ($3x10^{14}cm^{-2}$ boron delta layers separated by 100nm Si layers).

8.6 Annealing of B delta layers

In order for devices to be fabricated from delta doped structures it is necessary to undergo a number of thermal treatments. To investigate the effects of these, we annealed a boron delta layer at temperatures from 650 ^{o}C to 850 ^{o}C, the 113 rocking curves obtained from these samples are shown in Fig 8.14.

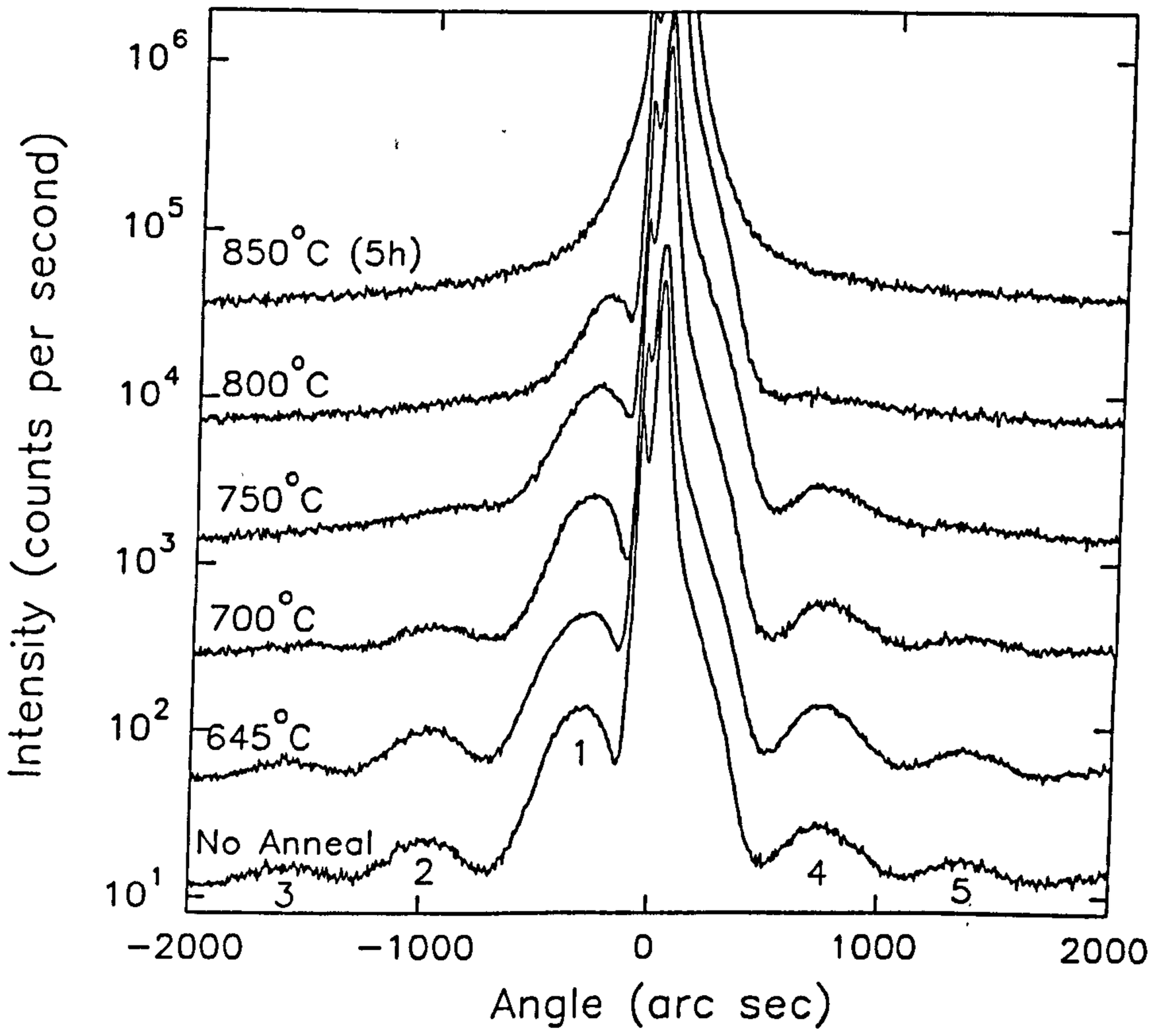

Fig 8.14 The effect of 1 hour anneals on a $3.6 \times 10^{14} cm^{-2}$ boron delta layer showing significant broadening at temperatures above $700^{o}C$

As the annealing temperature is increased diffusion of the boron is seen to occur. At temperatures above 750 ^{o}C the diffusion becomes too great and the loss of a clear interface between the delta layer and the surrounding Si reduces the interference effects seen. However at lower temperatures the delta width can be measured as below;

Table 8.2

Broadening Of B Delta Layers On Annealing

Anneal Temperature	Peak ratio		Delta Layer Width
	3/5	2/4	
No Anneal	0.8	0.67	0.3 ± 0.5 nm
650 °C 1 hour	0.75	0.65	0.8 ± 0.5 nm
700 °C 1 hour	0.6	0.55	4.5 ± 1 nm
750 °C 1 hour	-	0.3	15 ± 10 nm
800 °C 1 hour	-	-	-
850 °C 5 hours	-	-	-

These results show that even with the boron concentration in the delta layer as high as 10 At% the layer can be annealed at 650 °C for 1 hour and the width remains thinner than the 3 nm required for two dimensional confinement of the carriers.

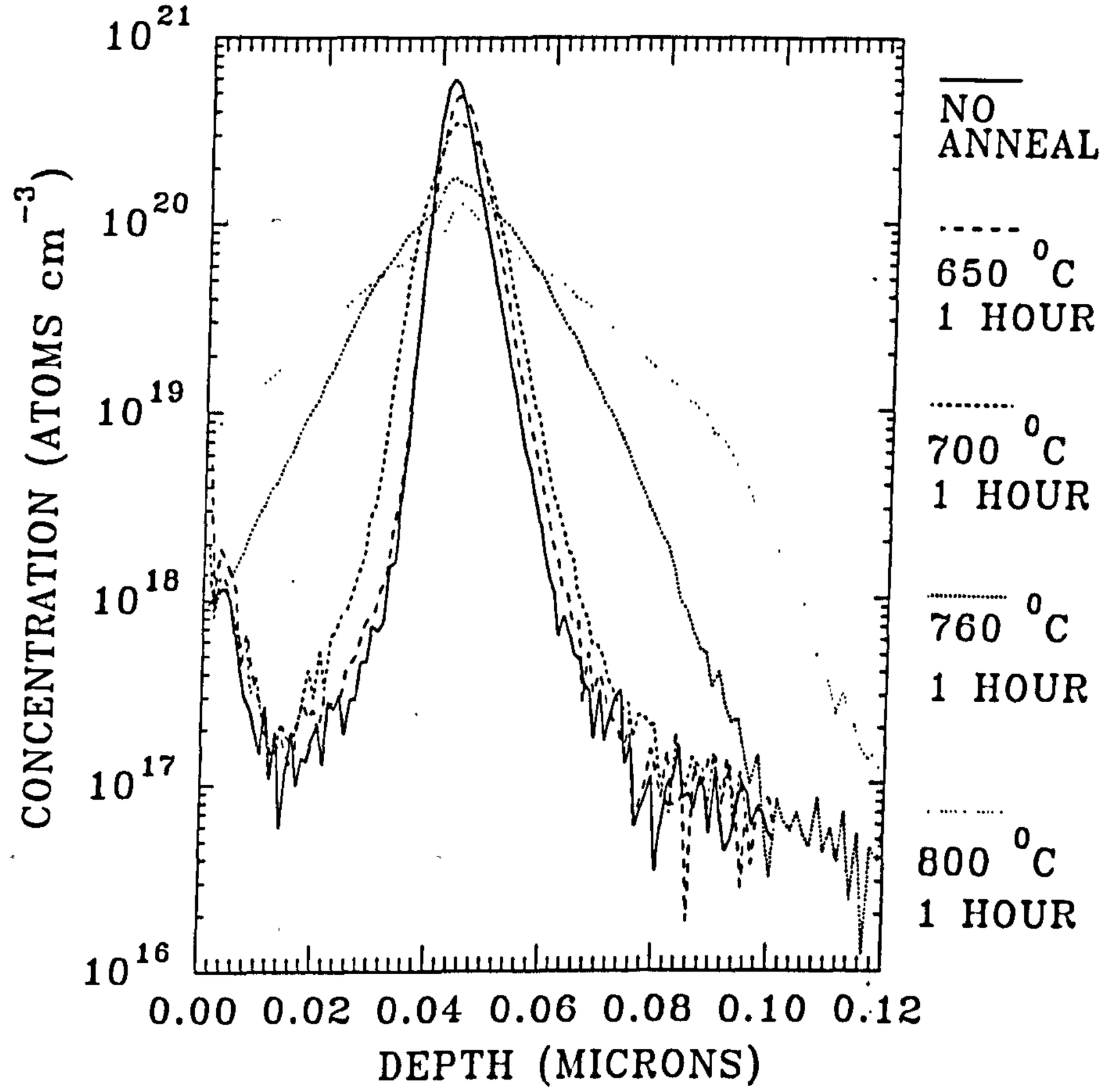

Fig 8.15 SIMS profiles of the $3.6 \times 10^{14} cm^{-2}$ boron delta layer showing significant broadening at temperatures above 700°C

These annealed samples were also examined using SIMS; the profiles obtained are shown in Fig 8.15. It can be seen that for anneals below 700°C no significant broadening can be detected. After higher temperature anneals some diffusion is observed, however, this broadening does not involve the whole profile as a significant proportion of the B has remained in the delta region. In order to explain this effect it is necessary to consider the solid solubility of the B at these higher temperatures. As the anneal temperature goes beyond 750°C the distances that the

boron atoms can diffuse becomes comparable to the delta layer width. The dopant can either diffuse away from the delta layer or it may cluster to form precipitates. This effect has been seen in B doped layers during growth [Parry et al 1992, Jackman et al 1989]. In these structures it is suggested that there is an equilibrium situation between the boron clustering in precipitates and diffusing away from the precipitates. The levels of the shoulders seen on the peaks in Fig 8.15 are within the range of shoulder values seen for highly doped boron layers thus indicating that the same effects may be occurring.

8.7 Delta layers in compound layers

When a delta doped layer is positioned within a SiGe epitaxial layer it is the SiGe peak and its associated Pendellosung fringes which are modulated by the presence of the delta layer. The presence of the Pendellosung fringes for the SiGe layer adds to the complexity of the rocking curve and makes determination of delta layer width and concentration more difficult. Fig 8.16 shows the rocking curve for a 100 nm 16 At% SiGe layer in the middle of which is a boron delta layer with a sheet density of $1.5 \pm 0.3 \times 10^{14}$ cm^{-2} (SIMS).

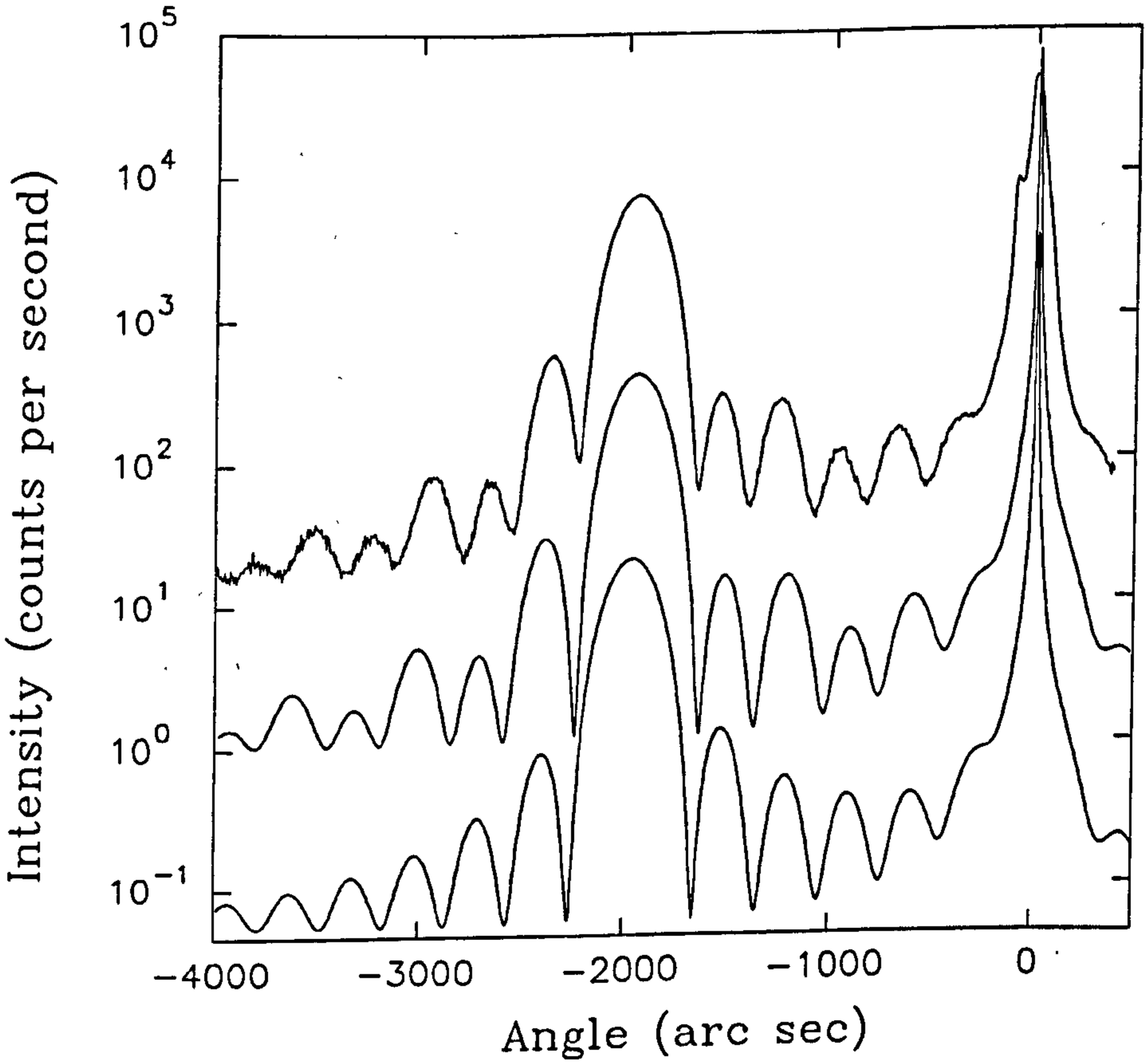

Fig 8.16 (top) Experimental rocking curve obtained from a 100 nm SiGe layer with a boron delta layer at a depth of 50 nm. (middle) Simulation with a boron delta layer with a sheet density of 1.3 x $10^{14}cm^{-2}$. (bottom) Simulation of the SiGe epitaxial layer with no delta layer.

By using dynamical theory simulation the sheet density of activated boron was found to be 1.3 ± 0.2 x $10^{14}cm^{-2}$ which agrees with the sheet boron density as determined by SIMS (1.5 ±0.3 x $10^{14}cm^{-2}$). This result indicates that as with the delta layer in Si the boron is fully activated in the SiGe matrix.

8.8 Conclusion

In this chapter the double crystal diffraction technique has been developed to provide a non destructive method of characterising sub-monolayer delta layers in Si material. It has been shown that the technique is capable of resolving the width of delta layers to ±0.5 nm. In addition to this the depth of the delta can be found from the period of the fringes and the strain induced by the dopant is found, (as this is what the X-Ray diffraction actually measures). This improvement in the delta width resolution has allowed studies of the dopant diffusion and precipitation as a function of temperature showing that B delta layers remain well defined in width, i.e., 1nm or less, for anneals in which the total thermal processing does not exceed 650°C for 1 hour. As temperature / time values exceed this, the diffusion of the boron away from the delta layer can be clearly seen.

Chapter 9

Conclusions

This thesis has considered two main areas; first the characterisation of low dimensional structures, and secondly, an investigation of the relaxation properties of SiGe with a view to making relaxed buffer layers with low threading dislocation densities.

Consider first the low dimensional structure characterisation. The use of X-ray diffraction and reflectivity has enabled SiGe structures to be characterised to sub nm accuracies in this work. X-ray diffraction has been demonstrated to be a fast and non-destructive method for general composition and layer thickness measurement with a sufficiently fast turn-around time to allow calibration of the growth system. It has also been used to provide information on the repeatability of layer thicknesses, ie z direction uniformity, during growth runs allowing period dispersion to be measured to ± 0.3nm. By demonstrating the high levels of x, y, and z direction uniformity of the epitaxial layers, further experiments can be carried out on any region of a wafer without fear of varying material parameters. The diffraction characterisation of highly dislocated layers has been furthered by the use of triple crystal diffraction. This has allowed structural analysis of complicated, relaxed buffer structures.

X-ray reflectivity has also been examined as a characterisation technique for SiGe structures. It has proved to be of great use particularly for structural characterisation of thin, (<100nm), or highly dislocated layers where the diffracted beam from such layers becomes too weak for X-ray diffraction to give accurate results. In addition X-ray reflectivity has been used along with T.E.M. to examine interface roughness in SiGe superlattice structures, showing the interfaces to have a short range r.m.s. roughness of ~ 0.5 nm. However, where the Ge content of the alloy layers is high (>30%) then a long range roughness (~70 nm) is seen on the SiGe layers which may be indicative of the start of three dimensional growth. Further work is required to examine the possibilities of reducing this roughness by altering growth conditions such as reducing the growth rate and determining the effect of strain in this effect by growing structures on relaxed SiGe buffers.

The characterisation of low dimensional boron and antimony doping structures in Si has also been achieved. Double crystal X-ray diffraction using channel-cut collimators and computer simulation has been shown to be an excellent technique for probing these layers. It is capable of determining the delta layer width to ±0.5 nm and in addition providing information on the state of strain (for boron doping this also gives the degree of activation) and depth of the layer. The high resolution available from the diffraction technique has enabled an annealing study to be carried out which demonstrates that no significant broadening of the delta layer occurs for anneals less than 650°C for 1 hour thus showing that the delta layers will be able to withstand the temperatures involved in their processing into devices. Higher temperature anneals of a $3.5x10^{14}cm^{-2}$ delta layers produce both a broadening of the dopant layer due to diffusion and precipitation of the boron due to the

concentration exceeding the solid solubility of the boron in the Si matrix. Thus for lower doped layers this precipitation is not expected to be present.

Initial work has been carried out on the use of X-ray fluorescence as a technique to provide depth profiles of elements present within the top few microns of a sample. Preliminary results show that Ge in a SiGe structure can be profiled and further refinements of the technique should allow depth profiles to be obtained for dopant and perhaps impurity atoms.

Alongside the examination of X-ray characterisation techniques for SiGe the relaxation properties of SiGe have been considered.

Limited area growth of SiGe has been achieved on mesa islands showing that for small dimensions, (<10μm for a lattice mis-match of 0.001), elastic relaxation becomes dominant and allows strain relaxation without the creation of dislocations. By creating rectangular mesas an asymmetrical relaxation of strain is created which may allow the design of novel device structures.

The production of relaxed buffer layers with low dislocation levels would allow the production of a number of novel devices and possibly lead to a quasi-direct bandgap material compatible with Si VLSI technology. Initially single SiGe epitaxial layers grown on Si to well beyond the metastable critical thickness were considered. For these the relaxation of strain was found to be incomplete and a relationship between the residual strain and the thickness/metastable critical thickness discovered. However these buffer layers had a high level of threading dislocations ($10^{10}cm^{-2}$) and further work on these was eclipsed by the graded layer buffer structures.

Investigation of SiGe layers grown in the metastable region showed that upon annealing, and consequent relaxation, layers with lower levels of strain produced longer misfit dislocations and consequentially fewer threading dislocations. For the

annealing temperatures available in an MBE system ie ~ 850°C, layers not more than 4 times the equilibrium critical thickness showed no sign of relaxation and significant relaxation (several percent to near total relaxation) was found in layers more than 10 times the equilibrium critical thickness. The long misfit dislocations found in these layers led to the growth of the stepped buffer layers where the layers of the buffer were grown at 550°C and then annealed prior to the growth of the next layer of slightly higher Ge composition. These relaxed buffer layers were found to have threading dislocation levels of ~ $10^6 cm^{-2}$ which may be sufficiently low to allow device fabrication. In addition the roughness of the step graded/annealed buffer layers was found to be only 1.5 nm whereas similar structures grown at higher temperature exhibit surface roughnesses of the order of 5 nm. Thus there is great promise for optoelectronic devices grown on this low dislocation, almost planar, buffer structure.

References

Azaroff L.V, Kaplow R, Kato N, Weiss R.J, Wilson A.J.C, and Young R.A, X-Ray Diffraction 1974, McGraw-Hill, New York.

Barlow Private Communication.

Batterman B.W, and Cole H, 1964 Dynamical diffraction of X-rays by perfect crystals. Rev of Mod Phys **36** 681.

Becker G.E, and Bean J.C 1977, J.Appl Phys **48** 3395.

Becker P, and Scheffler M, 1984. Acta.Cryst.Suppl.C (1984) 341.

Bio-Rad manual, 1989 semiconductor profiler plotter PN4300, Bio-Rad Microscience Division, USA.

Born M, and Wolf E, 1970, Principles of Optics page 51 , Pergamon Press, Oxford.

Bowen D.K, Tanner B.K, Loxley N, Cooke L, and Capano M, Mat. Soc. Symp. Proc **206** (1991) 113.

Bradwell M.C, and Rodes J.G, 1985 J Vac.Sci.Technol **A3** 472.

Braslau A, Pershan P.S, Swislow G, Ocko B.M, and Als-Nielsen J, 1988, Phys. Rev. A **38** 2457.

Briggs D, and Seah M, Practical Surface Analysis, J Wiley and Sons, to be published.

Burton W.K, Cabrera N, Frank F.C, 1951, Philos. Trans. Roy. Soc. **243A**, 299 (1951).

Cargill G.S, III, Angilello J, and Kavanagh K.L, 1988. Phys.Rev.Lett **61** 1748.

Cembali F, Fabbri R, Servidori M, Zani A, and Iyer S, 1991, Proc.Mat.Res.Soc **208** 225.

Cohen B.G 1966, Solid State Electronics **10** 33.

Dismukes J.P, Ekstrom L, and Paff R.J, 1964 J.Phys. Chem. **10** 3021.

Dodson B.W, Tsao J.Y, 1988, Phys Rev **B 38** 12383.

Dohler G.H, 1978, Surf.Sci. **73** 97.

Dowsett M.G, priv comm.

Dowsett M.G, Barlow R.D, Fox H.S, Kubiak R.A.A and Collins R, 1992, J.Vac.Sci.Technol. **10** 336.

Du Mond, J.W.M., Phys Rev. **52**, 872 (1937).

Eaglesham D.J, Kvam E.P, Maher D.M, Humphreys C.J, and Bean J.C, 1989 Phil Mag **A 5** 1059.

Eaglesham D.J, Gossmann H.J, Cerullo M, Pfeiffer L.N, and West K.W, 1991, J.Cryst.Growth **111** 883.

Fewster P.F, and Curling C, 1987, J. Appl. Phy **62** 4154 .

Fitzgerald E.A, Kirchner P.D, Proano R, Pettit G.D, Woodall J.M, and Ast D.G, 1988, Appl.Phys.Lett **52** 1496.

Fitzgerald E.A, Xie Y.H, Green M.L, Brasen D, Kortan A.R, Mii Y.J, Michel J, Weir B.E, Feldman L.C, and Kuo J.M, 1991, Proc Mat Res Soc **220** 211.

Freund L.B, Bower A, and Ramirez,1989, Proc.Mat.Res.Soc. **130** 139.

Fukuhara A, and Takano Y, 1977. Acta.Cryst. **A33** 137.

Gell M.A, 1988. Phys Rev **B 38** 7535.

Gibbins C.J, Tuppen C.G, and Hockly M 1989 Appl.Phys.Lett **54** 148.

Gibbins C.J, Tuppen C.G, and Higgs V, 1991, Proc Mat Res Soc **220** 205.

Hart M, 1971, Rep. Prog. Phys. **34** 435.

Headrick R.L, Weir B.E, Levi A.F.G, Eaglesham D.J, and Feldman L.C, 1990, Appl. Phys. Lett. **57**(26), 2779.

Horn M, Gotter U, and Henzler M, 1987 J.Vac.Sci.Technol **B6** 727.

Houghton D.C, 1990 Appl.Phys.Lett **57** 2124.

Houghton D.C, Gibbings C.J, Tuppen C.G, Lyons M.H, and Halliwell M.A.G, 1990, Appl.Phys.Lett **56** 460.

Houghton R.F, 1989 PhD Thesis. Warwick University, UK.

Hull R, Bean.J.C, Eaglesham D.J, Bonar M.J and Buescher C, 1989 , Thin Solid Films, **183** 117.

Iida A, Yoshinaga A, Sakurai K, and Gohshi Y, 1986 Anal. Chem **58** 394.

Jackman T.E, Houghton D.C, Jackman J.A, Denhoff M.W, Kechang S, McCaffrey J, and Rockett A, 1989, J. Appl. Phys. **66**(5), 1984.

Jain S.C, and Hayes W, 1991, Semicond.Sci Technol. **6** 547.

James R.W, 1948, The optical properties of the diffraction of X-rays, Bell, London.

Jenichen.B, Kohler R,and Mohling W, 1988 J.Phys.E:Sci Instrum. **24** 1062.

Jorke H, and Kibbel H, 1990, Appl.Phys.Lett **57** 1763.

Jorke H, Kibbel H, Shaffler F, and Herzog H-J, 1989, Thin Solid Films **183**, 307.

Kasper E, and Bean J.C, 1988 , Silicon Molecular Beam Epitaxy, CRC Press Florida.

Kavanagh K.L, Chang C.P, Cargill G.S, and Boehme R.F, IBM internal report.

Kiessig H, 1931 Ann.Physik, **10** 715.

Koch F, and Zrenner A, 1989, Materials Science and Engineering, **B1** (1989) 221.

Kubiak R.A.A, Leong W.Y, and Parker E.H.C 1985 a, Appl. Phys. Lett **46** 565.

Kubiak R.A.A, Leong W.Y, and Parker E.H.C 1985 b, J.Elec Soc **132** 2738.

Kubiak R.A.A, Leong W.Y, and Parker E.H.C, 1985 c, J.Vacuum Sci. Technol. **B3** 592.

Kubiak R.A.A, Newstead S.M, Powell A.R, Parker E.H.C, Whall T.E, Naylor T, and Bowen D.K, 1992 submitted to J.Vacuum Science.

Landolt-Bornstein, 1987 Numerical data and functional relationships in science and technology, Springer-Verlaag Berlin, vol 22 p 291 .

Langevelde F.van, Tros G.H.J, Bowen D.K, and Vis R.D, 1990 Nucl. Instr. and Meth in Phys. Res. **B49**, 544.

LeGoues F.K, Meyerson B.S, and Morar J.F, 1991 Phys Rev Lett **66** 2903.

Loxley N, Bowen D.K, and Tanner B.K, 1991, Mat. Soc. Symp. Poc **208** 107.

Luryi S and Suhir E, 1986, Appl.Phys.Lett **49** 140.

Magee C.W, and Honig R.E, 1982 Surface and Interface Analysis **4** (2) 35.

Manasevit H.M, Gergis I.S, and Jones A.B, 1982 APL
41 464.

Matthews J.W, and Blakeslee A.E, 1974 J.Cryst. Growth **27** 118.

Mattey N.L, Hopkinson M, Houghton R.F, Dowsett M.G, Whall T.E, Parker E.H.C, Booker G.R, and Whitehurst J, 1990, Thin Solid Films **15**, 184.

Mullins W.W, and Hirth J.P 1963, J.Phys.Chem.Solids **24** 1391.

Nevot L, and Croce P, 1980, Revue Phys Appl **15** 761.

Parry C.P, Newstead S.M, Barlow R.D, Augustas P, Kubiak R.A.A, Dowsett M.G, Whall T.E, and Parker E.H.C, 1991. Appl.Phys.Lett **58** 481.

Parry C P, Kubiak R A, Newstead S M, Whall T E and Parker E H C P, 1992, J. Appl. Phys. **71** (1) 118.

Parratt L.G, 1954, Phys Rev **95** 395.

Patel G, 1990 PhD Thesis. Warwick University, UK.

Parratt L.G, 1954, Phys Rev **95** 395.

Pearsall T.P, and Bean J.C, 1986 IEEE Electron Device Lett **7** 308.

Pearsall T.P, Vandenberg J.M, Hull R, and Bonar J.M 1989 Phys.Rev.Lett. **63** 2104.

People R, 1985, Phys.Rev.B **32** 1405.

People R and Bean J.C 1985. Appl Phys Lett **48** 538.

Perovic D.D, priv comm.

Perovic D.D, Weatherly G.C, Baribeau J.M, Houghton D.C, 1989 Thin Solid Films **183** 141.

Philipp H.R and Taft E.A., 1982, J.Appl. Phys. **53** 5224.

Pike W.T, Brown L.M, Kubiak R.A.A, Newstead S.M, Powell A.R, Parker E.H.C, and Whall T.E, 1991a, J.Cryst Growth **111** 925.

Pike W.T, Kubiak R.A.A, Parker E.H.C, and Whall T.E, 1991b Proc. Mat. Res. Soc. **220** 223.

Pinsker Z.G, 1978, Dynamical scattering of X-rays in crystals. Springer-Verlag Berlin Heidelberg.

Powell A.R, Kubiak R.A.A, Newstead S.M, Parry C, Mattey N.L, Smith D.W, Brighten J.C, Emeleus C.J, Naylor T, Basaran E, Whall T.E, Dowsett R.D, Barlow R.D, Parker E.H.C, and Bowen D.K, 1991a, J.Cryst.Growth **111** 907.

Powell A.R, Mattey N.L, Kubiak R.A.A, Parker E.H.C, Whall T.E, and Bowen D.K, 1991b, Semicond Sci. Technol. **6** 227 .

Powell A.R, Kubiak R.A.A, Parker E.H.C, Bowen D.K, and Polcarova M, 1991c Proc. Mat. Res. Soc **206** 161.

Powell A.R, Kubiak R.A.A, Whall T.E, Parker E.H.C, and Bowen D.K, 1991d, Proc. Mat. Res. Soc. **220** 115.

Powell A.R, Kubiak R.A.A, Whall T.E, Parker E.H.C, and Bowen D.K, 1991e, Proc. Mat. Res. Soc. **220** 227.

Powell A.R, Bradler J, Thomas.C.R, Kubiak R.A.A, Hudson J, Bowen D.K, and Wormington M, 1992, Proc. Mat. Res. Soc. **238** 653.

Ravi K.V 1981 Imperfections and impurities in Semiconductor Silicon. John Wiley and Sons, New York page 215.

Roth A, "Vacuum technology", (North-Holland publishing Co., Amsterdam, 3rd Edition) 1979.

Tanner B.K, and Bowen D.K, 1980, Characterisation of crystal growth defects by x-ray methods, Plenum Press, London.

Tsaur B.Y, Geis M.W, Fan J.C.C, and Gale R.P, 1981 Appl.Phys.Lett **38** 779.

Tuppen C.G, Prior K.A, Gibbings C.J, Houghton D.C, and Jackman T.E, 1988, J.Appl.Phys **64** 2751.

Tuppen C.G, and Gibbins C.J, 1989, Thin Solid Films **183** 133.

Tuppen C.G, Gibbins C.J, and Higgs V, 1991a, Proc. Mat. Res. Soc. **220** 205.

Tuppen C.G, Gibbins C.J, Hockly M, and Halliwell M.A.G 1990, Appl.Phys.Lett **56** 140.

Tuppen C.G, Gibbins C.J, and Hockly M, 1991b. Proc. Mat. Res. Soc. **220** 187.

Schubert E.F, 1990 J.Vac.Sci.Technol **A8** 2980.

Schwarzchild M.M, 1928, Phys. Rev. **32**, 162.

Sinha S.K, Sirota E.B, Garoff S, and Stanly H.B, 1988 Phys.Rev.B, **38** 2297.

Shur M, 1986 , GaAs Devices and Circuits, Plenum Press 1986.

Van de Walle C.G, and Martin R.M, 1986, Physical Review **B 34** (8) 5621.

Willams K.L ,1987 , Introduction to X-ray Spectrometry, Allen and Unwin, Park Lane, Hemel Hempstead, UK.

Williams P, 1979, Surf Sci **90** 588.

Wormington M, Bowen D.K, and Tanner B.K, 1992, Proc. Mat. Res. Soc. **238** 119.

Yamaguchi K, Shiraki Y, Katayama Y, and Murayama Y, 1983. Jap Journal of Applied Physics **22** Supplement **22-1** 267 .

Zachai R, 1991, Proc. Mat. Res. Soc. **220** 311 .

Zeindil H.P, Wegehaupt T, Eisele I, Oppolzer H, Resinger H, Tempel G, and Koch F. 1987, A.P.L. **50** 1164.